

Defects and Distortions in Hybrid Halide Perovskites

Lucy Dorothy Whalley

Department of Materials

Imperial College London

A thesis submitted for the degree of

Doctor of Philosophy

August 2019

Abstract

Hybrid halide perovskites are being developed for use as an absorber material in solar cells, alongside other optoelectronic applications such as a light-emitting diode emitter or lasing material. Research interest in this material family has grown quickly over the decade, as photovoltaic efficiencies have increased from 10.9% in 2012 to the current record of 25.2%. In addition, the synthesis procedure is a low-temperature solution-deposition method which, when commercialised, may lead to a reduction in solar module production prices.

Materials theory and simulation has struggled to keep up with the rapid experimental progress as many of the physical processes that determine solar cell performance are related to defects (e.g. carrier capture and recombination) and temperature (e.g. degradation and ion migration), which are challenging to model from first-principles. Density Functional Theory (DFT) is used to predict ground-state properties only, and a typical DFT calculation for a crystalline material assumes that the material is perfectly periodic, with no point or extended defects. To model temperature effects or defects it is necessary to combine DFT with other methods, such as lattice dynamics or finite-size corrections. The aim of this PhD project is to move away from the idealised picture of a perfect material at absolute zero and towards a more realistic picture, where the defects and distortions of hybrid halide perovskites are considered.

Contents

Copyright	7
Statement of Authorship	8
Publications	9
Acknowledgements	10
List of Figures	12
List of Tables	15
Abbreviations	16
Symbols	17
1 Introduction	19
1.1 Motivation	19
1.1.1 Energy use and global warming	19
1.1.2 The sun as an energy source	20
1.1.3 Beyond silicon: the need for new photovoltaic materials	21
1.2 Key concepts in photovoltaics	23
1.2.1 Operating principles	23
1.2.2 Carrier recombination	27
1.2.3 Design principles for absorber materials	29
1.3 Summary	32
1.4 Thesis outline	32

2 Simulation of hybrid halide perovskites	34
2.1 Introduction	34
2.2 Crystal structures and lattice dynamics	35
2.2.1 Phase diversity	35
2.2.2 Local and average crystal environment	36
2.2.3 Thermodynamic and kinetic stability	37
2.2.4 Anharmonic lattice vibrations and thermal conductivity	39
2.3 Electronic structure	40
2.3.1 Many-body and relativistic effects	40
2.3.2 Electron-phonon coupling	41
2.3.3 Charge carrier transport	42
2.4 Photophysics and solar cells	42
2.4.1 Ion migration	43
2.4.2 Electron-hole recombination	45
2.4.3 Defect levels in the band-gap	45
2.4.4 Beyond the bulk: surfaces, grain boundaries and interfaces	46
2.5 Summary	47
3 Theory and methodology	49
3.1 Introduction	49
3.2 Density Functional Theory	49
3.2.1 Basic concepts	50
3.2.2 DFT in practice	53
3.3 Defects in semiconductors	60
3.3.1 Classification of crystal defects	61
3.3.2 Energetics of defect formation	62
3.3.3 Supercell method	63
3.4 Lattice dynamics	65
3.4.1 Harmonic approximation	66
3.4.2 Anharmonicity	67
3.4.3 Finite displacement method	68
3.5 Summary	68

4 Electronic band non-parabolicity	70
4.1 Introduction	70
4.2 Methods	74
4.2.1 Calculation procedures for effective mass	74
4.2.2 Electronic bandstructure calculations	76
4.3 Results	79
4.3.1 Comparison of methods used to calculate effective mass at the band edge	79
4.3.2 Deviations from the expected effective mass trend	80
4.3.3 Sensitivity of the curvature effective mass to the level of theory	81
4.3.4 Sensitivity of the Kane dispersion parameters to the level of theory	82
4.3.5 Consequences of non-parabolicity on optical and transport properties	84
4.4 Summary	89
5 Electron-phonon and phonon-phonon coupling	91
5.1 Introduction	91
5.1.1 Electron-phonon coupling	92
5.1.2 Hot carrier cooling in hybrid halide perovskites	94
5.2 Methods	95
5.2.1 Lattice dynamics calculations	95
5.2.2 Calculation procedure for the bandgap deformation potential	95
5.2.3 Classical model for hot carrier cooling	96
5.3 Results	97
5.3.1 Anharmonic bandgap deformation potential	97
5.3.2 Hot carrier cooling to equilibrium	100
5.4 Summary	104
6 Electron capture at H-centre defects	106
6.1 Introduction	106
6.2 Methods	108
6.2.1 Defect formation energy calculations	108
6.2.2 Lattice dynamics calculations	109

6.2.3	Calculation procedure for the carrier capture coefficient	110
6.2.4	Calculation procedure for the optically excited states	111
6.3	Results	111
6.3.1	I_i defect geometry	111
6.3.2	Charge localisation at the H-centre	112
6.3.3	I_i defect formation energies	113
6.3.4	Configuration coordinate diagram for electron capture	116
6.3.5	Vibrational properties of the negative charge state	119
6.3.6	Electron capture coefficient	121
	Closing Remarks	125
	Appendices	126
A	DFT bandstructures for PV materials	128
B	Effective mass and k -point spacing	132
C	EFFMASS: An effective mass package	133
D	Bandgap deformation potential and supercell size	135
E	Diffusion equation for a hot sphere	136
F	Charge transition diagram for I_i	137
G	Additional I_i potential energy surfaces	138
H	Copyright permissions	140

Copyright

The copyright of this thesis rests with the author. Unless otherwise indicated, its contents are licensed under a Creative Commons Attribution-Non Commercial 4.0 International Licence (CC BY-NC). Under this licence, you may copy and redistribute the material in any medium or format. You may also create and distribute modified versions of the work. This is on the condition that: you credit the author and do not use it, or any derivative works, for a commercial purpose. When reusing or sharing this work, ensure you make the licence terms clear to others by naming the licence and linking to the licence text. Where a work has been adapted, you should indicate that the work has been changed and describe those changes. Please seek permission from the copyright holder for uses of this work that are not included in this licence or permitted under UK Copyright Law.

Statement of Authorship

I declare that this thesis and the work presented in it are my own and has been generated by me as the result of my own original research. This work has included: identifying research questions, preparing input files for calculations, submitting and monitoring calculations, writing scripts and software packages for analysis, interpreting the results and writing research papers. Where work is not my own references are given. In addition, I list below the instances where work has been done in conjunction with others.

Theory and simulation of hybrid halide perovskites

The central idea of this chapter (to review the theory and simulation of hybrid halide perovskites) was provided by Aron Walsh. The contents of the review were a product of discussions between myself, Aron Walsh and Jarvist Frost. Aron Walsh prepared Figures 2.1, 2.2 and 2.4, and Young-Kwang Jung prepared Figure 2.3. This chapter is a literature review; the primary research underpinning this chapter was performed by Jarvist M. Frost (molecular dynamic and Monte Carlo investigations), Federico Brivio (crystal and electronic structure), Jonathan M. Skelton (lattice dynamics and vibrational spectroscopy), and myself (band-gap deformations).

Electronic band non-parabolicity

The initial research direction (to investigate, across a range of photovoltaic materials, the sensitivity of DFT calculated effective mass to fitting parameters) was provided by Aron Walsh and Benjamin Morgan. Jarvist Frost suggested weighting the fit to a Fermi-Dirac distribution.

Electron-phonon and phonon-phonon coupling

Jarvist Frost suggested using a classical heat diffusion model for hot carrier cooling and calculated the temperature dependent bandgap shifts. Jonathan M. Skelton provided scripts to implement the frozen phonon method. Aron Walsh prepared Figure 5.1.

Electron trapping at H-centre defects

The central idea of this chapter (to investigate hole capture at an iodine interstitial in $\text{CH}_3\text{NH}_3\text{PbI}_3$) was provided by Aron Walsh. Sunghyun Kim and Samantha Hood provided early (pre-publication) access to the software package CARRIERCAPTURE.JL, which I used to analyse the data presented in Section 6.3. Aron Walsh prepared Figures 1.3a and 1.3c. The energies of the H-centre optically excited states were calculated by Rachel Crespo-Otero.

Publications

The following publications have arisen from this PhD work. Where copyright is retained by the publisher, text and figures are reprinted with permission, as detailed in Appendix H.

Theory and simulation of hybrid halide perovskites

Text and figures 1–4 adapted from Whalley, L. D., Frost, J. M., Jung, Y. -K. and Walsh, A. (2017). Perspective: Theory and simulation of hybrid halide perovskites. *The Journal of Chemical Physics*, 146(22), p.220901. © 2017 CC-BY

Electronic band non-parabolicity

Text and figures 1–11 adapted from Whalley, L. D., Frost, J., Morgan, B. and Walsh, A. (2019). Impact of nonparabolic electronic band structure on the optical and transport properties of photovoltaic materials. *Physical Review B*, 99(8). © 2019 American Physical Society

Electron-phonon and phonon-phonon coupling

Excerpts and figures 2–4 adapted from Whalley, L. D., Skelton, J. M., Frost, J. M. and Walsh, A. (2016). Phonon anharmonicity, lifetimes, and thermal transport in $\text{CH}_3\text{NH}_3\text{PbI}_3$ from many-body perturbation theory. *Physical Review B*, 94(22). © 2016 American Physical Society

Excerpts and figures 1,5–6 adapted from Frost, J. M., Whalley, L. D and Walsh, A. (2017). Slow Cooling of Hot Polarons in Halide Perovskite Solar Cells. *ACS Energy Letters*, 2(12), pp.2647-2652. © 2017 CC-BY

Electron trapping at H-centre defects

Excerpts adapted from Whalley, L. D., Crespo-Otero, R. and Walsh, A. (2017). H-Center and V-Center Defects in Hybrid Halide Perovskites. *ACS Energy Letters*, 2(12), pp.2713-2714. © 2017 American Chemical Society

Appendix C: effmass: An effective mass package

Text reprinted from Whalley, L. D. (2018). effmass: An effective mass package. *Journal of Open Source Software*, 3(28), p.797. © 2018 CC-BY

Acknowledgements

Leaving an enjoyable job and returning to study is not an easy decision, but starting a PhD in the Walsh group was one of the best I have made. A huge thanks must be given to Aron Walsh for creating and maintaining a supportive, friendly and productive working environment. I have gained a *huge* amount from working with Aron and other members of the group. Although I have learnt something from every member I will not list everyone here, but a special thanks must go to Jarvist Frost who led the book group and helped to clarify my sometimes muddled understanding of solid state physics. Another special thanks to the women I have worked with: we are still too few and far between in the physical sciences, but what we lack in quantity we make up for in quality! Thanks also to Benjamin Morgan, my second supervisor, who guided me through my first research project and has provided useful feedback on my scientific writing.

During the third year of my PhD I became involved with the Research Software Engineering community at Imperial. I would like to thank Katerina Michalickova for organising the Software Carpentry workshops – it is no easy job co-ordinating a rabble of volunteers from across Imperial, but teaching software carpentry has greatly increased my confidence around programming. Thanks also to fellow members of the Imperial RSE community committee, especially Jeremy Cohen who is mentoring me as part of my Software Sustainability Institute fellowship.

The vast majority of the computational analysis in this thesis depends to some degree on the open-source community. Thousands of person-hours, often I suspect squeezed in at weekends or evenings, has produced well-tested, well-documented, easily accessible code. Without the magical Python ‘import’ statement and the generosity of strangers I would probably still be writing an integration routine for my first year project. I have referenced the domain-specific software packages used in the main text of the thesis, but here I acknowledge the general-purpose software tools I have used: Python and Julia for scripting, the scientific Python stack (Numpy, Scipy, Pandas, Matplotlib and Jupyter) for data analysis and plotting, Sphinx and ReadTheDocs for documentation, Vim and Sublime for text editing, Git for version control, and LaTeX for type setting.

Thanks also to the admin and technical staff who keep the supercomputers Archer, Thomas and Piz-Daint running. I rarely think about the infrastructure behind my calculations, and this is exactly why I need to say thanks.

Funding for my PhD came from the EPSRC, via the Centre for Doctoral Training in New and Sustainable Photovoltaics. It seems that running a CDT requires staff to go above and beyond – thanks to Ken Durose, Alison Walker, Rob Treharne and Asim Mumtaz for doing just that.

The biggest thanks must go to my family and friends. I met Richard towards the start of my PhD. It is now four years on, and we have bought a house, got married and created a very small human being (currently still residing in my tummy). I wouldn't have expected that all this was compatible with doing a PhD, but being with Richard has made it seem like the most natural thing in the world. He has been with me, and supported me, throughout. It is through Richard's parents, Andrew and Elspeth, that I was introduced to John and Karen. By gifting me the use of their flat twice a week for three years, John and Karen enabled me to live in Birmingham and work in London. I don't think it would have been possible for me and Richard to settle down otherwise and for this I am very grateful.

I'm lucky to have close, reliable and hilarious friends who are always suggesting things to take my mind off work. Thanks especially to Hetta and Blanche for Lipsync and our other projects, and Caz for her loyalty and warmth. Ruby, my sister, is also a close friend who understands me (and sees through me!) in a way that no-one else can. Finally, thank you to my parents John and Alison, whose love and support instilled in me a self-confidence that I think is so important when doing science. All of my achievements are theirs, as none of this would have been possible without their belief in me.

List of Figures

1.1	Historic cost of renewable energy generation	21
1.2	Typical solar cell architectures	24
1.3	Solar cell current-voltage curve	25
1.4	AM1.5 spectral intensity and Shockley-Queisser efficiency	26
1.5	Electron-hole recombination pathways	27
2.1	$\text{CH}_3\text{NH}_3\text{PbI}_3$ powder neutron diffraction pattern and crystallographic unit cells	35
2.2	$\text{CH}_3\text{NH}_3\text{PbI}_3$ phonon dispersion and double-well potential energy surface	36
2.3	Electronic band structures of CsPbBr_3 and $\text{CH}_3\text{NH}_3\text{PbBr}_3$	38
2.4	Simple phase segregation model	43
3.1	Interacting and non-interacting particle systems	51
3.2	Dimensionality of variational objects	53
3.3	Jacob's ladder of exchange-correlation functionals	54
3.4	Translational symmetry and supercell construction	55
3.5	In-phase and out-of-phase states in an infinite 1D crystal	57
3.6	Nested iterative method for geometry optimisation	58
3.7	CsSnI_3 k -point convergence	60
3.8	Classification of crystal point-defects	61
3.9	Formation energies of the Te vacancy in CdTe	63
3.10	Crystal potential energy expanded with respect to atomic displacement	66
3.11	3-phonon processes and anharmonic potential energy surfaces	68
4.1	Schematic of the three definitions for effective mass	72
4.2	Numerical methods for fitting a band dispersion	73
4.3	Band non-parabolicity vs effective mass	80
4.4	Transport effective mass of the CdTe heavy hole	81

4.5	Transport effective mass of the CdTe light hole	82
4.6	Effective mass vs bandgap	83
4.7	Band non-parabolicity vs bandgap	84
4.8	Band non-parabolicity and spin-orbit coupling	85
4.9	Burstein–Moss band gap shift	86
4.10	Electron effective mass as a function of carrier concentration	87
4.11	Polaron mobility as a function of carrier concentration	88
5.1	Schematic of the hot carrier cooling model	95
5.2	Harmonic phonon dispersion and eigenvectors at the M and R q -points	97
5.3	Bandgap deformation potential	98
5.4	Total and projected density of states	99
5.5	Bandgap deformation potential at three levels of theory	101
5.6	Polaron temperature as a function of polaron radius	103
5.7	Hot carrier cooling rate	104
6.1	Atomic relaxation procedure for point defects in hybrid halide perovskites	111
6.2	Defect geometries of I_i^+, I_i^- and I_i^0	113
6.3	H-centre spin localisation and optical excitation energies	114
6.4	Tilting correction for the pseudo-cubic perovskite lattice	115
6.5	Charge transition levels of I_i	116
6.6	Configuration coordinate diagram for carrier capture between I_i^- and I_i^0	118
6.7	Classification of normal phonon modes found in a crystal with a defect	120
6.8	Phonon dispersion and Inverse Participation Ratio of I_i^-	121
6.9	Evolution of the H-centre Kohn-Sham eigenstates	122
6.10	H-centre electron capture coefficient	123
A.1	$\text{CH}_3\text{NH}_3\text{PbI}_3$ bandstructure, HSE06, no-SoC	128
A.2	$\text{CH}_3\text{NH}_3\text{PbI}_3$ bandstructure, HSE06, SoC	128
A.3	$\text{Cu}_2\text{ZnSnS}_4$ bandstructure, HSE06, no-SoC	129
A.4	$\text{Cu}_2\text{ZnSnS}_4$ bandstructure, HSE06, SoC	129
A.5	GaAs bandstructure, HSE06, no-SoC	130

A.6	GaAs bandstructure, HSE06, SoC	130
A.7	CdTe bandstructure, HSE06, no-SoC	131
A.8	CdTe bandstructure, HSE06, SoC	131
D.1	Bandgap deformation potential and supercell size	135
F.1	Charge transition levels of I_i	137
G.1	Potential energy surface of I_i^0 calculated at various levels of theory	138
G.2	Potential energy surface of I_i^- calculated at various levels of theory	138
G.3	Potential energy surfaces for all-atom or inorganic-only lattice distortions	139

List of Tables

2.1	Donor defect levels in $\text{CH}_3\text{NH}_3\text{PbI}_3$, Si and CdTe	46
2.2	Common issues that arise in the simulation of hybrid perovskites	48
4.1	Values for the effective mass and alpha parameter	78
4.2	Electron effective mass and polaron mobility at various carrier concentrations . .	88
5.1	Residual sum of squares for quadratic and bi-quadratic fits to the bandgap . . .	98
5.2	Pb-I bond lengths	100
5.3	Bi-quadratic fit coefficients at three levels of theory	100
5.4	Valence- and conduction-band deformation potentials	101
6.1	Defect orientation and bond length of I_i^+ , I_i^- and I_i^0	112
6.2	Tilting corrections for supercell expansions of the pseudo-cubic perovskite lattice	114
B.1	Effective mass and k -point spacing	132

Abbreviations

AM	Air mass
CBM	Conduction band minimum
CZTS	Copper zinc tin sulfide
DFT	Density functional theory
GGA	Generalised gradient approximation
HF	Hartree-Fock
HSE06	Heyd-Scuseria-Ernzerhof screened hybrid DFT functional
LDA	Local density approximation
PBE	Perdew-Burke-Ernzerhof DFT functional
PBEsol	Perdew-Burke-Ernzerhof DFT functional developed for solids
QM/MM	Quantum mechanics/molecular mechanics
MAPI	Methylammonium lead iodide
MD	Molecular dynamics
PV	Photovoltaic
SRH	Shockley-Reed-Hall
SoC	Spin-orbit coupling
TRPL	Time-resolved photoluminescence
VBM	Valence band maximum

Symbols

∇	Vector differential operator
ϵ	Energy of a state
ϵ_0	Static dielectric constant
ϵ_{inf}	High frequency (optical) dielectric constant
η	Photovoltaic efficiency
κ	Thermal conductivity
μ	Chemical potential
ν	Phonon frequency
π	Pi constant
ρ	Electron density
σ	Carrier capture cross section
τ	Carrier lifetime
ϕ	Kohn-Sham orbital
Ψ	Many-body wavefunction
e	Exponential constant
h	Planck constant
\hbar	Reduced Planck constant $\frac{h}{2\pi}$
\mathbf{k}	Wavevector associated with periodic electronic structure
k_B	Boltzmann constant
m^*	Effective mass
m_c	Conductivity effective mass
m_{opt}	Optical effective mass
m_t	Transport effective mass
n	Carrier concentration

\mathbf{r}	Position vector
t	Time
v	Group velocity
C_p	Specific heat capacity
E	Total energy
E_0	Ground state energy
E_F	Fermi level
FF	Fill factor
I_{sc}	Short circuit current
N_t	Trap density
P	Pressure
S	Entropy
T	Temperature
V	Volume
V_{oc}	Open circuit voltage

For generations, we have assumed that the efforts of mankind would leave the fundamental equilibrium of the world's systems and atmosphere stable. But it is possible that with all these enormous changes (population, agricultural, use of fossil fuels) concentrated into such a short period of time, we have unwittingly begun a massive experiment with the system of this planet itself.

— Margaret Thatcher, 1988

1

Introduction

1.1 Motivation

In this section I justify photovoltaic materials research. First, the challenge we face as a human race – global warming – is introduced, followed by why we should take advantage of the sun as an energy source. The section ends with a discussion around the three generations of solar cell materials, and the inherent limitations of silicon solar cells.

1.1.1 Energy use and global warming

Anthropogenic climate change is one of the greatest challenges we face as a human race and, as we have twelve years to limit climate change catastrophe, we are running against the clock. This viewpoint is not the political hyperbole of the green left, as I have alluded to with the opening quote – it is the current scientific understanding as established by the International Panel on Climate Change.¹

The story begins in the 18th century when the industrial revolution enabled unprecedented population growth, from 0.8 billion in 1750 to 7.5 billion in 2017.² Industrial expansion combined with a growing population led to an exponential growth in the amount of coal and oil being burnt; between the years 1769 and 2006 there was an 800-fold increase in the world annual coal production.³ Atmospheric CO₂ concentrations increased as a result, leading to an increase in global temperatures, rising sea levels, and ocean acidification. The years 2014–2018 were the five hottest years on record⁴ and there has been a recent increase in extreme weather (heat waves, drought and floods) across the globe.⁵ Studies have shown that the probability of heat waves,⁶ wildfires⁷ and flooding^{8,9} have increased as a result climate change.

The threat of climate change seems not to have had a proportionate response from governments or many individuals. One reason for this is that changes in weather patterns are significant only when looked at over long time periods, and so it is difficult to communicate the risk carried by

climate change. Another is that this is an inherently international problem, and that we do not have the political mechanisms in place to coordinate a global response. Despite the dramatic consequences of inaction, there seems to be little public appetite for changes which require a reduction in energy use. Instead there is a push towards technological solutions which may be able to reduce the negative effects of climate change without impacting upon our perceived quality of life.

1.1.2 The sun as an energy source

One way to reduce the rate of climate change is to generate energy through processes that do not release net positive amounts of CO₂ into the atmosphere, and harnessing the vast amount of energy that is released from the sun is one way of doing this. This idea has been around for more than sixty years; in 1954 Bell Labs demonstrated that it was possible to convert sunlight into electricity by powering a small toy Ferris wheel and radio transmitter with a silicon solar cell. Reporting this event, The New York Times wrote:¹⁰

“[the solar cell] may mark the beginning of a new era, leading eventually to the realization of one of mankind’s most cherished dreams — the harnessing of the almost limitless energy of the sun for the uses of civilization.”

An average solar flux density of 1361 Wm⁻² reaches the earth’s atmosphere each second, which is almost 10⁴ times larger than any other external energy source.¹¹ A quick back-of-the-envelope calculation shows that if we assume a sunlight to electricity conversion efficiency of 40% (achievable using concentrated solar power) and zero transmission loss, we could meet the world’s electricity demands (22PWh in 2015)¹² by covering an area equivalent to Northumberland county (5000km²) with photovoltaic solar panels. I am not suggesting that this would be a viable way to meet the world’s energy demands, merely that solar energy could make a significant contribution to the future energy mix. However to harness this power we must be able to convert sunlight into electrical energy at a competitive price and at scale. Photovoltaic efficiency is key to price reduction as there are significant costs that scale with area,^{13,14} and a higher efficiency module can deliver the same energy for a smaller area.

The first photovoltaic devices could transform sunlight into electrical energy with an efficiency of around 6%. The computing boom of the 1980s encouraged large investment into silicon research and silicon cells with 20% efficiency were reported in 1986.¹⁵ Since 1980 the cost to generate photovoltaic electricity decreased at an average rate of 10% per year¹⁶ and is now comparable with the cost to generate electricity from nuclear and coal (Figure 1.1). This price reduction was driven in part by a growing global market for photovoltaics, which has increased from a capacity of 1.9 GW in 2005 to 102 GW in 2016.¹⁷

In the UK the growth in renewable energy has led to a decreasing dependence on fossil fuels. The UK had its first day without coal in 2017¹⁹ and ran for three days without coal in 2018.²⁰ There appears to be an increasing political will to take advantage of renewable energy; the first

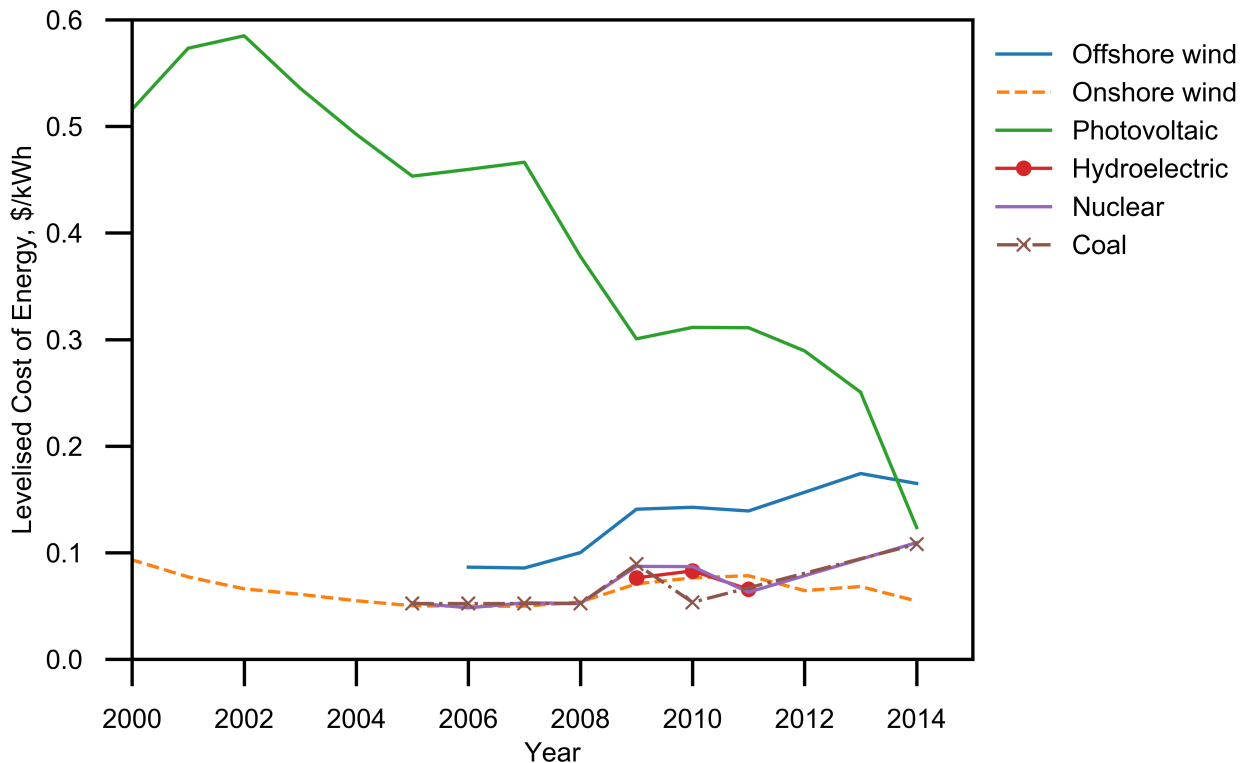


Figure 1.1: Historic cost of renewable energy generation. The levelised cost of energy (LCOE) is an estimate of the total electricity cost, including payback of the initial investment and operating costs. The LCOE of solar energy has been decreasing year on year and is now comparable with the LCOE of energy generated from nuclear power and coal. The data is taken from a mean average across all sources in the Open Energy Information transparent costs database.¹⁸

UK National Infrastructure Assessment recommends halting the development of nuclear power stations and diverting investment into solar and wind energy generation instead.²¹ This switch away from nuclear energy is projected to be at no cost to the consumer.

It is widely predicted that solar power will continue to grow – to what extent depends on the source: a recent study from Imperial College London estimates that solar power could supply 23% of global energy demand in 2040.²² ExxonMobil, a company heavily invested in fossil fuels, predicts that all renewables combined will supply 20% of global power generation in 2040.²³ Note that previous models have consistently underestimated the scale of photovoltaic deployment.²⁴

1.1.3 Beyond silicon: the need for new photovoltaic materials

Photovoltaic devices are commonly split into three generations. In this section I introduce each generation and discuss what is driving the development of new PV materials in a competitive market that is dominated by silicon.

First generation

The first generation devices are based upon mono- and poly-crystalline silicon wafers. They dominate the PV market; in 2016 90% of total PV module production used this technology.¹⁷. They are high efficiency (>20%), reliable (25 year lifetimes) and low cost (<0.5 \$/W). There has been a steady decrease in cost due to i) device engineering improvements (eg: textured surfaces); ii) the economies of scale as silicon industrial processes are driven by a demand for computer chips; and iii) improved industrial practices which allow thinner and thinner wafers to be fabricated with less waste. However there are technological and physical limits to how much the cost of a crystalline silicon wafer can be reduced. First, the manufacturing process for silicon wafers is energy intensive and requires high temperatures. Second, silicon is an indirect bandgap material and as a result does not absorb sunlight efficiently; wafers have to be a minimum thickness ($\sim 60\mu\text{m}$) to compensate for this. It is difficult to reach this limit without snapping the material during fabrication as silicon is a hard and brittle material.

Second generation

Second generation devices are fabricated from the direct bandgap materials gallium arsenide (GaAs), cadmium telluride (CdTe), cadmium indium gallium diselenide (CIGS) and amorphous silicon (a-Si). These materials have higher absorption coefficients, so they can be built into lighter thin-film ($\sim 10\mu\text{m}$) architectures. A thin-film is not mechanically stable, it needs a substrate, but this opens up possibility of it being a flexible film.

CdTe was the first thin film to be commercialised and development has been led by the company First Solar, who have installed a total capacity of 17 GW. Lifecycle assessments indicate that the CdTe energy payback time (the time required to generate as much energy as is consumed during production and lifetime operation of the system) is shorter than that of Si.²⁵ However lower efficiencies are stifling the growth of this technology and there are also concerns about the elemental toxicity and scarcity. CIGS and a-Si each have a smaller market share than CdTe. High efficiency (~40%) GaAs devices have been developed for the high-value, low-volume space market.

Third generation

Third generation devices are emerging technologies which are not yet in the market. This includes organic and dye-sensitised materials, hybrid halide perovskites, and copper zinc tin sulfide (CZTS). These are abundant materials which can be fabricated through low-cost solution-deposition methods. Only the hybrid-halide perovskites have efficiencies high enough for commercialisation (currently 24.2%).

Commercial success for the third generation materials may come from opening up new markets rather than trying to compete directly with the well established silicon technologies. For example, organic and hybrid perovskite technologies have tunable bandgaps and are being developed for semi-transparent building integrated photovoltaics. There has also been recent research interest and commercial investment into silicon-perovskite single junction tandem cells.

1.2 Key concepts in photovoltaics

This section outlines the physical principles underlying solar cell operation, with a focus on carrier recombination. After introducing the key concepts and vocabulary, the design rules or ‘wish list’ for a successful PV material are outlined.

1.2.1 Operating principles

A solar cell converts light into electricity through the following (simplified) process: i) a photon enters the device; ii) the photon is absorbed and creates an electron-hole pair in the absorber layer; iii) the electron and hole disassociate; iv) the electron and hole travel through the absorber layer to their respective contacts; v) the electron and hole are extracted to the external circuit to do electrical work.

Device architecture

The device architecture is determined by the properties of the absorber material. For example, in a hybrid halide perovskite material the photogenerated electron and hole are loosely bound to one another and thermal energy is enough to separate them. In this case, a planar *n-i-p* architecture can be used, where *n* is a n-type (electron-doped) material contacted to the cathode, *p* is a p-type (hole-doped) material contacted to the anode and *i* is the intrinsic (undoped) perovskite material (Figure 1.2). In contrast, the photogenerated electron-hole pair in an organic solar cell is strongly bound. In this case, the electron-hole pair disassociate only at an interface and a mesoscopic architecture is used to facilitate this (Figure 1.2). The conventional organic architecture is *p-i-n*, where the anode and p-type material are deposited onto the substrate first. The conventional architectures can be inverted to give *p-i-n* junctions (for inorganic / hybrid absorber layers) or *n-i-p* junctions (for organic absorber layers). In all cases, the n-type and p-type layers block photogenerated electrons from reaching the anode and block photogenerated holes from reaching the cathode.

Various strategies exist to increase device efficiency via device architecture engineering. For example, the current world record single junction silicon cell ($\eta = 26.6\%$) has an additional wide bandgap material inserted between the absorption layer and contact material to reduce interfacial recombination, and interdigitated back contacts to reduce optical loss.²⁶ The most efficient solar cells ($\eta = 46.0\%$) combine a multiple pn-junction (tandem) architecture with a lens to concentrate the incoming sunlight.

Efficiency and reciprocity

For an external circuit with load R , a current I and voltage V is developed across the cell so that

$$V = IR. \quad (1.1)$$

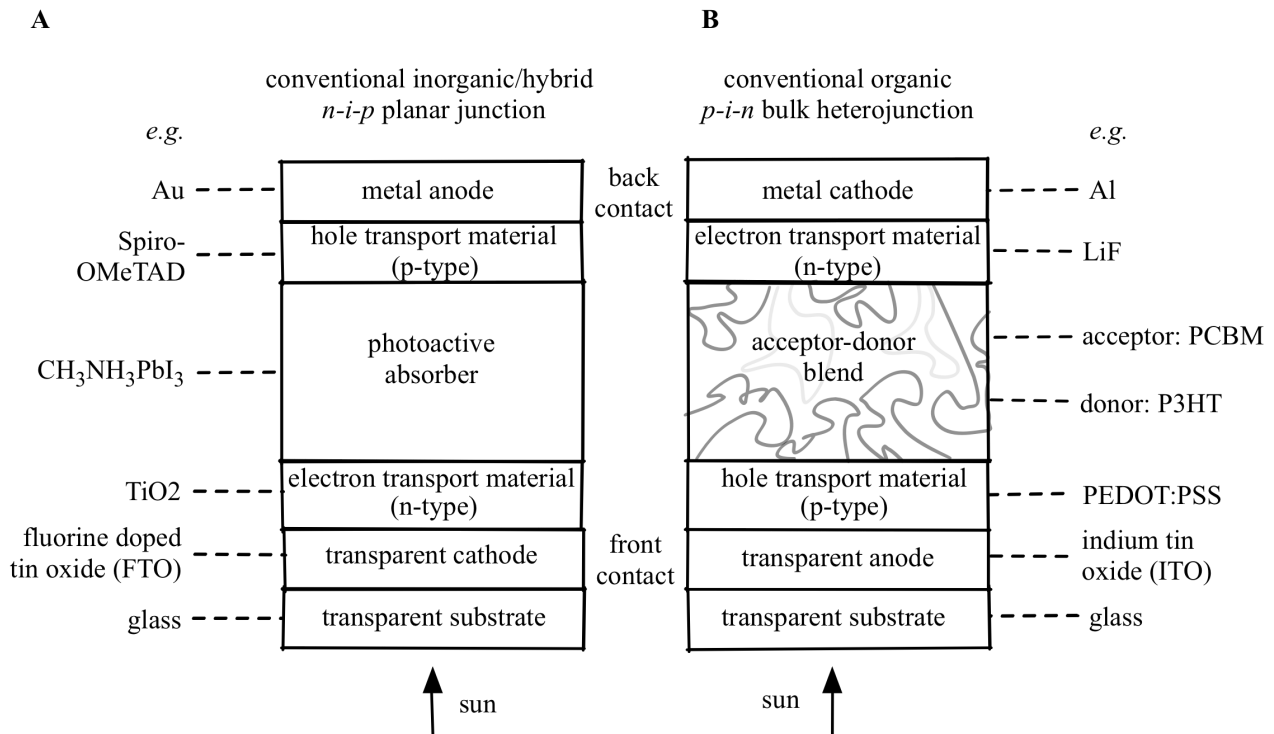


Figure 1.2: (A) Schematic of the typical planar junction solar cell architecture used for an inorganic or hybrid material absorber layer (B) Schematic of the typical bulk heterojunction solar cell architecture used for an organic absorber layer. The mesoscopic architecture provides many interfaces where the electron-hole pair can disassociate. In both cases there is a built-in electric field that drives photogenerated electrons towards the electron transport material and holes towards the hole transport material.

I and V are related by a current-voltage curve (Figure 1.3). A solar module operates at the maximum power point P_m , which is where the product of the voltage and current is maximum:

$$P_m = I_m V_m. \quad (1.2)$$

The open-circuit voltage V_{oc} is the voltage produced when there is no contact to the external circuit (or, equivalently, the external circuit has an infinite load). The short-circuit current I_{sc} is the current that flows when there is no load on the external circuit. The fill factor FF is defined as:

$$\text{FF} = \frac{I_m V_m}{I_{sc} V_{oc}}. \quad (1.3)$$

The higher the fill factor, the higher the maximum powerpoint for a given V_{oc} and I_{sc} .²⁷ A fill factor of one would correspond to a current-voltage curve which is not *actually* a curve, but a right angle.

The efficiency η of the solar cell under an incident light power of P_s is given by

$$\eta = \frac{P_m}{P_s} = \frac{I_m V_m}{P_s} = \frac{I_{sc} V_{oc} \text{FF}}{P_s}. \quad (1.4)$$

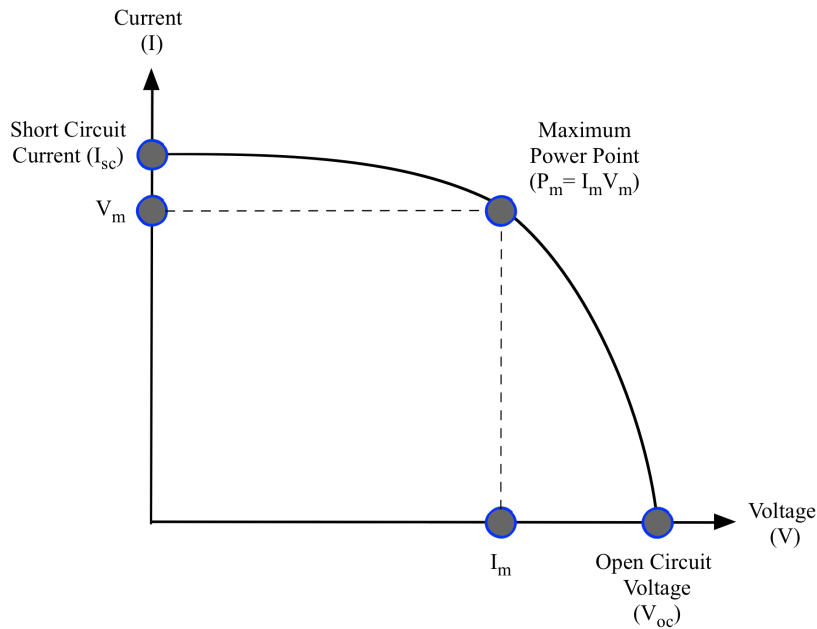


Figure 1.3: Schematic of a current-voltage curve for a typical solar cell.

Thus the three key figures of merit for a solar cell are the V_{oc} , I_{sc} and FF, and these combine to give the efficiency η . However in all absorber materials there is a trade off between current and voltage; as the bandgap of a material decreases, more photons can be absorbed (higher I_{sc}) but the photogenerated charge carriers have less energy (lower V_{oc}).

At open circuit, all electrons and holes must recombine in the solar cell. In an efficient PV material the recombination is radiative as this is a thermodynamically unavoidable process via the energy level transitions needed for absorption. Non-radiative recombination, where the energy is dissipated as heat and eventually lost, is avoidable and should be minimised. For a fixed carrier concentration, a higher rate of photon emission corresponds to reduced non-radiative recombination; high radiative efficiency (as measured through e.g. electroluminescence) translates to high open circuit voltage.²⁸ As a consequence of this reciprocity relation, we can predict the V_{oc} and I_{sc} from photoluminescence and photoconductivity studies respectively. This approach has been recently applied to hybrid halide perovskites.²⁹

The Shockley-Queisser limit

The principle of detailed balance states that at equilibrium each microscopic process is balanced by its reverse process: for a photovoltaic device operating at open-circuit this means that the rate of photon absorption equals the rate of photon emission. Shockley and Queisser used the principle of detailed balance to calculate the maximum possible efficiency of a photovoltaic device³⁰ (an alternative derivation is given in Ref. [27]). The PV efficiency is dependent upon the direct bandgap E_g of the absorber material and the spectrum of the incident light. Assuming illumination under a standard AM1.5 solar spectrum, the efficiency can be plotted as a function

of bandgap. For a single junction solar cell the maximum possible efficiency across is 33%, which corresponds to an ideal bandgap of $\sim 1.4\text{ eV}$ (Figure 1.4).

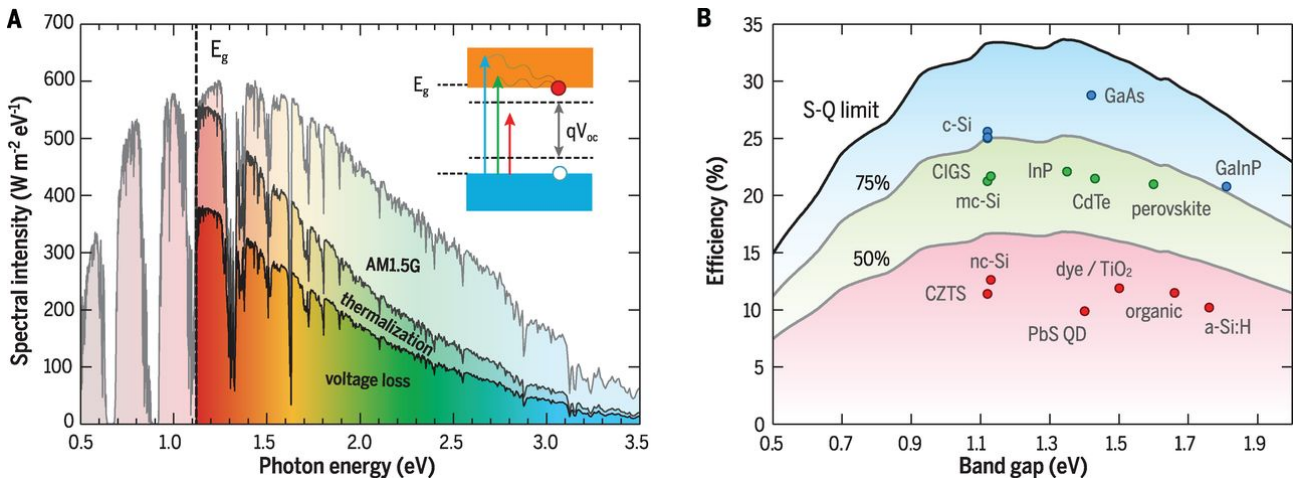


Figure 1.4: (A) The AM1.5 spectrum. Photons below the bandgap are not absorbed, whilst energy is lost from above bandgap photons via carrier thermalisation. (B) The Shockley-Queisser efficiency of a single bandgap solar cell under AM1.5 illumination (thick black line). Also included are the top cell efficiencies for various PV materials. From the work of Polman et al.³¹ Reprinted with permission from AAAS.³²

The model used to calculate the Shockley-Queisser limit is highly idealised. It assumes that all incident light is absorbed, that every absorbed photon creates an electron-hole pair, and that every electron is extracted to the external circuit. In real materials the absorption coefficient is not a step-function, and excited charge carriers can recombine through non-radiative processes before reaching the circuit. Only three materials have an efficiency above 75% of the Shockley-Queisser limit: crystalline silicon (c-Si), GaAs and GaInP (Figure 1.4). Another metric, the spectroscopic limited maximum efficiency (SLME), accounts for absorption and emission characteristics and reduces the maximum theoretical efficiency.³³ For example, the candidate absorber material CuInS₂ has a Shockley-Queisser maximum efficiency of 33% and SLME of 29%.³⁴ Non-radiative processes which contribute to the efficiency deficit will be discussed further in Section 1.2.2.

It is possible to exceed the Shockley-Queisser limit by challenging some of the assumptions built into the derivation. For example, the model assumes that once an electron is excited it will thermalise to the band edge, emitting the energy as phonons. This heat energy can no longer do useful work and results in a reduction of the V_{OC} . However ‘hot carrier’ cells, which extract electrons before they are able to thermalise, were successfully fabricated in 2014 (although it should be noted that they are currently limited to cryogenic temperatures and an incoming spectrum which is intense and monochromatic).³⁵

Another approach is to use tandem solar cells, where several absorber materials are stacked on top of each other. The materials are chosen to have complementary bandgaps, so that more of the solar spectrum can be absorbed with minimal thermalisation losses. GaAs-based

four-junction tandem cells have reached an efficiency of 33% and are used for space applications, though their uptake is limited by the costly wafer bonding method required for fabrication. The constraint of lattice matching – that the strain at the interfaces must be minimised for device stability – puts severe limitations on the material combinations which can be used for this approach.

1.2.2 Carrier recombination

Electron-hole recombination competes with charge extraction to the external circuit, and as such it is a well examined process. Three pathways for electron-hole recombination are outlined in Figure 1.5. During radiative recombination the electron directly recombines with a hole to produce a photon and, in the case of indirect recombination, phonons. This recombination channel is unavoidable in PV devices as the same channel is used for light absorption. The second pathway, Shockley-Reed-Hall (SRH) recombination, is a two step process mediated via a defect trap state. In PV devices this pathway should be minimised as the kinetic energy of the electron and hole is transformed to vibrational energy (phonons) and cannot be used for useful work. The third pathway, Auger recombination, is also a non-radiative process. Here the electron directly recombines with a hole, and the resulting energy and momentum is transferred to another conduction band electron.

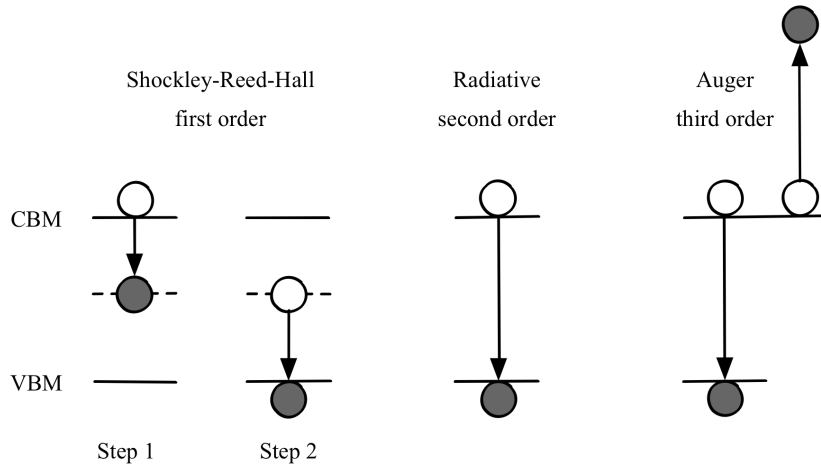


Figure 1.5: A schematic of the three possible electron-hole recombination pathways. In each case, an electron at the conduction band minimum combines with a hole at the valence band maximum. Empty (filled) circles correspond to the electron before (after) each transition. First-, second- and third-order processes correspond to one, two and three particle processes respectively.

Radiative recombination and Auger recombination are unavoidable processes intrinsic to the material, whereas SRH recombination is an avoidable process that can be controlled through defect engineering. The SRH recombination rate is given by²⁷

$$U_{\text{SRH}} = \frac{np - n_i^2}{\tau_{n,\text{SRH}}(p + p_t) + \tau_{p,\text{SRH}}(n + n_t)}, \quad (1.5)$$

where n (p) is the density of electrons (holes), n_i is the intrinsic carrier density and n_t (p_t) is the value of the electron (hole) density when the electron Fermi level is equal to the trap level E_t :

$$n_t = n_i e^{\frac{(E_t - E_c)}{k_B T}} \quad (1.6)$$

$$p_t = n_i e^{\frac{(E_v - E_t)}{k_B T}}, \quad (1.7)$$

where E_c and E_v are the energies of the CBM and VBM respectively. The recombination rate has a maximum when the rates of hole capture and electron capture are comparable. This happens when the trap level is in the middle of the bandgap, and $n_t = p_t$.

$\tau_{n,SRH}$ ($\tau_{p,SRH}$) is the electron (hole) lifetime. For a trap density N_t , mean thermal electron (hole) velocity v_n (v_p) and electron (hole) capture cross section σ_n (σ_p), the lifetimes can be approximated as²⁷

$$\tau_{n,SRH} = \frac{1}{\langle v_n \rangle \sigma_n N_t} \quad (1.8)$$

$$\tau_{p,SRH} = \frac{1}{\langle v_p \rangle \sigma_p N_t}. \quad (1.9)$$

The standard approach for calculating the trap density from first principles is give in Chapter 3, and a method for calculating the capture coefficient is outlined in the Chapter 6.

Experimental measurements of recombination rates

Carrier lifetimes and recombination rates are difficult to measure experimentally as ultra fast optical and electronic sensors are needed to capture transient behaviour, and this must be done in conditions relevant to photovoltaic performance. Time resolved photoluminescence (TRPL) and photoconductivity measurements are used to infer the recombination rates for each recombination pathway. Each pathway scales differently with carrier concentration, as specified by the following rate equation:³⁶

$$\frac{dn}{dt} = G - k_1 n - k_2 n^2 - k_3 n^3 \quad (1.10)$$

where G is the rate of electron-hole generation, k_1 is the rate constant for SRH recombination, k_2 is the rate constant for radiative recombination and k_3 is the rate constant for Auger recombination. SRH recombination via a trap state is a one particle process that scales linearly with the carrier concentration. Radiative recombination is a two particle process that depends on the electron density and hole density, so scales quadratically with carrier concentration. Auger recombination requires three particles and scales cubically. TRPL uses short laser pulses to excite excess electrons and holes which then decay via recombination or carrier extraction at an interface. Exponential curves are fitted to the TRPL signal at different laser fluences to extract carrier lifetimes. In general, for solar cells operating under 1.5AM illumination, second order SRH recombination is the dominant recombination mechanism.

1.2.3 Design principles for absorber materials

Solid state physics and computational chemistry can connect microscopic material processes to macroscopic observables. The tools of each field have been applied to a range of inorganic and organic materials, and have successfully explained the observed properties of existing materials. There is also a more recent approach to materials science called ‘inverse design’. This is where the desired functionality of a new material is stated first, and computational tools are used to predict which materials will exhibit such features.³⁷ The hope is that this approach will improve upon discovery by trial and error, and accelerate the design of new materials.

High-throughput computational screening is a brute force approach to inverse design. Here, an automated procedure calculates a set of properties across a large number of atomic structures. This approach has been used to identify battery electrolytes,³⁸ organic photovoltaic materials³⁹ and materials for carbon capture and storage,⁴⁰ amongst others. Materials screening criteria must be defined so that successful materials are identified and selected for further study. Some criteria are easy to identify - for example the thermodynamic stability, which ensures that the material is synthesisable. This criteria can be expanded to include the features found in existing successful materials. For example, hybrid halide perovskites are defect tolerant - they contain a low concentration of defects which are detrimental to optoelectronic performance. The electronic parameters which underpin the defect tolerance of hybrid halide perovskites have been identified so that they may be used to screen for new defect-tolerant materials.⁴¹

With the concept of inverse design in mind, items for a successful PV material shopping list are listed below. The final three items (toughness, elemental abundance, elemental non-toxicity) are not necessary for successful devices in the lab, but would promote commercialisation of the technology.

Thermodynamic stability

The material should be thermodynamically stable with regard to competing phases so that it does not degrade over years of operation. The binary compound CdTe was the first thin film PV material to be commercialised and, similar to GaAs, it has no competing phases. Quaternary chalcogenide compounds such as CISSe and CZTS have many more competing phases to consider and the chemical potentials during synthesis must be very finely tuned for stability, which hinders their development.

Optimum bandgap

Ultimately, it is the spectrum of the sun and features of our atmosphere (light scattering and absorption) that dictates the design of solar cells; we must optimise our solar technology to take advantage of the spectrum that is particular to our planet. The Shockley-Queisser limit, discussed in subsection 1.2.1, gives an optimum bandgap of 1.4 eV.⁴² Atomic disorder or point defects can reduce the material band gap. Quaternaries with elemental species of a comparable

atomic radii are more likely to exhibit atomic disorder – for example in CZTS this leads to a bandgap reduction of 30 meV.⁴³

Strong light absorption

The absorption coefficient specifies how much light of a particular wavelength is absorbed by a material. Different semiconductor materials have different absorption coefficients; those with a higher absorption coefficient will more readily absorb light. Silicon is an indirect bandgap material that requires phonon-assisted absorption. As a result, crystalline silicon absorbs 92% of light in a thickness of 200 μm, whilst CdTe can absorb the same amount in a thickness of 1 μm.⁴⁴

Low exciton binding energy

After light absorption, a bound electron-hole pair (exciton) is created. The electron and hole must disassociate so that they can travel to their respective contacts. Here, the dielectric response is key, as this determines how readily a material will screen electrostatic perturbations. Organic solar cell materials are limited by low dielectric constants ($\epsilon_0 \approx 3\text{--}4$) that lead to large exciton binding strengths.⁴⁵ In inorganic or hybrid materials the dielectric constants are higher ($\epsilon_0 = 10.4$ for CdTe,⁴⁶ whilst values vary from $\epsilon_0 = 16.6$ to $\epsilon_0 = 28.5$ for MAPI).⁴⁷

High carrier mobility

Some materials may have suitable optical properties but are unable to transport the photo-generated charge efficiently to the contact layers. Carrier mobility μ quantifies how quickly an electron or hole can move through a material when pulled by an electric field; it is the magnitude of the carrier drift velocity v per unit of electric field E :⁴⁸

$$\mu = \frac{|v|}{E}. \quad (1.11)$$

At the macroscopic level Equation 1.11 results from averaging over a large number of possible carrier trajectories. In the classical Drude model the carriers are free (the effect of the ion core potential is ignored), independent (the electron-electron Coulomb interaction is ignored) and they accelerate until colliding with a static ion core. For a carrier with charge q and effective mass m the mobility is given by⁴⁸

$$\mu = \frac{q\tau}{m}, \quad (1.12)$$

where τ is the relaxation time between scattering events. The Drude-Sommerfeld model extends the Drude model to treat the electrons as quantum mechanical particles that obey Fermi statistics and the Pauli Exclusion Principle. Using this model the same expression for mobility is derived. Note that for some scattering mechanisms the relaxation time is not independent of the effective mass and this will lead to a more complex relationship between effective mass and mobility, as explored further in Chapter 4.

In Equation 1.12 we see that light carrier effective masses (high band dispersions) correspond to higher mobilities. However light effective masses are not sufficient in themselves as there are

various scattering channels to consider: lattice scattering, carrier-carrier scattering and defect scattering. The most significant scattering mechanisms in a PV material are lattice scattering and ionized defect scattering. A high dielectric constant is beneficial to carrier mobility as the rate of ionized defect scattering is proportional to $\frac{1}{\epsilon^2}$. The composition of the material is also important – for example, vacancies in gallium nitride ($\text{Ga}^{3+}\text{N}^{3-}$) carry a larger charge and have a larger scattering cross section than vacancies in MAPI ($\text{CH}_3\text{NH}_3^{1+}\text{Pb}^{2+}\text{I}_3^{1+}$).

Long carrier lifetime

Carrier lifetime has already been discussed in the context of electron-hole recombination in Section 1.2.2. Whereas the concentration of defects is important for carrier mobility, here it is the energy of defect states with respect to the valence and conduction band which is important. This is discussed in Chapter 6. In summary, the key is to minimise non-radiative recombination via deep level defect states (also known as ‘killer defects’). Carrier diffusion length, another important figure of merit with regard to carrier transport, is proportional to the product of carrier mobility and lifetime.

Compatibility

For efficient charge extraction, the PV absorber layer must be compatible with suitable contact and/or buffer layers. Firstly, the energy levels of the interfacing materials must align so that there is an electrical potential gradient to extract the charge, without significant loss of V_{OC} . For example, band mis-alignments are reported to be the source of poor photovoltaic efficiencies in the candidate absorber materials BiSI and BiSeI.⁴⁹ Secondly, lattice mismatch at the interface should be avoided as this can lead to deep point defects that provide sites for non-radiative recombination and, in the case of more severe strain, an incoherent interface with many defect sites and weak chemical bonding. Computational screening procedures can be used to identify potential electronically and structurally matched contact layers and this has been recently applied to the hybrid halide perovskites.⁵⁰

Toughness

Silicon is a brittle material; the majority of Si material in a solar cell is used as a mechanical carrier to prevent crack propagation, and glass must be used as a protective layer. The resulting cell is often too heavy to be installed on structures which are made from wood or sheet metal. In addition, the bulk of system costs are higher for heavier cells. Organic photovoltaics, and to some extent perovskites, are tougher and can be made using roll-to-roll print processes onto a flexible substrate.

Elemental abundance

The power generated from PV installations must exceed 1 TW to make a real impact on global carbon emissions.⁵¹ To meet this demand, PV materials must be made from abundant elements that are in ready supply at reasonable cost. To quantify this criteria, the Herfindahl–Hirschman

index (HHI), which is used in economics as a measure of market concentration, can be applied to elements. The HHI indicates that Si is abundant but that production is highly concentrated in a few countries. Elements common to the third generation of materials—Cu, Zn, S, Se, Sn—are less abundant but their production is more highly distributed across the globe.⁵²

Elemental non-toxicity

Finally, toxic elements may hinder the successful commercialisation of future PV technologies. The problem is not insurmountable; cadmium telluride is toxic if ingested but is a commercial solar cell material. Encapsulation and recycling can reduce any risk, but add another level of complexity to the development of new solar technologies.

1.3 Summary

To reduce the rate of climate change we must decrease our reliance on fossil fuels, and increasing the proportion of electricity generated from photovoltaic conversion is one way to achieve this. This may only be politically feasible if the costs associated with PV energy generation continue to decrease. As the well-established silicon technologies are limited by high capital expenditures, there is an incentive to develop new low-cost, high-efficiency and reliable technologies. Flexible thin-film architectures also allow for expansion into the new market of building integrated photovoltaics. Currently no material has met these requirements,⁵³ but the promising performance from emerging technologies such as the hybrid halide perovskites motivates further research.

1.4 Thesis outline

Organic-inorganic halide perovskites present a number of challenges for first-principles atomistic materials modelling. These ‘plastic crystals’ feature dynamic processes across multiple length-scales and time-scales, which include mixed ionic-electronic transport, highly anharmonic lattice dynamics and strong relativistic (spin-orbit coupling) effects on the electronic band structure. These issues, which affect the operation of solar cells, are outlined in a review of the literature. This is followed by a brief introduction to the theory that underlies almost all of the work in this thesis – Density Functional Theory (DFT). To model an imperfect material (one with crystal defects), or a material at finite temperature, there are a series of post-processing steps that follow the DFT calculation. These are also outlined in Chapter Three.

Chapters Four to Six contain the thesis results. Each results chapter contains any additional theory, where required, and an outline of the calculation procedures used. Bulk transport and optical properties of the perfect material are calculated using Effective Mass Theory (EMT) in Chapter Three. EMT often assumes that the electronic band dispersion is parabolic, however in this chapter non-parabolic distortions are considered. Temperature effects are introduced in

Chapter Four. At room temperature the inorganic octahedral PbI_3 units tilt back and forth, and the coupling strength between this tilting and the electronic sub-system is quantified. Finally, the iodine interstitial point defect is introduced to our model in Chapter Six. Point defects can be benign or harmful to device performance – in the context of photovoltaics harmful defects are those which trap charge. This chapter investigates charge trapping at the iodine interstitial point defect.

It's simple mathematics.

— Mos Def, *Mathematics*

2

Simulation of hybrid halide perovskites

The text and figures in this chapter are adapted from Whalley, L. D., Frost, J. M., Jung, Y. -K. and Walsh, A. (2017). Perspective: Theory and simulation of hybrid halide perovskites. *The Journal of Chemical Physics*, 146(22), p.220901. © 2017 CC-BY

2.1 Introduction

In this chapter I address recent progress and current challenges in the theory and simulation of hybrid perovskites. Particular attention is paid to predicting properties that assess the photovoltaic potential of a material. Factors to consider include: light absorption, charge transport, absolute band energies, defect physics and chemical stability.

The perovskite mineral, CaTiO_3 , is the archetype for the structure of many functional materials.⁵⁴ Metal halide perovskites have been studied for their semiconducting properties since the 1950s⁵⁵; yet only recently have organic-inorganic perovskites such as $\text{CH}_3\text{NH}_3\text{PbI}_3$ (MAPI) been applied to solar energy conversion, showing remarkably strong photovoltaic action for a solution processed material.⁵⁶ The field has progressed rapidly in the past eight years, with the increase in power conversion efficiency supported by over three thousand research publications.^{57–61} Other potential application areas of these materials include thermoelectrics,^{62,63} light-emitting diodes,^{57,64} and solid-state memory.^{65,66}

These materials combine a complex crystal structure, modulated by static and dynamic disorder, with an electronic structure requiring methods beyond density functional theory to treat many-body and relativistic effects. As such, the halide perovskites represent a challenge to predictive materials modelling.

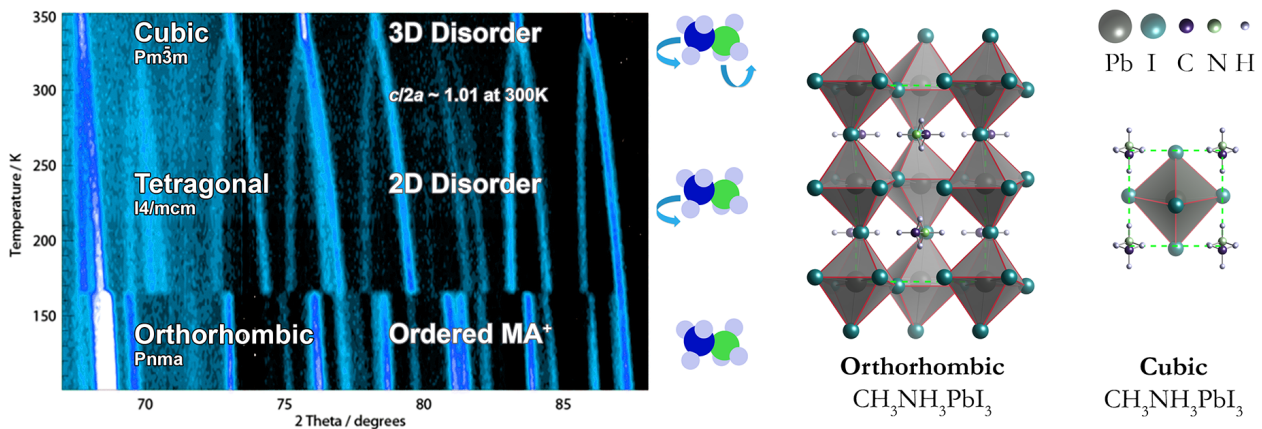


Figure 2.1: The high-resolution powder neutron diffraction pattern of the hybrid halide perovskite $\text{CH}_3\text{NH}_3\text{PbI}_3$ is shown in the left panel (adapted with permission from Ref.⁶⁷ based on data in Ref.⁶⁸), which illustrates the low and high temperature phase transitions. While an ordered CH_3NH_3^+ sub-lattice is expected in the orthorhombic phase, orientation disorder increases with temperature. The crystallographic unit cells of the pseudo-cubic and orthorhombic perovskite phases are shown in the right panel (adapted with permission from Ref.⁶⁹). The associated structure files can be accessed from <https://github.com/WMD-group/hybrid-perovskites>. Figure prepared by Aron Walsh.

2.2 Crystal structures and lattice dynamics

2.2.1 Phase diversity

Hybrid perovskites of the type ABX_3 form a crystal structure with an organic A site cation contained in an inorganic BX_3 framework of corner sharing octahedra. Halide substitution on the X site ($\text{X} = \text{Cl}^-, \text{Br}^-, \text{I}^-$), metal substitutions on the B site ($\text{B} = \text{Pb}^{2+}, \text{Sn}^{2+}$), and cation substitution on the A site ($\text{A} = \text{CH}_3\text{NH}_3^+, \text{HC}(\text{NH}_2)_2^+, \text{Cs}^+, \text{Rb}^+$) lead to various chemical and physical properties.^{70,71} In addition to isoelectronic substitutions (e.g. replacing Pb^{2+} by Sn^{2+}), it is possible to perform pairwise substitutions to form double perovskites (e.g. replacing 2Pb^{2+} by Bi^{3+} and Ag^+).^{72,73}

In the first report of MAPI by Weber in 1978, the crystal structure was assigned as cubic perovskite (space group $\text{Pm}\bar{3}\text{m}$).^{74,75} The anionic PbI_3^- network is charge balanced by the CH_3NH_3^+ molecular cation. The symmetry of CH_3NH_3^+ (C_{3v}) is incompatible with the space group symmetry (O_h) unless orientation disorder (static or dynamic) is present. The crystal structure solved from X-ray or neutron diffraction data usually spread the molecules over a number of orientations with partial occupancy of the associated lattice sites. A common feature of perovskites is the existence of phase changes during heating (typically from lower to higher symmetry) as shown in Figure 2.1. In hybrid halides containing methylammonium, these are orthorhombic (Pnma), tetragonal ($\text{I}4/\text{mcm}$) and cubic ($\text{Pm}\bar{3}\text{m}$) phases.⁶⁸ For MAPI the Pnma to $\text{I}4/\text{mcm}$ phase transition is first-order with an associated discontinuity in physical properties, while the $\text{I}4/\text{mcm}$ to $\text{Pm}\bar{3}\text{m}$ phase transition is second-order with a continuous evolution of the structure and properties.^{68,76}

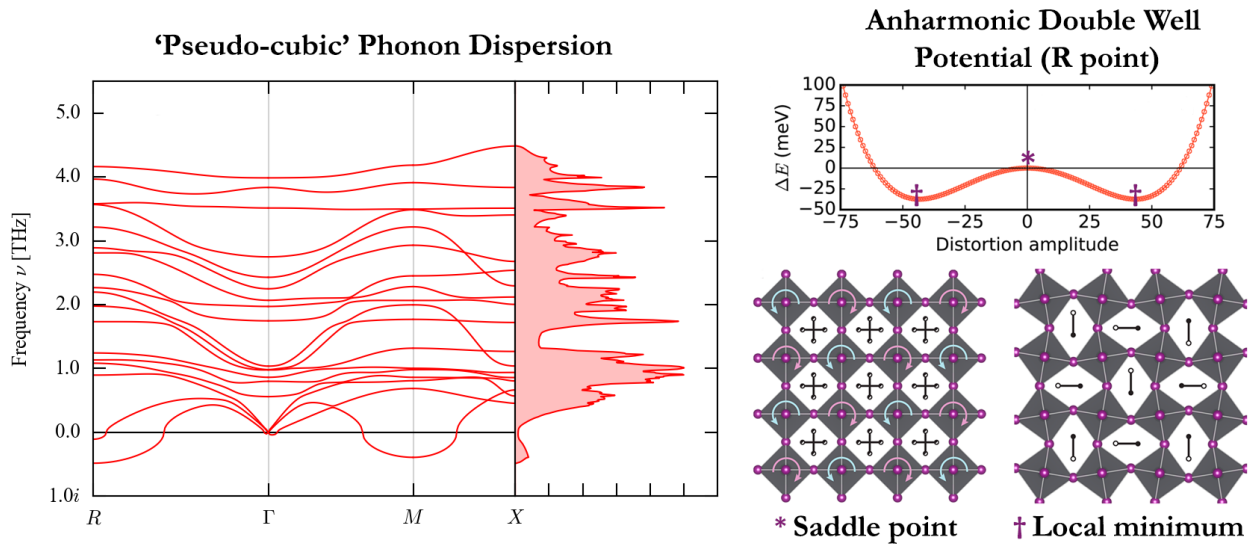


Figure 2.2: (Left) The harmonic phonon dispersion for $\text{CH}_3\text{NH}_3\text{PbI}_3$ from a ‘pseudo-cubic’ structure. The imaginary frequencies of acoustic modes at the M ($q = \frac{1}{2}, \frac{1}{2}, 0$) and R ($q = \frac{1}{2}, \frac{1}{2}, \frac{1}{2}$) Brillouin zone boundary correspond to an instability expressible in a supercell as alternate tilting of the octahedra. (Right) Following the imaginary acoustic mode at the R Brillouin zone boundary in a $2 \times 2 \times 2$ supercell expansion shows a double-well potential in the DFT internal energy. The saddle point corresponds to a $1 \times 1 \times 1$ cubic structure, whilst the two local minima correspond to a distorted structure of lower symmetry. The energy barrier is small enough to allow both minima can be accessed at room temperature, so the system is expected to exhibit dynamic rather than static disorder. Similar behaviour is found at the M point. Figure adapted by Aron Walsh with permission from Refs. [81] and [82]. The underlying phonon data is available from <https://github.com/WMD-group/Phonons>.

The phase transitions are linked to a change in the tilting pattern of the inorganic octahedral cages, and order-disorder transitions of the molecular sub-lattice.^{76–78} X-ray diffraction (XRD) measurements upon cooling (heating) suggest the incursion of tetragonal in orthorhombic phases (and vice versa),⁷⁹ which is common for first-order solid-state phase transitions.

Similar phase behaviour tends to be seen for other compositions; however, the transition temperatures vary. In MAPI the orthorhombic to tetragonal transition temperature is 162 K, becoming cubic by around 328 K, while $\text{CH}_3\text{NH}_3\text{PbBr}_3$ is cubic above 237 K.⁸⁰

2.2.2 Local and average crystal environment

The first electronic structure calculation of hybrid halide perovskites was by Chang, Park and Matsushi in 2004,⁸³ in the local density approximation (LDA) of density functional theory (DFT). They modelled a static structure where the CH_3NH_3^+ molecule was aligned along $\langle 100 \rangle$ (towards the face of the corner-sharing PbI_3^- framework), but found that the barrier for rotation to $\langle 111 \rangle$ was less than 10 meV. This small barrier for cation rotation gave credence to a prior model that the molecular sub-lattice was dynamically disordered.⁸⁰ Similar barriers were later found within the generalised gradient approximation (GGA) of DFT.⁸⁴

Ab initio molecular dynamics (MD), neutron scattering^{85,86} and time-resolved infra-red⁸⁷ data all indicate a 1–10 picosecond reorientation process at room temperature. As a result of anharmonic molecular rotation, and large-scale dynamic distortions along soft vibrational modes, the local structure can deviate considerably from that sampled by diffraction techniques, which do not probe local disorder that preserves long-range order on average.

In spite of the larger cation, FAPI appears to possess a similar timescale of rotation to MAPI⁸⁸. A lighter halide (and therefore smaller cage) results in faster rotation, in spite of the greater steric hindrance.⁸⁹ Together, these data suggest that the molecular rotation is a function of the local inorganic cage tilting, where the relatively insignificant mass of the organic cation follows the pocket distortion.

The spontaneous distortions can also be observed in the vibrational spectra. The calculated harmonic phonon dispersion for MAPI in the cubic phase is presented in Figure 2.2. The acoustic modes soften as they approach the M ($q = \frac{1}{2}, \frac{1}{2}, 0$) and R ($q = \frac{1}{2}, \frac{1}{2}, \frac{1}{2}$) Brillouin zone boundaries. This zone boundary instability can only be realised in an even supercell expansion, where it corresponds to anti-phase tilting between successive unit cells. This behaviour is characteristic of the perovskite structure,⁹⁰ and can be described by the Glazer tilt notation.^{91,92}

Within the frozen-phonon approximation the potential energy surface can be traced along the soft acoustic M and R modes. In both cases this results in a double well with an energy barrier $\sim k_B T$ at the saddle point;⁸¹ at room temperature the structure is dynamically disordered, with continuous tilting. Indeed, MD simulations show continuous tilting of MAPI and FAPI at room temperature.^{88,93,94} As temperature decreases, the structural instability condenses via the R point (with an energy barrier of 37 meV) into the lower symmetry tetragonal phase. This is followed by condensation of the M point (with an energy barrier of 19 meV) to the orthorhombic phase.⁸¹

In the static picture – as in the case of an electronic band structure calculated for a single ionic snapshot – the organic cation plays no direct role in optoelectronic properties of the material as the molecular electronic levels lie below that of the inorganic framework. Once motion is considered, the electrostatic and steric interaction between the organic molecule and inorganic framework couples tilting and distortion of the octahedra to the organic cation motion. These tilts and distortions vary the orbital overlap between states, perturbing the band-structure and band-gap.^{81,94–96} The electronic structure thus becomes sensitive to temperature, which will be discussed further in Section 2.3.2 and Chapter 5.

2.2.3 Thermodynamic and kinetic stability

Ab initio thermodynamics has emerged as a powerful tool in materials modelling, with the ability to assess the stability of new materials and place them on equilibrium phase diagrams even before experimental data is available.^{97–99} The total energy from DFT calculations approximates

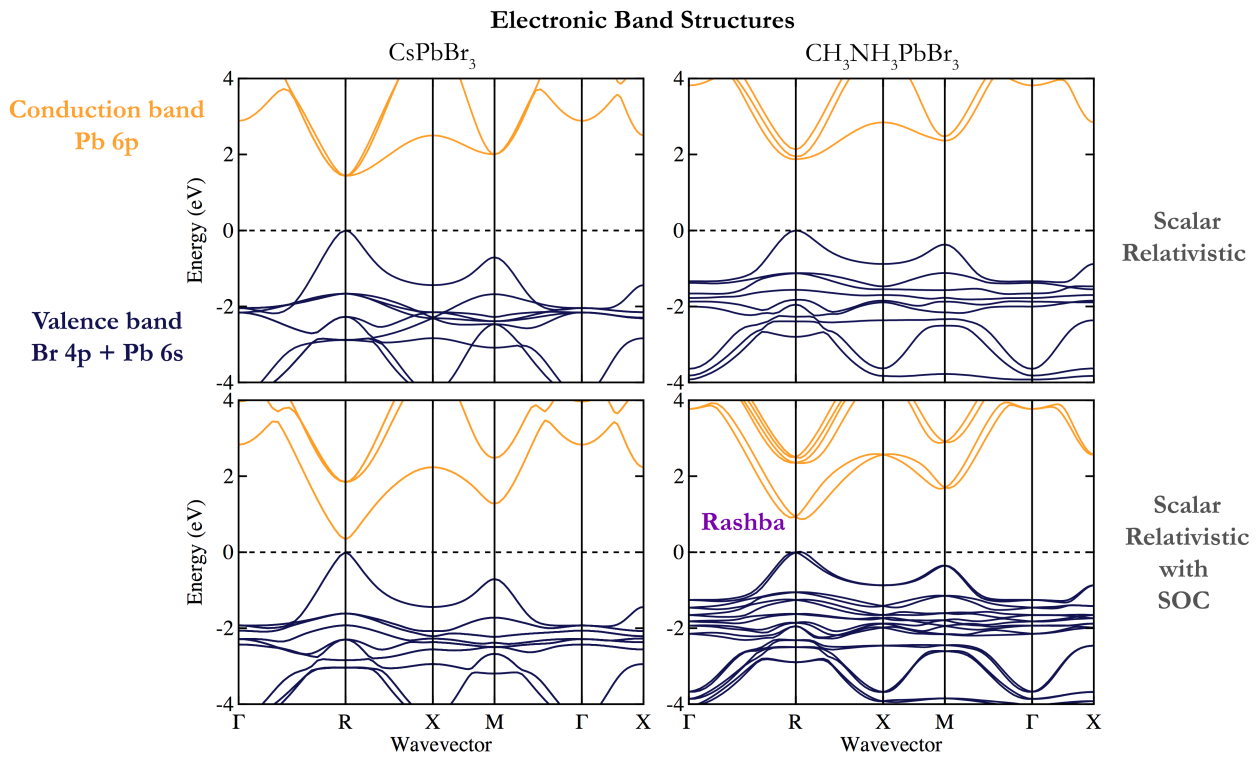
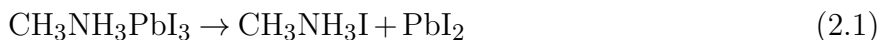


Figure 2.3: The electronic band structures of the inorganic perovskite CsPbBr_3 and hybrid perovskite $\text{CH}_3\text{NH}_3\text{PbBr}_3$ in the cubic phase. One effect of the organic cation is to widen the band-gap located at the R point due to the larger lattice constant. Spin-orbit coupling reduces the band-gap in both materials. The presence of CH_3NH_3^+ in the hybrid perovskite results in a non-centrosymmetric crystal, with an associated relativistic Rashba-Dresselhaus splitting of the lower conduction band. While labels of the special points are those of the cubic perovskite structure (space group $Pm\bar{3}m$), the static model of the hybrid perovskite formally has $P1$ symmetry. Points equivalent for a cubic crystal (e.g. $M = \frac{1}{2}, \frac{1}{2}, 0$; $M' = 0, \frac{1}{2}, \frac{1}{2}$; $M'' = \frac{1}{2}, 0, \frac{1}{2}$) are inequivalent here. Figure prepared by Young-Kwang Jung.

the internal energy of the system. By including lattice vibration (phonon) and thermal expansion contributions, the Gibbs free energy and other thermodynamic derivatives can be evaluated.¹⁰⁰ In the context of photovoltaic materials, this has been applied to $\text{Cu}_2\text{ZnSnS}_4$ and used to identify the processing window where a single-phase compound can be grown in equilibrium.¹⁰¹ An issue with hybrid perovskites and other metal-organic frameworks is that the calculated heat of formation is close to zero. The decomposition reaction



has been predicted to be exothermic. Subsequent calorimetric experiments have supported the prediction that hybrid lead halide perovskites are metastable.¹⁰² It is likely that these materials are only formed due to entropic (configurational, vibrational and rotational) contributions to the free energy.

2.2.4 Anharmonic lattice vibrations and thermal conductivity

Kohn-Sham density functional theory is most often carried out in the Born-Oppenheimer approximation where the nuclei are static classical point charges. To consider thermal vibrations, expansion or heat flow the theoretical framework of lattice dynamics can be used.¹⁰⁰

In the harmonic approximation, the lattice dynamics are fully specified by second-order force-constants of individual atoms, which are then used to build the dynamical matrix. The eigenstates of this matrix are the normal modes of vibration with an associated phonon energy. Thermal expansion coefficients, system anharmonicity (e.g. Grüneisen parameters) and the temperature-dependence of other properties can be calculated in the quasi-harmonic approximation (QHA). Here the lattice dynamics are harmonic at a given temperature; however, the cell volume is scaled by thermal expansion to give the first-order contribution of finite temperature effects.

The thermal expansion coefficient of MAPI in the cubic phase has been calculated with the QHA. The value is sensitive to the density functional used. For example, a value of $3.0 \times 10^{-5}/K$ is calculated with the PBE functional with Tkatchenko-Scheffler dispersion corrections,⁹⁶ while the PBEsol functional produces a value of $12.5 \times 10^{-5}/K$.⁶⁹ These compare to finite temperature scattering measures of $1.91 \times 10^{-5}/K$ by X-ray,¹⁰³ and $13.2 \times 10^{-5}/K$ by neutron diffraction.⁶⁸ Even taking the smallest value above, the expansion coefficient is one order of magnitude greater than silicon,⁴⁶ highlighting the strong deviation from harmonic behaviour in halide perovskites.

In the harmonic approximation (and similarly the QHA), the dynamic matrix eigenmodes are orthogonal and the resulting phonons are non-interacting. Consequently phonon lifetimes are infinite as the phonons do not scatter; thermal conductivity is infinite. To calculate phonon-phonon scattering, and so its contribution to finite thermal conductivity, anharmonic lattice dynamics need to be considered. A computational route is to use perturbative many-body expansion, e.g. as implemented in PHONO3PY,¹⁰⁴ which includes third-order force constants. For MAPI, 41,544 force evaluations are required for these third-order force constants, compared to 72 for second-order (harmonic) force constants.⁸¹ Consequently, these calculations are vastly more expensive. Using this approach phonon-phonon scattering rates are calculated to be three times larger in MAPI compared to standard covalent semiconductors CdTe and GaAs.⁸¹ Consequently, mean free paths are on the nanometer rather than more typical micrometer scale. Lattice thermal conductivity is extremely low, $0.05 \text{ Wm}^{-1}\text{K}^{-1}$ at 300 K.⁸¹ This combination of high electrical and low thermal conductivity makes these compounds potential thermoelectric materials.^{62,63}

In highly anharmonic systems third-order force constants and perturbation theory may not be sufficient to describe the true dynamics, but going further with lattice dynamics becomes prohibitive. Besides, it is not obvious whether the fundamental tenant of lattice dynamics, of expanding in small displacements around a minimum structure, is correct for these soft and highly anharmonic materials. In contrast, MD treats anharmonic contributions to all orders. As

MD stochastically explores the phase space, long integration times are required to sample rare events, and finite size effects mean that only phonon modes commensurate with the supercell are sampled.

2.3 Electronic structure

Despite the dynamic disorder just discussed, in many respects halide perovskites display characteristics of traditional inorganic semiconductors, with a well-defined electronic band structure and electron/hole dispersion relations. However, when the electronic structure is correctly modelled, various subtleties emerge.

2.3.1 Many-body and relativistic effects

Perhaps surprisingly, local and semi-local exchange-correlation functionals provide a reasonable estimate for the band-gaps of these heavy metal halide materials. This is due to a cancellation of errors. For Pb-based perovskites, the conduction band has mainly Pb 6p character. Due to the large nuclear charge, the electronic kinetic energy requires a relativistic treatment, and spin-orbit coupling (SoC) becomes significant. The first-order effect is a reduction in band-gap by as much as 1 eV¹⁰⁵, as the degenerate 6p orbitals are split and moved apart. This is shown in Figure 2.3 for the bromide compounds. The typical band-gap underestimation of GGA functionals is offset by the absence of relativistic renormalisation.

SoC is not expected to have a large impact on the structural properties of the Pb-based compounds as the (empty) conduction band is mainly affected, and the force on atoms depends on the electron density (occupied orbitals). Accurate force-constants can be calculated without SoC considerations.¹⁰⁶

There have been a number of electronic structure calculations considering many-body interactions beyond DFT. Quasi-particle self-consistent GW theory shows that the band dispersion (and so density of states, optical character and effective mass) is considerably affected by both the GW electron correlation and SoC.¹⁰⁵ Some materials see only a rigid shift of band structure (retaining DFT dispersion relations)^{50,107} but this is not the case for hybrid perovskites. The effect of SoC on the band dispersion of MAPI is discussed in Chapter 4.

A consequence of SoC when combined with a local electric field is the Rashba-Dresselhaus effect, a splitting of bands in momentum space.¹⁰⁸ This can be understood as an electromagnetic effect, where the magnetic moment (spin) of the electron interacts with a local electric field, to give rise to a force which displaces it in momentum space. Up and down spins are displaced in opposite directions, and this displacement is a function (in both size and direction) of the local electric field, which will depend on the local dynamic order. For a static structure, this is demonstrated in Figure 2.3 for $\text{CH}_3\text{NH}_3\text{PbBr}_3$. Neglecting SoC, the cubic phase has band extrema at the R point (a direct band-gap). With SoC the valence and conduction band each

split into valleys symmetrical around R . The splitting is much more pronounced in the Pb $6p$ conduction band (compared to the Br $4p$ valence band), as expected from the Z^4 dependence of spin-orbit coupling. This asymmetry in the band extrema results in direct-gap like absorption and indirect-gap like radiative recombination which is discussed later. For a comparison between SoC and non-SoC bandstructures across a range of materials see Appendix A.

The relativistic spin-splitting can only occur in crystals that lack a centre of inversion symmetry, a prerequisite for generating a local electric field. The cubic representation of CsPbBr₃ has an inversion centre, so while SoC affects the band-gap through the separation of Pb $6p$ into $p_{\frac{1}{2}}$ and $p_{\frac{3}{2}}$ combinations, no splitting of the band extrema away from the high symmetry points is observed (see Figure 2.3). This is true only for a static cubic structure and, as discussed earlier, hybrid halides will have continuous local symmetry breaking.

Point defect calculations will be particularly sensitive to the electronic structure method used. Neglection of SoC and self-interaction errors can result in an incorrect position of the valence or conduction band edges, thus introducing spurious errors in defect energy levels and predicted defect concentrations. Du¹⁰⁹ showed how for the case of an iodine vacancy, a deep (0/+) donor level is predicted for GGA without SoC, while a resonant donor level is predicted for GGA-SoC and HSE-SoC treatments of electron-exchange and correlation.

2.3.2 Electron-phonon coupling

Going beyond the Born-Oppenheimer approximation, the interaction of the electronic structure with vibrations of the lattice can be considered. Electron-phonon coupling can perturb the electronic band energies (changing the band-gap), and couple electronic excitations (the hole and electron quasi-particles) into vibrational excitations (phonon quasi-particles). In a semiconductor, charge carrier scattering is often dominated by this electron-phonon interaction, and so the strength of these processes set a limiting value on the mobility. Electron-phonon coupling is often calculated in a second-order density functional perturbation theory calculated for a static (rigid ion) structure. In the normal limit, this term is expected to dominate over the first order contribution from the acoustic deformation potential as vibrations are typically small.

Saidi et al. sampled all non-soft harmonic phonons at the Γ point using a Monte Carlo technique,⁹⁶ finding significant differences with the standard perturbation theory results. Electron-phonon interactions can be calculated with MD, but as with phonon-phonon scattering, achieving convergence with respect to electronic (k -point sampling and basis set) and vibrational (q -point sampling and supercell size), while maintaining sufficient integration time to capture rare processes, is costly.

Recently a ‘one shot’ method has been developed to calculate band-gap renormalization and phonon-assisted optical absorption, and applied to Si and GaAs.¹¹⁰ Nuclei positions are carefully chosen as a representative sample from the thermodynamic ensemble, and the electronic structure

is needed for this static structure only—a significant increase in computational efficiency. Such techniques may provide a promising method to calculate the electron-phonon coupling of complex materials, but they have not yet been tested for the family of hybrid halide perovskites or other more complicated crystal structures.

2.3.3 Charge carrier transport

Charge carrier transport in hybrid halide perovskites is now considered. The minority-carrier diffusion length is the average length a photo-excited (or electronically-injected) carrier travels before recombining. In a photovoltaic device, the diffusion length must be sufficient to reach the contacts. The minority-carrier diffusion length is a product of the diffusivity D and lifetime τ of minority charge carriers, $L_d = \sqrt{D\tau}$.

Minority-carrier diffusion lengths in MAPI are reported to be considerably larger than other solution processed semiconductors.¹¹¹ Long lifetimes (large τ) can be partly attributed to the ‘defect-tolerance’ of hybrid perovskites (discussed in Section 2.4.3), reducing the rate of ionised-impurity scattering and non-radiative recombination.

The effective masses of electrons and holes in hybrid halide perovskites are small. Given the effective mass of $< 0.2m_e$, the carrier mobility of MAPI ($< 100 \text{ cm}^2\text{V}^{-1}\text{s}^{-1}$) is modest in comparison to conventional semiconductors such as Si or GaAs ($> 1000 \text{ cm}^2\text{V}^{-1}\text{s}^{-1}$).⁵⁷ Carrier mobility must be limited by strong scattering.

Low temperature mobility in this material reduces as a function of temperature as $T^{-1.5}$, which provides circumstantial evidence for being limited by acoustic phonon scattering.^{112,113} However, if only the acoustic phonon scattering (which is elastic due to the population of acoustic modes) is considered, the calculated mobility is orders of magnitude larger than experiment. A key realisation is that the soft nature of these semiconductors results in optical phonon modes (see Figure 2.2) below thermal energy.^{69,106} Optical phonon scattering is inelastic and dominates once the charge carriers have sufficient energy to generate the phonon modes.¹¹⁴ Through solving the Boltzmann transport equation parameterised by DFT calculations, scattering from longitudinal optical phonons is identified as the process limiting mobility at room temperature.^{115,116}

Mobility will be further limited by scattering from point and extended lattice defects.¹¹⁷ Fluctuations in electrostatic potential resulting from dynamic disorder provide a macroscopic structure from which carriers will also scatter.^{93,118}

2.4 Photophysics and solar cells

Hybrid halide perovskites are, in the most part, being researched in the context of solar cell technology. There are areas of the underlying physics which are not yet developed, and which may be limiting progress in the field. Ion migration is poorly understood and has been correlated

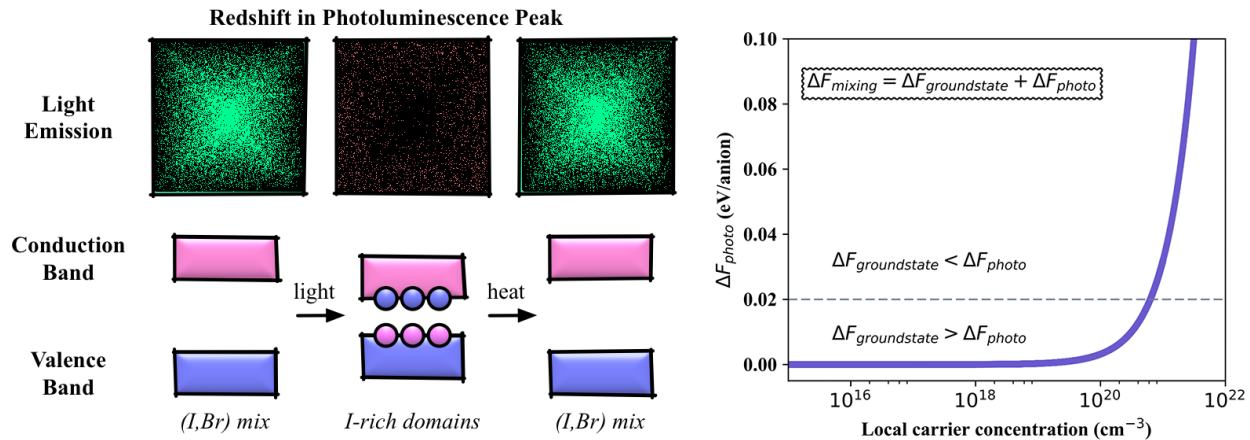


Figure 2.4: Halide perovskites are mixed ionic-electronic conductors. The vacancy-mediated diffusion of halide anions has been associated with both current-voltage hysteresis of solar cells and the rapid interchange between iodide, bromide and chloride materials. One point of controversy remains the reversible ion segregation observed in mixed (Br,I) systems. Alloyed materials have been found to phase separate upon illumination, but recover their initial state when the light source is removed. The phase separation is associated with a striking red-shift in photoluminescence spectra. A statistical mechanical analysis of ground-state DFT calculations suggested a large miscibility gap¹¹⁹, while the charge carriers generated upon illumination can provide an additional driving force for phase separation.¹²⁰ The results from a simple thermodynamic model are shown in the right panel, where the free energy of mixing contains contributions from the ground-state with an additional component due to the difference in band-gaps between the mixed (I,Br) and phase separated I-rich phases. The latter contribution requires local carrier concentrations approaching 10^{21} cm^{-3} to make a substantial contribution to the overall mixing energy. Figure prepared by Aron Walsh.

with the hysteresis effects^{121,122} and device degradation. In MAPI, the iodine interstitial defect has been identified as a site for charge trapping¹²³ (as reported in Chapter 6), but the role of impurities is not understood. Additionally, interfaces have not been optimised for optimal charge carrier extraction. These issues are outlined in the following section.

2.4.1 Ion migration

Charged point defects in the bulk allow for mass transport of ions and can result in spatial fluctuations of electrostatic potential. For solid-state diffusion to be appreciable in magnitude, there needs to be a high concentration of defects and a low activation energy for diffusion.

The equilibrium concentration of charged vacancy defects is calculated as being in excess of 0.4% at room temperature in MAPI.¹²⁴ Low defect formation energies and free-carrier concentrations found across the halide hybrid perovskites indicate that Schottky defects are prevalent across this family of materials. While each point defect is charged, they are formed in neutral combinations so that a high concentration of lattice vacancies does not require a high concentrations of electrons or holes to provide charge compensation.

The ion migration rate is given by:

$$\Gamma = \nu \exp\left(\frac{-\Delta H^{\text{diff}}}{k_B T}\right) \quad (2.2)$$

where ΔH^{diff} is the activation energy for solid-state diffusion, and ν is the attempt frequency. In MAPI the diffusion of methylammonium cations, iodide anions and protons have been considered in the literature. Activation energies calculated from first principles show that the predominant mechanism for ion migration is the vacancy assisted hopping of iodide ions.¹²¹ This has been confirmed using string simulations¹²⁵ which, like the nudged elastic band method, calculate minimum energy paths and from this infer transition rates.

Based on a bulk activation energy of 0.58 eV¹²¹, a rate of 733 hops per second would be expected at $T = 300$ K, with an associated diffusion coefficient of $10^{-12} \text{ cm}^{-2} \text{s}^{-1}$. Effective activation energies as low as 0.1 eV have been reported experimentally,^{126,127} which likely correspond to diffusion along extended defects (dislocations, grain boundaries, surfaces)^{128,129}. The corresponding diffusion rate of $10^{-5} \text{ cm}^{-2} \text{s}^{-1}$ is very fast, but comparable to surface diffusion of iodine observed in other compounds.¹³⁰

Modelling ion diffusion at device scales is not yet possible with *ab-initio* methods. Parametrised drift-diffusion modelling of ion and electron density indicate that slow moving ions can explain the slow device hysteresis.^{122,131} A vacancy diffusion coefficient of the order of $10^{-12} \text{ cm}^2 \text{s}^{-1}$ is consistent with both predictions and transient measurements.¹²¹

It has been suggested that ion migration within mixed-halide compositions is the result of a non-equilibrium process induced by photoexcitation. X-ray diffraction measurements by Hoke et al.¹³² show that under illumination the mixed halide perovskite $\text{MAPb}(\text{I}_{1-x}\text{Br}_x)_3$ segregates into two crystalline phases, one iodide-rich and the other bromide-rich. This segregation leads to reduced photovoltaic performance via charge carrier trapping at the iodide-rich regions. In some reports, after a few minutes in the dark the initial single phase XRD patterns are recovered. This reversible process is unusual and defies the common assumption made that ion and electron transport are decoupled.

A schematic outlining the phase segregation process is shown in Figure 2.4. A phase diagram constructed from first-principles thermodynamics found a miscibility gap for a range of stoichiometries at room temperature.¹¹⁹ This suggests that a mixed-halide material is metastable and will phase segregate after being excited by light, which follow a decreasing free energy gradient towards halide-rich areas formed prior to light excitation (such as grain boundaries). The accumulation of charge carriers increases lattice strain and drives further halide segregation. Our calculations indicate that the transition between mixing and segregation will occur at a local carrier concentration of 10^{21} cm^{-3} , so that charge accumulation in small regions of the material is required for this model.

2.4.2 Electron-hole recombination

The open-circuit voltage (V_{oc}) of a solar cell is determined by the rate of charge carrier recombination in the material, as no photogenerated charges are being extracted and so all are recombining. When operating to generate power, the rate of recombination competes with the rate of charge extraction, limiting the fill factor of the solar cell.

Recombination is usually separated into three channels: non-radiative; radiative; and Auger (see Section 1.2.2 for further discussion). While non-radiative recombination is limiting in many inorganic thin-film technologies, hybrid perovskites are not significantly affected. This is surprising given the high density of defects expected for a material processed from solution, leading to hybrid perovskites being described as ‘defect tolerant’.¹³³

Radiative (bimolecular) recombination is slower than would be expected for a direct band-gap semiconductor. Recent calculations reveal how relativistic Rashba splitting can suppress radiative recombination at an illumination intensity relevant to an operating solar cell.^{134,135} After photoexcitation, electrons thermalise to Rashba pockets in the conduction band minima away from the high symmetry point in reciprocal space. This leads to an indirect charge recombination pathway as the overlap in k -space between occupied states near upper valence and lower conduction bands diminishes. It has also been suggested that direct recombination is suppressed at very short timescales due to the pockets of minima being spin-protected.¹³⁵ Direct gap radiative recombination is reduced by a factor of 350 at solar fluences, as electrons must thermally repopulate back to the direct gap.¹³⁴ This is in agreement with the temperature-dependence of the bimolecular rate measured experimentally⁷⁹ and calls into question the validity of models where a global radiative recombination rate independent of carrier concentration is used. Auger recombination is only significant at fluences well above solar radiation.

Ferroelectric effects could contribute to electron-hole separation due to electrostatic potential fluctuations in real space. Although the molecular cation plays no direct role in charge generation or separation it could influence charge transport through the formation of polar domains.^{118,136} This dynamic polarisation has been explored using a model Hamiltonian parameterized for the inter-molecular dipole interaction in MAPI.⁹³ This model predicts the formation of antiferroelectric domains that minimise energy via dipole-dipole interaction, and dominate a cage-strain term preferring ferroelectric alignment.⁸⁵ The domains would provide electrostatically preferred pathways for electrons and holes to conduct.

2.4.3 Defect levels in the band-gap

To understand why defects appear to have a minimal impact upon charge carrier mobility and lifetime,¹³⁷ the defect properties of hybrid perovskites can be considered. Under the Shockley-Read-Hall model for semiconductor statistics non-radiative recombination is mediated through deep defect states in the gap.¹³⁸ Shallow defect states can act as traps but the carriers are

Table 2.1: The first shallow donor defect level in MAPI, Si and CdTe calculated from effective mass theory using Equation 2.3. The dielectric constant ϵ_0 is an important descriptor for photovoltaic materials as several important properties (e.g. rate of impurity scattering) scale with its square.

Material	$\frac{m^*}{m_0}$	ϵ_0	$E_1(\text{meV})$
MAPI	0.15 ¹³⁶	25.7 ¹³⁶	3
Si	0.45 ¹⁴²	11.7 ¹⁴²	45
CdTe	0.11 ¹⁴³	10.2 ⁴⁶	14

thermally released to the band before recombination can occur. Hybrid perovskites – with high dielectric constant and low effective mass – show a tendency towards benign shallow defects under the hydrogenic model:¹³⁹

$$E_n = -\frac{m^*}{m_0} \frac{1}{2n^2\epsilon_0^2} \quad (2.3)$$

where $\frac{m^*}{m_0}$ is the effective mass ratio, ϵ_0 is the static dielectric constant and n is an integer number that labels the energy level. Atomic units are used and so the energy E_n is given in Hartrees.

In Table 2.1 the first hydrogenic defect levels for MAPI, Si and CdTe are given. The binding energy for MAPI is only 3 meV. For ionic materials, one would expect a large central cell correction that could result in much deeper levels, as seen for the colour centres in alkali halides.¹⁴⁰ However on-site electrostatic potentials in the I-II-VII₃ perovskites are relatively weak due to the small charge of the ions (e.g. Cs⁺Pb²⁺I₃⁻) compared to other perovskite types (e.g. Sr²⁺Ti⁴⁺O₃²⁻),¹⁴¹ which supports the existence of shallow levels. In addition, arguments based on covalency have also been proposed.¹³⁷

2.4.4 Beyond the bulk: surfaces, grain boundaries and interfaces

As perovskite solar cells approach commercial viability,⁵⁹ there are considerations to be made beyond the bulk material. Surfaces, grain boundaries and interfaces will influence device performance and long-term stability, and become increasingly important as the science is scaled up from lab to production line. Halide migration, ion accumulation, charge carrier transport and charge carrier recombination at the defect states are some of the processes to consider when building an accurate interface model. There has been preliminary work, that provides insights, but real systems offer much deeper complexity.

Perovskite films fabricated through solution processing methods are multicrystalline and so the formation of grain boundaries is inevitable. The resulting microstructure provides pathways for ion conduction, electron-hole separation and recombination. Improved device performance with increasing grain size¹⁴⁴ is evidence for shallow traps associated with the grain boundary. Initial calculations suggest that grain boundaries do not introduce deep defects and consequently have negligible effect upon the rate of non-radiative recombination.¹⁴⁵ This is in conflict

with spatially resolved photoluminescence¹⁴⁶ and cathodoluminescence¹⁴⁷ measurements which evidence greater non-radiative loss at grain boundaries. Nonadiabatic MD and time-domain density DFT¹⁴⁸ indicate that grain boundaries localize the electron and hole wavefunctions and provide additional phonon modes. This leads to increased electron-phonon coupling which in turn will give a higher rate of non-radiative recombination.

A commonly used hole transport material is spiro-OMeTAD. This material is hygroscopic so stability in humid air is a concern,¹⁴⁹ and screening procedures have been used to identify alternative contacts.^{150,151} Band alignment, lattice match and chemical viability via the overlap of atomic positions are used to determine the electronic-lattice-site (ELS) figure of merit.¹⁵⁰ Using this approach Cu₂O is identified as a possible earth abundant hole extractor, whilst oxide perovskites such as SrTiO₃ and NaNbO₃ are identified as possible electron extractors. As with the majority of screening techniques, the candidate materials meet the necessary but perhaps not sufficient conditions. Further refinements to the screening procedure could consider the change in electronic properties as lattice strain and chemical inhomogeneity at the interface is introduced.

2.5 Summary

I have outlined the physical properties which make hybrid perovskites unique semiconductors that are a challenge for theory and simulation. Common issues that can arise in the simulation of hybrid perovskites are summarized in Table 2.2. The volume of work in this area means that all active areas of research cannot be addressed, including perovskite-like structures with lower dimensionality (e.g. Ruddleston-Popper phases)^{58,152,153} and double perovskites with pairwise substitutions on the B site,^{72,73,154,155} which are both attracting significant interest.

The properties of hybrid halide perovskites which are difficult to model are also those which make them a successful PV material. For example, calculating ground state electronic properties using the approximation of a single static lattice does not capture the effects of strong electronic-ionic coupling. However, it is this coupling which screens charge, produces a defect tolerant material, facilitates fast charge separation and suppresses excitonic states. As another example the transport behaviour of halide ions via Schottky-like charged vacancy defects requires a multi-scale modelling approach. However, it is these defects that provide the low free carrier background concentration necessary for high efficiencies in a p-i-n architecture. Attempts are now being made to distill this understanding into descriptors for the large-scale screening of novel, earth-abundant, non-toxic semiconductors.^{49,137}

Technique	Symptom	Solution
Geometry optimisation	Partial occupancy in structure files	Test different configurations and check total energy
Geometry optimisation	Missing H in structure files	Include H based on chemical knowledge and electron counting
Geometry optimisation	Slow ionic convergence	Try changing algorithm type and settings
Electronic structure	Bandgap is too large	Include spin-orbit coupling and consider excitonic effects
Electronic structure	Bandgap is too small	Use a more sophisticated exchange-correlation functional
Electronic structure	Bandgap is still too small	Try breaking symmetry, especially for cubic perovskites
Electronic structure	Workfunction is positive	Align to external vacuum level using a non-polar surface
Supercell convergence	Unusual convergence behaviour	Use only even cell expansions (e.g. $2 \times 2 \times 2$)
Ab initio thermodynamics	No stable chemical potential range	No easy fix (many hybrid materials are metastable)
Berry phase polarisation	Polarisation is too large	Use appropriate reference structure and pathway
Point defects	Negative formation energies	Check for balanced chemical reaction and chemical potential limits
Point defects	Transition levels are deep in band-gap	Check supercell expansion and charged defect corrections
Alloyed systems	Many possible configurations	Use appropriate statistical mechanics
Lattice dynamics	Many imaginary phonon modes	Check supercell size and force convergence
Lattice dynamics	Imaginary modes at zone boundaries	Use mode-following to map out potential energy surface
Molecular dynamics	System melts or decomposes	Check k -points and basis set convergence
Molecular dynamics	Unphysical dynamics	Check equilibration and supercell expansion
Molecular dynamics	No tilting observed	Use an even supercell expansion
Electron-phonon coupling	Values far from experiment	Consider anharmonic terms beyond linear response theory
Drift-diffusion model	Current-voltage behaviour incorrect	Consider role of fluctuating ions and electrostatic potentials

Table 2.2: Common issues that arise in the simulation of hybrid perovskites, sourced from members of the Walsh Materials Design Group.

Two MCs can't occupy the same space at the same time, it's against the laws of physics.

— Lauryn Hill, *Zealots*

3

Theory and methodology

3.1 Introduction

In this chapter I present the theory and methodology that underlies the work in this thesis. The chapter starts with an introduction to Density Functional Theory (DFT): first I introduce the theoretical concepts, then I provide some details about how DFT is implemented in practice. In the second part of the chapter I outline how we can use DFT energies combined with a series of post-processing steps to predict defect formation energies and charge transition levels. The chapter ends with an introduction to the theory of lattice dynamics and how this theory is used to calculate the vibrational properties of a material.

3.2 Density Functional Theory

Density Functional Theory is the most commonly used electronic structure method in condensed matter physics and quantum chemistry. DFT can be used to predict the ground state properties of a material including electron density, total energy, equilibrium structure, vibrational frequencies, and properties relating to differences in total energy, such as defect formation energy or surface energy. As DFT is a ground state theory we are not able to calculate properties relating to excited states and, without further calculations such as those outlined in Section 3.4, results do not incorporate the effects of temperature.

The theoretical basis for DFT was established in 1964 through the work of Walter Kohn and Pierre Hohenberg.¹⁵⁶ This was further developed by Walter Kohn and Lu Jeu Sham to produce Kohn-Sham DFT.¹⁵⁷ However it was not until the late 1980's approximations to the exchange-correlation functional were built so that DFT could be used in practice.

There are a growing number of codes that implement DFT. Although some codes aspire to a blackbox approach, with the user protected from the underlying mechanics of DFT, for most

systems of interest an understanding of the underlying approximations and parameters used are required for reliable results.

3.2.1 Basic concepts

Firstly, a note on the name. A function accepts one or more numbers as input and produces a number as output. Likewise, a functional accepts one or more *functions* as inputs, and produces a number as output. In DFT the functional is the electron density which is itself a function of space and time.

Throughout this chapter, unless stated otherwise, we use the Born-Oppenheimer approximation: the heavy atomic nuclei are treated as fixed points, and we solve the ground state quantum mechanical problem for the electrons only. This reduces the number of degrees of freedom of the system, a tactic that will be used again later in the chapter.

Although no one single text is followed, concepts for the underlying theory have been taken from References [158], [159] and [160].

The Schrödinger equation

A fundamental postulate of quantum mechanics is that for any physical system there is an associated wavefunction that contains all the system information. The Schrödinger equation describes the wavefunction Ψ of a quantum mechanical system. Once the Schrödinger equation is solved, and a wavefunction is found, all the physical properties for that system follow. To take the simplest possible example, the time-independent non-relativistic Schrödinger equation for a single particle can be written as:

$$\left[\frac{-\hbar^2}{2m} \nabla^2 + v_{\text{ext}}(\mathbf{r}) \right] \Psi(\mathbf{r}) = E\Psi(\mathbf{r}), \quad (3.1)$$

where the first term in the bracket corresponds to the kinetic energy and the second term corresponds to the potential energy. For a single particle in a simple potential, such as the particle in a box system or hydrogen atom, the Schrödinger equation can be solved exactly. Unfortunately it is not possible to solve the Schrödinger equation exactly for more complex systems, where there are multiple electrons interacting with each other (N-body or many-body systems). In this case, the Schrödinger equation takes the form:

$$\left[\frac{-\hbar^2}{2m} \sum_{i=1}^N \nabla_i^2 + \sum_{i=1}^N v_{\text{ext}}(\mathbf{r}_i) + \sum_{i < j}^N \frac{q_i q_j}{|\mathbf{r}_i - \mathbf{r}_j|} \right] \Psi(\mathbf{r}_i) = E\Psi(\mathbf{r}_i), \quad (3.2)$$

where the third term in the square bracket describes the electrostatic interaction between two particles of charges q_i and q_j , and couples the coordinates of the particles together.

Hartree-Fock methods and Kohn-Sham DFT provide ways to obtain an approximate solution to the Schrödinger equation for systems of interest. They do this by mapping the interacting problem

onto a non-interacting problem with an effective potential $v_{ee}(\mathbf{r})$. In doing so, the dimensionality of the problem is greatly reduced. Instead of solving one N-dimensional computationally intractable problem, N one-dimensional problems are solved (Figure 3.1). These methods provide a compromise between accuracy and computational efficiency.

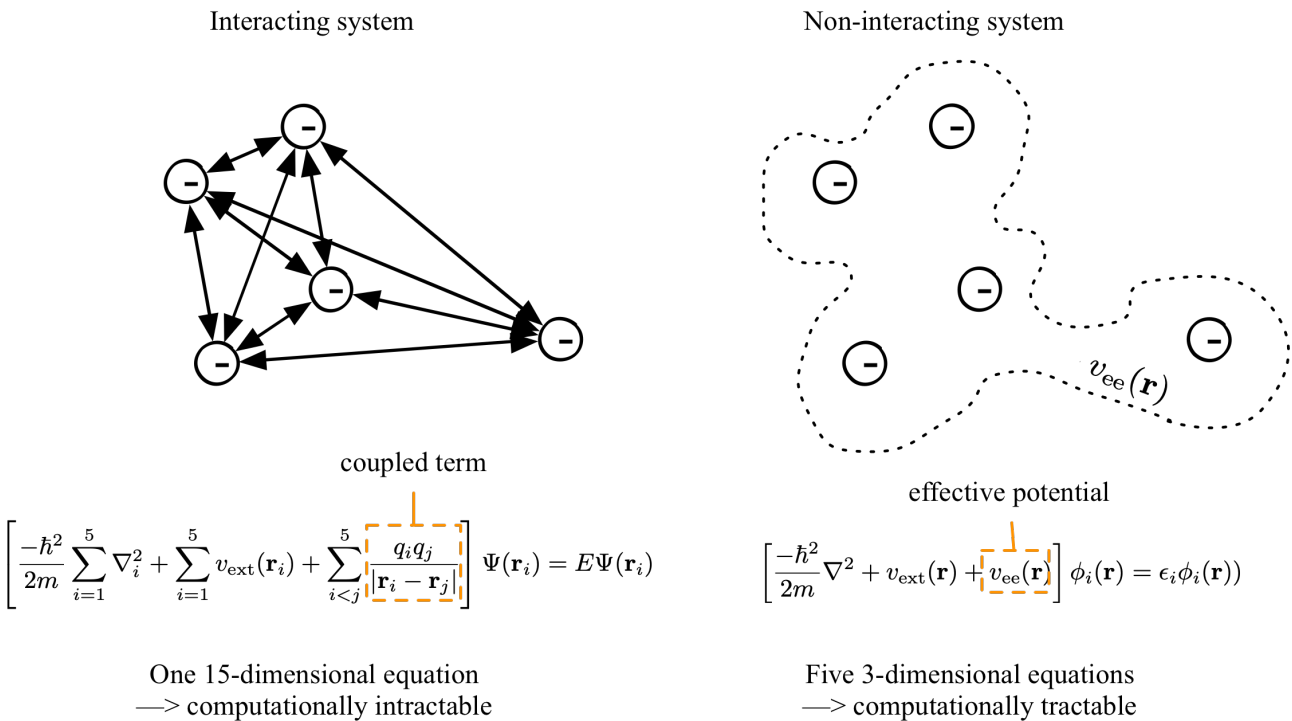


Figure 3.1: Schematic outlining the equivalence between a system of interacting particles and a system of non-interacting particles in an effective potential. The underlying idea is that an interaction can be replaced by the equivalent potential. This maps the interacting $3N$ -dimensional problem onto N 3-dimensional problems. A consequence of this mapping is that the effective potential depends on the electron density which is itself dependent on the effective potential – a self-consistent set of equations is formed. For the non-interacting case ϕ_i is used to denote a single particle wavefunction.

Hartree-Fock methods

Hartree-Fock (HF) methods introduce the concept of fictitious non-interacting one-electron orbitals ϕ as a way of solving the Schrödinger equation. The one-electron orbitals are combined using a Slater determinant to produce the HF many-body wavefunction.¹⁵⁸

The effective potential, introduced in Figure 3.1, is given by $v_{ee} = U + E_x$. U accounts for the electrostatic interaction between electrons. Hartree-Fock methods model the charge interaction as a coulomb potential for a system of fixed electrons; the electrons feel the average electrostatic field due to the other electrons. E_x accounts for the spin exchange interaction between electrons. Electrons with the same spin are indistinguishable, and a consequence of this is that the many body wavefunction must be anti-symmetric. This leads to the Pauli Exclusion Principle, whereby two identical electrons (i.e. electrons with the same spin and momentum) cannot occupy the

same space at the same time. Hartree Fock methods account for electron exchange E_x , the repulsion between electrons with parallel spins, exactly.

Hartree-Fock methods do not give an exact solution to the Schrödinger equation as the true many body wavefunction is not formed from a simple Slater determinant. As a result of using a Slater determinant, electron correlation is ignored. This is the correlated motion of electrons with anti-parallel spins as a result of their mutual coulombic repulsion.

The Hohenberg-Kohn theorems

The 1964 Hohenberg-Kohn paper¹⁵⁶ contains two key results: (i) the ground state electron density uniquely determines the ground state electronic wave function and, following this, all properties of the system; (ii) the true density functional for the electronic energy assumes its minimum for the correct ground-state density.

The potentials (external, coulomb and exchange) in Hartree-Fock methods determine the properties of a system. Hohenberg and Kohn demonstrate that the electron density ρ can be used instead to uniquely characterise the system; rather than solving the Schrödinger equation for the wavefunction, we can solve it for the electron density. The total energy $E[\rho]$ can be expressed as

$$E[\rho] = \int v_{\text{ext}}(\mathbf{r})\rho(\mathbf{r})d\mathbf{r} + T[\rho] + J[\rho] + E_{\text{xc}}[\rho], \quad (3.3)$$

where $T[\rho]$, $J[\rho]$ and $E_{\text{xc}}[\rho]$ describe the kinetic, classical electrostatic and exchange-correlation energies respectively. For a fixed number of electrons the functional $F[\rho] = T[\rho] + J[\rho] + E_{\text{xc}}[\rho]$ is universal, and the only thing that varies between systems is the external potential (determined by the electron-nuclei interaction).

In reference [156] Hohenberg and Kohn also demonstrate that the ground state energy can be found variationally; the density that minimises the total energy is the true ground state density. This formalism has the advantage that the electron density has a lower dimensionality than the N-electron wavefunction (Figure 3.2). The problem is that although the Hohenberg-Kohn theorem tells us that the terms $T[\rho]$ and $E_{\text{xc}}[\rho]$ exist, they are unknown and must be approximated.

The Kohn-Sham theorem

The Kohn-Sham theorem shows that for any interacting system with ground state density $\rho(\mathbf{r})$ there exists a non-interacting system with the same ground-state $\rho(\mathbf{r})$. To find the ground state energy of the real interacting system, the occupation numbers of *fictitious*, non-interacting one-electron orbitals can be optimised. For a non-interacting system we know how to calculate $T[\rho]$ and this provides a good approximation to the true kinetic energy, so the Kohn-Sham theorem provide a more practical way to apply DFT. However, the exchange-correlation density functional $E_{\text{xc}}[\rho]$ is still not known. Only approximations to this functional can be made, leading to approximations for the electronic density, total energy and other system properties.

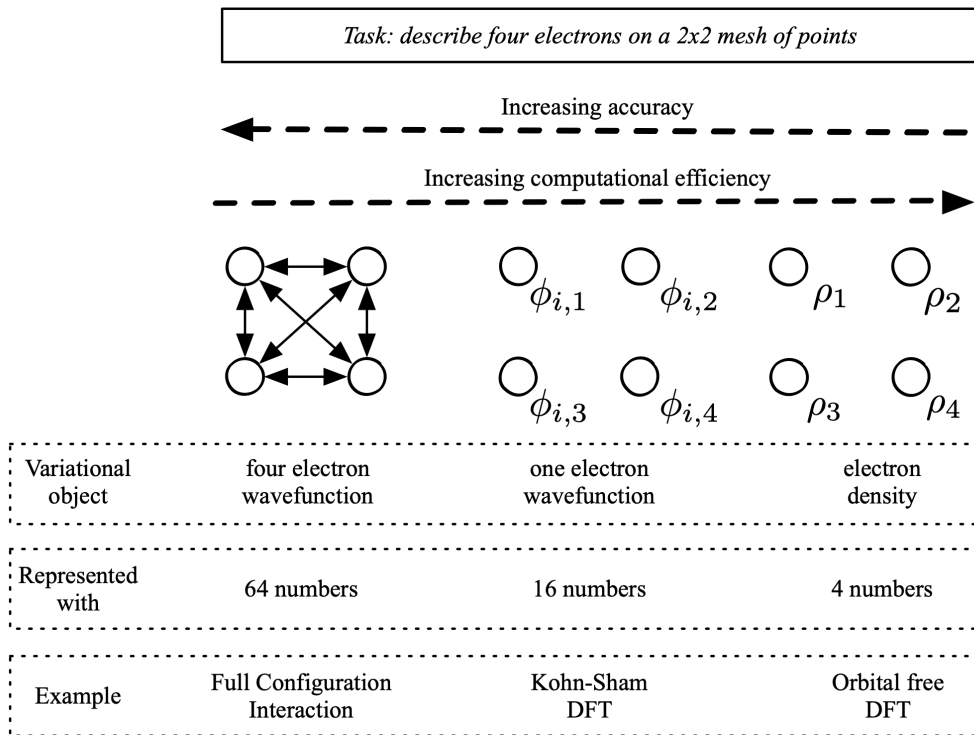


Figure 3.2: To solve the Schrödinger equation we can use a variational object with lower dimensionality and higher computational efficiency, although this will come at the cost of accuracy. This schematic is based on a discussion in Walter Kohn's Nobel Prize lecture.¹⁶¹

3.2.2 DFT in practice

Exchange-correlation functionals

To use Kohn-Sham DFT we must approximate the exchange-correlation functional, and there is a growing list of functionals at varying levels of complexity. John Perdew proposed ‘Jacob’s Ladder’ as a way to categorise these functionals (Figure 3.3). As a general rule, more accurate functionals are constructed by including more parameters and variables.

Local Density Approximation

At the lowest rung of the ladder is the local density approximation where only one variable, the electron density for an infinitesimal 3-dimensional volume element, is used to calculate the exchange correlation energy. The exchange energy is calculated exactly

$$E_{\text{LDA,x}}[\rho] = -\frac{3}{4} \left(\frac{3}{\pi}\right)^{\frac{1}{3}} \rho^{\frac{4}{3}}(\mathbf{r}) d\mathbf{r}, \quad (3.4)$$

and the correlation energy is calculated numerically by fitting to many-body quantum Monte Carlo calculations for an homogeneous electron gas.¹⁶² Strictly, the LDA should only be used for slowly varying densities, however it has performed surprisingly well for predicting the properties of a variety of atoms, solids and molecules. This is due to a cancellation of errors: LDA underestimates the exchange energy and overestimates the correlation energy.¹⁵⁸ However there

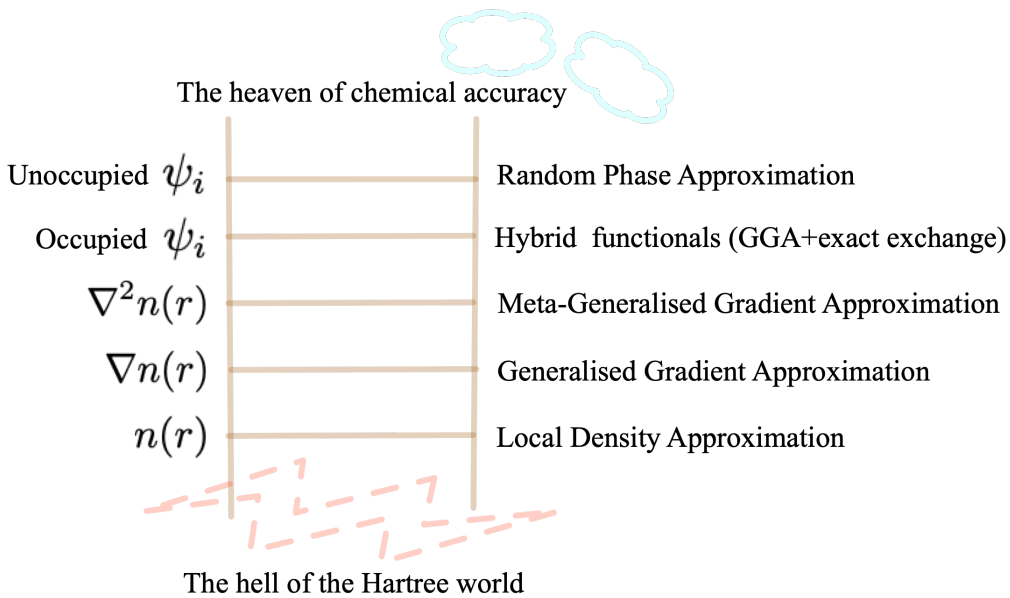


Figure 3.3: Jacob's ladder of exchange correlation functionals. On the right hand side are the various categories of exchange-correlation functionals and on the left hand side are the additional input variables included at each level of theory. As we move up the ladder the chemical accuracy increases, alongside computational expense.

is a tendency for LDA to overestimate the binding energy and underestimate lattice parameters. This is a particularly pronounced problem in weakly bonded systems.

Generalised Gradient Approximation

At the next level of theory, two variables are used to determine the exchange-correlation energy: electron density and the density gradient. Due to their dependence on the GGA functionals are semi-local. The parameters of GGA functionals can be derived from physical constraints (non-empirical, as in the widely used PBE functional), or obtained from fitting procedures (empirical, as in the case of the B88 functional). GGAs improve the over-binding of LDA, but tend to underestimate the bandgap of the material.

Hybrid functionals

In DFT each electron interacts with itself as the potential derives from the total charge density of the system. This error is particularly pronounced for localised states, after trapping an electron or hole at a defect site for example. Hybrid functionals combine GGA functionals with a proportion of the exact HF exchange energy to partially correct the self-interaction error. The simplest hybrid functional takes the form

$$E_{\text{hybrid,xc}}[\rho] = \alpha E_{\text{exact,x}} + (1 - \alpha) E_{\text{GGA,xc}}. \quad (3.5)$$

In some studies the proportion of exact exchange is tuned to reproduce the property of interest correctly. For example, $\alpha = 0.43$ is commonly used to correctly reproduce the bandgap of the hybrid halide perovskite MAPI.

Random Phase Approximation

Closest to heaven is the Random Phase Approximation (RPA), which uses all of the Kohn-Sham orbitals (occupied and unoccupied) as input variables. The functionals listed so far are inaccurate when there are significant long range effects, as they have no information about the electron density far from an electron. The RPA is able to correctly predict long-range interactions, such as the van der Waals interaction, between non-overlapping electron orbitals.

Exploiting symmetry

The material studied in this thesis, MAPI, is a crystalline solid. Although we want to understand the properties of a finite piece of material, we use the standard approach and model the finite crystal as an infinite crystal. This is acceptable if the crystal piece is large enough so that its properties do not depend on size. Born-von Karman (periodic) boundary conditions are used so that the infinite crystal is built from a repeating array of unit cells. There are an infinite number of unit cells of different shapes and sizes that can be used to build an infinite crystal. Any physically significant function of the crystal must have the same periodicity.

In real materials translational symmetry can be broken, for example when there are point defects (as in Chapter 6). Furthermore, lattice vibrations have a periodicity larger than the unit cell. To model defects or lattice vibrations a supercell is built from multiple unit cells and this is used as the basic repeating unit (Figure 3.4).

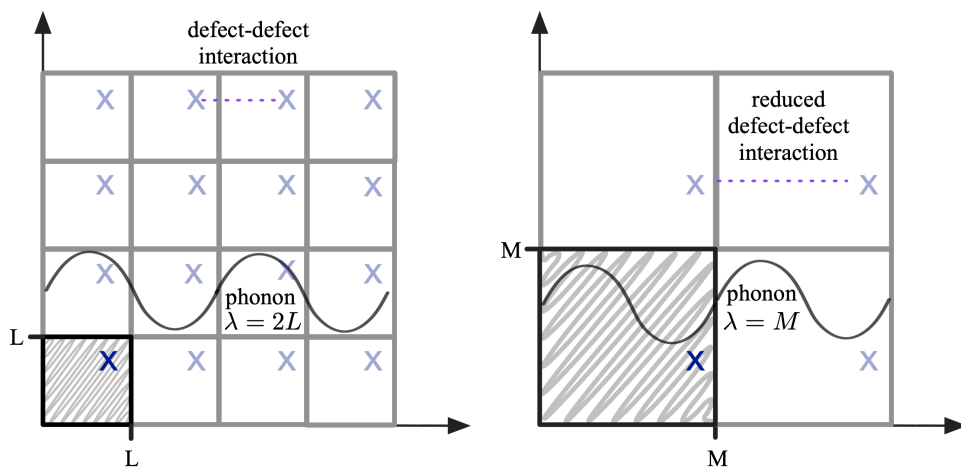


Figure 3.4: (LHS) An infinite crystal is built from a repeating unit cell of length L . Point defects (marked with an ‘x’) break translational symmetry in real crystals and care must be taken when modelling these as neighbouring defects can interact with each other in an unphysical way. In addition, vibrational modes can have $\nu > L$ (sine wave). (RHS) A supercell of length $M = 2L$ can be built to reduce defect-defect interactions and model longer wavelength phonons.

When the Schrödinger equation is solved for a hydrogen atom the solution gives wavefunctions corresponding to the $1s$, $2s$, $2p$, etc orbitals found in chemistry. When the Schrödinger equation

is solved for a periodic system, wavefunctions are formed by Bloch functions $\psi_{\mathbf{k}}$:¹⁶³

$$\psi_{\mathbf{k}} = u_{\mathbf{k}} e^{i\mathbf{k}\cdot\mathbf{r}}. \quad (3.6)$$

The Bloch function is formed from the product of a basis function $u_{\mathbf{k}}$ with the same periodicity as the crystal lattice, and a plane wave $e^{i\mathbf{k}\cdot\mathbf{r}}$. \mathbf{k} is the crystal wave vector which forms a space known as reciprocal space; to understand the physical significance of \mathbf{k} we consider an infinite 1D chain of hydrogen atoms separated at distance L . The electron states can be described as a linear combination of hydrogen 1s orbitals u_n centred at each lattice point:

$$\psi_k = \sum_n u_n e^{iknL}. \quad (3.7)$$

$k = 0$ corresponds to the lowest energy state, and $k = \frac{\pi}{L}$ corresponds to the highest energy state

$$\psi_0 = \sum_n u_n e^0 = u_0 + u_1 + u_2 + u_3 \dots \quad (3.8)$$

$$\psi_{\frac{\pi}{L}} = \sum_n u_n e^{i\pi n} = u_0 - u_1 + u_2 - u_3 \dots \quad (3.9)$$

Between these two extremes there is a continuum of states forming an electronic band (Figure 3.5).

Returning to the mathematical description of any periodic system, Equation 3.6 substituted into Equation 3.1 gives:

$$\left[\frac{1}{2m} \left(\frac{\hbar}{i} \nabla + \hbar \mathbf{k} \right)^2 + v_{\text{ext}}(\mathbf{r}) \right] u_{\mathbf{k}} = E(\mathbf{k}) u_{\mathbf{k}}. \quad (3.10)$$

For any \mathbf{k} we can solve Equation 3.10 with periodic boundary conditions to calculate the electronic bandstructure $E(\mathbf{k})$. There are an infinite number of eigenvalues $E_n(\mathbf{k})$, where n is used to label a particular eigenvalue (band). As a result of crystal symmetry, $E_n(\mathbf{k})$ is periodic and only k -vectors within a region of space known as the Brillouin zone ($|\mathbf{k}| < \frac{\pi}{a}$) need to be considered.¹⁶⁴

Basis Sets

In the example of a 1D linear chain, the lattice periodic part of the Bloch function took the form of a hydrogen 1s orbital. For more complex systems, u_k can itself be expanded into a plane wave basis set whose wave vectors \mathbf{G} are reciprocal lattice vectors

$$u_{\mathbf{k}} = \sum_{\mathbf{G}} c_{\mathbf{k}, \mathbf{G}} e^{i\mathbf{G}\cdot\mathbf{r}}, \quad (3.11)$$

and the complete expanded Kohn-Sham orbital can be expressed as

$$\psi_{\mathbf{k}} = \sum_{\mathbf{G}} c_{\mathbf{k}, \mathbf{G}} e^{i(\mathbf{k}+\mathbf{G})\cdot\mathbf{r}}. \quad (3.12)$$

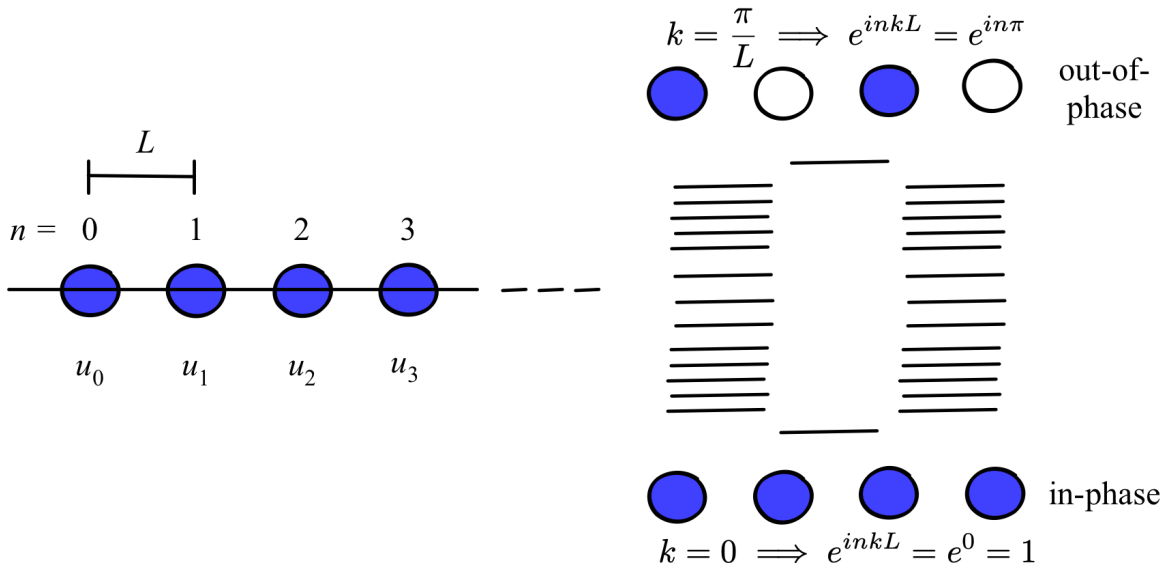


Figure 3.5: (LHS) A one dimensional infinite lattice where the points are labelled $n = 0, 1, 2, \dots$. The point spacing (unit cell length) is L , and there is a hydrogen 1s orbital (basis function) u_n centred at each point. The electron states for this system are formed from Bloch functions as given in Equation 3.7. (RHS) $k = 0$ corresponds to a low energy in-phase state and $k = \frac{\pi}{L}$ corresponds to a high energy out-of-phase state. Between these two extremes there exists a continuum of states.

As a plane wave is inherently periodic this basis set is often used for extended systems. The software used for the DFT calculations in this thesis, VASP¹⁶⁵, uses a plane wave basis set. For DFT calculations applied to localised systems, such as molecules or nanoparticles, localised basis sets such as gaussian orbitals are more likely to be used.

Sudden changes in electron density are hard to capture using a plane wave basis set; to take an extreme example, the fourier decomposition of a simple top hat in real space requires an infinite summation in reciprocal space. This can be problematic when describing the region around the nucleus where there are strong oscillations in the KS orbitals. However these oscillations are associated with the core electrons which are less important in chemical bonding, and so pseudopotentials - an effective potential without oscillations - can be used. It has been established that for certain systems pseudopotentials are as precise as all-electron calculations.¹⁶⁶

Optimising the atomic and electronic structure

In this section the process of optimising the atomic and electronic structure of a system towards the ground-state (minimum energy) configuration is outlined.

As discussed in Section 3.2, the potential v_{ee} is dependent on the electron density ρ , which is itself dependent on v_{ee} . Therefore an iterative approach called the Self Consistent Field method is used to calculate the ground-state electronic structure (Figure 3.6, dashed section). An initial guess for the density $\rho(\mathbf{r})$ is given by a superposition of the atomic charge densities. This is used to calculate the potential and solve the KS equations, which gives a new $\rho(\mathbf{r})$. This process

continues until there is convergence within a given energy tolerance. Various optimisation routines are provided in DFT codes for finding the ground state configuration, including the conjugate gradient scheme, Davidson Scheme and RMM-DIIS.

DFT is also used to find the ground state atomic structure. Structures calculated from X-ray Diffraction data are used as a starting guess, so that finding the energetic minimum becomes a local optimisation problem. Atoms in the systems are displaced (either the internal coordinates of the unit cell or the unit cell parameters themselves are adjusted) and the electronic structure for that geometry is solved self-consistently. This process repeats until the forces on each atom are zero to within a given tolerance (Figure 3.6).

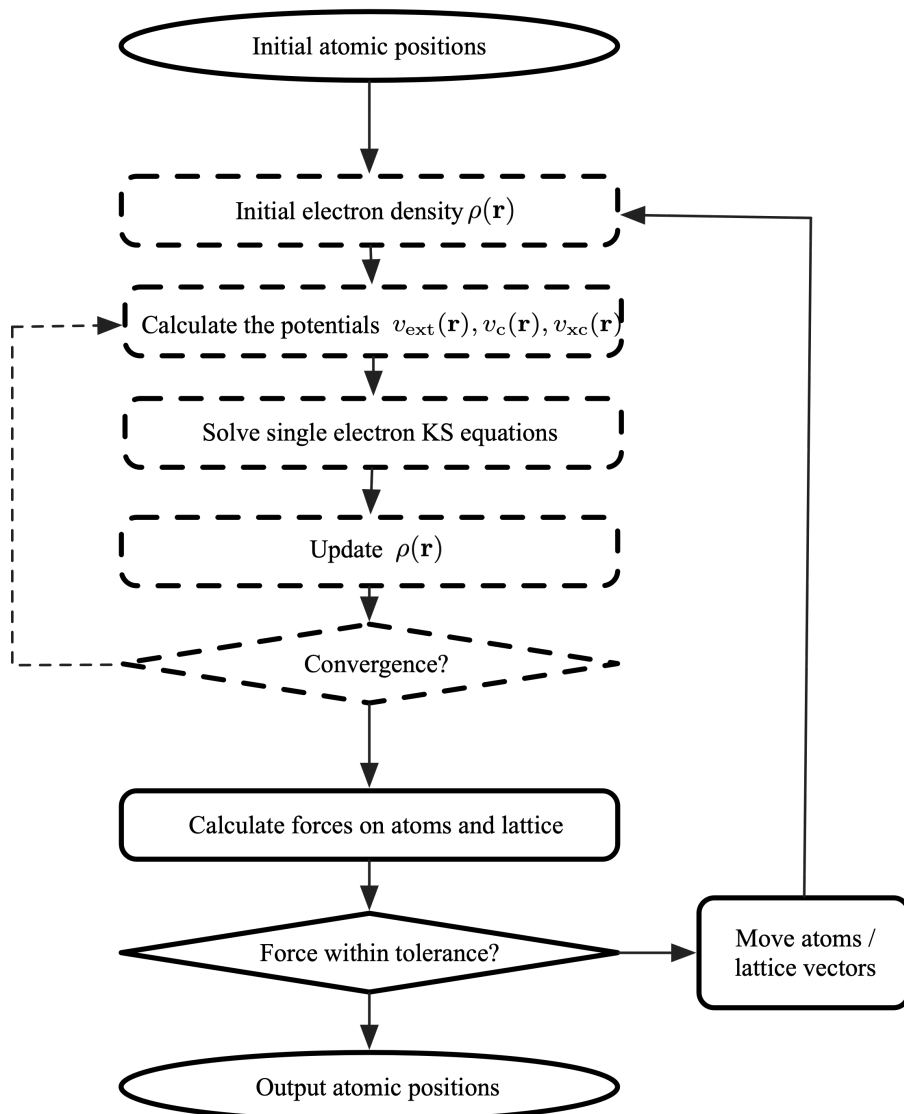


Figure 3.6: Nested iterative method for geometry optimisation. The electronic structure relaxation (dashed lines) is nested within the atomic structure relaxation (solid lines). $v_{\text{ext}}(\mathbf{r})$, $v_c(\mathbf{r})$ and $v_{\text{xc}}(\mathbf{r})$ correspond to the external, classical (electrostatic) and exchange-correlation potentials respectively.

The limits of DFT

Theoretical limitations

In Section 3.2 the approximations inherent to DFT calculations were outlined: the Born–Oppenheimer approximation and the unknown exchange-correlation functional. Higher levels of theory, which incorporate the effects of spin and relativity (e.g. spin-orbit coupling) are included in many DFT implementations. However DFT is still restricted to ground-state properties and higher levels of theory (GW or time-dependent DFT) are required to describe excited states. Another inherent limitation is that the KS eigenvalues are artificial; only the ground state electron density and derived properties are correct. However in practice the KS eigenvalues are used to calculate the bandgap. Quantitatively correct bandgaps often require the use of hybrid functionals that are parameterised to give the correct bandgap.

Numerical limitations

There are also approximations that relate to numerical convergence rather than the underlying theory. We have seen that the KS orbital are expanded in a basis set. In principle an infinite set may be needed to describe the orbitals, but in practice the basis set must be truncated. The kinetic energy operator is given by $-\frac{\hbar^2}{2m}$ and when this is applied to the plane wave KS orbitals as given in Equation 3.12, we find that the kinetic energy is proportional to $|k + G|^2$; faster oscillations correspond to higher energy. A cutoff energy E_{cut} is defined so that

$$\frac{1}{2}|k + G|^2 < E_{\text{cut}}. \quad (3.13)$$

This cutoff energy must be tested to ensure that the property of interest, most often energy, is converged to within a certain tolerance.

To calculate many properties of interest we need to integrate over the Brillouin zone in reciprocal space. To calculate the total energy of an insulator for example, we use

$$E = \frac{\Omega}{(2\pi)^3} \sum_{\text{occ.}} \int_{\text{BZ}} E(\mathbf{k}) d^3 k \quad (3.14)$$

where Ω is the volume of the Brillouin zone and the sum is over all occupied bands. In practice we do not know the continuous form for $E(\mathbf{k})$ and so we numerically evaluate Equation 3.14 as a weighted sum over special points in reciprocal space. These points often form an equally spaced mesh centred on the Γ -point ($\mathbf{k} = (0, 0, 0)$) in reciprocal space. For any given system, the k -point density scales inversely with cell size; for example, if the unit cell in Figure 3.4 requires a 6×6 k -point grid, then the larger 2×2 supercell requires a 3×3 k -point grid. As with plane waves, there is a balance between accuracy (the higher the number of k -points, the higher the accuracy) and computational expense. An example convergence study is given in Figure 3.7 where a $5 \times 5 \times 5$ k -point grid is required to converge pressure to within 1 kbar and energy to within 0.1 eV in CsSnI₃.

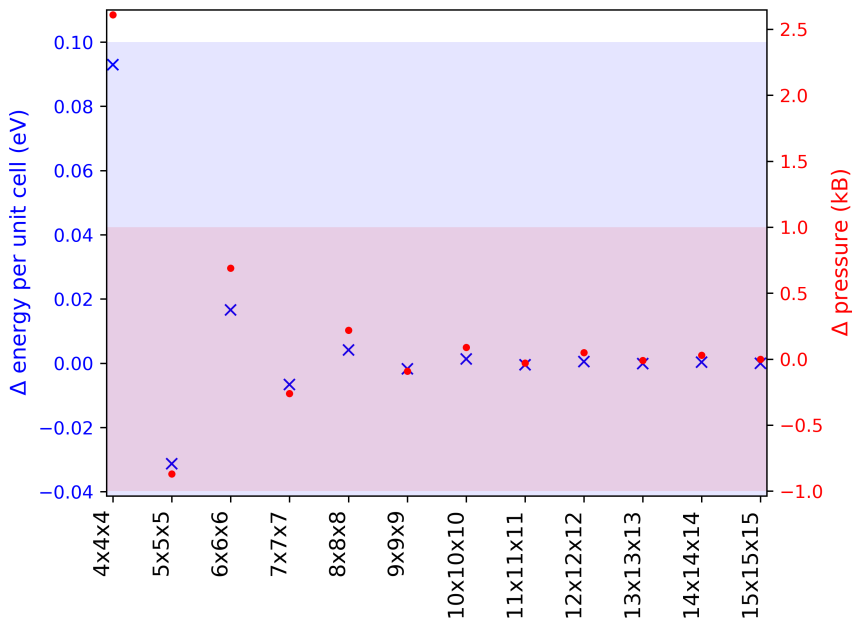


Figure 3.7: k -point convergence of CsSnI_3 . The k -point grid size is on the x -axis. Red dots denote pressure; the region which is within the convergence criteria of 1 kbar is shaded red. Blue crosses denote total energy; the region which is within the 0.1 eV convergence criteria is shaded in blue. Only odd grids sample the Γ -point and so there is an oscillation in energy and pressure as points move between odd and even grids.

3.3 Defects in semiconductors

The second law of thermodynamics states that an isolated system tends towards an equilibrium state with maximum entropy. A consequence of this is that all solids in equilibrium and at finite temperature contain point defects, as the cost in lattice energy is balanced by the increase in configurational entropy. Point defects are associated with a number of microscopic processes that can be either beneficial or detrimental to material performance, including:

- optical: colour centres, up/down conversion
- electrical: conductivity, carrier trapping, ionic hopping
- mechanical: material hardening
- thermal: conductivity, decomposition

Theoretical methods are particularly useful in this area as although it is often possible to estimate the quantity of defects in a material using experimental methods, it is much more challenging to identify the defect species.¹⁶⁷

In this section I outline the different types of crystal defects and discuss the thermodynamics of (charged) defect formation. The supercell method for calculating defect properties is also outlined. This method is used in Chapter 6.

3.3.1 Classification of crystal defects

The first way to classify defects is via their dimensionality. 0-dimensional point defects are localised around isolated sites in the crystal. 1-dimensional dislocations are lines along which the crystal pattern is broken. 2-dimensional grain boundaries or interfaces are surfaces along which distinct crystallites are joined. 3-dimensional defects are changes to the crystal pattern in a finite volume.

0-dimensional point defects are the subject of Chapter 6. Point defects can be further split into extrinsic or intrinsic defects. Extrinsic point defects (also known as impurities) are a different species from that of the host. These defects may be added intentionally (for example, to increase electrical conductivity) or unintentionally (as a result of the fabrication method). Intrinsic point defects are associated with the host species.

Point defects can also be classified as non-stoichiometric or stoichiometric. Non-stoichiometric defects include interstitials (where an additional atom occupies a site that is unoccupied in the perfect lattice), vacancies (missing atoms) and antisites (where an atom occupies a site that would have been occupied by another species in the perfect lattice). Interstitials can have a split structure, in which two atoms are split symmetrically around a single lattice site. Stoichiometric defects include Frenkel pairs and Shottky pairs. Stoichiometric and non-stoichiometric point defects are illustrated in Figure 3.8.

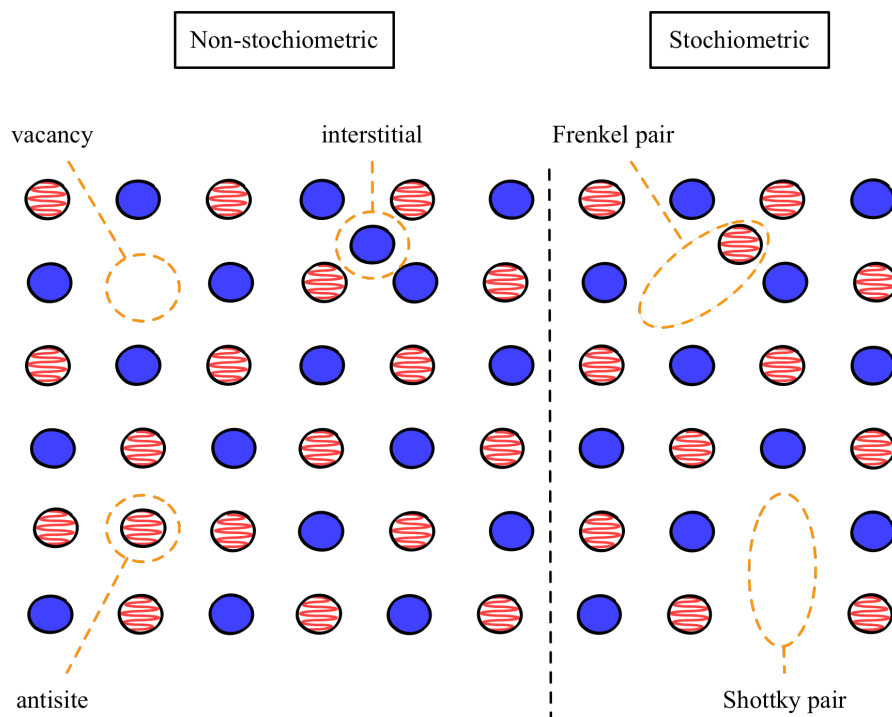


Figure 3.8: Non-stoichiometric defects include interstitials (an additional atom), vacancies (a missing atom) and anti-sites. Stoichiometric defects include a Frenkel pair (a vacancy close to an interstitial of the same species), and a Shottky pair (a vacancy on both the anion and cation sub-lattices).

The final classification is into electrically active and electrically benign defects. Whilst electrically benign defects exist only in one charge state, electrically active defects can take more than one charge state; for example, single acceptors exist in a neutral or negatively charged state and single donors exist in a neutral or positively charged states. Amphoteric defects can exist in a negatively charged or positively charged state.

3.3.2 Energetics of defect formation

In the dilute limit, the equilibrium concentration of defects n at a fixed temperature and pressure is given by the density that minimizes free energy.

$$n = N_{\text{sites}} \exp\left(-\frac{\Delta G}{k_{\text{B}} T}\right), \quad (3.15)$$

where ΔG is the Gibbs free energy of defect formation. The Gibbs free energy is approximated as the formation energy E_f of the defect as this dominates over entropic contributions. The formation energy is given by:

$$E_f(q) = E_d(q) - E_b - \sum_i \mu_i n_i + q(\epsilon_{\text{VBM}} + E_F) + E_{\text{corr}}, \quad (3.16)$$

where $E_d(q)$ is the total energy of the supercell with a defect of charge q and E_b is the total energy of the perfect bulk. E_{corr} is a correction energy that is needed when using a finite-sized supercell and is discussed Section 3.3.3. The remaining terms describe the energy needed to add or remove atoms or electrons. μ_i is the chemical potential of atom i and can be adjusted to describe different growth conditions. n_i is the number of atoms that are added or removed and E_F is the Fermi level of the electrons, referenced to the valence band maximum ϵ_{VBM} .

The total energies can be calculated using DFT. Convergence criteria for calculations must be tight as, due to the exponential dependence of defect concentration on formation energy, small errors in the energy difference can lead to large errors in the defect concentration.

The Fermi level is treated as a parameter, of which the defect formation energy is a linear function with a gradient equal to the defect charge. This allows us to plot a graph of formation energy against Fermi level, as shown in Figure 3.9. Charge transition levels mark the Fermi level at which two charge states have the same defect formation energy. Electrically active defects have at least one charge transition level in the bandgap. The charge transition level is equivalent to thermal ionization energy, the energy needed to add or remove electron(s).

Deep carrier traps have a defect level towards the middle of the bandgap and produce localised wavefunctions. Carrier capture processes to these defect states are often associated with a large lattice distortion. Shallow defect levels (within thermal energy $k_{\text{B}}T$ of the valence or conduction band) produce delocalised, hydrogenic-like defect wavefunctions.

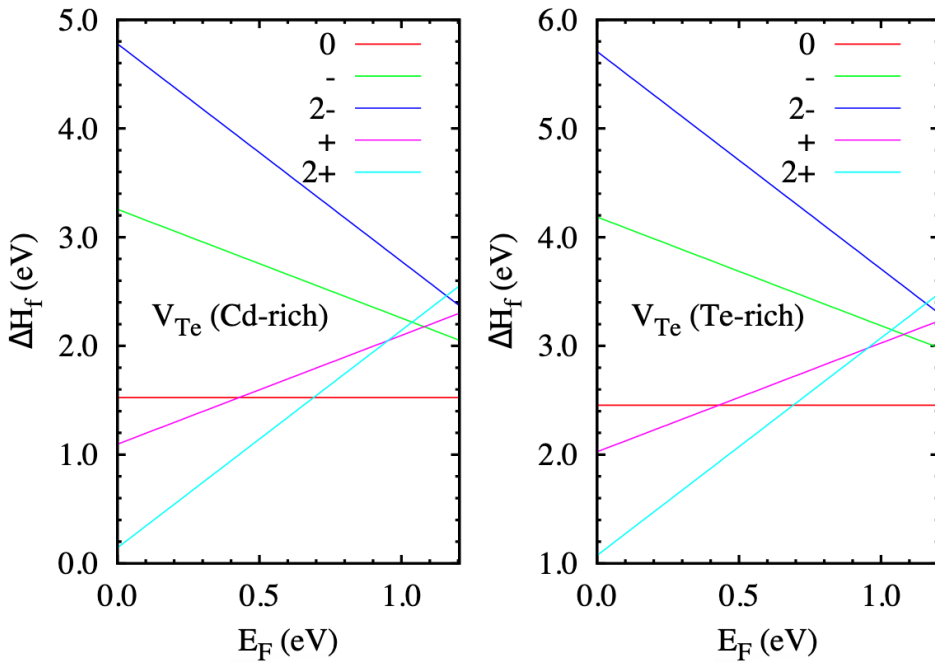


Figure 3.9: Formation energies ΔH_f as a function of the Fermi energy for the Te vacancy in CdTe. In a Te-rich environment it is more energetically unfavourable to form a Te-vacancy, as intuition would suggest. The slope of each line corresponds to the defect charge. Charge transition levels correspond to the energies at which the lines intersect. Figure reproduced with permission from the work of Menendez et al.¹⁶⁸

3.3.3 Supercell method

Defect concentrations as low as one part in one million can have an influence on device performance. One way to model point defects in the dilute limit, when defect-defect interactions are negligible, is to build a supercell from multiple unit cells (Figure 3.4). This supercell must be large enough so that there is no interaction between a defect and its periodic images. Although the supercell method captures localised defects well, it cannot capture the behaviour of delocalised (or band resonant) defects due to the enforced periodicity. To remove the constraint of translational symmetry it is possible to use an embedded QM/MM approach whereby a region around the defect is modelled using DFT and embedded in a region that is modelled classically.

Supercell corrections

Point defects can be electrically charged, and are able to change charge state through the trapping and de-trapping of electrons and holes. The charge state of a defect can affect a number of defect properties including the preferred lattice position, surrounding lattice distortion, and the rates of diffusion, carrier capture, and carrier recombination. However, due to the long range nature of the Coulomb interaction, understanding the properties of charged defects is a challenge for DFT with periodic boundary conditions. There are two issues to resolve: Firstly, charged defects can interact with their periodic images; Secondly, a homogeneous jellium background

charge is introduced to ensure overall charge neutrality and results in an unknown shift to the average electrostatic potential. These are finite-size effects that only a very large, almost infinite, supercell would overcome. However a system this size is computationally intractable, especially considering that higher levels of theory (for example, hybrid functionals) are often required to calculate accurate total energies.

A number of correction schemes have been developed to deal with these issues; a brief historical overview is given below. These schemes are designed to be used as a post-processing step and provide a value for the E_{corr} term in Equation 6.4. A more complete description of these issues can be found in References [169] and [170].

The Leslie Gillan correction E^{LG} models the defect charge q as a point charge interacting with its periodic images through an isotropic dielectric medium.¹⁷¹ This correction takes a simple analytic form that depends on the charge state q , static dielectric constant ϵ_0 , separation between defect images L and the Madelung constant α_m , which is determined by the lattice geometry:

$$E^{\text{LG}} = \frac{q^2 \alpha_m}{2\epsilon L}. \quad (3.17)$$

The Markov-Payne correction E^{MP} extends the Leslie Gillan correction by including an additional term that accounts for the delocalised part of the defect charge.

$$E^{\text{MP}} = \frac{q^2 \alpha_m}{2\epsilon L} + qQ L^{-3}. \quad (3.18)$$

The challenge of the Markov-Payne approach is in calculating the quadrupole moment Q . The Lany-Zunger correction¹⁷² combines the Markov-Payne correction, including an approach for calculating Q , with a potential alignment procedure to correct for the shift in electrostatic potential. The Freyholdt, Neugebauer and van de Walle (FNV) method¹⁷³ models the defect charge as a localised gaussian distribution. The difference between the electrostatic potential of the charged defect supercell and the electrostatic potential of the perfect bulk supercell, calculated far from the defect, is aligned with the defect model potential. Kumagai and Oba have extended to FNV method by using atomic site potentials combined with a point charge model for an anisotropic medium.¹⁷⁴

There is still no standardised approach to defect charge corrections, which can lead to a spread in calculated defect formation energies in the literature, and predicted defect densities which differ by orders of magnitude. Two widely used approaches in the recent literature are the FNV method, and the extension to this provided by Kumagai and Oba. This extension is applied to the iodine interstitial defect in Chapter 6, using an implementation in the package SXDEFECTALIGN.

3.4 Lattice dynamics

This section includes a brief overview of the theory of lattice dynamics, with a particular focus on anharmonic atomic motion. The finite difference method, an intuitive way to calculate the vibrational properties of a crystal, is outlined. This method has been applied to the perfect bulk in Chapter 5 and a defect supercell in Chapter 6.

Heisenberg's uncertainty principle states that it is not possible to know both the position and momentum of a particle exactly. Thus the static lattice model used so far is only an approximation; even at $T = 0\text{K}$ there is zero point atomic motion. As temperature increases, this vibrational motion increases in amplitude.

The lattice vibrations of a crystal must be considered to calculate a number of physical properties. Atomic motion has an associated vibrational energy, and this determines crystal stability as a function of temperature via the Gibbs free energy:¹⁷⁵

$$G = E_0 + E_{\text{vib}} + PV - TS \quad (3.19)$$

where E_0 is the ground state energy, which can be calculated using DFT, and E_{vib} is the vibrational contribution to internal energy. Atomic motion also influences the electrical and optical properties of a crystal; this can be seen experimentally in the homogeneous broadening of photoluminescence linewidths with temperature, for example.¹⁷⁶ Other material properties which are only accessible via lattice dynamics include: heat capacity, thermal conductivity, elasticity, thermal expansion coefficients, electron-phonon coupling strengths and static polarization.

For atomic motion at small amplitudes around the potential energy minimum it is common to use the harmonic approximation, where the atom moves as if it is connected by a spring to its neighbouring atoms (Figure 3.10). This is discussed in Section 3.4.1. At larger vibration amplitudes, and to understand processes relating to the creation and annihilation of phonons, we must consider anharmonic motion, and this is considered in Section 3.4.2.

These motions are determined by the force on each atom. For simple systems, for example a one-dimensional diatomic chain, we can calculate atomic position as a function of time analytically. Otherwise methods such as DFT can be used to build a force constant matrix which, after some post-processing steps, gives the eigenvectors (direction and amplitude) and eigenvalues (frequencies of motion). This is discussed in Section 3.4.3. As in the previous sections of this chapter, we use the Born-Oppenheimer approximation and assume that the equilibrium positions in a crystal are the minima of the potential energy surface when the electron and nuclear motion are decoupled.

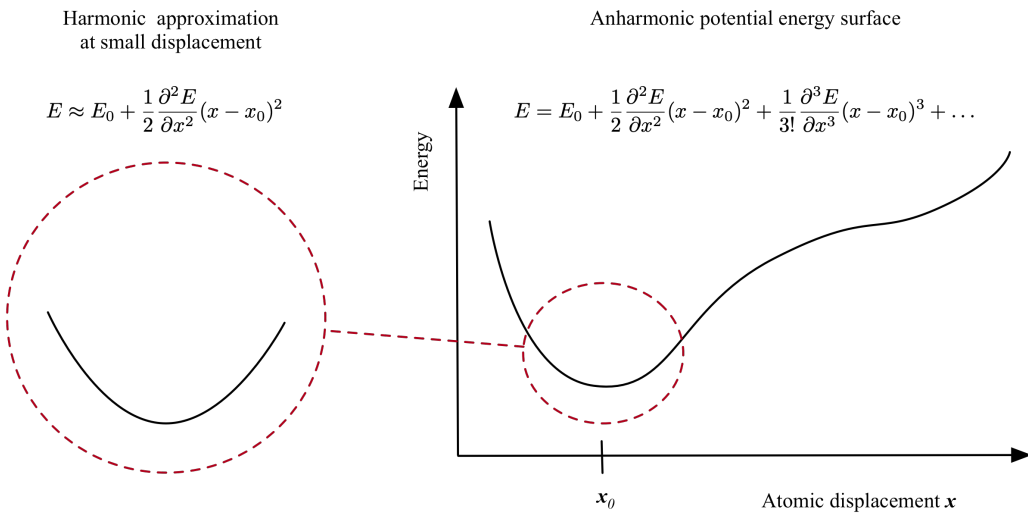


Figure 3.10: The crystal potential energy can be expanded in powers of atomic displacement $x - x_0$, where x_0 is the equilibrium position. At small displacements, the anharmonic terms (third order and above) can be ignored, giving the harmonic approximation. For larger displacements, higher order anharmonic terms must be considered. The crystal lattice is relaxed so that all forces on the atoms are zero and there is no first order force term.

3.4.1 Harmonic approximation

In this section I connect, using a minimum amount of mathematics, an expression for total lattice energy with the force constant matrix (which can be calculated using DFT calculations). For a more complete derivation I refer the reader to Section 2.2 of Reference [177].

If the atomic displacement from equilibrium is small, the total energy can be Taylor expanded in the form¹⁷⁷

$$E = \text{kinetic energy} + \text{potential energy} \quad (3.20)$$

$$= \sum_i \frac{1}{2} M \dot{x}_i^2 + \sum_{ij} \frac{1}{2} \mathbf{x}_i \cdot \mathbf{A}_{ij} \cdot \mathbf{x}_j + \text{higher-order terms}, \quad (3.21)$$

where it is assumed that the structure is relaxed and forces are equal to zero so that there is no term linear in \mathbf{x} . The harmonic approximation ignores the higher order terms in Equation 3.20. For these harmonic systems there exists a basis set so that \mathbf{A}_{ij} is diagonal and the oscillators are independent of one another:

$$= \sum_j \frac{1}{2} \tilde{M} \dot{Q}_j^2 + \sum_j \frac{1}{2} \tilde{\mathbf{A}}_j Q_j^2, \quad (3.22)$$

where the linear transformation has cast coordinates x into Q . The general solution to this system of equations for N -atoms in three dimensions is a superposition of $3N$ normal modes of vibration, each with its own frequency and eigenvector. To calculate the normal modes Newton's second law, $F = ma$, is applied. For crystalline solids we take advantage of symmetry and seek normal modes $\mathbf{e}(\mathbf{k}, t)$ that for a chosen wavevector \mathbf{k} are a linear combination of a

relative displacement within the unit cell ($\mathbf{u}_0(i, \mathbf{k})$), a phase that depends on the origin \mathbf{R}_I of cell I ($\exp(i\mathbf{k} \cdot \mathbf{R}_I)$), and an oscillation in time of well defined frequency $\omega(\mathbf{k})$ ($\exp(i\omega(\mathbf{k})t)$):

$$\mathbf{e}(\mathbf{k}, t) = \mathbf{u}_0(i, \mathbf{k}) \exp(i\mathbf{k} \cdot \mathbf{R}_I) \exp(i\omega(\mathbf{k})t). \quad (3.23)$$

For displacements of this form, Newton's second law has consistent solutions only if the following secular equation is satisfied:

$$\text{Det} \left| \sum_J A_{\alpha\beta}(iI, jJ) \exp(i\mathbf{k} \cdot \mathbf{R}_J) - M_i \delta_{ij} \omega^2(\mathbf{k}) \right| = 0, \quad (3.24)$$

where the first term in the determinant is the dynamical matrix. The dynamical matrix is built from the force constant matrix $A_{\alpha\beta}$:

$$\mathbf{A} = \begin{pmatrix} \frac{\partial^2 E}{\partial x_1^2} & \frac{\partial^2 E}{\partial x_1 \partial x_2} & \dots & \frac{\partial^2 E}{\partial x_1 \partial x_n} \\ \frac{\partial^2 E}{\partial x_2 \partial x_1} & \frac{\partial^2 E}{\partial x_2^2} & \dots & \frac{\partial^2 E}{\partial x_2 \partial x_n} \\ \vdots & \vdots & \ddots & \vdots \\ \frac{\partial^2 E}{\partial x_n \partial x_1} & \frac{\partial^2 E}{\partial x_n \partial x_2} & \dots & \frac{\partial^2 E}{\partial x_n^2} \end{pmatrix} \quad (3.25)$$

The normal mode frequencies $\omega(\mathbf{k})$ are roots of the secular equation 3.23 and can be found through matrix diagonalisation. Plotting the frequency ω against wavevector \mathbf{k} for a lattice with a periodicity of length L gives a bandstructure plot with a periodicity of $\frac{2\pi}{L}$.

The discussion so far has only used classical mechanics. To introduce quantum effects we recognise that the harmonic lattice vibrations are analogous to a quantum simple harmonic oscillator and so will be restricted to certain energy values $E_n = \hbar\omega(\mathbf{k})(n + \frac{1}{2})$. The discrete (quantised) unit of energy $\hbar\omega(\mathbf{k})$ is a phonon quasiparticle that corresponds to a collective excitation of the crystal lattice.

3.4.2 Anharmonicity

Anharmonic atomic motion is described by the higher order terms in Equation 3.20. The third order term accounts for phonon-phonon scattering which, due to the conservation of energy and momentum, is a three particle process (Figure 3.11).¹⁶⁴

The linear boltzmann transport equation (LBTE) describes a thermodynamic system out of equilibrium. Solving the LBTE under the single mode relaxation time approximation gives an expression for the lattice thermal conductivity κ . The phonon-phonon scattering rate determines the phonon lifetime τ_λ which is a key quantity in the expression for κ :¹⁷⁸

$$\kappa = \frac{1}{NV_0} \sum_\lambda C_\lambda v_\lambda \times v_\lambda \tau_\lambda, \quad (3.26)$$

where N is the number of unit cells in the crystal, V_0 is the unit cell volume, and C_λ , v_λ and τ_λ are the mode-dependent heat capacity, group velocity and lifetime respectively. C_λ and v_λ can

be calculated using the harmonic approximation. To quantify the strength of the anharmonic phonon interactions that determine τ_λ it is necessary to calculate a third-order force constant matrix. This is often at high computational cost; in Reference [81] 41,544 DFT calculations were required to calculate the thermal conductivity of a 96-atom unit cell.

Lattice anharmonicity can also be used to describe materials with dynamic disorder. In the halide and oxide perovskites the onset temperature for dynamic disorder is determined by the depth of the double well potential energy surface (Figure 3.26).⁹⁰ Chapter 5 calculates the coupling between the anharmonic double well phonon modes and electronic states in MAPI.

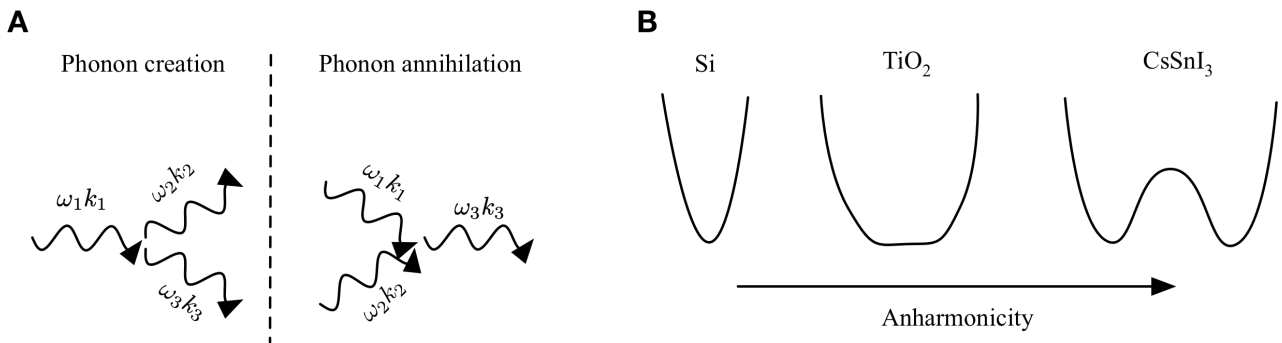


Figure 3.11: A) Energy and momentum are conserved during the creation or annihilation of phonons, so these are three-phonon processes (or higher); B) Some materials, such as silicon (Si) are well-described by a harmonic potential energy surface at typical solar cell operating temperatures. However other materials with dynamic disorder, such as the organic and inorganic perovskite halides, have highly anharmonic double well potentials.

3.4.3 Finite displacement method

There are a number of ways to calculate the second order force constant matrix in Equation 3.25 including: the finite displacement method; density functional perturbation theory; ab-initio molecular dynamics and compressed sensing lattice dynamics. In this work the finite displacement method (also known as the direct or supercell method) is used: a single atom is displaced a small distance from its energetic minimum and there is a self-consistent electronic structure optimisation to calculate the resultant forces. The maximum number of displacements for a system with N atoms in the unit cell is $6N$, although this is reduced through symmetry. To consider phonon wavelengths greater than the unit cell length a supercell is required, and all forces must be well converged (typically to less than $0.01 \text{ eV} \text{ Å}^{-1}$).

3.5 Summary

In this chapter I have introduced the key concepts that underly DFT, and the post-processing steps required to calculate the defect and vibrational properties of a crystal. Much of solid state physics is built upon the idea of a translationally invariant crystal, so it should come as little

surprise that additional steps are needed to describe defects that break translational symmetry and work against the fundamental assumptions of the theoretical framework. In contrast, phonons at the gamma point preserve the underlying translational symmetry, but additional steps are needed to build the force constant matrix from multiple DFT calculations. In this chapter I have presented the defect and vibrational calculations separately. In Chapter 6 I combine the two approaches, and calculate the vibrational properties of the iodine interstitial defect in MAPI.

Ok, everyone back to the lab, try again.

— MF DOOM, *Books of War*

4

Electronic band non-parabolicity

The text and figures in this chapter are adapted from Whalley, L. D., Frost, J., Morgan, B. and Walsh, A. (2019). Impact of nonparabolic electronic band structure on the optical and transport properties of photovoltaic materials. *Physical Review B*, 99(8). © 2019 American Physical Society

4.1 Introduction

Many semiconductor properties depend on the response of electrons to an external perturbation. This perturbation could take the form of an electric field, change in temperature or an applied lattice stress. In a crystal, this response depends on the interaction of the electrons with a periodic potential. The effective mass approximation assumes that the response of an electron in a periodic potential is equivalent to that of a free electron with a renormalised mass (called the ‘effective mass’). This makes the effective mass a critical parameter in models for the optical and transport properties of a semiconductor. Recently there has been renewed interest in this research area, in particular the impact of electronic bandstructure anisotropy and non-parabolicity on the properties of thermoelectric materials.^{179,180}

The conventional definition of effective mass is

$$\frac{1}{m_c} = \frac{1}{\hbar^2} \frac{\partial^2 E}{\partial k^2}. \quad (4.1)$$

This is derived using Newton’s second law^{181,182} and so is commonly referred to as the inertial effective mass or conductivity effective mass (as it describes the acceleration of an electron in an applied electric field). In principle, this allows effective masses to be calculated directly from *ab-initio* bandstructures, as m_c is inversely proportional to the curvature of the electronic dispersion in reciprocal space (Figure 4.1). We will refer to this definition as the curvature effective mass.

For semiconductor materials with a low carrier concentration we are often interested in eigenstates close to the band extrema where the dispersion can be approximated with an isotropic parabola

$$E(k) = \frac{\hbar^2 k^2}{2m^*}. \quad (4.2)$$

This approximation leads to an effective mass which is independant of the sampling density and range in reciprocal space. However, non-parabolic deviations in the true dispersion mean that the effective mass obtained from a particular bandstructure depends on the approach used to numerically calculate Eqn. 4.1.

At greater carrier concentrations and higher temperatures, higher energy eigenstates are accessed and it becomes increasingly important to account for band non-parabolicity.¹⁸³ To describe a non-parabolic band dispersion we keep the second order k^2 ellipsoidal energy surfaces and introduce a non-linear dependence on the energy,

$$\frac{\hbar^2 k^2}{2m^*} = \gamma(E) = E + \alpha E^2 + \beta E^3 + \dots \quad (4.3)$$

Keeping the first non-linear term gives the Kane quasi-linear dispersion relation¹⁸⁴

$$\frac{\hbar^2 k^2}{2m^*} = E(1 + \alpha E), \quad (4.4)$$

where α is a parameter that quantifies the extent of non-parabolicity; for the perfectly parabolic material this would be equal to zero. α is positive for electrons in the conduction band (CB) and negative for electrons in the valence band (VB). This corresponds to a flattening of the band as the difference between the eigenstate energy and the band edge energy is increased (Figure 4.2).

For non-parabolic dispersions we use the following definition of effective mass

$$\frac{1}{m_t} = \frac{1}{\hbar^2 k} \frac{\partial E}{\partial k}. \quad (4.5)$$

This is the mass which relates the momentum and velocity of an electron wavepacket in the equation $mv = \hbar k$,¹⁸² thus it is often referred to as the transport effective mass. For parabolic dispersions, it is equal to the curvature effective mass given in Eqn. 4.1. For the Kane quasi-linear dispersion, the transport effective mass is given by

$$m_t(E) = m_0(1 + 2\alpha E), \quad (4.6)$$

where m_0 is the transport effective mass at the band edge.¹⁸⁵ By using the Kane dispersion as a more accurate approximation to the real material dispersion, the effective mass becomes linearly dependant on the particle energy. As a result, the effective mass will increase as we fill the band with charge carriers through doping, photo-excitation or an increase in temperature.¹⁸⁶

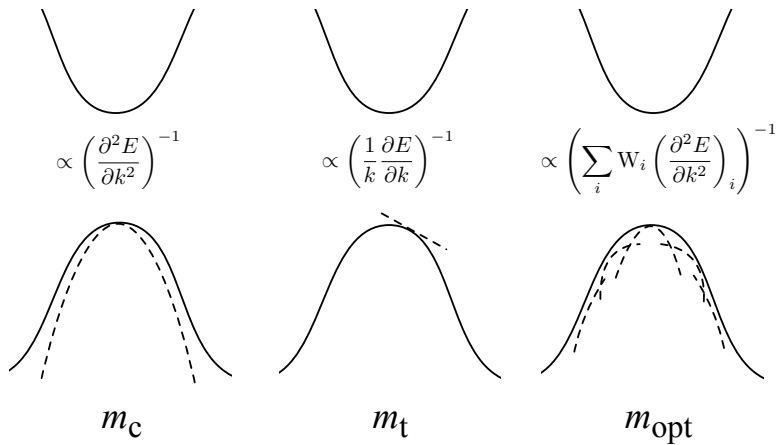


Figure 4.1: The three definitions for effective mass used in this chapter are: i) the curvature effective mass m_c , which is inversely proportional to the curvature of the electronic dispersion in reciprocal space; ii) the optical effective mass m_{opt} , which is the average curvature effective mass, weighted according to the Fermi–Dirac distribution; and iii) the transport effective mass m_t .

Material properties which are dependant on effective mass, such as electron and hole mobility, will also change as the carrier concentration is increased. This is in contrast to the parabolic approximation which leads to a constant effective mass that is independant of energy.

There are multiple definitions for effective mass, each valid according to the perturbation which is under consideration. To calculate an effective mass which is comparable to that measured in optical experiments we use the definition for optical effective mass

$$\frac{1}{m_{\text{opt}}} = \frac{2}{n_e} \sum_1^{\text{occ}} \sum_{\mathbf{k}} \frac{1}{m_c^1(k)}, \quad (4.7)$$

where m_c^1 is the curvature effective mass for band 1 and n_e is the carrier concentration. The summation over all occupied eigenstates k of each band 1 accounts for any non-parabolicity. This definition has been used in the context of thermoelectric materials¹⁷⁹ and transparent conducting oxides.¹⁸⁷

Using Fermi–Dirac statistics, and following a derivation from Huy *et al.*,¹⁸⁸ we can replace the summation over occupied states with an integral along one-dimensional slices of reciprocal space

$$\frac{1}{m_{\text{opt}}} = \frac{\sum_1 \int f(E, T) \frac{\partial^2 E}{\partial k^2} dk}{\sum_1 \int f(E, T) dk}, \quad (4.8)$$

where $f(E, T)$ is the Fermi–Dirac distribution for particle at energy E and system at temperature T

$$f(E, T) = \frac{1}{\exp\left(\frac{E-E_F}{k_B T}\right) + 1}. \quad (4.9)$$

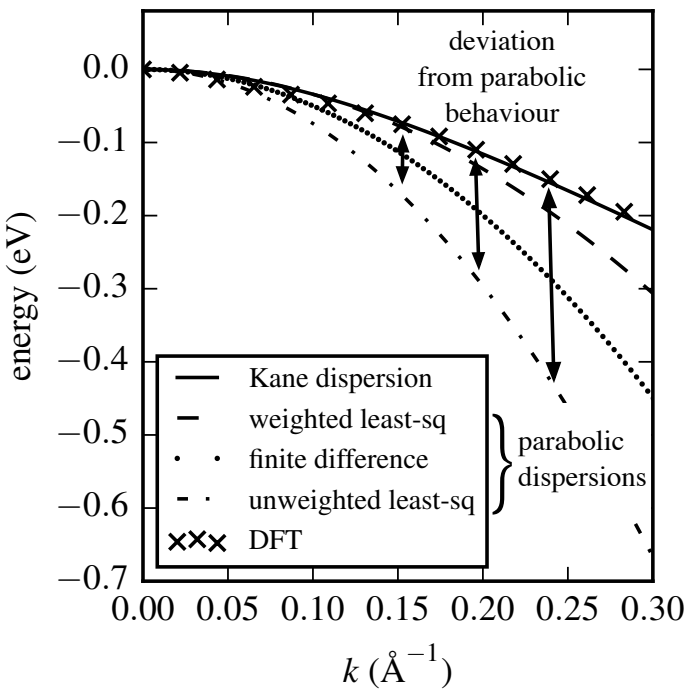


Figure 4.2: The electronic valence band dispersion in the [110] direction of $\text{Cu}_2\text{ZnSnS}_4$. The DFT dispersion is non-parabolic away from the band edge with α , the Kane dispersion parameter, equal to 2.2. The curvature effective mass depends upon the numerical method used, as shown by the three different parabolas (dash, dot and dash-dot lines). At higher binding energies the Kane quasi-linear dispersion (continuous line) gives a better approximation to the DFT dispersion. Calculations use the hybrid exchange-correlation functional HSE06 with spin-orbit coupling.

In the case of one occupied branch at $T = 0\text{K}$ we reach the transport effective mass evaluated at the Fermi level

$$\frac{1}{m_{\text{opt}}} = \frac{\int_0^k \frac{1}{\hbar^2} \frac{\partial^2 E}{\partial k^2} dk}{\int_0^k dk} = \frac{1}{\hbar^2 k_F} \frac{\partial E}{\partial k} \Big|_{k=k_F}, \quad (4.10)$$

where k_F is the Fermi wavevector.

The extent to which this value of effective mass will increase as the carrier concentration increases depends on the extent of band non-parabolicity and the level to which the bands are filled. The level of band-filling can be measured experimentally via the Burstein–Moss band gap shift.^{189,190} This is a concentration-dependant shift in the absorption edge which was used for the characterisation of GaAs and other small bandgap semiconductors in the 1970's.

Transient absorption spectroscopy can be used to measure the Burstein–Moss band gap shift, from which the effective mass and shape (parabolicity) of the electronic bands can be inferred. Three studies have calculated the Burstein–Moss shift in the hybrid halide perovskite $\text{CH}_3\text{NH}_3\text{PbI}_3$ (MAPI), with values for the effective mass ranging from $0.14 m_e$ – $0.30 m_e$ (where m_e is the electron rest mass).^{191–193} Although each model differs in detail (Yang *et al.* consider band

gap renormalisation,¹⁹² whilst Price *et al.* consider photoinduced refractive index changes¹⁹³), none of the models account for bandstructure non-parabolicity, despite previous computational studies which report significant non-parabolicity in MAPI within an energy range accessible at room temperature ($k_B T = 25\text{ meV}$ at $T = 300\text{ K}$).

As outlined previously, for any dispersion that is not parabolic, the calculated effective mass will depend upon the numerical method used to calculate band curvature and carrier concentration. For materials with a significant number of excited carriers, the discrepancy between the parabolic and non-parabolic effective mass can be large.^{183,186} An *ab-intio* effective mass which recognises the non-parabolicity of real materials allows for better prediction of important material properties such as carrier mobility.

In this chapter I calculate the curvature effective mass and α parameter of four photovoltaic materials: CdTe, GaAs, MAPI and CZTS. First I consider how sensitive the effective mass is to the method and sampling density used to calculate the band curvature. For this, the results obtained using three different methods are compared. Two of these are widely used to calculate the curvature effective mass: a three-point finite difference and a least-squares quadratic fit. The third method is a new approach which uses a least-squares quadratic fit weighted according to Fermi–Dirac statistics. The results at different levels of theory are then compared to assess the impact of spin-orbit coupling and electron exchange-correlation on the calculated values for effective mass and α . Finally, the effect of non-parabolicity on the optical and transport properties of MAPI at high carrier concentrations is considered. It is shown that the Burstein–Moss shift is severely overestimated if calculated within the parabolic approximation, and that the Kane quasi-linear dispersion leads to accurate predictions. The optical effective mass and electron mobility is predicted, over a carrier concentration range of $10^{16}\text{--}10^{20}\text{ cm}^{-3}$, which is the relevant range for concentrated solar power systems ($\sim 10^{18}\text{ cm}^{-3}$)¹⁹⁴, or when excited under a laser for transient absorption or photoluminescence studies ($\sim 10^{19}\text{ cm}^{-3}$). It is found that non-parabolicity leads to a significant change in transport properties for carrier concentrations above 10^{18} cm^{-3} .

4.2 Methods

4.2.1 Calculation procedures for effective mass

One-dimensional slices through the Brillouin zone are considered so that the effective mass tensor is reduced to a function of one variable k . Unless otherwise stated, the Fermi–Dirac distribution is calculated at $T = 300\text{ K}$ with the Fermi level set in the middle of the bandgap.

Curvature effective mass at the band edge

Three approaches are used to calculate the curvature effective mass at the band edge: i) a three point forward finite difference method; ii) an unweighted quadratic least-squares fit¹⁹⁵ to three points; iii) a quadratic least-squares fit, weighted according to the Fermi–Dirac distribution across all points up to energy $10k_B T (= 0.25\text{eV})$.

Finite difference:

A three point forward finite difference equation is used to calculate the curvature at point i .¹⁹⁶

$$\left(\frac{\partial^2 E}{\partial k^2} \right)_i = \frac{E_{i+2} - 2E_{i+1} + E_i}{|k_{i+1} - k_i|^2}, \quad (4.11)$$

where E_i is the energy eigenvalue at position k_i in reciprocal space.

Unweighted least-squares fit:

To obtain an estimate for the coefficient c of a parabolic dispersion

$$E = ck^2, \quad (4.12)$$

A least-squares method as implemented in the NUMPY Python library is used to minimise the summed square of residuals

$$\sum_{i=1}^5 (ck_i^2 - E_i)^2. \quad (4.13)$$

This is a five point fit; three points from the DFT-calculated dispersion plus two from the symmetry of the dispersion ($E(k) = E(-k)$).

Weighted least-squares fit:

To obtain an estimate for the coefficient c of a parabolic dispersion

$$E = ck^2, \quad (4.14)$$

A weighted least-squares method is used as implemented in the NUMPY Python library to minimise the summed square of residuals

$$\sum_{i=1}^n W_i (ck_i^2 - E_i)^2. \quad (4.15)$$

The summation is over all points up to an energy of 0.25 eV, including points generated from the symmetry of the dispersion ($E(k) = E(-k)$). W_i is given by

$$W_i(E_i, T = 300\text{K}) = \frac{1}{\exp\left(\frac{E_i - E_f}{k_B T}\right) + 1}. \quad (4.16)$$

Due to the exponential term in W_i , points with an energy difference larger than 0.25 eV contribute a negligible amount to the weighted sum.

Kane dispersion parameters

To calculate the parameters for the Kane dispersion a sixth order polynomial is fitted to the DFT calculated electronic band dispersion;

$$E = a + bk + ck^2 + dk^3 + ek^4 + fk^5 + gk^6. \quad (4.17)$$

As in the parabolic dispersion fit, a least-squares method as implemented in the NUMPY Python library minimises the summed square of the residuals and the fit is over an energy range of 0.25eV. To determine the transport effective mass the first derivative of this continuous function is used

$$\frac{\partial E}{\partial k} = b + ck + dk^2 + ek^3 + fk^4 + gk^5. \quad (4.18)$$

The transport effective mass is plotted against energy to give values for α and the effective mass at the band edge. The dispersion is truncated where the second derivative changes sign as this corresponds to an inflection point where the Kane dispersion is no longer valid.

Optical effective mass

To calculate the optical effective mass the integrand in Eqn. 4.10 is numerically integrated with $E(k)$ given by the Kane dispersion. Convergence with respect to energy is fast as the Fermi–Dirac distribution kills the probability of eigenstate occupation exponentially.

4.2.2 Electronic bandstructure calculations

For each system, the atomic structures and calculated band dispersions were relaxed using density functional theory (DFT) as implemented in the Vienna *Ab-initio* Simulation Package (VASP).¹⁶⁵ The valence wavefunctions were expanded in a plane wave basis set with a cut-off of 500eV. Scalar-relativistic corrections for the core electrons were used within the projector augmented wave formalism.¹⁹⁷ The initial structure was determined as follows: Si and GaAs structures were taken from the Madelung handbook,⁴⁶ CdTe¹⁹⁸ and CZTS¹⁹⁹ (in the tetragonal phase) were determined from X-ray diffraction data, whilst MAPI was optimised starting from a pseudo-cubic (high temperature) structure available online.²⁰⁰ For all relaxations a quasi-Newtonian algorithm and the PBEsol exchange-correlation functional were used.

For each calculation the Brillouin zone was sampled using a Monkhorst-Pack Γ -centred k -point mesh. For silicon, CdTe, GaAs and MAPI a $6 \times 6 \times 6$ grid was used. For CZTS, which has a tetragonal crystal structure, a $6 \times 6 \times 4$ grid was used. This was followed with a non-self-consistent calculation along high symmetry lines²⁰¹, with points spaced 0.005 \AA^{-1} apart in reciprocal space, except in the case of the hybrid HSE06 functional with spin-orbit coupling, where a spacing of 0.02 \AA^{-1} was used. The total energy of each material was converged to within 10^{-6} eV. Exchange and correlation was modelled using: (i) the local density approximation (LDA); (ii) the PBEsol²⁰² generalized gradient approximation, and (iii) the screened hybrid functional

HSE06.²⁰³ Spin-orbit coupling (SoC) was used at the PBEsol and HSE06 levels of theory to investigate relativistic effects. A comparison between the bandstructures with and without SoC can be found in Appendix A. The density-of-states of MAPI was investigated using tetragonal smearing and the HSE06 functional with SoC.

	finite diff $m_c(m_e)$			unweighted $m_c(m_e)$			weighted $m_c(m_e)$			$\alpha(\text{eV}^{-1})$		
	[100]	[110]	[111]*	[100]	[110]	[111]*	[100]	[110]	[111]*	[100]	[110]	[111]*
GaAs												
light hole	0.09	0.08	0.05	0.08	0.07	0.07	0.09	0.08	0.08	3.32	3.64	3.69
heavy hole	0.37	0.73	0.79	0.31	0.58	0.25	0.32	0.75	0.53	0.38	3.37	1.70
electron	0.07	0.07	0.06	0.06	0.06	0.06	0.06	0.07	0.07	1.05	1.15	1.23
CdTe												
light hole	0.11	0.10	0.10	0.11	0.10	0.10	0.12	0.10	0.10	1.25	1.49	1.64
heavy hole	0.45	0.86	1.09	0.44	0.83	1.20	0.45	0.83	1.06	0.38	0.99	0.77
electron	0.09	0.09	0.09	0.09	0.09	0.09	0.09	0.10	0.10	0.72	0.94	1.02
MAPI												
hole	0.28	0.15	0.14	0.15	0.09	0.12	0.23	0.10	0.12	4.27	1.88	1.32
electron	0.15	0.13	0.12	0.18	0.10	0.19	0.19	0.10	0.18	2.21	1.35	0.16
CZTS												
hole	0.23	0.74	0.75	0.22	0.54	0.60	0.32	1.16	1.23	3.96	2.21	1.50
electron	0.19	0.19	0.19	0.18	0.18	0.18	0.19	0.19	0.19	0.91	1.19	0.87

Table 4.1: The curvature effective mass at the band edge (calculated using three different methods, as outlined in Section 4.2) and α (a measure of band non-parabolicity). Calculations use the hybrid exchange-correlation functional HSE06 with spin-orbit coupling. The effective mass is calculated for the bands which are degenerate at the conduction band minima / valence band maxima. The mean average of the spin-up and spin-down states is taken. *Direction is [010] in the case of tetragonal Cu₂ZnSnS₄.

4.3 Results

4.3.1 Comparison of methods used to calculate effective mass at the band edge

Two methods are widely used for calculating the curvature effective mass: the finite-difference approach which approximates the differential equation in Eqn. 4.1 with a difference equation, and the least-squares approach which fits an unweighted second order polynomial to the DFT-calculated dispersion. For calculations of parabolic bands with negligible numerical noise a three-point finite difference method or least-squares fit would be sufficient. However the DFT calculation can introduce noise into the energy eigenvalues calculated at each k -point due to the numerical imprecision of the linear algebra routines, and any errors in the energy eigenvalues will be magnified by a finite difference method.²⁰⁴ A recent perturbative approach has been developed to overcome the problem of numerical noise.²⁰⁵

For a non-parabolic dispersion, the value calculated using either method will also depend on the sampling range and density in reciprocal space. We take the VB of CZTS in the [100] direction as an example, calculated using PBEsol with SoC. Using an unweighted least squares fit to three points, we calculate an effective mass ranging from $0.05 m_e$ to $0.08 m_e$ as the spacing in reciprocal space is varied from 0.005 \AA^{-1} to 0.025 \AA^{-1} . Using a three-point finite difference method, we calculate an effective mass ranging from $0.06 m_e$ to $0.12 m_e$. To avoid this sensitivity, we propose using a least-squares fit where each point is weighted according to the Fermi–Dirac distribution. We have found that the weighted least-squares method is less sensitive to the sampling density; for the previous example, we calculate a value of $0.07 m_e$ at all sampling densities (Appendix B). The weighting accounts for the thermal distribution of electrons, as even when the Fermi level is in the bandgap, higher energy states are occupied according to the Fermi–Dirac distribution.

We compare values for the curvature effective mass in Table 4.1. We find that electrons in the CB have light, highly isotropic masses and that there is good agreement between values calculated using the finite difference and least-squares fitting approaches. We find larger discrepancies between the methods used for calculating VB hole effective masses. This can be attributed to the increased non-parabolicity of the VB (see the α values in Table 4.1). The weighted effective mass assumes a parabolic dispersion, however the curvature of this parabola accounts for the flattening of the dispersion away from the band edge, as shown in Figure 4.2. As a result, we calculate heavier effective masses using the weighted least-squares method compared to the unweighted least-squares method.

We compare the weighted to unweighted calculation methods further by considering the ratio of their effective mass values. The ratio between the weighted and unweighted effective mass values is large when the values for α and the effective mass are large, as shown in Figure 4.3. A large α is required as it is non-parabolicity which adjusts the value of effective mass away from

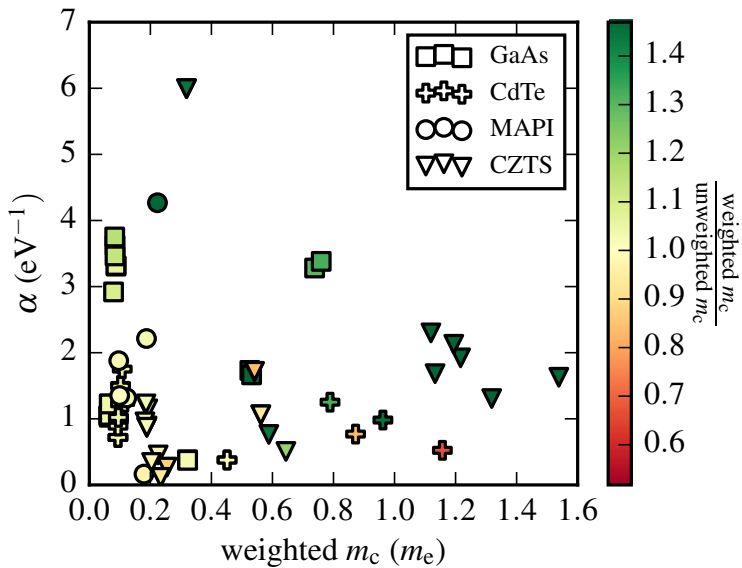


Figure 4.3: α (a measure of band non-parabolicity) is plotted against the curvature effective mass m_c . The colour scale represents the ratio between the masses calculated using a Fermi–Dirac weighting and no weighting. We use the data from Table 4.2, plus two extra valence bands in $\text{Cu}_2\text{ZnSnS}_4$ which are higher in binding energy due to crystal field splitting. All results use the HSE06 functional with spin-orbit coupling.

the band edge. A large mass is required as more eigenstates are then available at energies where the occupation probability, determined by the Fermi–Dirac distribution, is appreciable. As a result, the ratio between weighted and unweighted masses is small for the light CB electrons, and larger for the heavy VB holes in CZTS and GaAs.

The weighted least-squares fit is an improvement over previous calculation methods as it is less sensitive to the sampling density used, and gives a physically-intuitive energy range to fit over. It avoids polynomial fitting to an arbitrarily chosen energy range. For light, parabolic bands we find that the three different methods we compare lead to comparable results. The difference between the calculation methods is greatest for bands with low dispersion and high non-parabolicity.

4.3.2 Deviations from the expected effective mass trend

There are two deviations from the general trends found for the effective mass results presented in Table 4.1. Firstly, in Table 4.1 we see that the GaAs unweighted heavy-hole mass along [111] is smaller than for [100], while this is the opposite for the other methods. To explain this we should consider the non-parabolicity of the GaAs heavy-hole in the [111] direction (denoted $m_{hh}[111]$). The alpha parameter for $m_{hh}[111]$ is 1.7 eV^{-1} and so we expect the weighted effective mass to be heavier than the unweighted effective mass (as it samples the heavier states away from band edge). This is confirmed (weighted: $0.53 m_e$, unweighted: $0.25 m_e$). Compare this to the alpha parameter for $m_{hh}[100]$ which is 0.38 eV^{-1} . This alpha parameter indicates

that the dispersion in the [100] direction is near parabolic, and so we would expect the weighted and unweighted masses to be similar. This is also confirmed in our calculations (weighted: $0.32m_e$, unweighted: $0.31m_e$). This means that at band edge $m_{hh}[111] < m_{hh}[100]$ but due to high non-parabolicity in the [111] direction, when we use our weighted approach and take into account eigenstates away from band edge, $m_{hh}[111] > m_{hh}[100]$.

Secondly, in Table 4.1 we see that the CdTe $m_{hh}[111]$ is larger for the unweighted method than for the weighted method. This is not the trend seen for the other materials, nor is it the trend we would expect, as the weighted method samples eigenstates away from band edge where the band (approximated by the Kane dispersion) flattens. This deviation indicates that the Kane dispersion is not an accurate approximation for the CdTe heavy hole band in the [111] direction. The Kane dispersion we use to describe the electronic bands is accurate when the transport effective mass grows linearly with the electron eigenstate energy (Equation 4.6 of main text). This is the case for most band dispersions in this study, however a plot of transport mass against energy for the CdTe heavy hole in the [111] direction shows that the transport mass is almost constant at small energies - this corresponds to a flattening at the top of the valence band (Figure 4.4). We compare this to the light hole in the [111] direction, which shows a linear relationship between transport mass and energy (Figure 4.5). This light hole has a weighted mass heavier than the unweighted mass (Table 4.1), as would be expected for an electronic band described by the Kane dispersion.

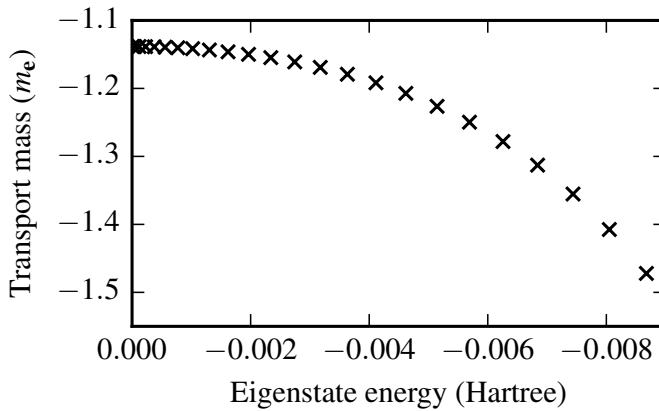


Figure 4.4: Transport effective mass of the CdTe heavy hole band in the [111] direction, as a function of eigenstate energy (referenced from the valence band maximum).

4.3.3 Sensitivity of the curvature effective mass to the level of theory

In the previous section we considered the sensitivity of the curvature effective mass to the numerical method used. In this section we consider how sensitive the curvature effective mass is to the exchange-correlation functional (LDA/GGA/HSE06) and spin-orbit coupling. We plot the weighted curvature effective mass against the bandgap, at different levels of theory,

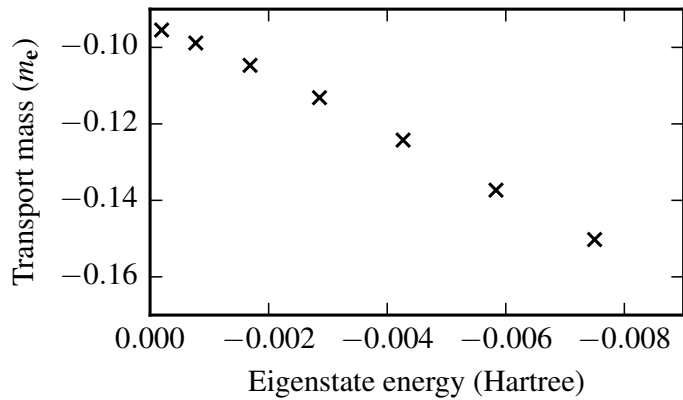


Figure 4.5: Transport effective mass of the CdTe light hole band in the [111] direction, as a function of eigenstate energy (referenced from the valence band maximum).

in Figure 4.6. For CZTS, CdTe and GaAs we find that the local (LDA) and semilocal (GGA) approximations for the exchange energy underestimate the bandgap whereas HSE06 provides a better description. This agrees with previous work.^{203,206} MAPI has an experimental bandgap of 1.53 eV,²⁰⁷ which, due to a cancellation of errors, is in good agreement with the value calculated using PBEsol with no spin-orbit coupling.

Tight binding theory states that the effective mass is inversely proportional to the coupling strength between the valence and conduction bands.⁴⁸ This agrees with the positive correlation between the bandgap and the effective mass shown in Figure 4.6. For CZTS, CdTe and GaAs, the effective mass calculated with the HSE06 functional gives the best agreement with experimental data, as has been found previously.²⁰⁸ The electron effective mass in CZTS is particularly sensitive to the exchange-correlation energy; the value calculated using the HSE06 functional ($0.19 m_e$) is over three times that calculated using the LDA or GGA functional ($0.06 m_e$).

Spin-orbit coupling has a negligible impact of the effective mass values calculated for CdTe, GaAs and CZTS. In contrast, spin-orbit coupling does have a large influence on the effective mass values calculated for MAPI, due to the atomic weight of lead. A reduced effective mass ($(m_e^{*-1} + m_h^{*-1})^{-1}$) of 0.104 has been reported experimentally,²⁰⁹ for MAPI. This is equal to the reduced mass calculated in the [100] direction using the hybrid HSE06 functional with spin-orbit coupling ($m_h^* = 0.23$, $m_e^* = 0.19$). Without spin-orbit coupling the effective masses are significantly overestimated.

4.3.4 Sensitivity of the Kane dispersion parameters to the level of theory

Until this point we have approximated the bandstructures with a parabola, and the effective mass could be described with a single parameter. We will now approximate the bandstructures

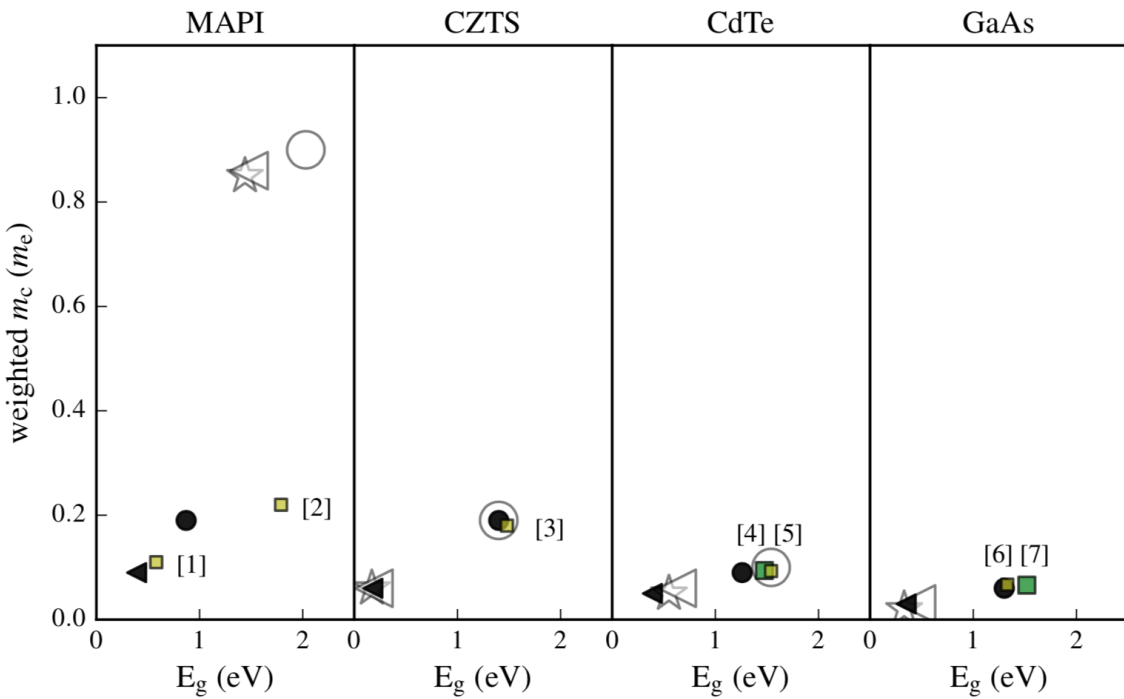


Figure 4.6: The effective mass of conduction band electrons in the [100] direction is plotted against the bandgap and Fermi level (referenced to the CBM). The effective mass is calculated using a weighted quadratic least-squares fit as outlined in Section 4.2. We use filled shapes to denote a calculation with spin-orbit coupling. We use stars, triangles and circles to denote the use of the LDA, PBEsol and HSE06 exchange-correlation functionals respectively. Yellow squares denote results from other computational studies: [1] DFT+SoC²¹⁰ [2] GW²¹⁰ [3] DFT+SoC²¹¹ [5] GW²¹² [6] 30-band $k \cdot p$ method.²¹³ Green squares denote results from experimental studies [4] (obscured by [5]) cyclotron resonance⁴⁶ [7] cyclotron resonance.⁴⁶

with the Kane quasi-linear dispersion. As a result, the effective mass will have two parameters; the effective mass at the band edge and the α parameter (Eqn. 4.6).

We find that α is inversely correlated with the band gap of the material for all materials in this study (Figure 4.7). In CZTS, for example, we find that the CB is highly non-parabolic ($\alpha \approx 3.5 \text{ eV}^{-1}$) at lower levels of theory (LDA/GGA). However, when we use a hybrid functional the bandgap is increased and the CB becomes more parabolic ($\alpha \approx 1 \text{ eV}^{-1}$). We attribute this to the $k \cdot p$ interaction between the conduction and valence bands,¹⁸⁴ which makes non-parabolicity particularly pronounced in narrow bandgap semiconductors such as GaAs.²¹⁴

The non-parabolicity of bands in CZTS²¹⁵ and MAPI^{141,216} has been previously attributed to the spin-orbit interaction. We find that, for CZTS, non-parabolicity in the CB is due to the change in bandgap; spin-orbit coupling has only small effect (Figure 4.8). Spin-orbit coupling has a larger effect on the non-parabolicity of the CZTS VB, which has an α value of 3.96 eV^{-1} when calculated with spin-orbit coupling and 1.47 eV^{-1} when calculated without. For MAPI, there is increased non-parabolicity in both the VB and CB when spin-orbit effects are considered.

To accurately calculate effective mass parameters, it is important to reproduce the correct band gap. For CdTe, GaAs and CZTS this is achieved through use of the HSE06 functional. Without

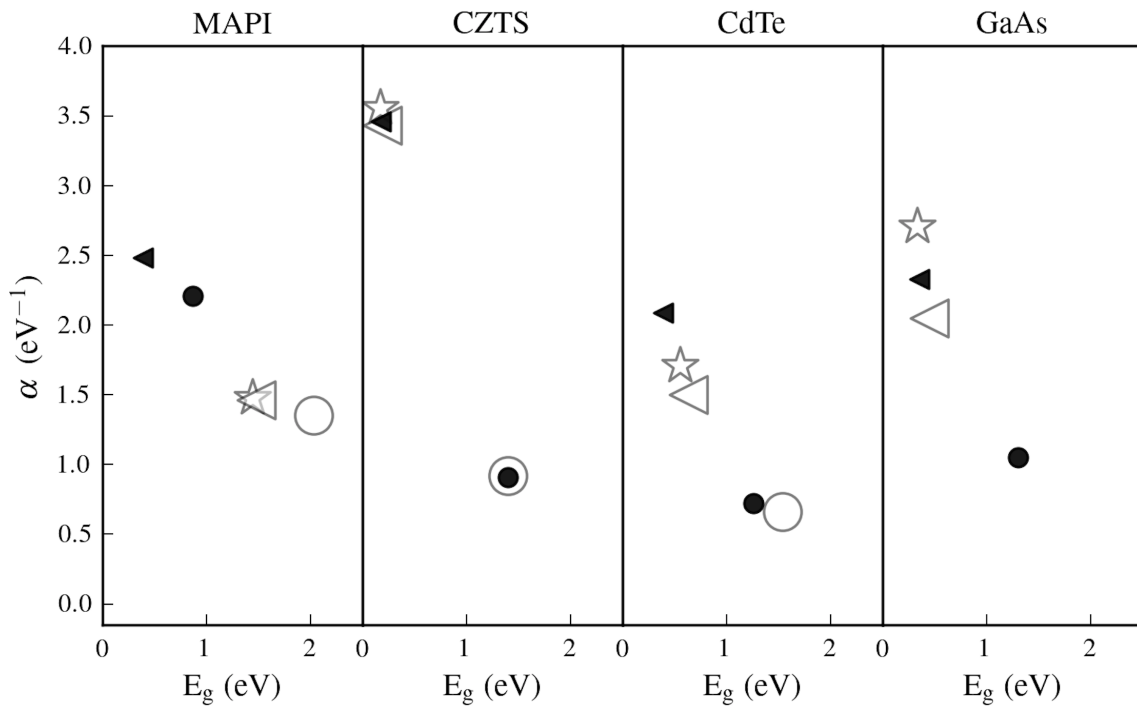


Figure 4.7: α (a measure of band non-parabolicity) is plotted against bandgap at various levels of theory. α is calculated for the CB in the [100] direction. We use filled shapes to denote a calculation with spin-orbit coupling. We use stars, triangles and circles to denote the use of the LDA, PBEsol and HSE06 exchange-correlation functionals, respectively.

this, the effective mass is under-estimated and band non-parabolicity is over-estimated. CZTS is particularly sensitive to the exchange-correlation functional used. The story is different for MAPI: reproducing the correct bandgap does not necessarily lead to accurate effective mass values. Instead, to calculate accurate effective mass values and capture the full extent of band non-parabolicity, we must account for spin-orbit effects.

4.3.5 Consequences of non-parabolicity on the optical and transport properties of MAPI

The effective mass is commonly calculated and compared across materials because it can be used to model differences in various optical and transport properties. This also means that the effective mass can be inferred from a number of different measurements, which can lead to discrepancies. For non-parabolic bandstructures, *e.g.* MAPI, these values will also vary with temperature and carrier concentration. In interpreting the photophysical behaviour of MAPI a range of effective mass values can be found in the literature, from $0.09 m_e$ – $0.30 m_e$.^{191–193,209,217,218} We will focus briefly on the results from transient absorption spectroscopy (TAS). Manser *et al.* calculated the Burstein–Moss shift in MAPI up to a carrier concentration of $1.5 \times 10^{19} \text{ cm}^{-3}$.¹⁹¹ Assuming a parabolic band dispersion, they calculated an effective mass at band edge of $0.3 m_e$. Yang *et al.* found that a parabolic effective mass value of $0.23 m_e$ reproduced TAS carrier concentration data.¹⁹² Their model requires a shift in energy due to ‘band gap renormalisation’, a concept

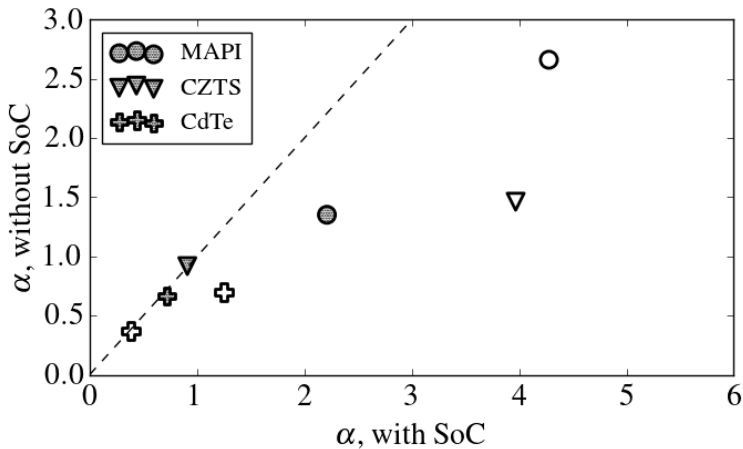


Figure 4.8: α (a measure of band non-parabolicity, eV^{-1}) in the [100] direction, calculated with and without spin-orbit coupling. We use hatched shapes to denote an electron in the conduction band, and empty shapes to denote a hole in the valence band. Note the scale; the dashed line indicates where the values would lie if spin-orbit coupling had no influence on the value of α . The hybrid HSE06 exchange-correlation functional was used for all calculations.

that incorporates multiple physical phenomena, but that can be partially attributed to band non-parabolicity.²¹⁹ Price *et al.* have developed a model which includes photoinduced changes to the refractive index.¹⁹³ This gives a value of $0.14 m_e$ for the reduced effective mass, assuming a parabolic dispersion, which is in line with results from magneto-absorption experiments^{209,217,218} and theory.^{141,220} The error bar in this value, $0.04 m_e$, is significant and may be attributed to an effective mass which varies with carrier concentration.

In this section we will quantify the extent to which non-parabolicity impacts upon the Burstein–Moss bandgap shift, optical effective mass, and polaron mobility. To do so, we assume a Kane quasi-linear dispersion and predict, for MAPI, how these observables will vary as a function of carrier concentration.

Burstein–Moss bandgap shift

A consequence of the Pauli exclusion principle is that at a particular carrier concentration the Fermi level is pushed into the conduction (or valence) band. This band filling leads to the experimentally observable Burstein–Moss shift where the optical bandgap of the material is increased. The magnitude of the Burstein–Moss shift is given by

$$\Delta_{\text{BM}} = \frac{\hbar^2}{2m^*} (3\pi^2 n_e)^{2/3}, \quad (4.19)$$

where m^* is the reduced effective mass and $(3\pi^2 n_e)^{2/3}$ is the Fermi wavevector up to which all states are occupied under the free electron model. It is most commonly considered in the context of degenerately doped semiconductors; here we consider photo-excited carriers in an undoped material.

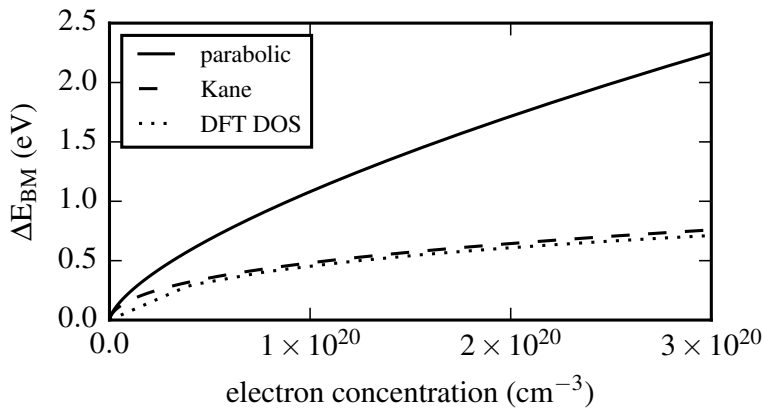


Figure 4.9: The Burstein–Moss band gap shift is plotted as a function of carrier concentration. The shift is calculated assuming a parabolic dispersion, Kane quasi-linear dispersion and from a DFT calculated density of states. Beyond this carrier concentration range we begin to fill bands higher in energy (the secondary band in MAPI is calculated to be at 0.78 eV). To average across different directions we use the geometric mean of the effective mass and the arithmetic mean of α .

The insulator-metal transition marks the point at which a semiconductor becomes degenerate and it is above this point that the Burstein–Moss shift occurs. Manser *et al.* report an abrupt onset of the Burstein–Moss effect at carrier concentrations of $7.5 \times 10^{17} \text{ cm}^{-3}$.¹⁹¹ They account for this through trap filling, with traps estimated to be at a density of $2 \times 10^{17} \text{ cm}^{-3}$. We add to this the density at which the electron polaron wavefunctions overlap, as given by the phenomenological Mott criterion²²¹, $4 \times 10^{17} \text{ cm}^{-3}$.²²² This brings us to a total of $6 \times 10^{17} \text{ cm}^{-3}$, which is closer to the reported experimental value. This is beyond the operating conditions under one sun, for which we expect a maximum carrier concentration of $\sim 10^{16} \text{ cm}^{-3}$.³⁶ However concentrator systems can achieve carrier concentrations of 10^{18} cm^{-3} ¹⁹⁴ and will fall into the degenerate regime. Furthermore, carrier concentrations of up to 10^{19} cm^{-3} are reached when exciting with a laser as in photoluminescence and transient absorption spectroscopy measurements,²²³ and there has been recent research interest in developing a hybrid halide perovskite lasing material which would require concentrations of up to 10^{21} cm^{-3} .²²⁴

We assume a parabolic dispersion and use the curvature effective mass to calculate values of the Burstein–Moss shift using Eqn. 4.19. When we compare our results to the density of states data calculated from DFT, which makes no assumption about the form of the dispersion, we see that the parabolic approximation leads to a large overestimation (Figure 4.9). Walsh *et al.*²¹⁹ demonstrated that non-parabolicity can cause this discrepancy, as non-parabolicity increases the density of states, which results in the Fermi level increasing more slowly. We account for non-parabolicity by substituting the energy-dependant mass given by Eqn. 4.6 into Eqn. 4.19 and solving self-consistently. With this amendment we see good agreement with the density of states data; this demonstrates that the Kane quasi-linear dispersion provides a suitable approximation at high carrier concentrations.

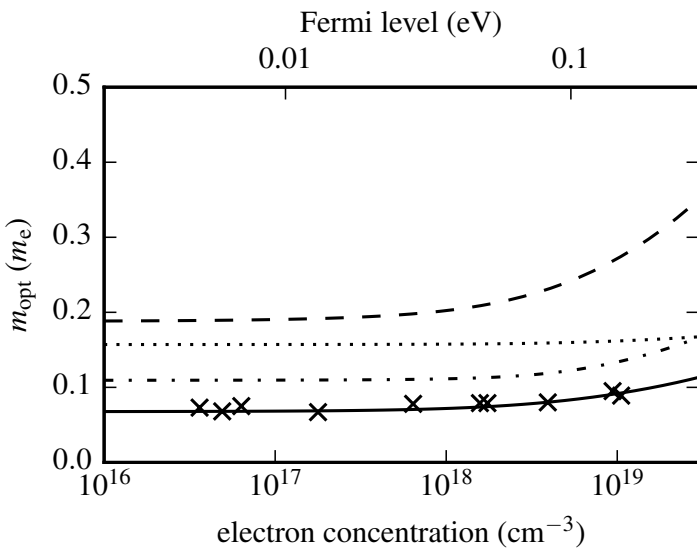


Figure 4.10: The conduction band electron optical effective mass is plotted as a function of carrier concentration. Values for the [100] (dash line), [111] (dot line) and [110] (dash-dot line) directions are given. To validate our results we include results for GaAs (continuous line) and compare this against experimental data (crosses).²²⁵ The Kane quasi-linear dispersion in the [100] direction does not give a good approximation to the DFT-calculated dispersion beyond carrier concentrations of $3 \times 10^{19} \text{ cm}^{-3}$.

Optical effective mass

To calculate the effective mass which is measured in optical experiments, we integrate the analytic expression given in Eqn. 4.10 with $E(k)$ given by the Kane dispersion in Eqn. 4.4. We set the Fermi level equal to the Burstein–Moss shift, which gives a dependance on carrier concentration.

At a concentration of $3 \times 10^{19} \text{ cm}^{-3}$ there is a significant increase in the optical effective mass in the [100] direction, from $0.19 m_e$ at the band edge to a value of $0.35 m_e$ (Figure 4.10). To put this in context, the effective mass values calculated using GW+SoC and DFT+SoC differ by up to only $0.03 m_e$.²²⁰ Clearly, at high carrier concentrations, we must account for non-parabolicity to achieve accurate estimates for the optical effective mass. This result is highly dependant on the non-parabolicity of the bandstructure; we see a negligible increase in the optical effective mass in the [111] direction due to the small value of α in this direction.

Polaron mobility

The relationship between the mobility μ , relaxation time τ and effective mass m^* of a particle with charge q is given by

$$\mu = \frac{q\tau}{m^*}. \quad (4.20)$$

Table 4.2: The optical effective mass and polaron mobility for a conduction band electron in the [110] direction of $\text{CH}_3\text{NH}_3\text{PbI}_3$. AM1.5 is the global standard solar spectrum for non-concentrator systems.

conc. (cm^{-3})	eff. mass m_{opt} (m_e)	mobility ($\frac{\text{cm}^2}{\text{Vs}}$)	application
10^{15}	0.11	158	solar cell AM1.5
10^{18}	0.11	158	concentrator system
10^{19}	0.13	120	photoluminescence
10^{20}	0.23	46	lasing material

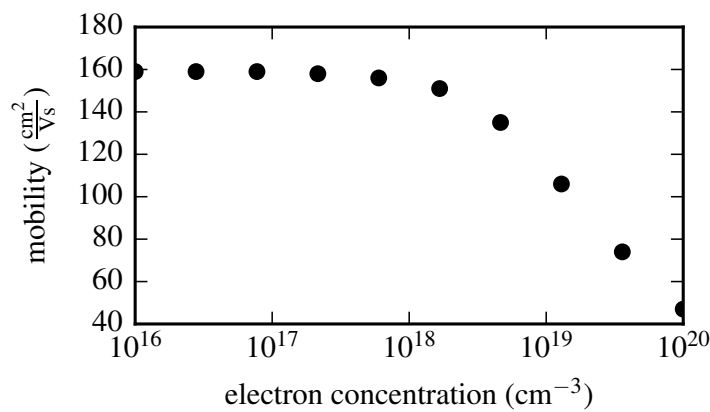


Figure 4.11: Polaron mobility, limited by optic-mode scattering, is plotted as a function of carrier concentration for a conduction band electron in the [110] direction of $\text{CH}_3\text{NH}_3\text{PbI}_3$. This is calculated using parameters taken from the literature:²²⁶ high-frequency dielectric constant = 4.5, low-frequency dielectric constant = 24.1 and characteristic phonon frequency = $2.25 \times 10^{12} \text{ cm}^{-1}$.

On first inspection it would seem that the mobility must be directly proportional to the inverse of the effective mass. However, for a range of scattering processes, the relaxation time is not independent of the effective mass and this will lead to a more complex relationship between effective mass and mobility. We use a model which considers scattering from polar optical phonon modes, as this is the process which limits the charge carrier mobility in MAPI at room temperature.¹¹⁵

We calculate polaron mobility using a recently implemented *ab-initio* method based on a Feynman path integral approach.²²⁶ The parameters for this model are the effective mass, high- and low-frequency dielectric constants and a characteristic phonon mode. Here we study the effects of band non-parabolicity by calculating electron polaron mobility as a function of the optical effective mass. We justify using the optical effective mass to calculate a transport property with reference to Eqn. 4.10.

The mobility at a concentration of 10^{20} cm^{-3} is $\sim 30\%$ of that calculated for low carrier concentrations (Figure 4.11 and Table 4.2). This significant reduction happens even in the absence of the electron-electron scattering that will be enhanced at higher carrier concentrations,

and agrees with a previous report which states that mobility is particularly sensitive to effective mass.²²⁷

Our results show that non-parabolicity has a negligible effect on the optical effective mass and mobility of MAPI at concentrations of $\sim 10^{18} \text{ cm}^{-3}$ (Table 4.2). At a concentration of $1.5 \times 10^{18} \text{ cm}^{-3}$, the Burstein–Moss bandgap shifts we predict using the parabolic and Kane quasi-linear dispersion differ by 0.008 eV. This is significantly less than the typical energetic disorder at room temperature ($k_B T = 0.025 \text{ eV}$), and so we predict the parabolic approximation to be sufficient at these carrier concentrations. At higher concentrations it is important to account for band non-parabolicity to make accurate predictions for the Burstein–Moss bandgap shift, optical effective mass and polaron mobility. At a concentration of 10^{20} cm^{-3} there is a doubling in the optical effective mass and a three-fold decrease in polaron mobility.

4.4 Summary

The effective mass plays a central role in the description of several material properties, and is a key parameter when assessing the suitability of materials for use in, for example, photovoltaic applications. Several alternative definitions exist for the effective mass, and there are also different ways to numerically calculate these from calculated electronic structure data.

I have introduced a method to calculate the curvature effective mass which uses a physically intuitive energy range given by the Fermi–Dirac distribution. This accounts for the thermal smearing of charge carriers, which is inevitable above 0K. I have shown that this method is less sensitive to the sampling density in reciprocal space.

We then moved beyond the parabolic approximation to consider bandstructures described by Kane quasi-linear dispersion. The α parameter provides a good description of the dispersion away from band edge and could be used as a screening parameter for materials which operate at high carrier concentrations, for example transparent conducting oxides. It is found that, across the four materials, accurate non-parabolic effective mass values require hybrid functionals as band gap underestimation generally results in artificially high levels of non-parabolicity. It is also important to account for spin-orbit coupling when describing the non-parabolicity of the valence bands via the α parameter.

Finally, I have considered how non-parabolicity impacts upon optical and transport properties at high carrier concentrations. For this the lead halide perovskite MAPI was used as a case study, as it was found to be the most highly non-parabolic of the four materials. It was found that the parabolic approximation severely overestimates the Burstein–Moss shift, whilst the Kane quasi-linear dispersion shows good agreement with density of states calculations. Using the Burstein–Moss shift as a proxy for the Fermi level, I calculated the change in electron effective mass and mobility as a function of carrier concentration. The assumption previously used in the literature—that the effective mass is independent of carrier concentration—is not valid.

At carrier concentrations above 10^{18} cm^{-3} , non-parabolicity must be built into photophysical models to give accurate values for the effective mass and derived properties.

Data Access Statement

The crystal structures and electronic structure data reported in this chapter, alongside a Jupyter notebook which outlines the key calculation steps, are available in an online repository.²²⁸ Effective mass values can be calculated using EFFMASS package,²²⁹ which is outlined in Appendix C. Polaron mobility can be calculated using the POLARONMOBILITY.JL package.²³⁰

Acknowledgements

This work used the ARCHER UK National Supercomputing Service (<http://www.archer.ac.uk>) which we have access to via membership of the UK's HEC Materials Chemistry Consortium (funded by EPSRC Grant No. EP/L000202). I am also grateful to the UK Materials and Molecular Modelling Hub for computational resources, which is partially funded by EPSRC Grant No. EP/P020194/1.

*I take lettuce, onions, tomato
Add a dab of mayo plus the fish fillet-o
Appetizing gray matter with a strange platter
The symmetry of energy with chemistry and plasma*

— Edan, *I see colours*

5

Electron-phonon and phonon-phonon coupling

Excerpts of this chapter and Figures 2–4 are adapted from Whalley, L. D., Skelton, J. M., Frost, J. M. and Walsh, A. (2016). Phonon anharmonicity, lifetimes, and thermal transport in $\text{CH}_3\text{NH}_3\text{PbI}_3$ from many-body perturbation theory. *Physical Review B*, 94(22). © 2016 American Physical Society

Figures 1,5–6 are adapted from Frost, J. M., Whalley, L. D and Walsh, A. (2017). Slow Cooling of Hot Polarons in Halide Perovskite Solar Cells. *ACS Energy Letters*, 2(12), pp.2647-2652. © 2017 CC-BY

5.1 Introduction

In the simplest approximation of a semiconductor – a single electron in a perfect lattice at zero kelvin – electrons do not scatter and as a consequence they have infinite mobility. In the next best approximation, harmonic phonons are introduced. Now the electrons scatter from the phonons, and the electron mobility becomes finite. This electron-phonon interaction underpins many phenomena in condensed matter physics and materials science including carrier mobility, polaron formation, hot carrier thermalisation and carrier capture. However in the harmonic phonon approximation, the phonons do not interact with one another – they have an infinite lifetime. To calculate thermal conductivity and understand how a polaron cools to equilibrium we need to consider anharmonic phonon-phonon interactions. Some processes involve both electron-phonon and phonon-phonon interactions; for example during non-radiative recombination, carrier capture and lattice relaxation proceed via the electron-phonon and phonon-phonon interactions.

This chapter begins with an introduction to electron-phonon coupling, with coupling to the acoustic and optical phonon modes considered. This extends the MAPI-focused discussion in Section 2.3.2 to consider the broader underlying theory. Later in the chapter I show that

there is strong coupling between the highly anharmonic phonon modes that are associated with octahedral tilting in MAPI and the electronic states at the band edge.

Phonon-phonon coupling, and how this relates to hot-carrier cooling in MAPI, is also introduced. Using a simple classical model for heat diffusion, I show that the ultra-low thermal conductivity of perovskites can be used to explain the experimentally observed slow cooling of photoexcited above bandgap electrons.

5.1.1 Electron-phonon coupling

We have previously considered a system where the electronic and vibrational substates are decoupled. However to model electron-phonon interactions we must remove this approximation and employ a Hamiltonian that describes the coupled system. The crystal Hamiltonian can be split into three terms:²³¹

$$\hat{H} = H_e + H_{ion} + H_{e-ion}. \quad (5.1)$$

The electronic sub-system corresponds to non-interacting band electrons in a periodic lattice with energy $\epsilon_{n\mathbf{k}}$. Using the formalism of second-quantisation this electronic Hamiltonian H_e can be expressed in a relatively compact form:²³²

$$H_e = \sum_{n\mathbf{k}} \epsilon_{n\mathbf{k}} \hat{c}_{n\mathbf{k}}^\dagger \hat{c}_{n\mathbf{k}}, \quad (5.2)$$

where $\hat{c}_{n\mathbf{k}} \hat{c}_{n\mathbf{k}}^\dagger$ is a number operator which tells us how many electrons are in a state with band index n and crystal momentum \mathbf{k} . The lattice sub-system corresponds to non-interacting quantised harmonic vibrations (phonons) with energy $\hbar\nu_{\mathbf{q}v}$ and can be expressed in the language of second quantisation as:

$$H_{ion} = \sum_{\mathbf{q}v} \hbar\nu_{\mathbf{q}v} (\hat{a}_{\mathbf{q}v}^\dagger \hat{a}_{\mathbf{q}v} + \frac{1}{2}), \quad (5.3)$$

where $\hat{a}_{\mathbf{q}v} \hat{a}_{-\mathbf{q}v}^\dagger$ is a number operator which tells us how many phonons are in a state with branch index v with crystal momentum \mathbf{q} .

To describe the interaction between the electron and phonon sub-systems it is assumed that the electrons respond instantaneously to the ionic motion. This allows the electron-phonon interaction term of the Hamiltonian to be expressed as a Taylor series expansion of the electronic Hamiltonian:²³¹

$$H_{e-ion} = \sum_j \left(\frac{\partial H_e}{\partial R_j} \right) \Big|_{R_{j0}} \cdot \delta R_j \dots \quad (5.4)$$

where δR_j is the displacement of ion j from the equilibrium position R_{j0} . The zeroth order term is not included as this is the interaction of the electrons with the static lattice and is already included in the electronic Hamiltonian. The first order term of the expansion describes the lowest-order process that involves coupling between the electron and phonon sub-system, and

corresponds to the scattering of a single electron by a simultaneous creation or annihilation of a single phonon. In second quantised form electron-phonon coupling term can be expressed as:²³²

$$H_{e-ion} = N_p^{-\frac{1}{2}} \sum_{\mathbf{k}, \mathbf{q}} g_{mnv}(\mathbf{k}, \mathbf{q}) \hat{c}_{m\mathbf{k}+\mathbf{q}}^\dagger \hat{c}_{n\mathbf{k}} (\hat{a}_{\mathbf{q}v} + \hat{a}_{-\mathbf{q}v}^\dagger). \quad (5.5)$$

The matrix element $g_{mnv}(\mathbf{k}, \mathbf{q})$ determines the strength of the coupling and N_p is the number of unit cells in the supercell. $\hat{a}_{\mathbf{q}v}$ and $\hat{a}_{-\mathbf{q}v}^\dagger$ are the operators that destroy and create phonons, whilst $\hat{c}_{n\mathbf{k}}$ and $\hat{c}_{m\mathbf{k}+\mathbf{q}}^\dagger$ are the operators that destroy and create electrons.

Unfortunately Equation 5.5 does not tell us how to calculate the electron-phonon matrix $g_{mnv}(\mathbf{k}, \mathbf{q})$. The first expression for the matrix elements was derived by Bloch in 1929:²³²

$$g_{mnv}(\mathbf{q}) = -i \left(\frac{\hbar}{2N_p M_\kappa \nu_{\mathbf{q}v}} \right)^{\frac{1}{2}} \mathbf{q} \cdot \mathbf{e}_{\kappa v}(\mathbf{q}) V_0, \quad (5.6)$$

where V_0 is an average effective potential experienced by the electrons in the crystal, M_κ is the mass of the κ th nucleus and $\mathbf{e}_{\kappa v}(\mathbf{q})$ is a phonon eigenvector. The expression is derived for a monovalent metal with one atom in the unit cell and where the Kohn-Sham wavefunctions can be approximated by free electrons,^{232,233} and as a result of this the expression is independent of the electron momentum.

The electron-phonon coupling term in Equation 5.5 contains a summation over all states in the electronic and vibrational Brillouin Zones. Considering all possible states is computationally intractable for many systems of interest, but the problem can be simplified by only considering the terms which make the most dominant contributions. In the case of covalent materials, it is assumed that the dominant interaction is between long wavelength acoustic phonon modes and electronic states. For ionic materials it is assumed that the dominant interaction is with the electric field generated by longitudinal optic phonons.

Acoustic deformation potential scattering

In 1950 Bardeen and Shockley introduced the ‘deformation potential’ method,²³⁴ which gives an approximation to V_0 for semiconductors where the dominant electron-phonon scattering mechanisms involve long wavelength acoustic phonons.²³² In this approach average effective potential for a unit cell of volume Ω is given by:

$$V_0 = \Omega \frac{\partial \epsilon_{n\mathbf{k}}}{\partial \Omega}. \quad (5.7)$$

The deformation potential in Equation 5.7 can be determined empirically or calculated from first principles.

Frölich interactions

In the Frölich polaron model a free electron interacts with the electric field generated by dispersionless longitudinal optic (LO) phonons. This interaction only occurs in ionic crystals, where atomic displacements generate long-range electric fields. In this model the effective potential is replaced with

$$V_0 = \left[\frac{e^2 M_k \nu_{\mathbf{q}v}^2}{\epsilon_0 \Omega} \left(\frac{1}{\epsilon^\infty} - \frac{1}{\epsilon^0} \right) \right]^{\frac{1}{2}} \frac{1}{|\mathbf{q}|^2} \quad (5.8)$$

where ϵ_0, ϵ^0 and ϵ^∞ are the vacuum, static, and high-frequency permittivities respectively.

MAPI is a soft material, with structural distortions and dynamic disorder at room temperature, so electron-phonon interactions are expected to be significant. Furthermore, long charge carrier diffusion lengths (up to $10\text{ }\mu\text{m}$) but modest mobilities (up to $100\text{ cm}^2\text{ V}^{-1}\text{ s}^{-1}$) point to strong electron-phonon interactions.²³⁵ Photoluminescence studies of formamidinium-lead-iodide suggest that acoustic deformation potential scattering makes only a minor contribution to electron-phonon interactions at room temperature,¹¹⁵ as there is decreased electron-phonon coupling at temperatures below the relevant LO phonon for Frölich coupling. This suggests that Frölich interactions dominate, and is supported by a theoretical calculation which predicts a LO-phonon limited mobility in line with experiment.²²⁶

5.1.2 Hot carrier cooling in hybrid halide perovskites

Halide perovskites display unusual cooling kinetics for electrons photo-excited above the bandgap. The cooling of these ‘hot’ electrons is slower than that observed in other semiconductors and this has been attributed to a ‘hot phonon bottleneck’.^{236,237} As a result of strong Frölich coupling between the electronic and optical phonon modes, hot carrier cooling in the hybrid perovskites does not occur through a single process but can be split into three stages: i) transfer of energy from the electron to optical phonons (via the electron-phonon Frölich interaction); ii) optical phonon decay into acoustic phonons (phonon-phonon interaction); iii) acoustic phonon propagation (phonon-phonon interaction).

The hot phonon bottleneck results from the equilibration of hot carriers with a non-equilibrium phonon population; Frölich interactions strongly couple the hot electrons to longitudinal optical (LO) phonons, but the LO phonons are not able to dissipate their heat. Poor thermal transport could be attributed to weak coupling between the optical and acoustic phonon modes, or to reduced acoustic phonon mode propagation so that the phonon modes are able to re-heat carriers. In either case, we would expect two timescales to appear experimentally; fast initial thermalisation with optical phonons via the Frölich interaction, followed by slower cooling to equilibrium with the extended bulk solid (Figure 5.1). Here we make a distinction between thermalisation, which we define as equilibration with local phonon modes, and cooling, which is equilibration with the extended bulk solid.

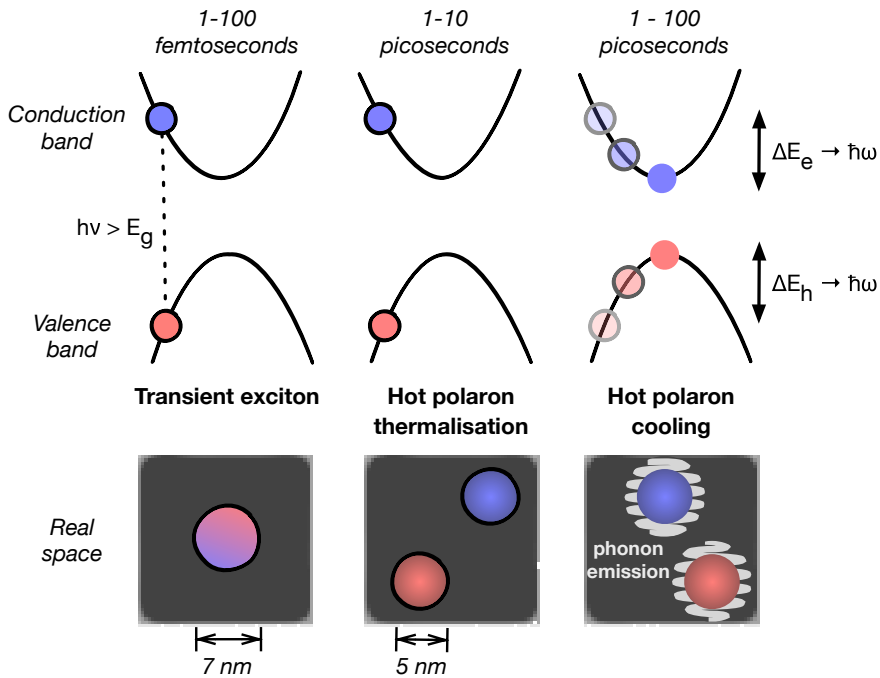


Figure 5.1: Physical processes involved with the photogeneration of charge carriers in hybrid halide perovskites: i) exciton generation; ii) exciton dissociation, hot polaron formation and thermalisation; iii) hot phonon cooling to the band edge. Note that we make a distinction between thermalisation, which we define as equilibration with local phonon modes, and cooling, which is equilibration with the extended bulk solid. Together, they form the hot carrier relaxation process. Figure prepared by Aron Walsh.

5.2 Methods

5.2.1 Lattice dynamics calculations

Harmonic lattice-dynamics calculations were performed with the PHONOPY package.¹⁰⁴ Displacement steps of 0.01 Å were used to evaluate the second-order force-constant matrix using the finite-displacement method. This step size is commonly reported in the literature^{104,238} and is the default value in the PHONOPY package. A $4 \times 4 \times 4$ supercell expansion was used to compute the second-order force constants (72 displacements in a 768-atom cell). Forces were computed within the Kohn-Sham density-functional theory (DFT) formalism as implemented in the VASP code,²³⁹ using the scalar relativistic corrections given in Section 5.2.2. The valence wavefunctions were expanded in a plane-wave basis set with a 800 eV cut-off and the exchange and correlation interactions between electrons were modelled using the PBEsol exchange-correlation functional.²⁴⁰ The electronic Brillouin zone was evaluated at the Γ -point, and a total-energy convergence criterion of 10^{-8} eV was used.

5.2.2 Calculation procedure for the bandgap deformation potential

Density-functional perturbation theory (DFPT) is a method commonly used to calculate the electron-phonon coupling. However DFPT assumes a small harmonic response for the

perturbative treatment to be correct and for anharmonic phonon modes this assumption does not hold. For MAPI, where the range of motion is large and anharmonic, the ‘frozen phonon’ method can be used: here the energy of the valence and conduction bands are tracked as the crystal lattice is distorted along a single phonon mode to give a bandgap deformation potential.

PHONOPY¹⁰⁴ was used to calculate the harmonic phonon eigenvalues and eigenvectors, as outlined above. ModeMap scripts available online²⁴¹ were used to generate a sequence of structures along the phonon eigenvectors at the M and R points in reciprocal space.

The deformation potentials were calculated by following the phonon mode vectors and mapping the change in bandgap as a function of normal mode coordinate Q . Bandgaps were computed within the Kohn-Sham density-functional theory (DFT) formalism as implemented in the VASP code.²³⁹ The valence wavefunctions were expanded in a plane-wave basis set with a 700 eV cut-off and the exchange and correlation interactions between electrons were modelled using the PBEsol exchange-correlation functional²⁴⁰ (Q from 0 to 150 amu $^{\frac{1}{2}}$ Å) and a screened hybrid functional (HSE06)^{242,243} (Q from 0 to 69 amu $^{\frac{1}{2}}$ Å). Scalar-relativistic corrections were used for the core electrons within the projector augmented-wave (PAW) formalism,¹⁹⁷ with the outermost s and p electrons of C, N and I, and the outermost s, p and d electrons of Pb, being treated as valence. The PAW projection was applied in reciprocal space (LREAL = .FALSE. in VASP). Spin-orbit coupling, which strongly affects the unoccupied conduction band, was considered for the PBEsol functional. A Monkhorst-Pack k -point grid, with a Γ -centered $6 \times 6 \times 6$ grid, was used to integrate the electronic Brillouin zone. A total-energy convergence criterion of 10^{-8} eV during the electronic minimisation was found to be necessary to remove noise in the absolute electronic eigenvalues. A least-squares polynomial fit using the PYTHON library NUMPY was applied to the symmetrised data.

The Cartesian displacement of atoms in a N_a atom unit cell for a phonon mode with amplitude Q scales as $\frac{Q}{\sqrt{N_a}}$. However, as evidenced and discussed further in Appendix D, the average bandgap for a given temperature does not scale with supercell size.

5.2.3 Classical model for hot carrier cooling

The hot carrier cooling rate was modelled classically. The polaron was considered as a hot-sphere in a continuum of ambient-temperature material. This reduces the problem to one-dimension, where the exponent is weighted by the r^2 increasing shell of available states over the surface of the sphere. The initial “top hat” heat distribution was convolved with a Gaussian kernel to give an analytical expression for the evolution of hot carrier energy with time. The analytical expression and derivation is given in Appendix (E). The rate of cooling was determined by the diffusivity D :

$$D = \frac{\kappa}{\rho c_p} \quad (5.9)$$

where κ is the thermal conductivity, ρ is the material density, and C_p is the specific heat capacity.

5.3 Results

5.3.1 Anharmonic bandgap deformation potential

Deformations along the soft acoustic phonon modes at q -points M and R in reciprocal space are considered, which correspond to in-phase and out-of-phase tilting of the inorganic octahedra respectively (Figure 5.2). The potential energy is plotted as a function of Q , which describes the amplitude of the displacement along a given phonon mode.⁸¹ To reduce the computational cost we take advantage of the symmetry of the double well potential energy surface (Figure 2.2) and consider distortions along positive Q values only. The corresponding single-well potential energy surface can be found in Appendix D.

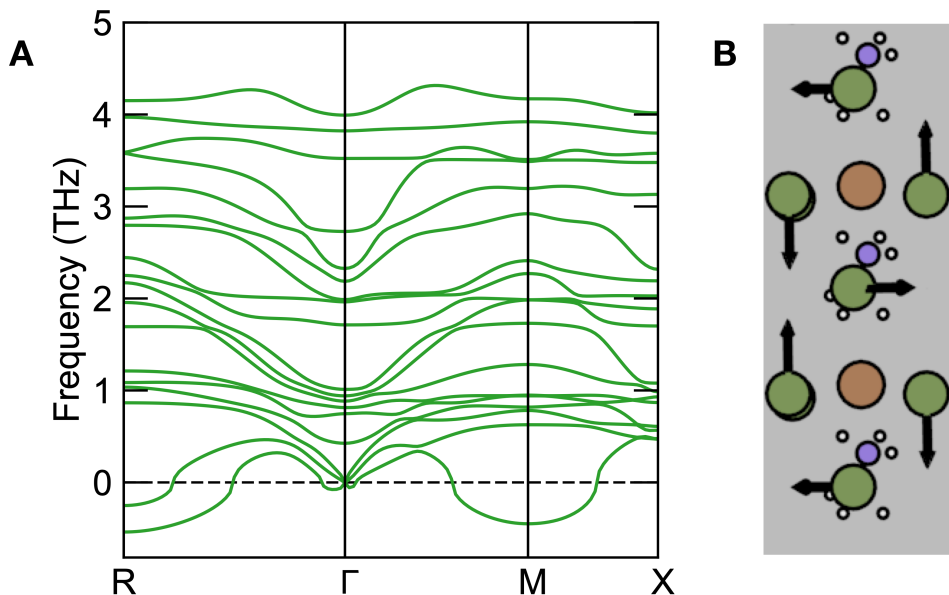


Figure 5.2: A) Harmonic phonon dispersion for MAPI. The bandgap deformation potentials are calculated for distortions along the imaginary mode eigenvectors at q -points M and R in reciprocal space. In the Frölich polaron model for MAPI phonon frequencies up to 5THz are considered, as wavenumbers above this correspond to the molecular vibrations of the organic cation.¹¹⁴ The imaginary modes at the Γ -point are a result of numerical noise. This image was generated using the SUMO software package.²⁴⁴ B) Eigenvector for the imaginary phonon mode at the M point in the Brillouin zone. The green and brown atoms correspond to iodine and lead, respectively. The remaining atoms form the inorganic cation. The magnitude of the vector arrow is increased by a factor of three for clarity, and only the motion of the inorganic cage is considered. This image was generated using the ASCII PHONONS package available at <https://github.com/ajjackson/ascii-phonons>.

The change in bandgap as a function of normal mode coordinate Q is plotted in Figure 5.3. We find that the bandgap $E_g(Q)$ is well described as quadratic over small Q , but that a bi-quadratic term is required to reproduce the correct behaviour at large Q (Table 5.1). The significance of the bi-quadratic term is apparent when calculating the average bandgap as a function of temperature (Section 5.3.1), as the quadratic fit leads to a predicted room temperature bandgap shift twice as large as that for the bi-quadratic fit.

The total bandgap deformation is split into separate contributions from the conduction and valence bands (i.e. electron and hole coupling) in Figure 5.3. The electrostatic summation under periodic boundary conditions does not allow for the determination of absolute electron eigenvalues, and so a reference energy is needed to track the change in eigenvalue across calculations. We track the change in the valence- and conduction-band energies with respect to the Pb 3d deep-lying core states. Fitting a quadratic function to the band energies shows the electron-phonon coupling to be roughly three times that of the hole-phonon coupling (i.e. the change in the conduction-band energy is three times the change in valence-band energy).

A similar bandgap deformation is found for the *M* and *R* modes (Table 5.1). This indicates that the out-of-phase tilting for successive planes in the *R* mode has little additional effect on the gap and that the local tilting dominates the interaction.

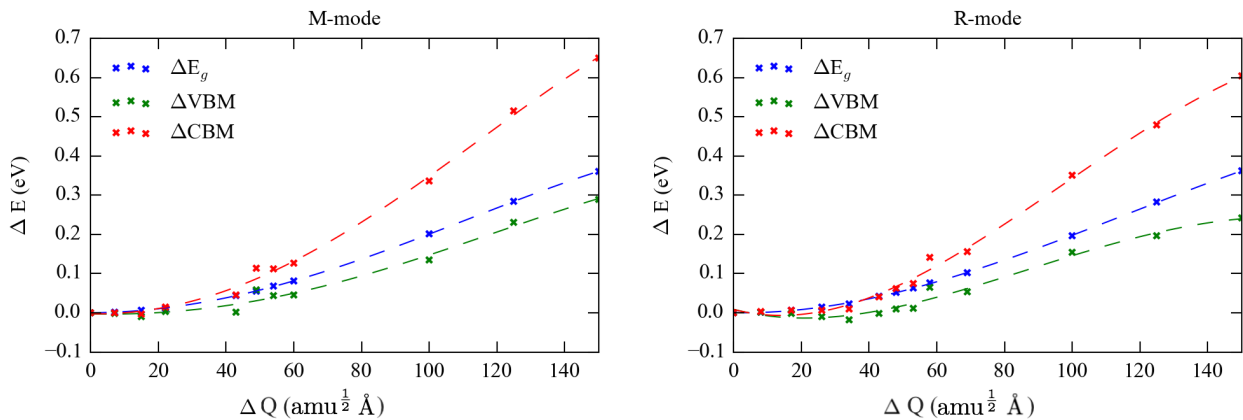


Figure 5.3: Energy change (ΔE) as a function of the normal-mode coordinate Q of the valence-band maximum (ΔVBM), conduction-band minimum (ΔCBM), and bandgap (ΔE_g) obtained from calculations using the PBEsol functional. The energies of the band extrema have been referenced to the energy of the Pb 3d core states.

Table 5.1: Residual sums of squares (RSS) for quadratic and biquadratic fits to the data in Figure 5.3. A smaller RSS indicates a better fit of the model to the data.

	ΔVBM	ΔCBM	ΔE_g
<i>M</i>			
Quadratic	4.1×10^{-3}	1.1×10^{-2}	3.7×10^{-3}
Biquadratic	3.2×10^{-3}	2.9×10^{-3}	2.0×10^{-5}
<i>R</i>			
Quadratic	9.8×10^{-3}	2.0×10^{-2}	3.5×10^{-3}
Biquadratic	6.4×10^{-3}	6.0×10^{-3}	6.0×10^{-5}

For most semiconductor materials the bandgap decreases with temperature. This is attributed to bonding at the frontier orbitals, with the CBM composed of bonding states and VBM composed

of antibonding states, so that thermal expansion leads to a decrease in VBM energy and increase in CBM energy.²⁴⁵ In contrast, relativistic calculations for MAPI predict an ‘inverted’ bandstructure with a VBM composed of antibonding hybridised Pb 6s- and I 5p orbitals and a CBM dominated by the non-bonding 6p-orbitals of lead (Figure 5.4).⁸⁴ As we distort the pseudo-cubic structure along the *M* or *R* phonon modes, the Pb-I bond length increases (Table 5.2), which indicates that there should be a decrease in CBM and VBM energies, contrary to the predicted energy increases.

Band edge energies as a function of various normal mode distortions have been investigated for the metal halide perovskite CsPbI₃, which shares the same VBM and CBM orbital character as MAPI.²⁴⁶ For displacements along the normal phonon mode corresponding to octahedral twisting (iodine motion) around Pb, there is: i) a significant increase in the CBM energy; ii) a decrease Pb *p*-orbital character at the CBM; iii) an increase in I *p*-orbital character at the CBM. The increase in CBM energy is attributed to a reduction in Pb-*p* character, as a result of reduced spin-orbit coupling. However tests on MAPI for two different descriptions of electron exchange and correlation and one including spin-orbit coupling, shows similar behaviour with respect to band deformation (Table 5.4 and Figure 5.5). Instead, we attribute the increase in energy to a decrease in orbital overlap between the Pb 6*p*-states, leading to a less dispersive band and decreased band width. The increase in the VBM site energy could be attributed to the hybridised Pb 6*p*- and I5*p* bonding orbitals which lie lower in the valence band,²⁴⁷ although further calculations to predict the orbital character as a function of phonon mode displacement are needed to confirm this hypothesis.

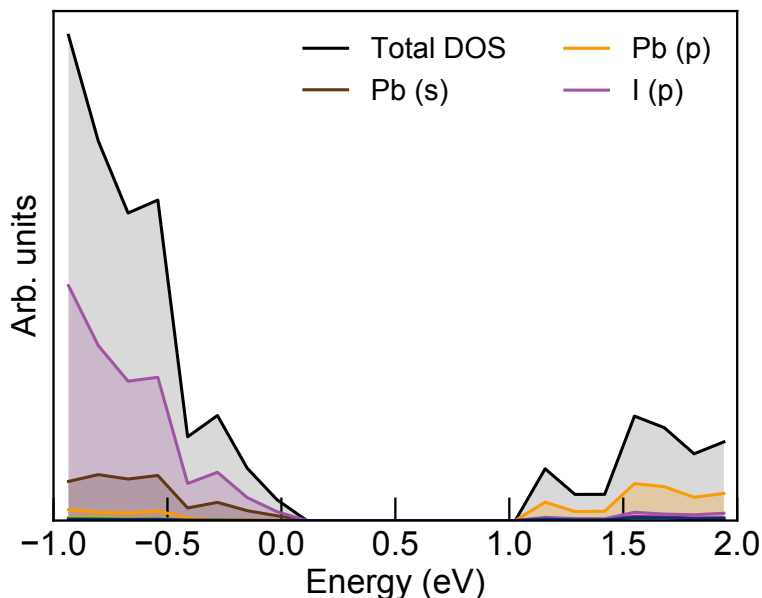


Figure 5.4: Total density of states for CH₃NH₃PbI₃, including projections onto I *p*-orbitals and Pb *p*- and *s*-orbitals. Calculation uses the HSE06 exchange-correlation functional and includes spin-orbit coupling. Calculation parameters are those used for the bandstructure calculation in Section 4.2.

Table 5.2: Pb-I bond lengths in MAPI for the pseudo-cubic and distorted structure. Distortion is along the M-mode with an amplitude of $64 \text{ amu}^{\frac{1}{2}}\text{\AA}$. Two bond lengths are not adjusted as the Pb-I1 and Pb-I4 bonds form an axis of rotation.

	Bond					
	Pb1-I1	Pb1-I2	Pb1-I3	Pb1-I4	Pb1-I5	Pb1-I6
Pseudo-cubic bond length (\text{\AA})	3.215	3.077	3.140	3.174	3.25	3.141
Distorted bond length (\text{\AA})	3.215	3.107	3.185	3.174	3.283	3.143
Difference (\text{\AA})	0	+0.03	+0.045	0	+0.033	+0.002

Table 5.3: Values of the a and b coefficients in the fitted function $E_g = E_0 + aQ^2 + bQ^4 + O(Q^6)$ used to model the bandgap deformation potentials evaluated from frozen-phonon calculations using the PBEsol, PBEsol+SoC and HSE06 exchange-correlation functionals.

Mode		PBEsol	PBEsol+SoC	HSE06
M	a	2.3×10^{-5}	2.3×10^{-5}	2.9×10^{-5}
	b	-3.3×10^{-10}	-3.6×10^{-10}	-5.4×10^{-10}
R	a	2.3×10^{-5}	2.5×10^{-5}	2.9×10^{-5}
	b	-3.0×10^{-10}	-4.3×10^{-10}	-7.0×10^{-10}

Temperature dependant bandgap broadening

The undistorted high-symmetry cubic perovskite structure is a saddle point between two equivalent broken-symmetry solutions (see Figure 2.2). Dynamic disorder is expected as the barriers are 37 meV and 19 meV for the R and M modes respectively, which is comparable to $k_B T$. The Schrödinger equation describing nuclear motion in the double well potential energy surface can be solved following a procedure outlined in Reference [248]. The average bandgap as a function of temperature, $E_g(T)$, can then be calculated from the thermally populated vibrational eigenstates $\chi(Q, T)$ that form a solution to the 1D Schrödinger equation:

$$E_g(T) = \langle \chi(Q, T) | E_g(Q) | \chi(Q, T) \rangle \quad (5.10)$$

Using this procedure, a positive band-gap shift of 35.5 meV (R -mode) and 27.9 meV (M -mode) at $T = 300$ K has been calculated, which is comparable in magnitude to an experimentally measured broadening of 40 meV.¹¹⁵

5.3.2 Hot carrier cooling to equilibrium

In the previous subsection the coupling between the electronic and vibrational sub-systems was considered. This section focuses on the coupling between phonon modes, and how this relates to thermal transport in the material. The source of excess thermal energy is a hot polaronic state that is formed after above bandgap carrier excitation. The formation of a hot polaron is discussed first, followed by results for the cooling time to equilibrium.

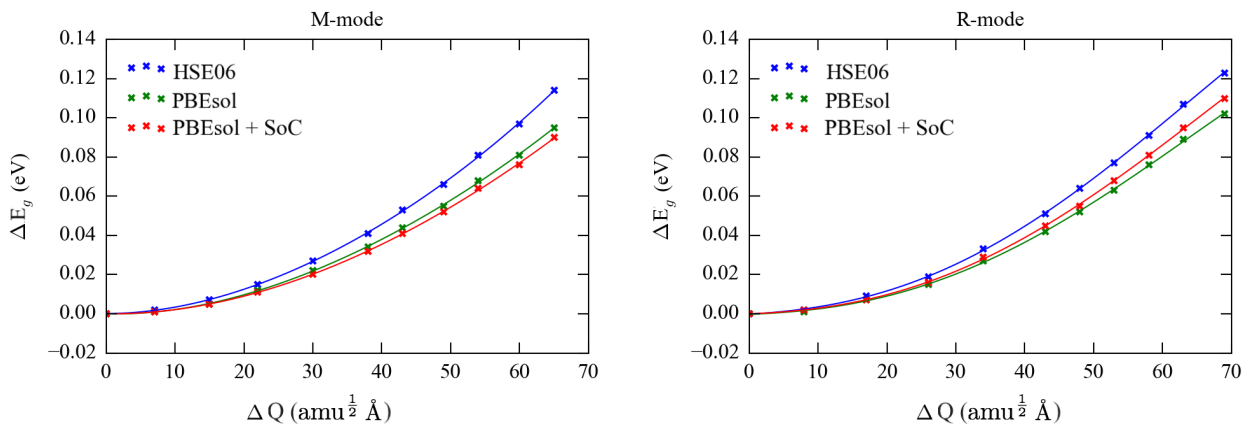


Figure 5.5: Change in bandgap (ΔE_g) as a function of the normal-mode coordinate Q obtained with three exchange-correlation treatments used in the electronic-structure calculations, *viz.* PBEsol, PBEsol with spin-orbit coupling (SoC), and HSE06.

Table 5.4: Valence- and conduction-band deformation potentials relative to the Pb 3d core energy level obtained from frozen-phonon calculations with three exchange-correlation treatments, *viz.* PBEsol, PBEsol with spin-orbit coupling (SoC), and HSE06. We assume that the deformation potential is quadratic and fit a quadratic function $E = bQ^2$ to the band energies given in Figure 5.3; the values in the table correspond to the coefficient b .

Mode		PBEsol	PBEsol+SoC	HSE06
M	VBM	1.61×10^{-5}	1.55×10^{-5}	0.97×10^{-5}
	CBM	3.88×10^{-5}	3.68×10^{-5}	3.66×10^{-5}
	$\frac{CBM}{VBM}$	2.14	2.37	3.77
R	VBM	1.34×10^{-5}	1.01×10^{-5}	1.33×10^{-5}
	CBM	3.52×10^{-5}	3.37×10^{-5}	3.96×10^{-5}
	$\frac{CBM}{VBM}$	2.63	3.34	2.98

Hot polaron formation

The Frölich polaron model has been recently applied to MAPI to calculate a polaron mobility from first principles.²²⁶ When the polaron coupling is weak the kinetic energy is larger than the polaron binding energy, and the polaron radius is larger than a unit cell – a large polaron is formed. When the polaron coupling is strong the electron is self-trapped, and the polaron radius is the size of a unit cell or smaller – a small polaron is formed. The solution to the Frölich model in Reference [226] gives Frölich coupling constants of $\alpha = 2.4$ and $\alpha = 2.7$ for the electron and hole in MAPI, respectively. These values fall in the intermediate coupling regime where the large polaron model is valid, and correspond to a polaron radii of 26.8 Å for the electron and 25.3 Å for the hole, at 300 K. Note that the calculated polaron radii are an upper bound, as bulk polaron states are further localised by disorder, point defects and extended

defects such as surfaces, interfaces and grain boundaries.

In metals and other materials where the electron-phonon coupling is relatively homogeneous across the electron and phonon sub-systems, above-bandgap electrons cool over a single characteristic time scale. The excited electrons lose their energy through phonon emission and the electron and phonon sub-systems are assumed to remain in distinct thermal equilibria, each described by time-dependent temperatures $T_{\text{el}}(t)$ and $T_{\text{ph}}(t)$. This is the two-temperature model.²⁴⁹ For materials where the electron-phonon coupling is heterogeneous, such as polar semiconductors with Frölich interactions, this model is not applicable, as the assumption that the phonon sub-system has reached a thermal equilibrium is not valid. For these materials, the above-bandgap electrons will transfer kinetic energy into the phonon modes which couple strongly to the electron sub-system, and these “hot” phonon modes will thermalise to a temperature above that of the remaining bulk modes. A recent computational study across 12 cubic semiconductors found that in each system studied there are hot phonon modes which equilibrate with the electron sub-system rather than with the phonon sub-system.²⁵⁰ This is in contrast to the two-temperature model where all phonons are in thermal equilibrium.

Transient spectroscopic studies^{193,236,251} suggest that a hot photoexcited state persists in hybrid halide perovskites with a characteristic cooling time of up to 100 ps. We consider the hot photoexcited state to be a Frölich polaron which resonates with a subpopulation of local phonon states; after polaron formation there is initial thermalisation, electron kinetic energy is transferred into the optical phonon modes and a hot polaron is formed. This is a fast picosecond process via the strong Frölich coupling between the charge carrier and localised, polar phonon population. Once fully thermalised, the above bandgap energy is distributed amongst all phonon states associated with the polaron.

The temperature of the resulting polaron depends on the polaron volume, the polaron specific heat capacity C_v and the initial excitation energy (Figure 5.6). We assume that the polaron forms a sphere with a radius determined by the Frölich model (26.8 Å) and that the initial excitation energy is distributed evenly between the electron and hole. The heat capacity is calculated from the bulk phonon calculation. Coupling to the optical cage modes ($\nu < 5 \text{ THz}$ ¹¹⁴) at the gamma point are considered. The average temperature dependent energy $E(T)$ is determined by the phonon energies, $\epsilon_i = \hbar\nu_i$, and occupation numbers, as given by the Bose-Einstein distribution $n_i(T, \epsilon_i)$:

$$E(T) = \sum_i \epsilon_i n_i(T, \epsilon_i) = \sum_i \frac{\epsilon_i}{e^{\frac{\epsilon_i}{k_B T}} - 1}. \quad (5.11)$$

Following this, the specific heat capacity C_v for a given temperature is given by:

$$C_v = \frac{\partial E_T}{\partial T} = k_B \sum_i \left(\frac{\epsilon_i}{k_B T} \right)^2 \frac{e^{\frac{\epsilon_i}{k_B T}}}{\left(e^{\frac{\epsilon_i}{k_B T}} - 1 \right)^2}. \quad (5.12)$$

For MAPI, the per-unit cell specific heat capacity is 1.25 meV K⁻¹ at 300 K. Near-UV excitation at 4 eV gives a maximum energy of 1.2 eV which can be transferred to the polaron, and the temperature increases with localisation ($T \propto r^{-3}$).

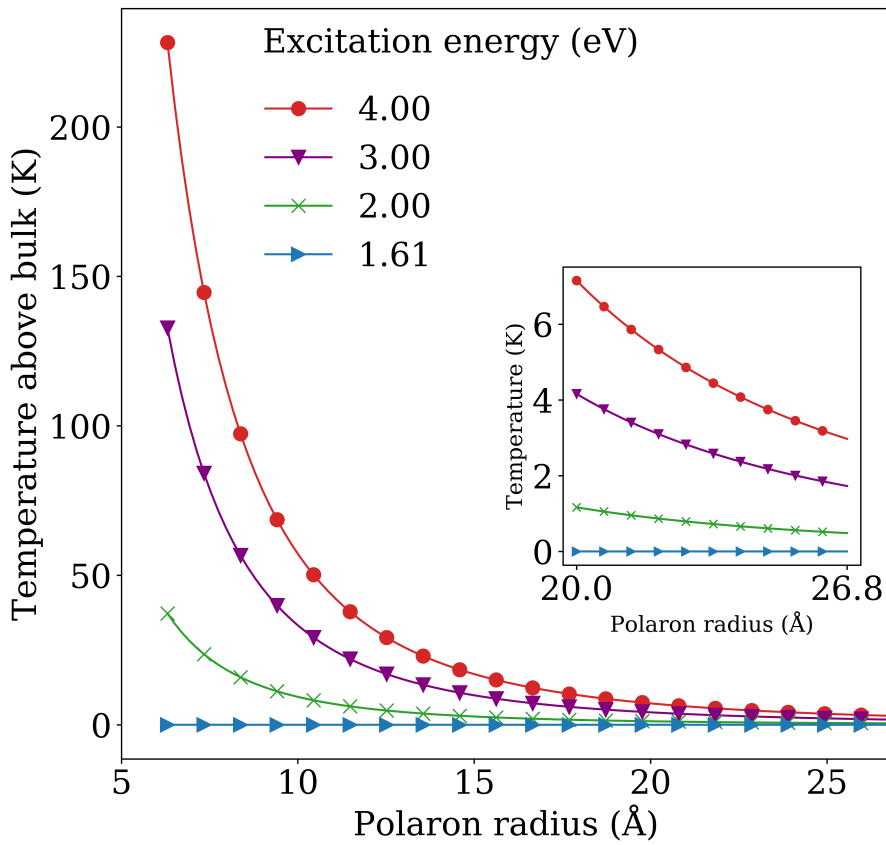


Figure 5.6: Thermalised polaron temperature in MAPI as a function of polaron radius and excitation energy assuming a bulk value of the heat capacity. The calculated bulk electron polaron radius of 26.8 Å provides an upper bound for polaron size. The lattice parameter (6.3 Å) is used as a lower bound – below this the continuum large polaron approach is not valid. Excitation from the bandgap to near-UV are considered. Inset shows detail at larger radii (axes same as main).

Cooling to equilibrium

After a fast initial thermalisation, the polaron will cool to equilibrium over a longer timeframe. During this cooling process the excited local optical phonon modes scatter into phonon modes that diffuse away from the polaron.

Due to energy and momentum conservation rules, three-phonon scattering is the lowest-order scattering process. The three-phonon interaction strengths have been calculated for MAPI,⁸¹ and they are found to be orders of magnitude stronger than for CdTe and GaAs. In addition, there are a large number of energy- and momentum conserving scattering pathways. As a result the bulk thermal conductivity, calculated from a solution of the Boltzmann transport equation in the relaxation time approximation, is extremely low; $0.05 \text{ W m}^{-1} \text{ K}^{-1}$ at 300 K.⁸¹ In contrast, the calculated conductivity for GaAs and CdTe is $38 \text{ W m}^{-1} \text{ K}^{-1}$ and $9 \text{ W m}^{-1} \text{ K}^{-1}$, respectively.

To model the third order phonon-phonon scattering processes we consider the polaron as a hot sphere in a continuum of ambient temperature material, which allows us to calculate temperature as a function of time using the heat diffusion equation. We consider the low fluence

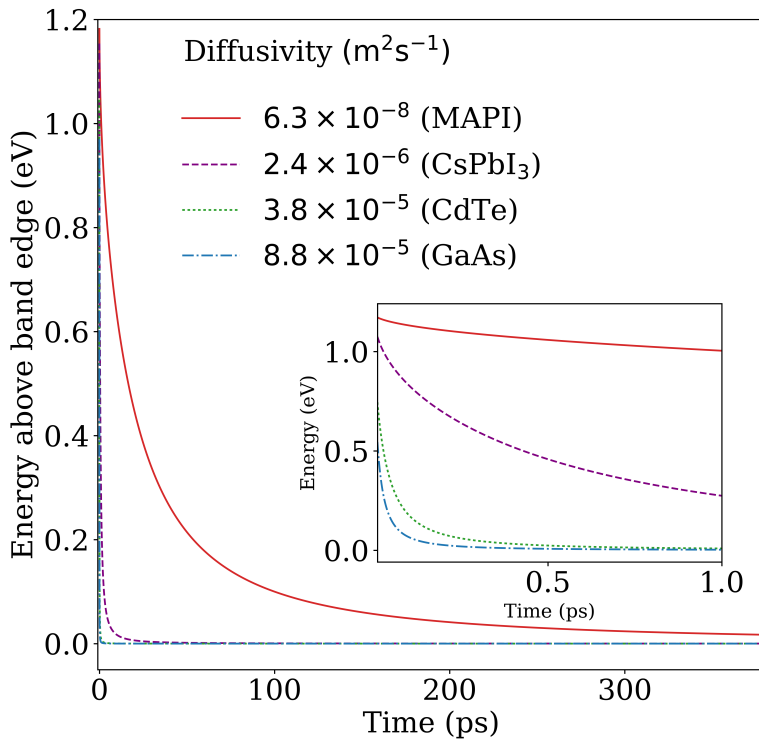


Figure 5.7: The energy of a large polaron state (starting at 1.2 eV above the conduction band minimum, with a polaron radius of 26.8 Å) in CH₃NH₃PbI₃ as a function of time. The slow rate is due to the low thermal conductivity in MAPI ($\kappa = 0.05 \text{ W m}^{-1} \text{ K}^{-1}$). For comparison, we show the behaviour using the thermal conductivities of CdTe ($\kappa = 9$) and GaAs ($\kappa = 38$).

limit where individual photon quanta are absorbed into isolated hot polarons. The rate of cooling is determined by the diffusivity D :

$$D = \frac{\kappa}{\rho C_p}, \quad (5.13)$$

where κ is the thermal conductivity, ρ is the density and C_p is the specific heat capacity.

Heat diffuses from MAPI on the order of 100 ps, whilst for other conductivities the process is much faster, on the order of 100 fs. This is in agreement with reported experimental values from References [251] (MAPI), [252] (CdTe) and [253] (GaAs). Note that at short timescales, measurements of hot carrier cooling in MAPI and CsPbI₃ ($\kappa = 0.5$) may appear linear due to the slower exponential decay.

5.4 Summary

In this chapter we have introduced the phonon quasi-particle into our description of MAPI. The first consequence of this is that the electronic states couple to the normal mode vibrations of the system. I have quantified the extent of this coupling to two highly anharmonic phonon modes at the M and R points in the Brillouin Zone. These modes, which are occupied at room temperature, have a large amplitude of motion and lead to a bandgap broadening comparable

to that found experimentally – i.e. they play a significant role in the overall electron-phonon coupling of the system. The second consequence of including phonons in our model is that temperature variations in the bulk material lead to heat diffusion. I have shown that a classical heat diffusion model, parameterised using Frölich polaron theory and first-principles calculations, can be used to describe the physical process behind the experimentally observed slow hot-carrier cooling rates observed for halide perovskites.

Data Access Statement

The crystal structures and phonon data are available at <https://github.com/WMD-group/Phonons>, and can be processed using the PHONOPY¹⁰⁴ and MODEMAP²⁴¹ packages. For visualising the phonon modes the ASCII PHONONS package can be used.²⁵⁴ The phonon dispersion can be plotted using the SUMO package.²⁴⁴

Data files and Jupyter notebooks outlining the calculation steps for hot carrier cooling are available as a repository on GitHub at <https://github.com/WMD-group/hot-carrier-cooling>.

Acknowledgements

Via our membership of the UK’s HEC Materials Chemistry Consortium, which is funded by EPSRC (EP/L000202), this work used the ARCHER UK National Supercomputing Service (<http://www.archer.ac.uk>). I also made use of the Balena HPC facility at the University of Bath, which is maintained by Bath University Computing Services.

*Energy can neither be created nor destroyed
Matter can neither be created nor destroyed
Every atom in my body goes back to the Big Bang
So rap is no big thang, I was created in the void*

— Grip Grand, *Conservation of Matter*

6

Electron capture at H-centre defects

Excerpts of this chapter are adapted from Whalley, L. D., Crespo-Otero, R. and Walsh, A. (2017). H-Center and V-Center Defects in Hybrid Halide Perovskites. *ACS Energy Letters*, 2(12), pp.2713-2714. © 2017 American Chemical Society

6.1 Introduction

Until this point we have considered a lattice with perfect translational symmetry and no missing or extra atoms. However at finite temperature a crystalline material always contains point defects, as the cost in lattice energy is balanced by the increase in configurational entropy. In this chapter we consider the iodine interstitial defect and predict that it will form a split-interstitial defect with self-trapped hole. The vibrational properties of the defect are studied to i) confirm the validity of the 1D configurational coordinate approach and ii) predict the electron capture coefficient at this defect site.

As outlined briefly in Section 1.2.2 we are often interested in semiconductor defects that form electronic states in the bandgap, as these can provide sites for fast non-radiative transitions such as minority carrier trapping and electron-hole recombination, both of which limit the photovoltaic efficiency of solar cell absorber materials. Such is the impact of these defects that special names have been coined to describe them - Marshall Stoneham uses the term ‘killer centre’¹⁷⁷ whilst William Shockley in his Nobel Lecture uses the term ‘deathnium’.²⁵⁵ Stoneham lists the defect types that may act as killer centres. Two of four in the list relate to the vibrational properties of the defect lattice:

2. Defects with favorable vibrational properties, that is, with large-amplitude modes promoting the transitions, and large-energy modes to take up the electronic energy.
3. Defects with very strong coupling to lattice distortions such as certain dislocations and some vacancy centers.

However historically there has been increased research emphasis on the electronic properties of killer centres, as the calculations required to predict the vibrational properties of imperfect crystals from first principles are more computationally demanding. With recent advances in first principles modelling^{167,256} and the growth in available computing power,²⁵⁷ it is now possible to calculate from first principles the coupling strength between the electronic states of the defect and bulk phonons to predict the rate of carrier capture and recombination for systems of interest. This methodology has been recently applied to CZTS where it has been found that the sulfur vacancy provides a site for fast non-radiative recombination.²⁵⁸

Hybrid halide perovskite materials are often classed in the literature as ‘defect tolerant’ materials with a low concentration of killer defects. This is for two reasons. Firstly, good device performance can be achieved using a low-temperature solution processing method which is expected to form a thin film with a high concentration of defects. Secondly, theoretical calculations show that Schottky and Frenkel point defects form at high concentrations, but that they form electronic states either in the electronic bands or at shallow energies in the bandgap (< kT from the band edge), so are unlikely to contribute to non-radiative recombination.²⁵⁹ Amongst the native non-stoichiometric defects in MAPI the iodine interstitial is predicted to be the only stable and active trap species.²⁶⁰

The halide sub-lattice is also associated with ionic migration, with iodine ions being the dominant mobile species in MAPI.²⁶¹ Experimental evidence points to a coupling between the electronic and ionic states, and various models exist which link trapping at the iodine ion with phase segregation and hysteresis in hybrid halide perovskites.²⁶² This has motivated the recent research interest in the point defect properties of halide perovskites, and in the properties of the iodine interstitial in particular.

Point defects in hybrid halide perovskites are challenging to model from first principles. Due to the organic cation the structure is low symmetry and there are three inequivalent iodine sites. The atomic lattice is soft and distorts easily, often requiring hundreds of ionic steps to achieve force convergence. Previous calculations reported in the literature demonstrate that the defect formation energies are sensitive to the level of theory used; hybrid functionals with spin-orbit coupling predict electrically active trap states that are not found at lower levels of theory. Furthermore, comparison with experimental results remains a challenge. Capacitive techniques including Deep Level Transient Spectroscopy (DLTS) and Thermal Admittance Spectroscopy (TAS) have been used to identify defect concentrations and trap levels in the halide perovskites. Defects have been observed with energies at 0.17 eV and 0.20 eV above the valence band edge using DLTS²⁶³ and at 0.17 eV and 0.35 eV using TAS. However capacitive features associated with the mobile ionic species, rather than electronic defect dynamics, can ‘present spectra with overlapping or even “fake” peaks’.²⁶⁴

Published defect formation energies predict that the neutral iodine interstitial is metastable at all fermi levels across the bandgap.^{109,260} However charge trapping at defect sites can result in

the formation of metastable defects. Meggiolaro et al. outline the expected charge trapping processes at the iodine interstitial using a configuration coordinate diagram.²⁶⁰ The configuration coordinate is a collective phonon mode describing the displacement between charge states and reduces the vibrational problem to one dimension. Their model predicts that electron (hole) trapping at the positive (negative) charge state will result in the formation of a metastable neutral defect, and that radiative electron trapping at the neutral defect will compete with non-radiative electron trapping. However the rate of electron capture is not calculated, and the motion of the defect species is assumed to be harmonic.

In this chapter the non-radiative electron capture rate at the neutral iodine interstitial is calculated based on a multiphonon single-mode carrier capture model. First, the electronic structures of the iodine interstitial in the neutral, negative and positive charge states are calculated. The neutral charge state is predicted to form a split-interstitial defect with self-trapped hole. The hole induces the formation of a bond between two iodine ions, producing an open-shell molecular dimer called a H-centre ($I_i^- + I_I^- + h^+ \rightarrow I_2^-$).²⁶⁵ Upon electron capture at the H-centre the molecular bond is broken and the iodine move apart, accompanied by an extensive re-organisation of the surrounding lattice. To calculate the electron capture coefficient, anharmonic potential energy surfaces for the neutral and negative charge states are combined with an electron-coupling term. To validate the single mode approximation used in this work, the normal phonon modes of the defect supercell are analysed to identify those associated with the electron capture process.

6.2 Methods

6.2.1 Defect formation energy calculations

The atomic and electronic structures of the iodine interstitial were calculated from first-principles within the framework of DFT. The projector-augmented wave (PAW) method¹⁹⁷ was used as implemented in a GPU port of VASP.²³⁹ Projection operators were optimised in real-space within an accuracy of 0.02 meV per atom. The wave functions were expanded in plane waves up to an energy cutoff of 400 eV and a $2 \times 2 \times 2$ gamma centred Monkhorst-Pack mesh was used for the Brillouin zone integration.

The interstitial was placed in a 192-atom supercell built from an expansion of the 12-atom pseudo-cubic unit cell, using the transformation matrix m_t :

$$m_t = \begin{bmatrix} 2 & -2 & 0 \\ 2 & 2 & 0 \\ 0 & 0 & 2 \end{bmatrix}$$

This supercell expansion scales the magnitude of the lattice vectors in the x , y and z directions by a factor of $2\sqrt{2}$, $2\sqrt{2}$ and 2, respectively. This expansion is more isotropic than the 192-atom

supercell built from a diagonal transformation matrix, which would increase errors due to elastic effects. For example, $m_t = \text{diag}(1, 2, 8)$ would increase the elastic error along the x axis, as the local relaxation extends beyond a single unit cell. For the atomic relaxations a spin-polarised calculation with the PBEsol functional was used.²⁴⁰ The internal atomic coordinates were relaxed until the force acting on each atom was less than $0.01 \text{ eV}\text{\AA}^{-1}$.

For the electronic relaxations the hybrid exchange-correlation functional of Heyd-Scuseria-Ernzerhof (HSE06) was used.^{242,243} The amount of exact Hartree-Fock exchange was adjusted to 0.43 to reproduce the correct bandgap and allow comparison with the previous literature.^{109,260} Spin-orbit coupling was included in the calculation. To reduce the computational expense the wavefunctions were first converged using a single point calculation at the gamma point for the Fock exchange, followed by convergence using the full $2 \times 2 \times 2$ Monkhorst-Pack mesh. At each step the total energy was converged to within 10^{-5} eV . The defect formation energies were calculated using the methodology outlined in Sections 3.3.2 and 3.3.3. The image charge-correction and potential alignment developed by Freysoldt, Neugebauer and Van de Walle, and implemented in SXDEFECTALIGN,²⁶⁶ was applied. A further ‘octahedral tilting’ correction was applied to account for the pristine reference structure being a time-averaged equilibrium structure. This correction is discussed further in Section 6.3.3.

6.2.2 Lattice dynamics calculations

The negative interstitial was placed in a $2 \times 2 \times 2$ supercell expansion of the pristine pseudo-cubic lattice. The resulting supercell contains 93 atoms. Atomic relaxations were computed within the Kohn-Sham DFT formalism as implemented in the VASP code²³⁹ and using the PBEsol functional. The wave functions were expanded in plane waves up to an energy cutoff of 700 eV and a $2 \times 2 \times 2$ gamma centred Monkhorst-Pack mesh was used for Brillouin zone integration. Projection operators were optimised in reciprocal space and forces converged to within $0.01 \text{ eV}\text{\AA}^{-1}$ per atom.

Harmonic lattice-dynamics calculations were performed with the PHONOPY package.¹⁰⁴ Displacement steps of 0.01 \AA were used to evaluate the second-order force-constant matrix using the finite-displacement method (582 displacements). Forces were computed using VASP using the PBEsol exchange-correlation functional.²⁴⁰ The valence wavefunctions were expanded in a plane-wave basis set with a 700 eV cut-off. The electronic Brillouin zone was evaluated using a $2 \times 2 \times 2$ gamma centred Monkhorst-Pack mesh and a total-energy convergence criterion of 10^{-8} eV .

6.2.3 Calculation procedure for the carrier capture coefficient

The procedure follows static coupling theory as implemented by Alkauskas et al.²⁵⁶ and recently extended to anharmonic potential energy surfaces by Kim et al. in the CARRIERCAPTURE.JL package.^{267,268} The capture coefficient is derived by considering electron phonon coupling at first order and using a one-dimensional approximation so that the problem reduces to a single phonon mode Q . For electron capture from an initial state i to a final state f , the carrier capture coefficient is given by

$$C_n = V \frac{2\pi}{\hbar} g W_{if}^2 \sum_m \omega_m \sum_n |\langle \chi_{im} | Q - Q_0 | \chi_{fn} \rangle|^2 \times \delta(\Delta E + m\hbar\Omega_i - n\hbar\Omega_f), \quad (6.1)$$

where V is the supercell volume, g is the energetic degeneracy of the final state, W_{if} is the electron-phonon coupling matrix element, ω_m is the thermal occupation of the vibrational state m , $\langle \chi_{im} | Q - Q_0 | \chi_{fn} \rangle$ is the overlap of the vibrational wavefunctions χ and $\delta(\Delta E + m\hbar\Omega_i - n\hbar\Omega_f)$ ensures that there is conservation of energy. In practice the δ term is replaced by a smearing function; for the calculations in this study this is a gaussian function of width 0.01 eV. The total energies and wavefunctions of the iodine interstitial in a neutral and negative charge state, for the equilibrium and distorted geometries, were calculated using the parameters outlined in Section 6.2.1. Total energies were calculated using the HSE06 hybrid exchange-correlation functional with spin-orbit coupling, whilst single particle wavefunctions for the electron-phonon coupling matrix were calculated using the PBEsol functional. We found that the shape of the potential energy surface is largely independent of the level of theory used (see Appendix G for a comparison at different levels of theory). The anharmonic potential energy surface was generated from fitting a spline of order four, as implemented in the DIERCKX.JL package,²⁶⁹ to the DFT total energies. We consider electron capture from the neutral charge state to the negative charge state which has a singly energy-degenerate geometry.

The 1D Schrödinger equation for the potential energy surface was solved using a finite difference method implemented in the BROOGLIE package²⁷⁰ to give the vibrational wavefunctions. Using the one-dimensional approximation discussed above, the electron-phonon coupling can be described with a single matrix element:²⁵⁶

$$W_{if} = \langle \Psi_i | \frac{\partial \hat{H}}{\partial Q} | \Psi_f \rangle, \quad (6.2)$$

where $\Psi_{\{i,f\}}$ are many-electron wavefunctions and \hat{H} is the many-body Hamiltonian of the system. We assume that the many-body Hamiltonian and many-electron wavefunctions can be replaced by their single particle counterparts, so that the electron-phonon coupling matrix element is given by:²⁵⁶

$$W_{if} = (\epsilon_f - \epsilon_i) \langle \psi_i | \frac{\partial \psi_f}{\partial Q} \rangle, \quad (6.3)$$

where the single particle wavefunction of the initial (final) charge state is given by ψ_i (ψ_f) and has an eigenstate energy of ϵ_i (ϵ_f). The PAWPYSEED package²⁷¹ was used to derive the orthogonal wavefunctions from the pseudo wavefunctions and perform the overlap integrals in real space. Further details of the methodology can be found in the literature.²⁵⁶

6.2.4 Calculation procedure for the optically excited states

The optically excited states of the I_2^- defect centres were calculated by Rachel Crespo Otero using the polarizable continuum (“molecule in a crystal”) model. The I_2^- molecule was embedded in a dielectric medium. Chloroform was considered as it has a dielectric constant of 4.8 which is close to the high-frequency dielectric constant of iodine ($\epsilon^\infty = 5.0$).²⁷² To calculate the optical excitation energies linear-response time-dependent DFT was used as implemented in the Dalton2016 program.²⁷³ The PBE0 functional was used to describe exchange-correlation and relativistic effects were included using the spin-orbit coupling mean-field approach in combination with the Douglas-Kroll method.²⁷⁴ The all-electron basis set ANO-RCC, optimised for relativistic effects, was used for all atoms.

6.3 Results

6.3.1 I_i defect geometry

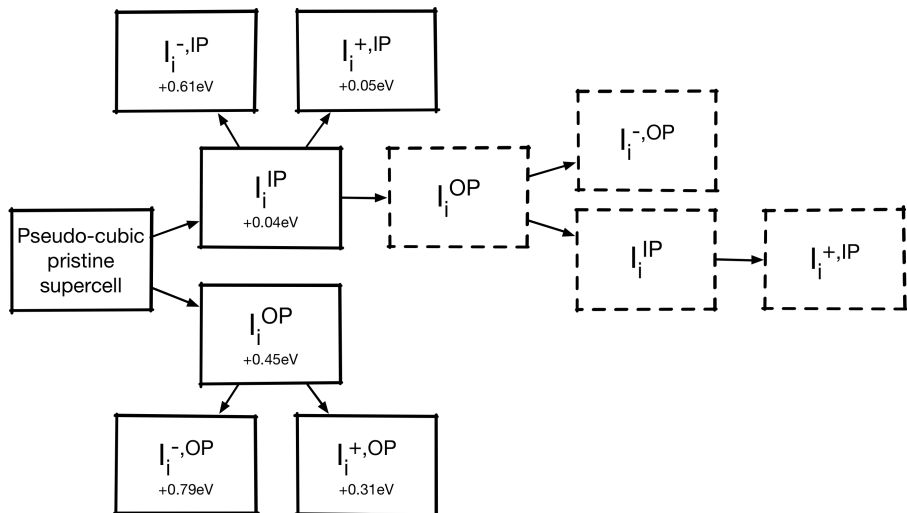


Figure 6.1: Atomic relaxation procedure for point defects in hybrid halide perovskites in the pseudo-cubic phase. IP indicates that the defect is lying in the ab -plane, and OP indicates that the defect is lying along the c -axis. The lowest energy structures are in a dash-line box. The hybrid halide perovskite structure has a number of local minima and multiple relaxations were required to break symmetry and reach a global minimum. For the higher energy defect structures the energy above the global minimum for that charge state is given.

In this section the defect geometries of the neutral, negative and positive charge states of the iodine interstitial are given. So that no preference was given to a particular combination of octahedral tilts the starting point for atomic relaxation was MAPI in the pseudo-cubic phase. Upon adding an iodine interstitial the structure was found to have a number of local minima and multiple relaxations between charge states were required to reach a global minimum. To calculate the collective atomic displacement (ΔQ) between charge states accurately the starting

point for relaxation of the charged states must be the neutral charge state geometry. The atomic relaxation procedure is outlined in Figure 6.2.

The neutral iodine interstitial I_i relaxes to two defect geometries which differ by only 0.04 eV in energy. The lowest energy structure contains a I_2^- split interstitial that lies out-of-plane (along the c -axis) with bond length 3.19 Å. This defect is denoted I_i^{OP} . The higher energy structure contains a I_2^- split interstitial that lies in the ab -plane with bond length 3.24 Å. This is denoted I_i^{IP} . The negative iodine interstitial I_i^- relaxes to an out-of-plane position along the c -axis. I_i^- forms a split interstitial around a lattice iodine site with two independently coordinated iodine ions symmetrically bridging two lead atoms. The I–I distance is 3.82 Å. As I_i^- lies out-of-plane, we expect potential charge trapping processes to occur between I_i^- and I_i^{OP} . The positive interstitial forms an in-plane trimer structure with bond lengths 2.90 Å and 2.96 Å. As I_i^+ lies in-plane, we expect potential charge trapping processes to occur between I_i^+ and I_i^{IP} . Table 6.1 contains a summary of the defect geometries and a comparison to values in the literature.

This work		Meggiolaro et al., Ref. [260]		Du, Ref. [109]
orientation	I–I bond length	orientation	I–I bond length	orientation
I_i^-	out-of-plane	3.82	out-of-plane	3.89
I_i^+	in-plane	2.90/2.96	in-plane	2.95 average
I_i^{OP}	out-of-plane	3.19	out-of-plane	3.24
I_i^{IP}	in-plane	3.24	in-plane	3.88

Table 6.1: Defect orientation and bond length of I_i^+, I_i^-, I_i^{IP} and I_i^{OP} in MAPI, with a comparison to computational results in the literature. The bond lengths are given in Å.

Iodine ions are well known to form polyiodide chains with bond lengths that are sensitive to the charge on each iodine. The I–I bond length in solid orthorhombic crystalline iodine is 2.67 Å, which lengthens to 3.23 Å upon formation of I_2^- .²⁷⁵ The bond lengths reported in this work are within 0.05 Å of this value. The asymmetric bonding of the trimer structure is a typical feature of the tri-iodide group I_3^- . For example the tri-iodide group in CsI_3 has interbond distances of 2.82 Å and 3.10 Å, with the longer bond possessing the majority of the additional charge.²⁷⁶

6.3.2 Charge localisation at the H-centre

The neutral iodine interstitial forms a spin-radical with a self-trapped hole, as demonstrated in the spin-density plot, Figure 6.3b. The hole induces the formation of a bond between two iodine ions, producing a molecular dimer called a H-centre (Figure 6.3a). The formation of a H-centre is a well-established process, and has been studied in metal halide crystals since the 1950s.²⁶⁵ In Figure 6.3b we see that there is some charge delocalisation across the outer halogens, as has been found for H-centres in the alkali halides.²⁷⁷ Whereas in the previous chapter we considered a large polaron, in this chapter we are studying a small polaron formed by the self trapped hole.

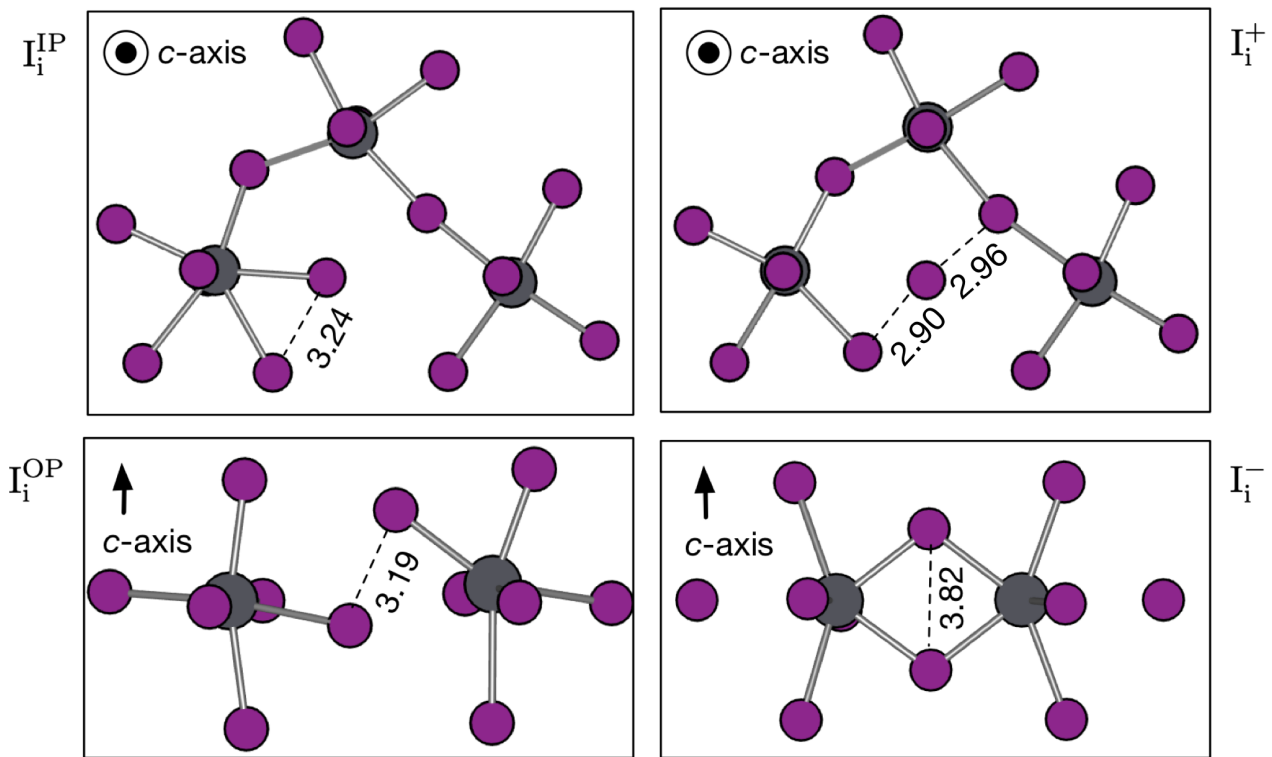


Figure 6.2: Defect geometries of I_i^+ , I_i^- , I_i^{IP} and I_i^{OP} in MAPI. IP indicates that the defect is lying in the ab -plane. OP indicates that the defect is lying along the c -axis. All distances are measured in Å.

The H-centre is a ‘molecule-in-a-crystal’ defect where the host weakly perturbs the I_2^- molecular ion. This allows us to consider the optically excited states using a dielectric embedding approach. A collaborator, Rachel Crespo-Otero, has computed the optically excited states of the H-centre defect as a function of bond lengths using time-dependent DFT including relativistic effects (Figure 6.3c).¹²³ For a bond length of 3.28 Å, the three lowest excited states occur at 1.26 eV (symmetry-allowed), 1.90 eV (forbidden), and 3.70 eV (symmetry-allowed). Two optically allowed transitions fall in the visible-ultraviolet range, and a sub-band gap absorption band at ca. 1.3 eV should be observable in long-wavelength absorption measurements if present in sufficient concentration.

6.3.3 I_i defect formation energies

The formation energy of a defect in charge state q is given by

$$E_f(q) = E_d(q) - E_b - \sum_i \mu_i n_i + q(\epsilon_{VBM} + E_F) + E_{\text{corr}}. \quad (6.4)$$

The total energy of the supercell $E_d(q)$, the total energy of the pristine lattice E_b and the iodine chemical potential μ_i were calculated using DFT, as outlined in the methods section. The defect correction E_{corr} consists of two terms – the image charge correction for charged defects and a tilting correction that is specific to pseudo-cubic perovskites. The static dielectric constant of MAPI is large ($\epsilon_0 = 22.67$)⁸⁴ and so the lattice can effectively screen charged defects, in addition

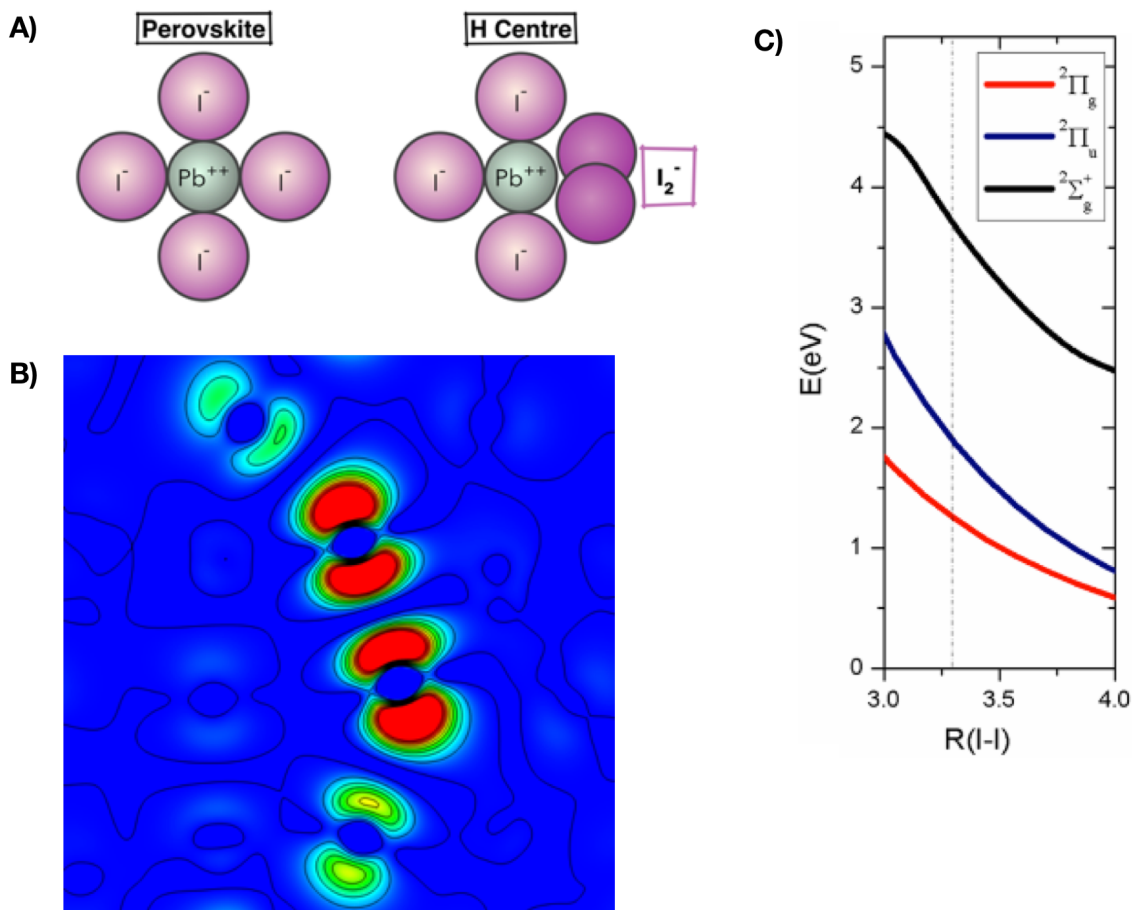


Figure 6.3: A) Change in local equatorial environment around Pb in a lead halide perovskite upon formation of a H-centre defect. The H-centre is formed from a lattice iodide and interstitial iodide. The I–I interatomic spacing of ca. 4.5 Å in the perfect lattice decreases to a bond length of 3.2 Å upon dimer formation. Figure adapted with permission from an original prepared by Aron Walsh. B) The difference between the density of the two spin channels in a spin-polarised calculation is plotted to show spin localisation around the H-centre defect in MAPI. C) Optical excitation energies as a function of dimer bond length for the iodine dimer in MAPI. The bond length is given in Å.

the point defects in this study have a maximum charge of one and the supercell is relatively large (193 atoms). These factors lead to a small image charge correction of -0.057 eV .

supercell expansion	# atoms	tilting correction (meV)
$2 \times 2 \times 2$	96	37 (calculated)
$2\sqrt{2} \times 2\sqrt{2} \times 2$	192	74 (predicted)
$4 \times 4 \times 4$	768	270 (calculated)

Table 6.2: Tilting corrections for supercell expansions of the pseudo-cubic perovskite lattice. The 768-atom supercell is eight times larger than the 96-atom supercell, so we expect the tilting correction to be eight times larger. It is calculated to be 7.5 times larger. The tilting correction for the 192-atom expansion, which cannot be calculated directly, is twice as large as the correction for the 96-atom supercell.

The tilting correction is a new correction introduced in this work and is particular to the

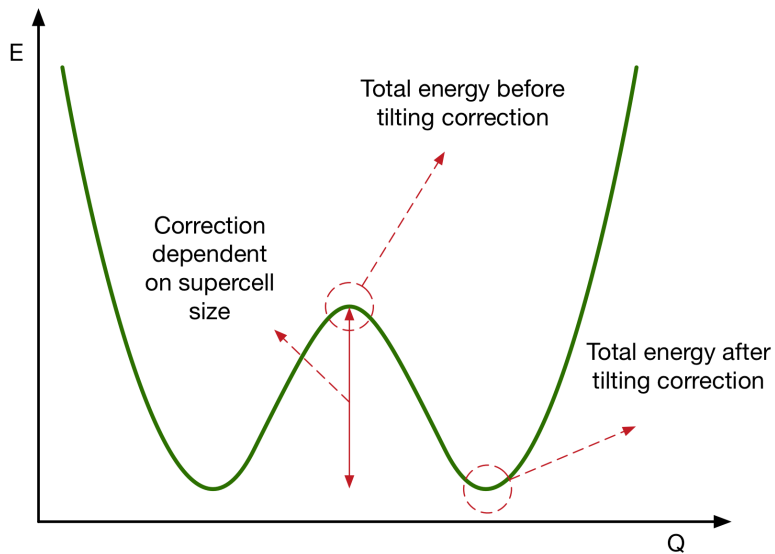


Figure 6.4: A schematic of the tilting correction. The green line is a double well potential energy surface that is typical of pseudo-cubic perovskite structures. The tilting correction is only needed when using a high-symmetry pseudo-cubic perovskite phase to calculate the pristine bulk energy.

pseudo-cubic perovskites. All of the defect formation energies are referenced to the minimum energy of the pristine lattice. However the geometry of the pristine lattice in the pseudo-cubic phase corresponds to a time average and is not the minimum energy structure (Figure 6.4). To calculate the minimum energy of the lattice the pseudo-cubic structure can be distorted along the soft mode at the R -point in q -space. This ‘modemapping’ procedure²⁴⁸ is not compatible with the supercell expansion used for the 197-atom supercell, but the correction energy can be inferred from modemapping other supercell expansions (Table 6.2).

The calculated charge transition levels are given in Figure 6.5. As is found in the previous literature^{109,260} there is negative-U behaviour, where the $(+/0)$ transition level is higher in energy than the $(0/-)$ transition. This indicates that upon electron trapping there is a strong structural relaxation around the defect. The neutral charge state in both orientations is thermodynamically unstable across the Fermi energy range and is formed after photo-excitation. As in Reference [260] the out-of-plane neutral charge state is lower in energy than the in-plane neutral charge state.

There is one active charge trapping level in the bandgap, corresponding to electron trapping at I_i^+ . The $(+/-)$ level corresponds to a two-electron transition and we assume that the cross section for this process is negligible. Our finding that there is a single active trap level disagrees with previous reports that find there are two active charge trapping levels in the bandgap –

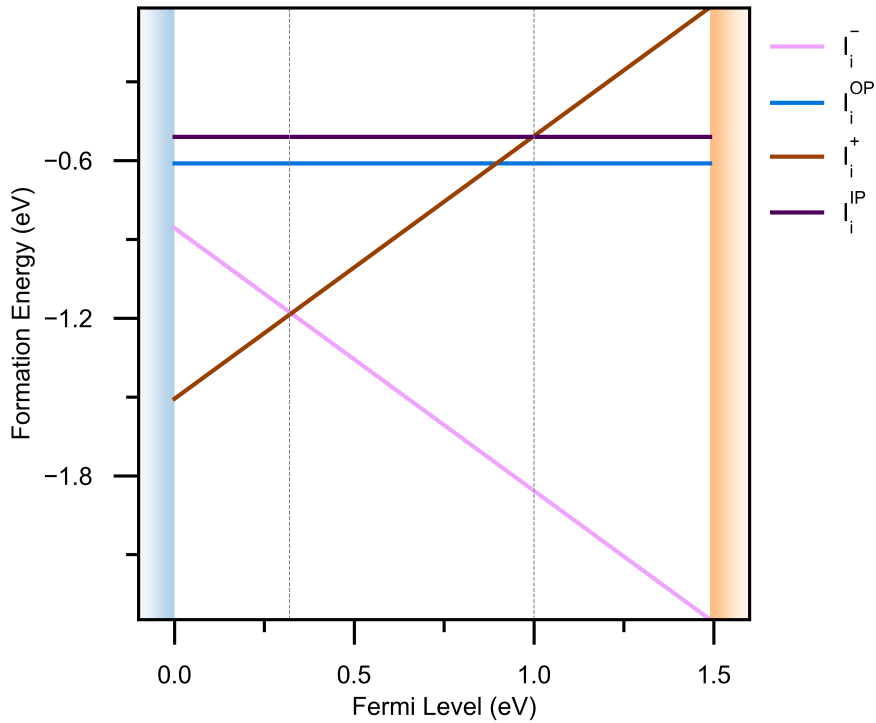


Figure 6.5: Charge transition levels of the iodine interstitial defect in MAPI, calculated using the hybrid HSE06 functional with spin-orbit coupling. IP indicates that the defect is lying in the *ab*-plane and OP indicates that the defect is lying along the *c*-axis.

electron trapping at I_i^+ and hole trapping at I_i^- . The charge transition levels generated using the intermediate higher energy structures (Figure 6.2) reproduce the results in the literature. This highlights how sensitive the defect energetics are to defect geometry. The charge transition levels of the intermediate higher-energy defect structures are given in Appendix F.

The final thing to note is that the defect formation energies are negative across the Fermi level range. This is unphysical, as for a thermodynamically stable material it costs lattice energy to create a point defect. The problem arises from the simple approximation used for the chemical potential of iodine, which considers bulk iodine only and no other competing phases such as PbI_2 . As a result, the chemical potential used in this defect calculation provides an upper bound. Consideration of other secondary phases would produce a lower chemical potential and increase the defect formation energy for all charge states.

6.3.4 Configuration coordinate diagram for electron capture

Charge trapping between the neutral and negative charge states of the iodine interstitial can be described using a configuration coordinate diagram (Figure 6.6), which gives the total system

energy as a function of a single vibrational mode Q .¹⁶⁷ The model assumes that the electronic states of the defect interact with only one phonon mode of the lattice, and that the minimum of each curve corresponds to the equilibrium position of the ions and the electronic ground state. To model electron trapping at the neutral charge state, the excited state of the system corresponds to the neutral defect with a photo-generated electron in the conduction band and hole in the valence band, and the ground state corresponds to the negatively charged defect with a hole in the valence band. Hole trapping at the negative charge state is not possible due to the large energetic barrier of ca. 1 eV.

In this work this the configuration coordinate Q is defined as $\sqrt{\sum_i m_i \Delta r_i^2}$, where the sum is over all inorganic atoms i with mass m_i and a displacement from equilibrium of Δr_i . Summing over all atoms, including those in the organic methylammonium molecule, leads to unphysical energies as the linear interpolation does not capture the rotation of the organic cation between charge states. The potential energy surface generated using a summation over all atomic displacements is given in Appendix G.

Lattice relaxation after electron capture leads to a large shift in the equilibrium position ($\Delta Q = 36 \text{ amu}^{1/2} \text{\AA}$). This is double that found for non-radiative recombination centres in CZTS²⁵⁸ and reflects the strong coupling between the electronic charge state of the defect and the lattice distortion. Another parameter used as a proxy for electron-phonon coupling strength is the Huang-Rhys factor S which quantifies the number of phonons emitted during an optical transition. For a harmonic potential energy surface the Huang-Rhys factor is given by

$$S = \frac{E}{\hbar\omega}. \quad (6.5)$$

The Huang-Rhys factor for lattice relaxation after electron capture at the neutral interstitial is 361.7. This is in the strong coupling limit where $S \gg 1$. The large lattice distortion and Huang-Rhys factor suggests that there will be fast non-radiative transitions at the defect site.^{177,278}

The configuration coordinate diagram for this charge capture process has been previously reported by Meggiolaro et al.,²⁶⁰ where it was found that electron trapping at the neutral iodine interstitial proceeds with a small geometrical rearrangement. However the structural parameter used was the root mean square displacement (RMSD) of the two bonding iodine ions, which excludes the large relaxation of the surrounding perovskite structure. The same RMSD definition applied to the defect geometries in this work gives a lattice distortion of 0.073 Å, which appears close to that given in Figure 2 of Reference [260]. By considering only the distortions of the bonding iodine, Meggiolaro et al. infer that the rate of radiative recombination will compete with non-radiative recombination. Figure 6.6 of this work demonstrates that this is not the case and that the significant structural re-organisation of the surrounding lattice will prevent radiative electron capture at the H-centre.

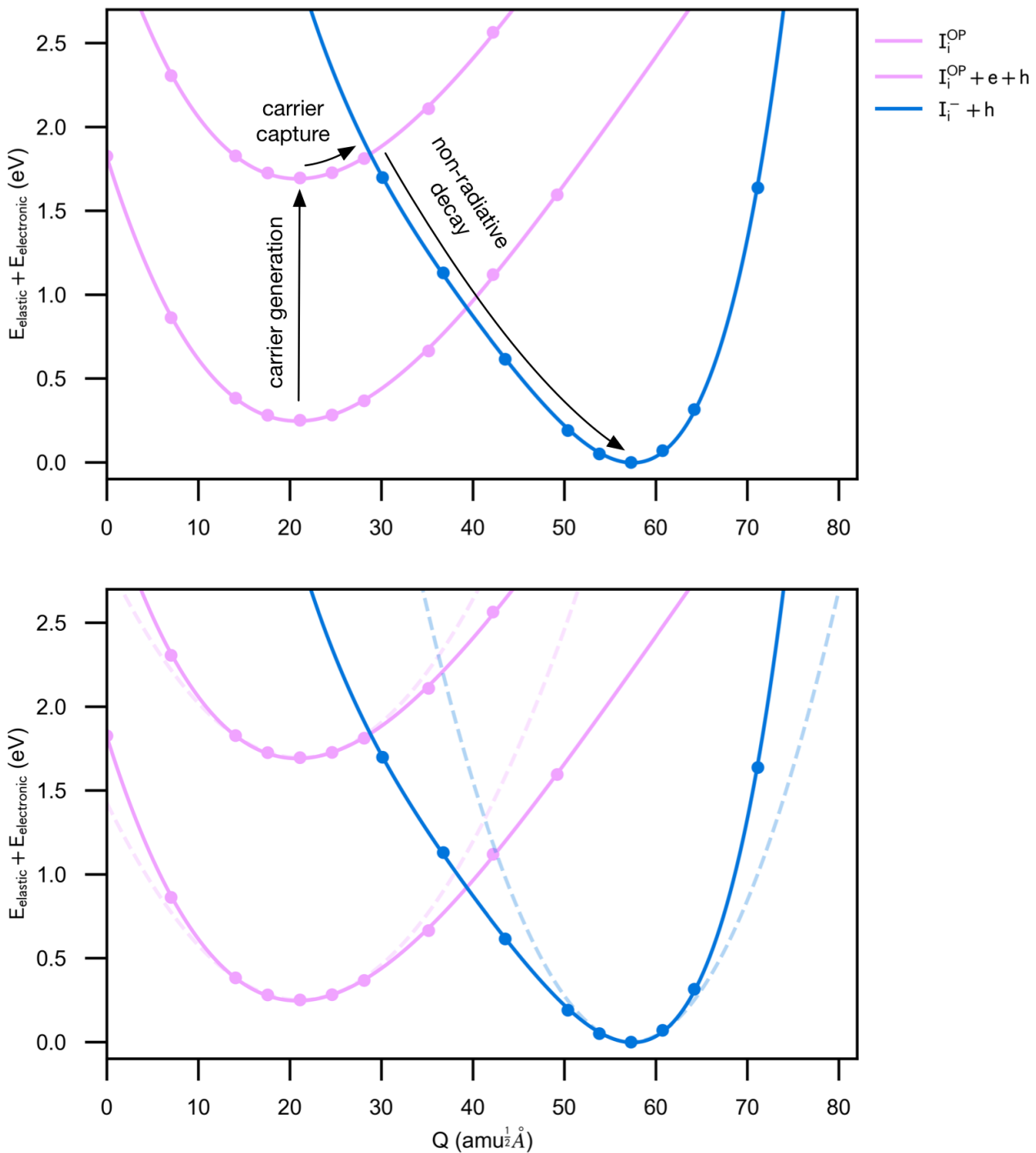


Figure 6.6: (Top) To model electron trapping at the neutral charge state of the iodine interstitial, the excited state of the system corresponds to the neutral defect with a photo-generated electron in the conduction band and hole in the valence band, and the ground state corresponds to the negatively charged defect with a hole in the valence band. The configuration coordinate diagram describes carrier capture between the negative and neutral charge states. The potential energy surfaces are calculated using the hybrid HSE06 functional with spin-orbit coupling. (Bottom) A comparison between the anharmonic and harmonic potential energy surfaces.

The lower part of Figure 6.6 compares the anharmonic potential energy surface (PES) to the harmonic PES. We see that the harmonic PES fits well to the DFT energies either side of the equilibrium structure, as we would expect. The potential energy surfaces of the neutral and negative charge states are extremely soft; for the neutral charge state $\hbar\omega = 4.7 \text{ meV}$ (1.14 THz) and for the negative charge state $\hbar\omega_0 = 6.6 \text{ meV}$ (1.59 THz). Phonon modes at this energy will lie in the optical band of the MAPI lattice modes and will be occupied at room temperature.

Figure 6.6 highlights the importance of using anharmonic potential energy surfaces to describe charge capture at the iodine interstitial in MAPI. The harmonic potential energy surfaces for the excited and ground state intercept at an energy ca. 0.5 eV above the excited state equilibrium energy, and this leads to a carrier capture coefficient eight orders of magnitude smaller than that calculated for the anharmonic surfaces (values for the coefficient are given in Section 6.3.6).

6.3.5 Vibrational properties of the negative charge state

In the previous section the coupling of the iodine interstitial to a single vibrational mode was considered without reference to the normal phonon modes of the crystal. In this section the harmonic phonon modes of MAPI:I_i⁻ are calculated and analysed. The normal phonon modes of a crystal containing a defect can be divided into three kinds: lattice modes (optic and acoustic branches), resonant modes, and local modes (Figure 6.7).¹⁷⁷ The lattice modes are largely unaffected by the defect and are well approximated by the the normal modes of the pristine crystal. They have the same amplitude throughout the crystal, except near the defect where there may be some slight modification. Resonant modes have frequencies that lie within the continuum of lattice modes. Atomic motion is strongly enhanced near the defect and diminishes away from the defect. Finally, local modes have frequencies that lie outside those of the pristine lattice modes. Here the motion is local and dies away to zero far from the defect.

The phonon dispersion for MAPI:I_i⁻ is given in Figure 6.8b, with the phonon dispersion for the pristine MAPI crystal in Figure 6.8a for comparison. The group velocity of a phonon mode is given by $\frac{\partial\omega_k}{\partial k}$. It follows that flat bands are associated with localised phonon modes that do not propagate through the crystal. When an iodine interstitial is introduced the translational symmetry of the crystal is broken and the energetically degenerate modes of the pristine crystal become non-degenerate and increasingly localised.

The complexity of the phonon bandstructure makes it difficult to draw conclusions from a visual inspection of the dispersion. To identify which modes are associated with the iodine interstitial defect we use the Inverse Participation Ratio (IPR) to quantify the localisation of each phonon mode. The IPR is calculated from the harmonic phonon eigenvectors e_i of the system and is given by

$$\text{IPR} = \frac{\left(\sum_{i=1}^N |e_i|\right)^2}{\sum_{i=1}^N (|e_i|)^2}, \quad (6.6)$$

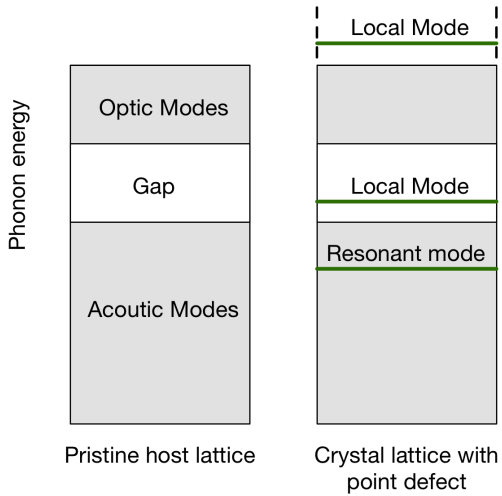


Figure 6.7: Classification of normal phonon modes found in a crystal with a defect. The lattice modes are largely unaffected by the defect and are well approximated by the normal modes of the pristine crystal. The resonant modes have frequencies that lie within the continuum of lattice modes and local modes have frequencies that lie outside those of the pristine lattice modes. The schematic is inspired by Figure 2.3 in Reference [177].

where N is the number of phonon modes. This provides a measure of how many atoms the phonon is distributed over. For example, for a chain of four atoms, a delocalised acoustic mode will have an $\text{IPR} = 4$. At the other extreme, a phonon mode whose polarisation displaces only one atom will have an $\text{IPR} = 1$. The IPR of the gamma point phonon modes for the pristine crystal and MAPI: I_i^- are given in Figure 6.8c. To allow for comparison, the IPR of the pristine lattice has been renormalised to give a maximum value of 97 for the fully delocalised modes. We find that the acoustic modes in the pristine and defect lattices have an IPR of 97, so that they are completely delocalised across all atoms, as is expected. Figure 6.8c supports the conclusions drawn from the phonon dispersion; after introduction of an iodine interstitial each phonon mode of the pristine lattice splits into multiple non-degenerate phonon modes of increased localisation. Figure 6.8d splits the contribution to the phonon mode energy by element type. Lower energy phonon modes up to 10 THz include contributions from the I and Pb species, whilst the higher energy modes describe vibrations of the light atomic species associated with the methylammonium molecule.

The phonon mode energy can also be analysed by individual atomic contributions to find that with the largest contribution from the two iodine interstitials associated with I_2^- bonding. This is a localised mode with an $\text{IPR} = 21.4$ and a frequency of 1.59 THz. An animation of the phonon mode, generated using the ascii-phonons package,²⁵⁴ is available at https://bit.ly/MAPI_phonon. The resonant mode frequency is equal to the frequency of the I_i^- harmonic potential energy surface calculated in Section 6.3.4. This is evidence that the single configuration coordinate Q provides a good approximation to the accepting modes (modes that take up the electronic energy) of the charge transition. As discussed by Alkauskas et al.,²⁵⁶

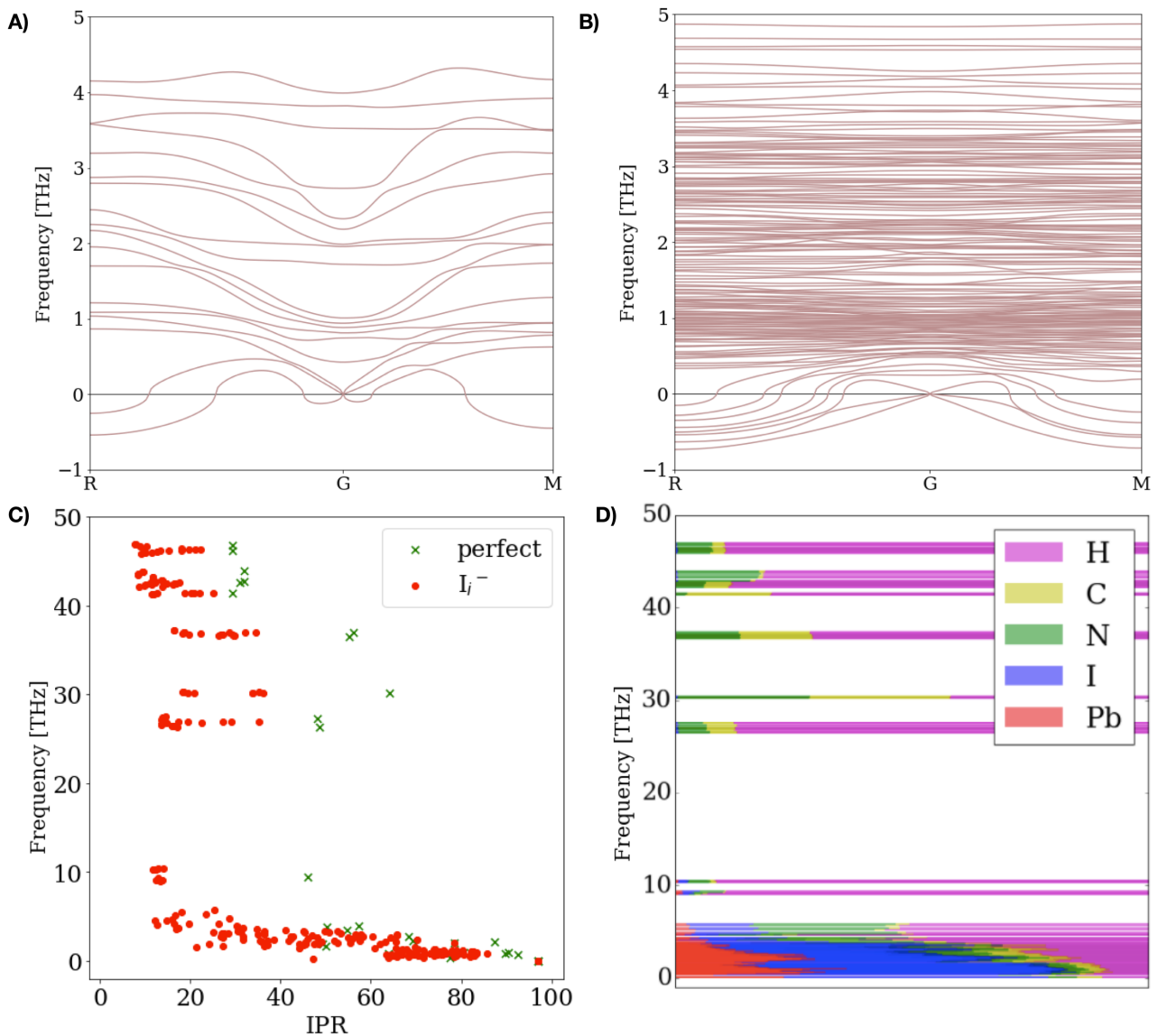


Figure 6.8: A) Harmonic phonon dispersion of the pristine lattice. The imaginary modes near the gamma point are the result of numerical noise, and the imaginary modes at R and M correspond to tilting of the inorganic octahedra. B) Harmonic phonon dispersion of MAPI: I_i^- . C) The Inverse Participation Ratio of a MAPI: I_i^- . D) Contribution to phonon mode energy by atomic species.

it may be surprising that a one-dimensional approximation to a multi-dimensional problem is sufficient, but this is often the case for defects with strong electron-phonon coupling, such as the iodine interstitial in MAPI.

6.3.6 Electron capture coefficient

In Section 6.3.4 we used the lattice relaxation ΔQ and Huang-Rhys factor S as proxies for the electron-phonon coupling term. In this section we calculate the electron-phonon coupling term (Equation 6.3) from first principles, and use this to predict the coefficient for electron capture at the H-centre. The electron capture coefficient C_n determines the rate of electron capture R_n

via the following equation

$$R_n = C_n N_t n \quad (6.7)$$

where N_t is the density of neutral defect traps and n is the electron density.

During electron capture, a delocalised electron in the conduction band is captured to a localised defect state, so it is important that there is a single particle level in the bulk band gap for the geometry Q_0 in Equation 6.3.²⁵⁶ There is an empty electronic defect state in the band gap at the equilibrium geometry for the neutral charge state (Figure 6.9) and so this is chosen as Q_0 . In Figure 6.9 we also see that as the lattice geometry is distorted towards that of the negative charge state the empty defect state decreases in energy until it is in the valence band. The inner product of the wavefunctions at the conduction band minimum ϕ_i and unoccupied defect level ϕ_f are calculated at various Q -values and substituted into Equation 6.1 to give a value of $0.0036 \text{ eV amu}^{-1/2} \text{\AA}^{-1}$ for the electron-phonon coupling matrix element. It is possible to estimate the electron-phonon coupling term using an estimate for the degree of localisation of ϕ_i and ϕ_f . For strong electron phonon coupling W_{if} corresponds to²⁵⁶

$$W_{if} \approx \frac{\Delta E}{\Delta Q} \sqrt{\frac{M_d}{M_b}}, \quad (6.8)$$

where M_b is the number of atoms in the supercell and M_d is the number of atoms the defect state is localised around. For our system $W_{if} \approx 0.0048$ and so electron-phonon coupling for the single mode Q is strong.

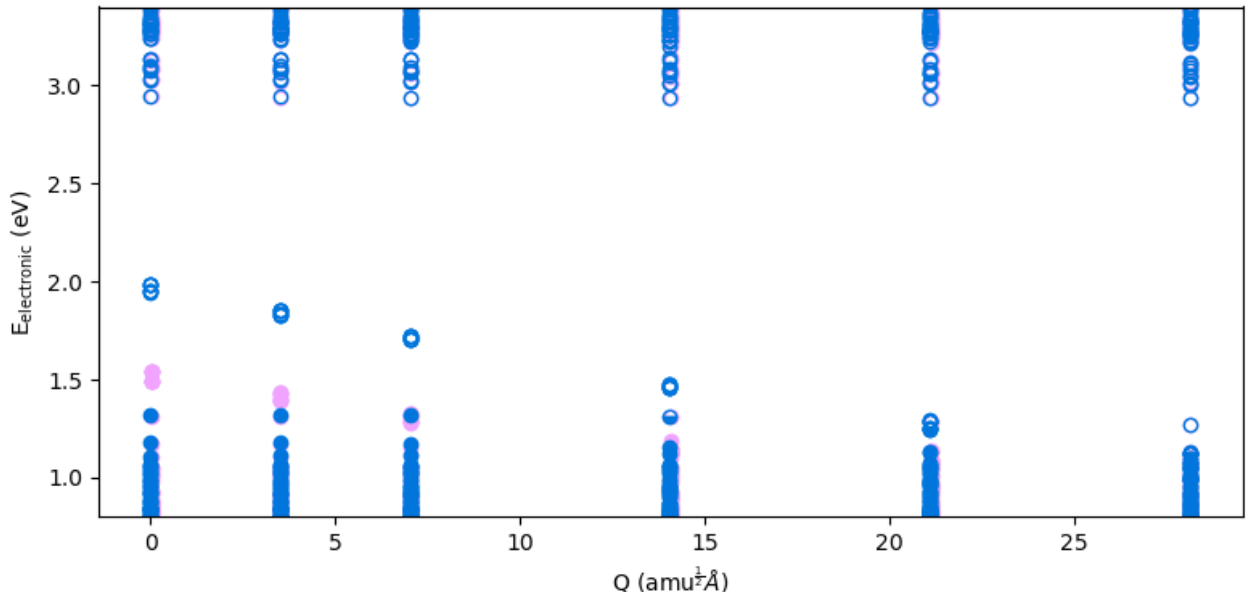


Figure 6.9: Evolution of H-centre Kohn-Sham eigenstates as the lattice geometry is deformed along coordinate Q . Solid and empty circles represent occupied and unoccupied states, respectively.

Combining the electron-phonon coupling term with the anharmonic vibrational wavefunctions, as in Equation 6.1, gives a carrier capture coefficient of $1.2 \times 10^{-10} \text{ cm}^3 \text{s}^{-1}$ at room temperature.

Radiative carrier capture can compete with non-radiative carrier capture at the defect, for semiconductors fast radiative capture coefficients are of the order $10^{-13} \text{ cm}^3 \text{s}^{-1}$.²⁵⁶ For the H-centre in MAPI, the large lattice distortion associated with charge capture suppresses radiative recombination, and as a result non-radiative transitions will be the dominant recombination process.

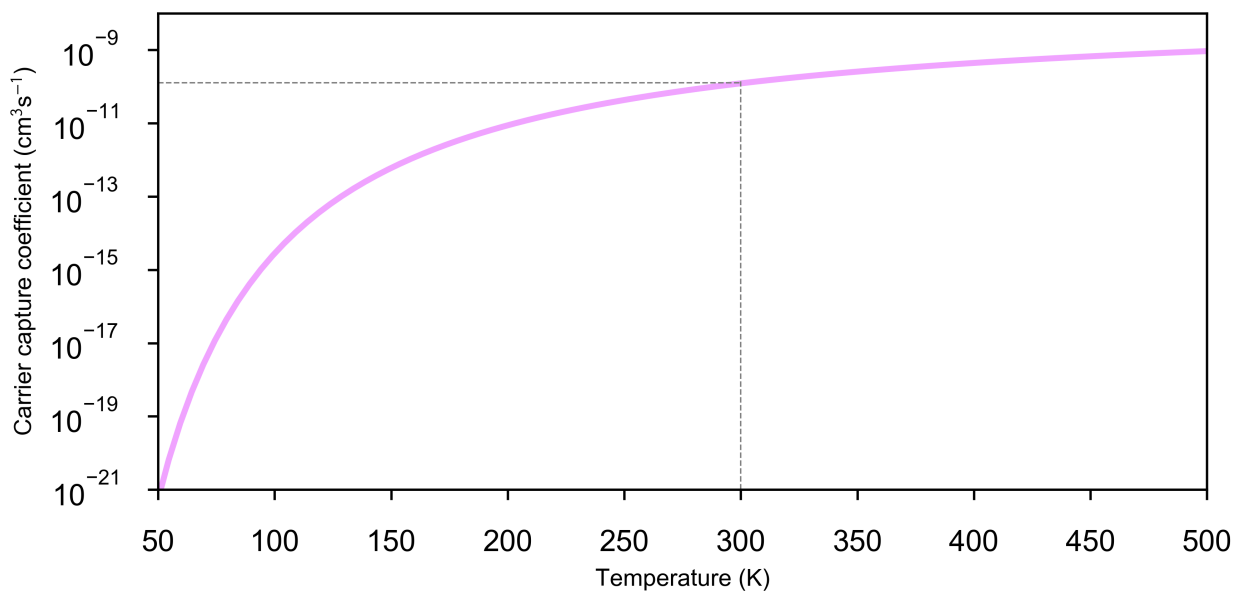


Figure 6.10: Electron capture coefficient of the H-centre defect in MAPI. This determines the rate of carrier capture via Equation 6.7 in the main text.

Summary

The main conclusion of this study is that electron capture at a H-centre is fast, and that this process is a ‘one way street’: due to a strong relaxation of the surrounding lattice, once a negative defect is formed it is both thermodynamically stable and stable under light irradiation. The H-centre is metastable and will be formed only after photo-excitation. We have shown that it cannot be formed from hole capture at the H-centre in the negative charge state, but the existing literature predicts that electron capture at the positive charge state is possible.²⁶⁰ Further calculations are needed to confirm that this electron capture process is possible, and future work could apply the methodology outlined here to this process.

Our results are consistent with the p-type doping observed in MAPI, which could be attributed to negatively charged interstitials,²⁷⁹ and the photo-induced ‘brightening’ of perovskite photoluminescence that is attributed to a reduction in trap state density.²⁶² However we must be very careful in extrapolating to results beyond the bounds of this study, as the model is limited in scope and hybrid halide perovskites are complex materials. For example, it could be that there are other charge trapping mechanisms simultaneously occurring that involve e.g. longer polyiodide chains, lithium from the p-doped hole transporting material Spiro-OMETAD, or Au

from the deposited electrodes. There are also open questions around charge trapping at the grain boundaries and surfaces.²⁸⁰

Our results provide guidance for future studies of charge trapping in the hybrid halide perovskites. We have shown that lattice anharmonicity is significant and that harmonic potential energy surfaces can lead to carrier capture coefficients that are many orders of magnitude too small (or large). We have also found that the electron-phonon coupling term is large and this has two important consequences. Firstly, the relaxation of the whole lattice, not only the bonding atoms, must be considered. Secondly, for the electron capture process considered here, the single mode approximation is valid and the configuration coordinate Q provides a good approximation to the accepting modes of the negative iodine interstitial.

Data access statement

The crystal structures for the iodine interstitial in the negative, neutral and positive charge states reported in this chapter are available in an online repository.²⁰⁰ The IPR data for the negative iodine interstitial, alongside the analysis steps taken to generate the results in this chapter are also available in an online repository.²⁸¹ The Inverse Participation Ratio (IPR) of the phonon modes can be calculated using the JULIAPHONONS package²⁸² and the carrier capture rates can be calculated using the CARRIERCAPTURE.JL package.²⁶⁷

Acknowledgements

Calculations were performed on the SiSu supercomputer at the IT Center for Science (CSC), Finland, via the Partnership for Advanced Computing in Europe (PRACE) project no. 13DECI0317/IsoSwitch. I thank Sunghyun Kim, Ji-Sang Park, Sam Hood and Puck Van Gerwen for our weekly defect discussions which have clarified my understanding of non-radiative recombination.

Closing Remarks

The subject of this PhD thesis has been to investigate distortions (in the form of nonparabolic electronic bandstructures and anharmonic potential energy surfaces) and defects (in the form of the iodine interstitial) in hybrid halide perovskites. There are three main components to this work:

First I assessed the impact of band nonparabolicity on the transport and optical properties of PV materials at high carrier concentration. **I have shown that effective masses of PV materials are not constants and that an increase in effective mass leads to a reduction in carrier mobility at high carrier concentration.** I have published a software package (Appendix C) so that researchers can apply this methodology to their systems of interest; application to materials that operate at high carrier concentrations, such as transparent conducting oxides or thermoelectric materials, could be particularly interesting.

I then considered the consequences of electron-phonon and phonon-phonon coupling in the hybrid halide perovskite $\text{CH}_3\text{NH}_3\text{PbI}_3$. **My results show that there is a strong coupling between the electronic states at band edge and the anharmonic phonon modes associated with octahedral tilting.** Using parameters derived from the Frölich polaron model, **I have found that the cooling of photoexcited, above bandgap carriers is limited by the ultralow thermal conductivity of the perovskite lattice and that cooling to equilibrium happens over 100s of picoseconds.** This compares well to the experimentally observed time scale of slow carrier cooling.

Finally, I studied the process of charge trapping at the iodine interstitial defect. **I predict that the iodine interstitial forms a H-centre defect with a self trapped hole (I_2^-), and that there is fast non-radiative electron capture at this defect site.** This line of research prompts a number of further questions:

- Do charge capture processes in the hybrid halide perovskites lead to device degradation? Hybrid halide perovskites have an ultra-low thermal conductivity⁸¹ which, when combined with fast carrier trapping (where electronic energy is converted to lattice energy), could lead to a build up of highly localised heat. This local heating could accelerate device degradation; experimental reports show that a raman laser can trigger decomposition of MAPbX ($\text{X} = \text{I}, \text{Br}$).²⁸³
- Do stoichiometric iodine pairs form V-centres? It is energetically favourable to form V-centres in metal halides such as KCl ,²⁶⁵ but formation of this defect in the the metal halide perovskites has not been considered. If favourable, the V-centre will form in

high concentrations as it is a stoichiometric defect (requires no excess or missing atomic species). The long diffusion length but mediocre mobility of charge carriers in hybrid halide perovskites²³⁵ supports the existence of the V-centre, although this could also be accounted for by other types of polaron formation.

- Is defect energy depth a good measure of wavefunction localisation? In the literature a deep defect state (with a charge transition level towards the centre of the bandgap) is often correlated with highly localised charge. This correlation between the defect depth and localisation is often assumed (with the terms sometimes used interchangeably), but to my knowledge there is no systematic study of this relationship. A potential study could consider e.g. anion vacancies across CdTe, GaAs and MAPI.

During my PhD studies I have made key datasets and analysis scripts openly available through the GitHub platform. My reasons for doing so are three-fold: for increased reproducibility; to reduce duplication of effort and so make efficient use of public money and researcher time; and to promote my work. Reproducibility is surprisingly difficult to achieve – I have found that making software available is not enough, and that software documentation and testing is needed to ensure that others can independently reproduce my results. It has taken time to develop the skills needed to write, document, test and publish code, but I consider it time well spent.

In the first chapter I motivated this work with reference to global warming. However it is clear that efficient photovoltaic materials alone will not slow global warming, and that the larger picture must be considered. For example, if PV is to provide a large proportion of our energy supply it will need to be combined with large scale energy storage networks. If we are serious about climate change as the motivating factor, it may be that we have to look beyond science, as some claim that it is the political will, rather than technological solutions, that are lacking.

If, however, we believe that scientific understanding is an end in itself, there is plenty of motivation for further research into hybrid halide perovskite materials. In addition to the open questions listed previously, there is a technologically important and fundamentally interesting question relating to the metal B-site species: is it possible to replace lead with a non-toxic element? Efforts so far have failed, partly due to the dispersive Pb *s*-orbital which is active in the valence band, leading to excellent transport properties that cannot be reproduced with tin on the B-site, for example. There are many opportunities ahead as we pick apart the relationship between organic and inorganic components, electronic and ionic states, as well as order and disorder in this complex family of materials.

Appendices

A DFT bandstructures for PV materials

The following pages contain the DFT calculated bandstructures which were analysed to give the effective mass values in Table 4.1. All DFT calculations use the HSE06 exchange correlation functional, and results are given with and without spin-orbit coupling. The output files for calculations using the LDA and PBEsol functionals can be found in an online repository.²²⁸

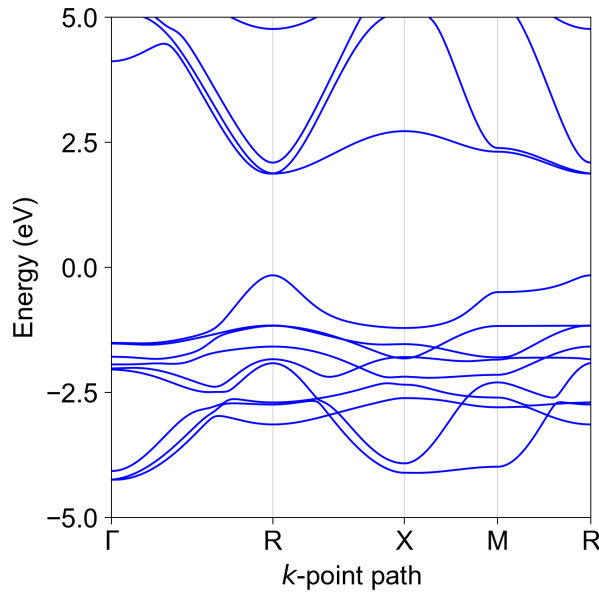


Figure A.1: MAPI bandstructure with the HSE06 functional, without spin-orbit coupling.

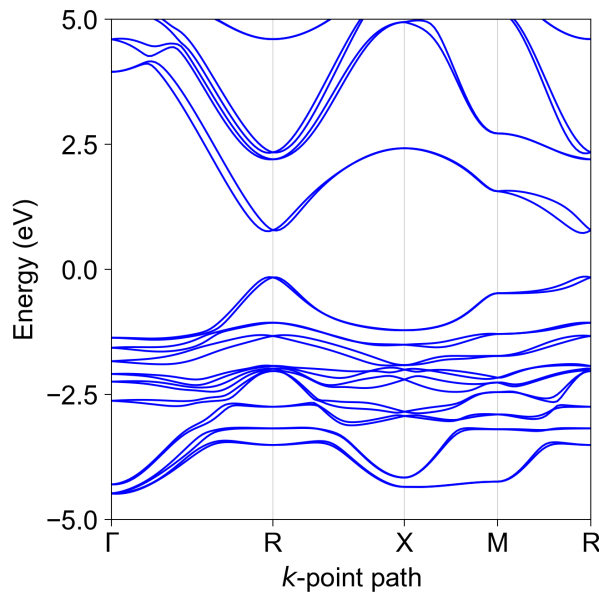


Figure A.2: MAPI bandstructure with the HSE06 functional, with spin-orbit coupling.

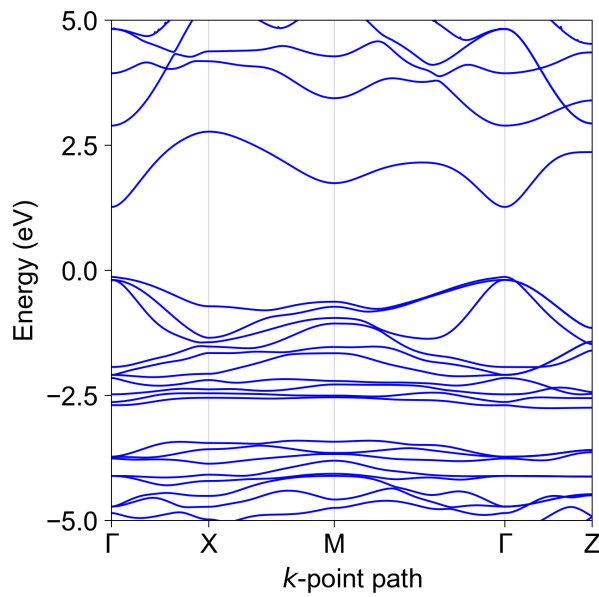


Figure A.3: CZTS bandstructure with the HSE06 functional, without spin-orbit coupling.

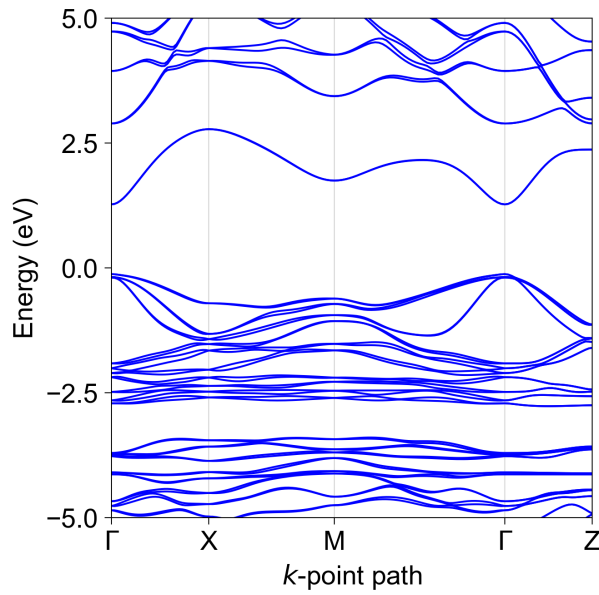


Figure A.4: CZTS bandstructure with the HSE06 functional, with spin-orbit coupling.

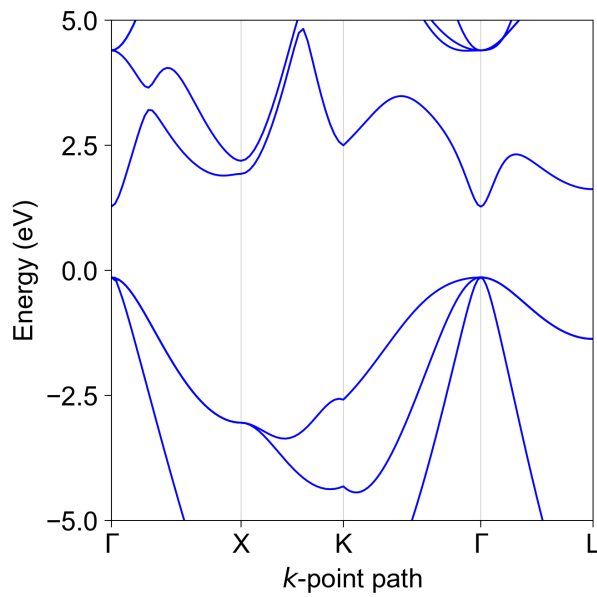


Figure A.5: GaAs bandstructure with the HSE06 functional, without spin-orbit coupling.

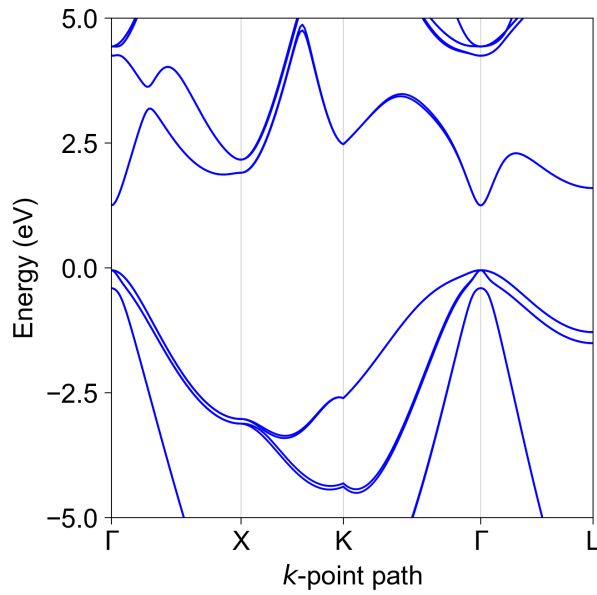


Figure A.6: GaAs bandstructure with the HSE06 functional, with spin-orbit coupling.

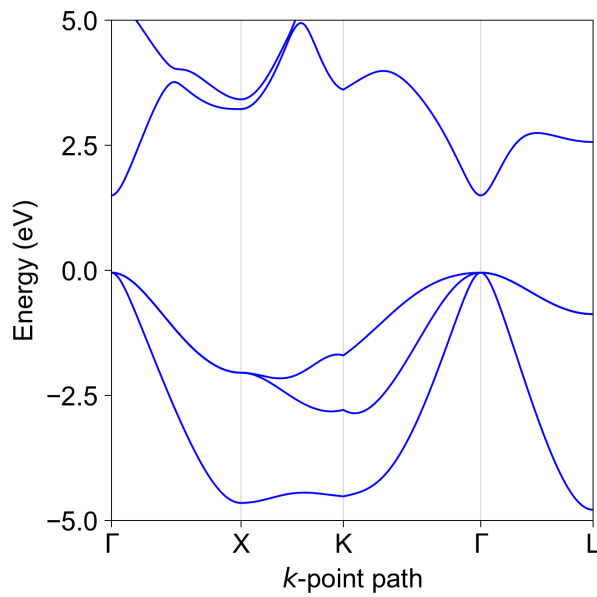


Figure A.7: CdTe bandstructure with the HSE06 functional, without spin-orbit coupling.

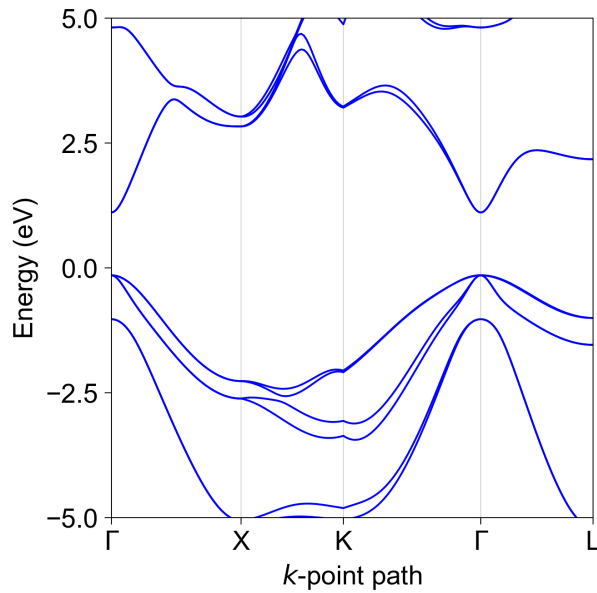


Figure A.8: CdTe bandstructure with the HSE06 functional, with spin-orbit coupling.

B Effective mass and k -point spacing

Table B.1: The curvature effective mass (Equation 4.1, in units of electron rest mass) calculated for different k -point spacings in reciprocal space for an electron in the [100] direction of CZTS. The finite difference fit and unweighted least-squares fit are calculated using three points. The weighted least squares fit is calculated using points up to 0.25 eV in energy. Details of each method are included in the Methods section of Chapter 4 in the main text. Calculations use the PBEsol exchange-correlation functional with spin-orbit coupling.

k -poing spacing (\AA^{-1})	finite diff.	unweighted	weighted
0.005	0.06	0.05	0.07
0.010	0.07	0.06	0.07
0.015	0.08	0.06	0.07
0.020	0.10	0.07	0.07
0.025	0.12	0.08	0.07

C effmass: An effective mass package

The following text is reprinted from Whalley, L. D. (2018). effmass: An effective mass package. *Journal of Open Source Software*, 3(28), p.797. © 2018 CC-BY

Summary

Many semiconductor properties depend on the response of electrons to an external perturbation. This perturbation could take the form of an electric field, change in temperature or an applied lattice stress. In a crystal, this response depends on the interaction of the electrons with a periodic potential. The effective mass approximation assumes that the response of an electron in a periodic potential is equivalent to that of a free electron with a renormalised mass (called the ‘effective mass’). This makes the effective mass a critical parameter in models for the optical and transport properties of a semiconductor.

The effective mass has a number of definitions, depending on the perturbation under consideration. The conventional definition of effective mass is inversely proportional to the second derivative of electron energy with respect to electron momentum.¹⁸¹ This allows the effective mass to be easily calculated from ab-initio band structures, and there are existing codes which have implemented this (see the ‘Related packages’ Section below).

We must approximate the band structure with a parabola for the previous definition to be valid.¹⁸² However, this approximation breaks down when there is a high concentration of electrons in the material - when, for example, the material is doped or excited under a laser. Instead, we can then approximate the band structure with the Kane quasi-linear dispersion,¹⁸⁴ and the definition of effective mass is adapted accordingly.

EFFMASS is a Python 3 package for calculating various definitions of effective mass from the electronic bandstructure of a semiconducting material. It contains a core class that calculates the effective mass and other associated properties of selected band structure segments. effmass also contains functions for locating band structure extrema, calculating the Kane quasi-linear dispersion parameters and plotting approximations to the true dispersion. Parsing of electronic structure data is facilitated by the VASPPY package.²⁸⁴

EFFMASS is aimed towards theoretical solid state physicists and chemists who have a basic familiarity with Python. Depending on the functionality and level of approximation you are looking for, it may be that one of the packages listed below will suit your needs better.

Related packages

Effective mass calculations are implemented in a number of other packages:

- VASPPY [284]: This is installed as a dependency of effmass. Calculates the effective mass using a least-squares quadratic fit for parabolic dispersions.

- SUMO [285]: Calculates the effective mass using a least-squares fit for parabolic and non-parabolic dispersions.
- EMC [286]: Calculates the effective mass tensor using a finite-difference method for parabolic dispersions.
- PYMATGEN [287]: This is installed as a dependency of effmass. Calculates an average effective mass tensor for non-parabolic dispersions with multiple bands and extrema. Also calculates the Seebeck effective mass as defined here.

Unique features of effmass

To our knowledge, the following features are unique to this package:

- Easily compare the values of curvature effective mass calculated using multiple numerical techniques (least-squares and polynomial fitting)
- Tailor the polynomial fitting used to approximate the DFT calculated dispersion: by choosing the order of the polynomial and the energy range to fit over.
- Visualise the dispersions used to approximate the DFT calculated dispersion
- Quantify non-parabolicity through the Kane dispersion parameters: effective mass at band-edge and alpha
- Calculate the optical effective mass assuming a Kane dispersion.

Acknowledgements

LW would like to thank Aron Walsh, Benjamin Morgan and Jarvist Moore Frost for their guidance during this project. This package was written during a PhD funded by the EPSRC through the Centre for Doctoral Training in New and Sustainable Photovoltaics (grant no. EP/L01551X/1). The input data used for developing and testing this package was generated using the ARCHER UK National Supercomputing Service. We have access to Archer via our membership of the UK's HEC Materials Chemistry Consortium, which is funded by EPSRC (EP/L000202).

D Bandgap deformation potential and supercell size

The cartesian displacement of an atom due to a polarisation by a phonon is inversely proportional to the square root of the number of atoms in the cell used to model the displacements.⁸¹ The bandgap deformation is a function of Cartesian displacement, so that doubling the size of the supercell will scale the atomic displacements and bandgap change by a factor of $\frac{1}{\sqrt{2}}$ (Figure D.1). Importantly, changing the supercell size scales the x-axis of the mode potential in the Schrödinger solver so that the average bandgap for a given temperature, a physical observable, does not scale with supercell size.

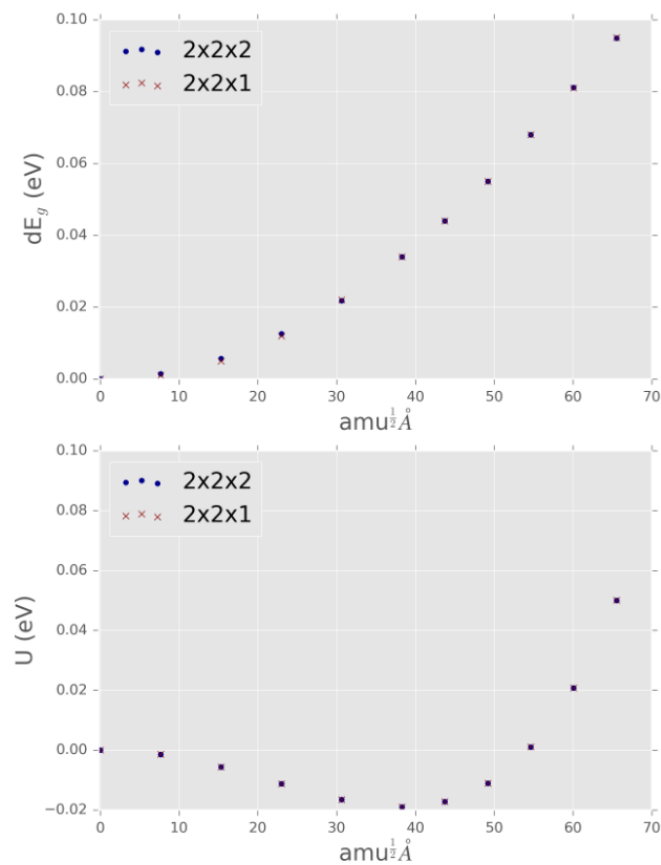


Figure D.1: Change in bandgap and the potential energy surface for two supercell sizes. To allow for comparison the x-axis values for the $2 \times 2 \times 1$ supercell have been scaled to match those of the $2 \times 2 \times 2$ supercell and the potential energy of the $2 \times 2 \times 1$ supercell has been doubled. Differences in the calculated bandgap are of the orders 10^{-4} eV.

E Diffusion equation for a hot sphere

In the case of spherical symmetry

$$\nabla^2 T = \frac{1}{r} \frac{\partial^2 (rT)}{\partial r^2}. \quad (9)$$

Substituting this into the fourier equation for heat diffusion gives

$$\frac{\partial T}{\partial t} = \frac{D}{r} \frac{d^2(rT)}{dr^2}, \quad (10)$$

and we set the boundary condition as $T = f(r)$ at $t = 0$. Substituting $u = rT$ into Equation 10 gives

$$\frac{\partial u}{\partial t} = D \frac{d^2(u)}{dr^2}, \quad (11)$$

with the boundary conditions $u = rf(r)$ at $t = 0$, $u = 0$ at $r = 0$. This solution is equivalent to the case of linear flow with one face at zero. To solve, we follow Reference [288] and consider a distribution on r which is equal to but the opposite sign of a distribution on $-r$. This initial distribution is convolved with a gaussian kernal to give temperature T as a function of time t and position r :

$$u = rT(r, t) = \frac{\eta}{\sqrt{\pi}} \left[\int_0^\infty \lambda f(\lambda) e^{-(\lambda-r)^2 \eta^2} \delta\lambda - \int_0^\infty \lambda f(\lambda) e^{-(\lambda+r)^2 \eta^2} \delta\lambda \right], \quad (12)$$

where $\eta = \frac{1}{\sqrt{4Dt}}$ and λ is a variable of integration. Using the following definition for β and β'

$$\begin{aligned} \beta &= (\lambda - r)\eta, & \lambda &= \frac{\beta}{\eta} + r \\ \beta' &= (\lambda + r)\eta, & \lambda &= \frac{\beta'}{\eta} - r, \end{aligned} \quad (13)$$

we recast Equation 12 as:

$$T(r, t) = \frac{1}{r\sqrt{\pi}} \left[\int_{rn}^\infty \left(\frac{\beta}{\eta} + r \right) f \left(\frac{\beta}{\eta} + r \right) e^{-\beta^2} \delta\beta - \int_{rn}^\infty \left(\frac{\beta'}{\eta} - r \right) f \left(\frac{\beta'}{\eta} - r \right) e^{-\beta'^2} \delta\beta' \right]. \quad (14)$$

For a sphere with radius R at temperature $T = T_0$, in a surrounding volume at zero temperature, the expression for $T(r, t)$ is given by:

$$T(r, t) = \frac{T_0}{r\sqrt{\pi}} \left[\int_{-r\eta}^{(R-r)\eta} \left(\frac{\beta}{\eta} + r \right) e^{-\beta^2} \delta\beta - \int_{r\eta}^{(R+r)\eta} \left(\frac{\beta}{\eta} - r \right) e^{-\beta^2} \delta\beta \right] \quad (15)$$

Using the integral identity

$$\int \beta e^{\beta^2} = \frac{1}{2} e^{\beta^2}, \quad (16)$$

and the error function

$$erf(x) = \int_0^x e^{-\beta^2} \delta\beta, \quad (17)$$

we reach the final analytical expression for temperature:

$$T(r, t) = \frac{T_0}{2} \left[erf((R-r)\eta) + erf((R+r)\eta) \right] - \frac{T_0 \sqrt{Dt}}{r\sqrt{\pi}} \left[e^{-\frac{(R-r)^2}{4Dt}} - e^{-\frac{(R+r)^2}{4Dt}} \right]. \quad (18)$$

F Charge transition diagram for I_i

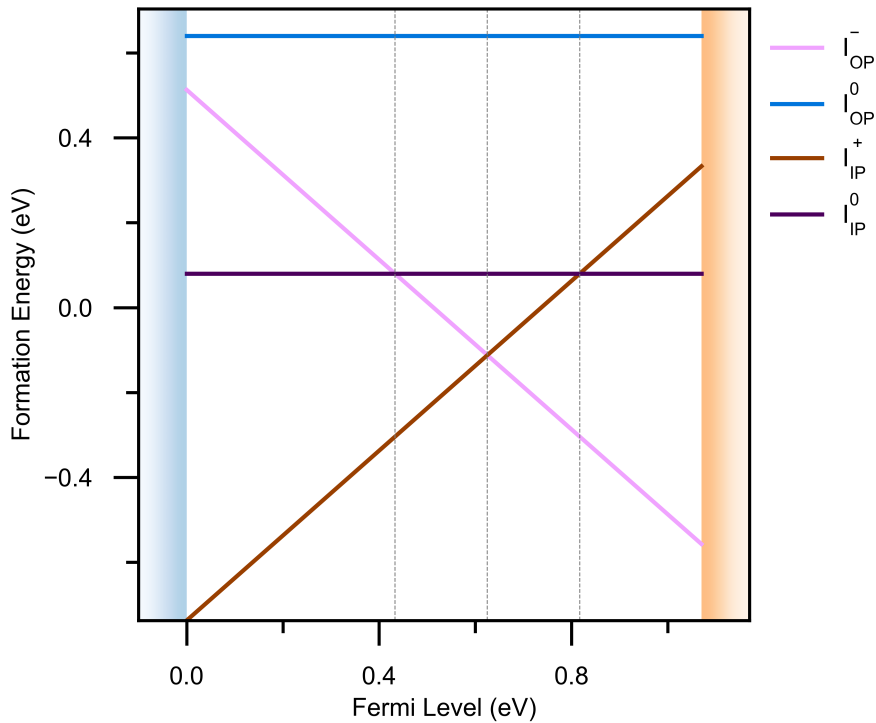


Figure F.1: Charge transition levels of the higher energy iodine interstitial defects in MAPI. The defect geometries correspond to those in the solid boxes in Figure 6.2. Defects with a lower energy were later found and the charge transition diagram for these are reported in the main text. For the defects reported here there are three charge transitions in the bandgap, as found in the previous literature.^{109,260}

G Additional I_i potential energy surfaces

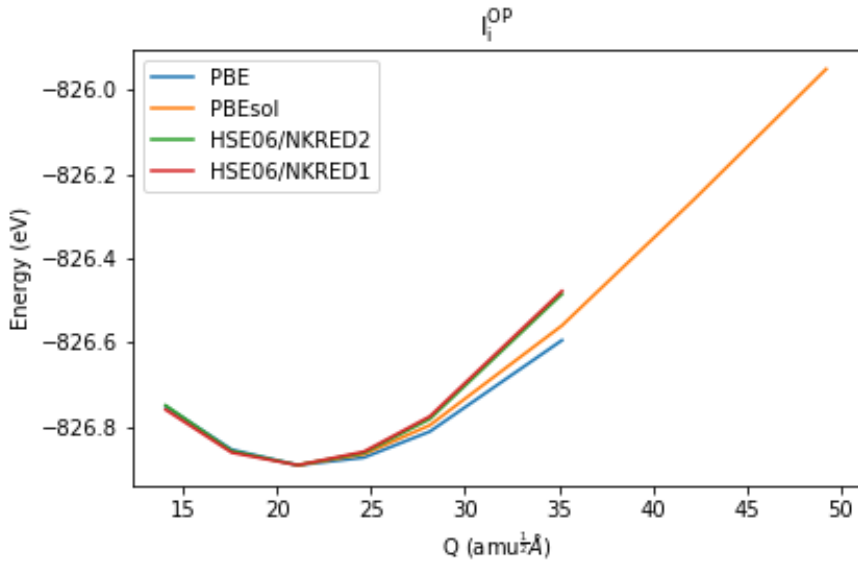


Figure G.1: Potential energy surface of the neutral iodine interstitial calculated at various levels of theory: GGA (PBE and PBEsol functionals) without spin-orbit coupling and hybrid (HSE06) with spin-orbit coupling. The hybrid wavefunctions have been converged using a single point calculation at the gamma point for the Fock exchange (NKRED=2) or using a $2\times 2\times 2$ Monkhorst-Pack mesh (NKRED=1).

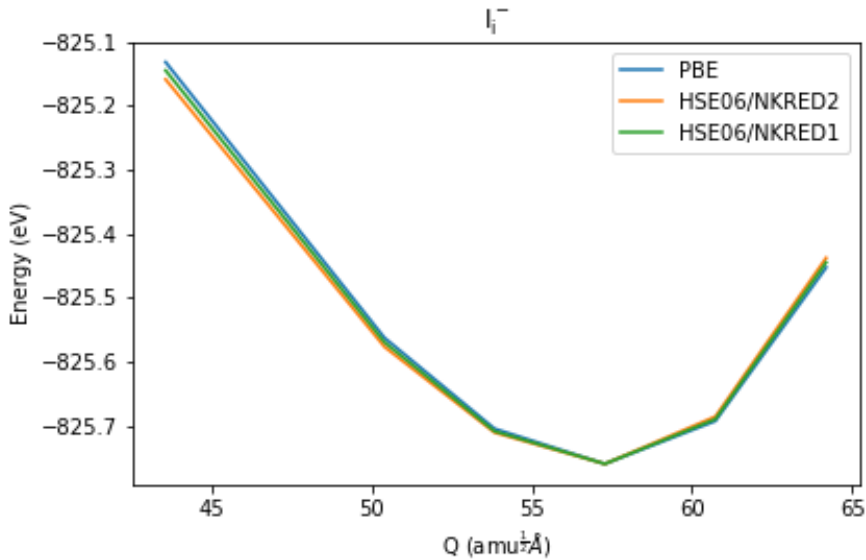


Figure G.2: Potential energy surface of the negative iodine interstitial calculated at various levels of theory: GGA (PBE and PBEsol functionals) without spin-orbit coupling and hybrid (HSE06) with spin-orbit coupling. The hybrid wavefunctions have been converged using a single point calculation at the gamma point for the Fock exchange (NKRED=2) or using a $2\times 2\times 2$ Monkhorst-Pack mesh (NKRED=1).

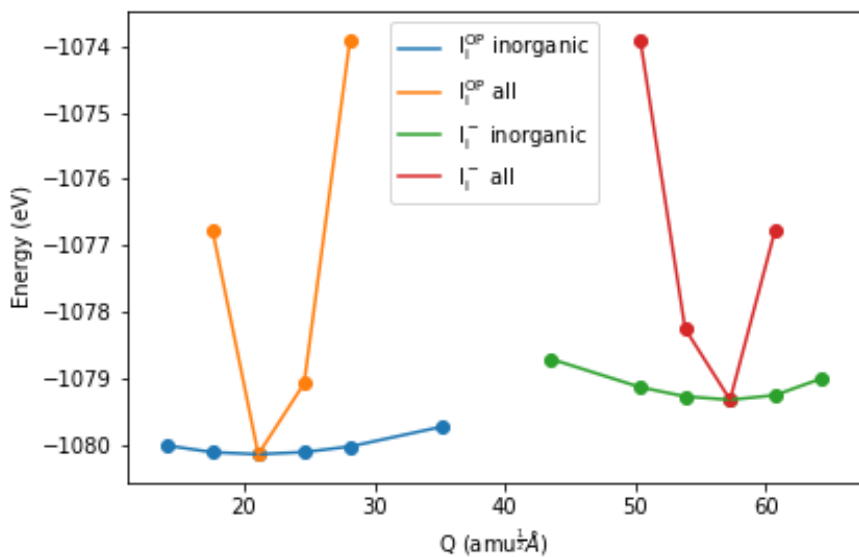


Figure G.3: Potential energy surfaces for all-atom or inorganic-only lattice distortions. In Chapter 6 the configuration coordinate Q is defined as $\sqrt{\sum_i m_i \Delta r_i^2}$, where the sum is over all inorganic atoms i with mass m_i and a displacement from equilibrium of Δr_i . As shown in this figure, summing over all atoms, including those in the organic methylammonium molecule, leads to unphysical energies as the linear interpolation does not capture the rotation of the organic cation between charge states.

H Copyright permissions

Rightslink® by Copyright Clearance Center

<https://s100.copyright.com/AppDispatchServlet>

The screenshot shows the RightsLink interface. At the top left is the Copyright Clearance Center logo. Next to it is the RightsLink logo. On the right side are buttons for "Home", "Create Account", "Help", and a "LIVE CHAT" icon. Below the header, there's a section for "ACS Publications" with the tagline "Most Trusted. Most Cited. Most Read." To the right of this is a detailed publication record:

ACS Publications	Title: H-Center and V-Center Defects in Hybrid Halide Perovskites
	Author: Lucy D. Whalley, Rachel Crespo-Otero, Aron Walsh
	Publication: ACS Energy Letters
	Publisher: American Chemical Society
	Date: Dec 1, 2017

Copyright © 2017, American Chemical Society

To the right of the publication details is a "LOGIN" box containing text about logging in with copyright.com credentials or becoming a RightsLink user.

PERMISSION/LICENSE IS GRANTED FOR YOUR ORDER AT NO CHARGE

This type of permission/license, instead of the standard Terms & Conditions, is sent to you because no fee is being charged for your order. Please note the following:

- Permission is granted for your request in both print and electronic formats, and translations.
- If figures and/or tables were requested, they may be adapted or used in part.
- Please print this page for your records and send a copy of it to your publisher/graduate school.
- Appropriate credit for the requested material should be given as follows: "Reprinted (adapted) with permission from (COMPLETE REFERENCE CITATION). Copyright (YEAR) American Chemical Society." Insert appropriate information in place of the capitalized words.
- One-time permission is granted only for the use specified in your request. No additional uses are granted (such as derivative works or other editions). For any other uses, please submit a new request.

[BACK](#) [CLOSE WINDOW](#)

Copyright © 2019 [Copyright Clearance Center, Inc.](#). All Rights Reserved. [Privacy statement](#). [Terms and Conditions](#).
Comments? We would like to hear from you. E-mail us at customercare@copyright.com



26-Jun-2019

This license agreement between the American Physical Society ("APS") and Lucy Whalley ("You") consists of your license details and the terms and conditions provided by the American Physical Society and SciPris.

Licensed Content Information

License Number:	RNP/19/JUN/016080
License date:	26-Jun-2019
DOI:	10.1103/PhysRevB.99.085207
Title:	Impact of nonparabolic electronic band structure on the optical and transport properties of photovoltaic materials
Author:	Lucy D. Whalley et al.
Publication:	Physical Review B
Publisher:	American Physical Society
Cost:	USD \$ 0.00

Request Details

Does your reuse require significant modifications: Yes

Modification Details:

Yes - I am first author. I have included text and figures from the supplemental information in the main text and made other small edits to maintain consistency throughout the thesis.

Specify intended distribution locations:	Worldwide
Reuse Category:	Reuse in a thesis/dissertation
Requestor Type:	Author of requested content
Items for Reuse:	Whole Article
Format for Reuse:	Print and Electronic
Total number of print copies:	Up to 1000

Information about New Publication:

University/Publisher:	Imperial College London
Title of dissertation/thesis:	Defects and Distortions in hybrid halide perovskites
Author(s):	Lucy Whalley
Expected completion date:	Sep. 2019

License Requestor Information

Name:	Lucy Whalley
Affiliation:	Individual
Email Id:	lucywhalley@gmail.com
Country:	United Kingdom



TERMS AND CONDITIONS

The American Physical Society (APS) is pleased to grant the Requestor of this license a non-exclusive, non-transferable permission, limited to Print and Electronic format, provided all criteria outlined below are followed.

1. You must also obtain permission from at least one of the lead authors for each separate work, if you haven't done so already. The author's name and affiliation can be found on the first page of the published Article.
2. For electronic format permissions, Requestor agrees to provide a hyperlink from the reprinted APS material using the source material's DOI on the web page where the work appears. The hyperlink should use the standard DOI resolution URL, <http://dx.doi.org/{DOI}>. The hyperlink may be embedded in the copyright credit line.
3. For print format permissions, Requestor agrees to print the required copyright credit line on the first page where the material appears: "Reprinted (abstract/excerpt/figure) with permission from [(FULL REFERENCE CITATION) as follows: Author's Names, APS Journal Title, Volume Number, Page Number and Year of Publication.] Copyright (YEAR) by the American Physical Society."
4. Permission granted in this license is for a one-time use and does not include permission for any future editions, updates, databases, formats or other matters. Permission must be sought for any additional use.
5. Use of the material does not and must not imply any endorsement by APS.
6. APS does not imply, purport or intend to grant permission to reuse materials to which it does not hold copyright. It is the requestor's sole responsibility to ensure the licensed material is original to APS and does not contain the copyright of another entity, and that the copyright notice of the figure, photograph, cover or table does not indicate it was reprinted by APS with permission from another source.
7. The permission granted herein is personal to the Requestor for the use specified and is not transferable or assignable without express written permission of APS. This license may not be amended except in writing by APS.
8. You may not alter, edit or modify the material in any manner.
9. You may translate the materials only when translation rights have been granted.
10. APS is not responsible for any errors or omissions due to translation.
11. You may not use the material for promotional, sales, advertising or marketing purposes.
12. The foregoing license shall not take effect unless and until APS or its agent, Aptara, receives payment in full in accordance with Aptara Billing and Payment Terms and Conditions, which are incorporated herein by reference.
13. Should the terms of this license be violated at any time, APS or Aptara may revoke the license with no refund to you and seek relief to the fullest extent of the laws of the USA. Official written notice will be made using the contact information provided with the permission request. Failure to receive such notice will not nullify revocation of the permission.
14. APS reserves all rights not specifically granted herein.
15. This document, including the Aptara Billing and Payment Terms and Conditions, shall be the entire agreement between the parties relating to the subject matter hereof.



26-Jun-2019

This license agreement between the American Physical Society ("APS") and Lucy Whalley ("You") consists of your license details and the terms and conditions provided by the American Physical Society and SciPris.

Licensed Content Information

License Number:	RNP/19/JUN/016081
License date:	26-Jun-2019
DOI:	10.1103/PhysRevB.94.220301
Title:	Phonon anharmonicity, lifetimes, and thermal transport in $\text{CH}_3\text{NH}_3\text{PbI}_3$ from many-body perturbation theory
Author:	Lucy D. Whalley et al.
Publication:	Physical Review B
Publisher:	American Physical Society
Cost:	USD \$ 0.00

Request Details

Does your reuse require significant modifications: Yes

Modification Details:

Yes - I am lead author I will use figures, tables and edited portions of text selected from the supplementary information and main text.

Specify intended distribution locations:	Worldwide
Reuse Category:	Reuse in a thesis/dissertation
Requestor Type:	Author of requested content
Items for Reuse:	Whole Article
Format for Reuse:	Print and Electronic
Total number of print copies:	Up to 1000

Information about New Publication:

University/Publisher:	Imperial College London
Title of dissertation/thesis:	Defects and Distortions in hybrid halide perovskites
Author(s):	Lucy Whalley
Expected completion date:	Sep. 2019

License Requestor Information

Name:	Lucy Whalley
Affiliation:	Individual
Email Id:	lucywhalley@gmail.com
Country:	United Kingdom



TERMS AND CONDITIONS

The American Physical Society (APS) is pleased to grant the Requestor of this license a non-exclusive, non-transferable permission, limited to Print and Electronic format, provided all criteria outlined below are followed.

1. You must also obtain permission from at least one of the lead authors for each separate work, if you haven't done so already. The author's name and affiliation can be found on the first page of the published Article.
2. For electronic format permissions, Requestor agrees to provide a hyperlink from the reprinted APS material using the source material's DOI on the web page where the work appears. The hyperlink should use the standard DOI resolution URL, <http://dx.doi.org/{DOI}>. The hyperlink may be embedded in the copyright credit line.
3. For print format permissions, Requestor agrees to print the required copyright credit line on the first page where the material appears: "Reprinted (abstract/excerpt/figure) with permission from [(FULL REFERENCE CITATION) as follows: Author's Names, APS Journal Title, Volume Number, Page Number and Year of Publication.] Copyright (YEAR) by the American Physical Society."
4. Permission granted in this license is for a one-time use and does not include permission for any future editions, updates, databases, formats or other matters. Permission must be sought for any additional use.
5. Use of the material does not and must not imply any endorsement by APS.
6. APS does not imply, purport or intend to grant permission to reuse materials to which it does not hold copyright. It is the requestor's sole responsibility to ensure the licensed material is original to APS and does not contain the copyright of another entity, and that the copyright notice of the figure, photograph, cover or table does not indicate it was reprinted by APS with permission from another source.
7. The permission granted herein is personal to the Requestor for the use specified and is not transferable or assignable without express written permission of APS. This license may not be amended except in writing by APS.
8. You may not alter, edit or modify the material in any manner.
9. You may translate the materials only when translation rights have been granted.
10. APS is not responsible for any errors or omissions due to translation.
11. You may not use the material for promotional, sales, advertising or marketing purposes.
12. The foregoing license shall not take effect unless and until APS or its agent, Aptara, receives payment in full in accordance with Aptara Billing and Payment Terms and Conditions, which are incorporated herein by reference.
13. Should the terms of this license be violated at any time, APS or Aptara may revoke the license with no refund to you and seek relief to the fullest extent of the laws of the USA. Official written notice will be made using the contact information provided with the permission request. Failure to receive such notice will not nullify revocation of the permission.
14. APS reserves all rights not specifically granted herein.
15. This document, including the Aptara Billing and Payment Terms and Conditions, shall be the entire agreement between the parties relating to the subject matter hereof.

References

1. Masson-Delmotte, V. *et al.* *Special Report: Global Warming of 1.5°C* tech. rep. (The Intergovernmental Panel on Climate Change, 2018).
2. Kaneda, T. & Dupuis, G. *2017 World Population data sheet* tech. rep. (Population Reference Bureau, 2017).
3. Mackay, D. J. *Sustainable energy - without the hot air* (UIT, 2009).
4. NASA Goddard Institute for Space Studies. *GISS Surface Temperature Analysis (GISTEMP)* <https://data.giss.nasa.gov/gistemp> (Sept. 14, 2018).
5. *Extreme weather events in europe* tech. rep. (European Academies Science Advisory Council, 2018).
6. Black, M. T. & Karoly, D. J. Southern Australia's warmest October on record. *Bull. Am. Meteor. Soc.* **97** (12 2016).
7. Abatzoglou, J. & Williams, A. Impact of anthropogenic climate change on wildfire across western US Forest. *Proc. Natl. Acad. Sci.* **113** (43 2016).
8. Sweet, W. V. In Tide's way - Southwestern Florida's 2015 sunny-day flood. *Bull. Am. Meteor. Soc.* **97** (12 2016).
9. Van der Wiel, K. *et al.* Rapid attribution of the August 2016 flood-inducing extreme precipitation in south Louisiana to climate change. *Hydrol. Earth Syst. Sci.* **21** (2017).
10. APS News. *This month in physics history* <https://www.aps.org/publications/apsnews/200904/physicshistory.cfm> (Aug. 10, 2019).
11. Kopp, G. & Lean, J. L. A new, lower value of total solar irradiance: Evidence and climate significance. *Geophys. Res. Lett.* **38** (2011).
12. *Key world energy statistics* tech. rep. (International Energy Agency, 2017).
13. Mayer, J., Philipps, S., Hussein, N. S., Schlegl, T. & Senkpiel, C. *Current and future cost of photovoltaics* tech. rep. (Fraunhofer ISE, 2015).
14. Green, M. A. & Bremner, S. P. Energy conversion approaches and materials for high-efficiency photovoltaics. *Nat. Mater.* **16**, 23 (2016).
15. Blakers, A. W. & Green, M. A. 20% efficiency silicon solar cells. *Appl. Phys. Lett.* **48**, 215–217 (1986).
16. Farmer, J. D. & Lafond, F. How predictable is technological progress? *Res. Policy* **45**, 647 –665 (2016).
17. Jager-Waldau, A. *PV Status Report 2017* tech. rep. (European Commission, 2017).
18. Open Energy Information. *Transparent cost database* https://openei.org/apps/TCDB/transparent_cost_database (Aug. 10, 2019).
19. The Guardian. *British power generation achieves first ever coal-free day* <https://www.theguardian.com/environment/2017/apr/21/britain-set-for-first-coal-free-day-since-the-industrial-revolution> (June 27, 2019).

20. The Guardian. *UK runs without coal power for three days in a row* <https://www.theguardian.com/business/2018/apr/24/uk-power-generation-coal-free-gas-renewables-nuclear> (June 27, 2019).
21. *National Infrastructure Assessment* tech. rep. (National Infrastructure Commission, 2018).
22. Grantham Institute. *Expect the unexpected: The Disruptive power of low-carbon technology* tech. rep. (2017).
23. *2018 Outlook for Energy: A View to 2040* tech. rep. (ExxonMobil, 2018).
24. Creutzig, F. *et al.* The underestimated potential of Solar Energy to mitigate climate change. *Nat. Energy* **2**, 17140 (2017).
25. Koppelaar, R. Solar-PV energy payback and net energy: Meta-assessment of study quality, reproducibility, and results harmonization. *Renewable Sustainable Energy Rev.* **72**, 1241–1255 (2017).
26. Yoshikawa, K. *et al.* Silicon heterojunction solar cell with interdigitated back contacts for a photoconversion efficiency over 26%. *Nat. Energy* **2**, 17032 (2017).
27. Nelson, J. *The Physics of Solar Cells* (Imperial College Press, 2003).
28. Rau, U. Reciprocity relation between photovoltaic quantum efficiency and electroluminescent emission of solar cells. *Phys. Rev. B* **76**, 085303 (8 2007).
29. Braly, I. L., Stoddard, R. J., Rajagopal, A., Jen, A. K.-Y.-. & Hillhouse, H. W. Photoluminescence and Photoconductivity to Assess Maximum Open-Circuit Voltage and Carrier Transport in Hybrid Perovskites and Other Photovoltaic Materials. *J. Phys. Chem. Lett.* **9**, 3779–3792 (2018).
30. Shockley, W. & Queisser, H. J. Detailed Balance Limit of Efficiency of p-n Junction Solar Cells. *J. Appl. Phys.* **32**, 510–519 (1961).
31. Polman, A., Knight, M., Garnett, E. C., Ehrler, B. & Sinke, W. C. Photovoltaic materials: Present efficiencies and future challenges. *Science* **352** (2016).
32. American Association for the Advancement of Science. *Reprints and permissions* <https://www.sciencemag.org/help/reprints-and-permissions> (Aug. 10, 2019).
33. Yu, L. & Zunger, A. Identification of Potential Photovoltaic Absorbers Based on First-Principles Spectroscopic Screening of Materials. *Phys. Rev. Lett.* **108**, 068701 (6 2012).
34. Bercx, M., Sarmadian, N., Saniz, R., Partoens, B. & Lamoen, D. First-principles analysis of the spectroscopic limited maximum efficiency of photovoltaic absorber layers for CuAu-like chalcogenides and silicon. *Phys. Chem. Chem. Phys.* **18**, 20542–20549 (30 2016).
35. Hirst, L. C., Walters, R. J., Führer, M. F. & Ekins-Daukes, N. J. Experimental demonstration of hot-carrier photo-current in an InGaAs quantum well solar cell. *Appl. Phys. Lett.* **104**, 231115 (2014).
36. Johnston, M. B. & Herz, L. M. Hybrid Perovskites for Photovoltaics: Charge-Carrier Recombination, Diffusion, and Radiative Efficiencies. *Acc. Chem. Res.* **49**, 146–154 (2016).
37. Zunger, A. Inverse design in search of materials with target functionalities. *Nat. Rev. Chem.* **2**, 121 (2018).
38. Qu, X. *et al.* The Electrolyte Genome project: A big data approach in battery materials discovery. *Comp. Mat. Sci.* **103**, 56–67 (2015).
39. Hachmann, J. *et al.* The Harvard Clean Energy Project: Large-Scale Computational Screening and Design of Organic Photovoltaics on the World Community Grid. *J. Phys. Chem. Lett.* **2**, 2241–2251 (2011).

40. Dunstan, M. T. *et al.* Large scale computational screening and experimental discovery of novel materials for high temperature CO₂ capture. *Energy Environ. Sci.* **9**, 1346–1360 (4 2016).
41. Brandt, R. E., Stevanović, V., Ginley, D. S. & Buonassisi, T. Identifying defect-tolerant semiconductors with high minority-carrier lifetimes: beyond hybrid lead halide perovskites. *MRS Commun.* **5**, 265–275 (2015).
42. Rühle, S. Tabulated values of the Shockley–Queisser limit for single junction solar cells. *Sol. Energy* **130**, 139–147 (2016).
43. Rey, G. *et al.* On the origin of band-tails in kesterite. *Sol. Energy Mater. Sol. Cells* **179**, 142–151 (2018).
44. Poortmans, J. & Arkhipov, V. *Thin Film Solar Cells: Fabrication, Characterization and Applications* (John Wiley and Sons, 2006).
45. Brebels, J., Manca, J. V., Lutsen, L., Vanderzande, D. & Maes, W. High dielectric constant conjugated materials for organic photovoltaics. *J. Mater. Chem. A* **5**, 24037–24050 (46 2017).
46. Madelung, O. *Semiconductors: Data Handbook* (Springer, 2004).
47. Wilson, J. N., Frost, J. M., Wallace, S. K. & Walsh, A. Dielectric and ferroic properties of metal halide perovskites. *APL Mater.* **7**, 010901 (2019).
48. Kittel, C. *Introduction to Solid State Physics* 8th, 232 (John Wiley & Sons, 2005).
49. Ganose, A. M., Butler, K. T., Walsh, A. & Scanlon, D. O. Relativistic electronic structure and band alignment of BiSI and BiSeI: candidate photovoltaic materials. *J. Mater. Chem. A* **4**, 2060–2068 (6 2016).
50. Butler, K. T., Kumagai, Y., Oba, F. & Walsh, A. Screening procedure for structurally and electronically matched contact layers for high-performance solar cells: hybrid perovskites. *J. Mater. Chem. C* **4**, 1149–1158 (6 2016).
51. Battersby, S. News Feature: The solar cell of the future. *Proc. Natl. Acad. Sci.* **116**, 7–10 (2019).
52. Gaulois, M. W. *et al.* Data-Driven Review of Thermoelectric Materials: Performance and Resource Considerations. *Chem. Mater.* **25**, 2911–2920 (2013).
53. Zakutayev, A. Brief review of emerging photovoltaic absorbers. *Curr. Opin. Green Sustainable Chem.* **4**, 8–15 (2017).
54. Schaak, R. E. & Mallouk, T. E. Perovskites by Design: A Toolbox of Solid-State Reactions. *Chem. Mater.* **14**, 1455–1471 (2002).
55. Møller, C. K. Crystal Structure and Photoconductivity of Cæsium Plumbohalides. *Nature* **182**, 1436–1436 (1958).
56. Kojima, A., Teshima, K., Shirai, Y. & Miyasaka, T. Organometal halide perovskites as visible-light sensitizers for photovoltaic cells. *J. Am. Chem. Soc.* **131**, 6050–6051 (2009).
57. Stranks, S. D. & Snaith, H. J. Metal-halide perovskites for photovoltaic and light-emitting devices. *Nat. Nanotechnol.* **10**, 391–402 (2015).
58. Saparov, B. & Mitzi, D. B. Organic–Inorganic Perovskites: Structural Versatility for Functional Materials Design. *Chem. Rev.* **116**, 4558–4596 (2016).
59. Park, N.-G., Grätzel, M., Miyasaka, T., Zhu, K. & Emery, K. Towards stable and commercially available perovskite solar cells. *Nat. Energy* **1**, 16152 (2016).
60. Walsh, A., Padure, N. P. & Il Seok, S. Physical chemistry of hybrid perovskite solar cells. *Phys. Chem. Chem. Phys.* **18**, 27024–27025 (2016).
61. Wallace, S. K., Mitzi, D. B. & Walsh, A. The Steady Rise of Kesterite Solar Cells. *ACS Energy Lett.* **2**, 776–779 (2017).

62. He, Y. & Galli, G. Perovskites for Solar Thermoelectric Applications: a First Principle Study of $\text{CH}_3\text{NH}_3\text{AlI}_3$ ($\text{A}=\text{Pb}$ and Sn). *Chem. Mater.* **26**, 5394–5400 (2014).
63. Tuning of the Thermoelectric Figure of Merit of $\text{CH}_3\text{NH}_3\text{MI}_3$ ($\text{M}=\text{Pb}, \text{Sn}$) Photovoltaic Perovskites. *J. Phys. Chem. C* **119**, 11506–11510 (2015).
64. Protesescu, L. *et al.* Nanocrystals of Cesium Lead Halide Perovskites (CsPbX_3 , $\text{X} = \text{Cl}$, Br , and I): Novel Optoelectronic Materials Showing Bright Emission with Wide Color Gamut. *Nano Lett.* **15**, 3692–3696 (2015).
65. Resistive Switching Behavior in Organic–Inorganic Hybrid $\text{CH}_3\text{NH}_3\text{PbI}_{3-x}\text{Cl}_x$ Perovskite for Resistive Random Access Memory Devices. *Adv. Mater.* **27**, 6170–6175 (2015).
66. Liu, D. *et al.* Flexible All-inorganic Perovskite CsPbBr_3 Non-volatile Memory Device. *ACS Appl. Mater. Interfaces* **9**, 6171–6176 (2017).
67. Frost, J. M. & Walsh, A. What Is Moving in Hybrid Halide Perovskite Solar Cells? *Acc. Chem. Res.* **49**, 528–535 (2016).
68. Weller, M. T., Weber, O. J., Henry, P. F., Di Pumbo, A. M. & Hansen, T. C. Complete structure and cation orientation in the perovskite photovoltaic methylammonium lead iodide between 100 and 352 K. *en. Chem. Commun.* **51**, 4180–4183 (2015).
69. Brivio, F. *et al.* Lattice dynamics and vibrational spectra of the orthorhombic, tetragonal, and cubic phases of methylammonium lead iodide. *Phys. Rev. B* **92**, 144308 (2015).
70. Mitzi, D. B. Templating and structural engineering in organic-inorganic perovskites. *J. Chem. Soc. Dalt. Trans.* **2001**, 1–12 (2001).
71. Mitzi, D. B. Solution-processed inorganic semiconductors. *J. Mater. Chem.* **14**, 2355 (2004).
72. Savory, C. N., Walsh, A. & Scanlon, D. O. Can Pb-free Halide Double Perovskites Support High-efficiency Solar Cells? *ACS Energy Lett.* **1**, 949–955 (2016).
73. Volonakis, G. *et al.* Lead-Free Halide Double Perovskites via Heterovalent Substitution of Noble Metals. *J. Phys. Chem. Lett.* **7**, 1254–1259 (2016).
74. Weber, D. $\text{CH}_3\text{NH}_3\text{PbX}_3$, a Pb(II)-System with Cubic Perovskite Structure. *Zeitschrift für Naturforsch. B* **33b**, 1443–1445 (1978).
75. Weber, D. $\text{CH}_3\text{NH}_3\text{SnBr}_x\text{I}_{3-x}$ ($x=0\text{--}3$), a Sn(II)-system with the cubic perovskite structure. *Zeitschrift für Naturforsch.* **33b**, 862–865 (1978).
76. Onoda-Yamamoto, N., Matsuo, T. & Suga, H. Calorimetric and IR spectroscopic studies of phase transitions in methylammonium trihalogenoplumbates (II). *J. Phys. Chem. Solids* **51**, 1383–1395 (1990).
77. Yamamoto, O. *et al.* Neutron diffraction and calorimetric studies of methylammonium iodide. *Acta Crystallogr. Sect. B Struct. Sci.* **48**, 329–336 (1992).
78. Dielectric Study of $\text{CH}_3\text{NH}_3\text{PbX}_3$ ($\text{X} = \text{Cl}$, Br , I). *J. Phys. Chem. Solids* **53**, 935–939 (1992).
79. Hutter, E. M. *et al.* Direct–indirect character of the bandgap in methylammonium lead iodide perovskite. *Nat. Mater.* **16**, 115–120 (2017).
80. Poglitsch, A. & Weber, D. Dynamic disorder in methylammonium tri-halogenoplumbates (II) observed by millimeter-wave spectroscopy. *J. Chem. Phys.* **87**, 6373 (1987).
81. Whalley, L. D., Skelton, J. M., Frost, J. M. & Walsh, A. Phonon anharmonicity, lifetimes, and thermal transport in $\text{CH}_3\text{NH}_3\text{PbI}_3$ from many-body perturbation theory. *Phys. Rev. B* **94** (22 2016).
82. Beecher, A. N. *et al.* Direct observation of dynamic symmetry breaking above room temperature in methylammonium lead iodide perovskite. *ACS Energy Lett.* **1**, 880–887 (2016).

83. Chang, Y. H., Park, C. H. & Matsuishi, K. First-principles study of the structural and the electronic properties of the lead-halide-based inorganic-organic perovskites $\text{CH}_3\text{NH}_3\text{PbX}_3$ and CsPbX_3 ($\text{X} = \text{Cl}, \text{Br}, \text{I}$). *J. Korean Phys. Soc.* **44**, 889–893 (2004).
84. Brivio, F., Walker, A. B. & Walsh, A. Structural and electronic properties of hybrid perovskites for high-efficiency thin-film photovoltaics from first-principles. *APL Mater.* **1**, 042111 (2013).
85. Leguy, A. M. A. *et al.* The dynamics of methylammonium ions in hybrid organic-inorganic perovskite solar cells. en. *Nat. Commun.* **6**, 7124 (2015).
86. Chen, T. *et al.* Rotational dynamics of organic cations in $\text{CH}_3\text{NH}_3\text{PbI}_3$ perovskite. *Phys. Chem. Chem. Phys.* **17**, 31278–31286 (2015).
87. Bakulin, A. A. *et al.* Real-Time Observation of Organic Cation Reorientation in Methylammonium Lead Iodide Perovskites. *J. Phys. Chem. Lett.* **6**, 3663–3669 (2015).
88. The Cubic Perovskite Structure of Black Formamidinium Lead Iodide at 298 K. *J. Phys. Chem. Lett.* **6**, 3209–3212 (2015).
89. Selig, O. *et al.* Organic Cation Rotation and Immobilisation in Pure and Mixed Methylammonium Lead-Halide Perovskites. *J. Am. Chem. Soc.* **139**, 4068 (2017).
90. Yang, R. X., Skelton, J. M., da Silva, E. L., Frost, J. M. & Walsh, A. Spontaneous Octahedral Tilting in the Cubic Inorganic Cesium Halide Perovskites CsSnX_3 and CsPbX_3 ($\text{X} = \text{F}, \text{Cl}, \text{Br}, \text{I}$). *J. Phys. Chem. Lett.* **8**, 4720–4726 (2017).
91. Glazer, A. M. The classification of tilted octahedra in perovskites. *Acta Crystallogr. Sect. B* **28**, 3384–3392 (1972).
92. Woodward, P. M. Octahedral Tilting in Perovskites. II. Structure Stabilizing Forces. *Acta Cryst. B* **53**, 44–66 (1997).
93. Frost, J. M., Butler, K. T. & Walsh, A. Molecular ferroelectric contributions to anomalous hysteresis in hybrid perovskite solar cells. *APL Mater.* **2**, 081506 (2014).
94. Quarti, C. *et al.* Structural and optical properties of methylammonium lead iodide across the tetragonal to cubic phase transition: implications for perovskite solar cells. en. *Energy Environ. Sci.* **16**, 155–163 (2016).
95. Mosconi, E., Quarti, C., Ivanovska, T., Ruani, G. & De Angelis, F. Structural and electronic properties of organo-halide lead perovskites: a combined IR-spectroscopy and ab initio molecular dynamics investigation. en. *Phys. Chem. Chem. Phys.* **16**, 16137–44 (2014).
96. Saidi, W. A., Poncé, S. & Monserrat, B. Temperature Dependence of the Energy Levels of Methylammonium Lead Iodide Perovskite from First-Principles. *J. Phys. Chem. Lett.* **7**, 5247–5252 (2016).
97. Reuter, K. & Scheffler, M. First-Principles Atomistic Thermodynamics for Oxidation Catalysis: Surface Phase Diagrams and Catalytically Interesting Regions. *Phys. Rev. Lett.* **90**, 046103 (2003).
98. Kim, Y. H., Kim, K. & Zhang, S. B. First-principles calculation of thermodynamic stability of acids and bases under pH environment: A microscopic pH theory. *J. Chem. Phys.* **136**, 134112–134114 (2012).
99. Jackson, A. J., Tiana, D. & Walsh, A. A universal chemical potential for sulfur vapours. *Chem. Sci.* **7**, 1082–1092 (2016).
100. Stoffel, R. P., Wessel, C., Lumey, M.-W. & Dronskowski, R. Ab initio thermochemistry of solid-state materials. *Angew. Chemie* **49**, 5242–66 (2010).
101. Jackson, A. J. & Walsh, A. Ab initio thermodynamic model of $\text{Cu}_2\text{ZnSnS}_4$. *J. Mater. Chem. A* **2**, 7829–7836 (2014).

102. Nagabhusana, G. P., Shivaramaiah, R. & Navrotsky, A. Direct calorimetric verification of thermodynamic instability of lead halide hybrid perovskites. *Proc. Natl. Acad. Sci.* **113**, 7717–7721 (2016).
103. Baikie, T. *et al.* Synthesis and crystal chemistry of the hybrid perovskite $\text{CH}_3\text{NH}_3\text{PbI}_3$ for solid-state sensitised solar cell applications. *J. Mater. Chem. A* **1**, 5628 (2013).
104. Togo, A. & Tanaka, I. First principles phonon calculations in materials science. *Scr. Mater.* **108**, 1–5 (2015).
105. Brivio, F., Butler, K. T., Walsh, A. & van Schilfgaarde, M. Relativistic Quasiparticle Self-consistent Electronic Structure of Hybrid Halide Perovskite Photovoltaic Absorbers. *Phys. Rev. B* **89**, 155204 (2014).
106. Pérez-Osorio, M. A. *et al.* Vibrational Properties of the Organic-Inorganic Halide Perovskite $\text{CH}_3\text{NH}_3\text{PbI}_3$ from Theory and Experiment: Factor Group Analysis, First-Principles Calculations, and Low-Temperature Infrared Spectra. *J. Phys. Chem. C* **119**, 25703–25718 (2015).
107. Van Schilfgaarde, M., Kotani, T. & Faleev, S. Quasiparticle self-consistent GW theory. *Phys. Rev. Lett.* **96**, 1–4 (2006).
108. Kepenekian, M. *et al.* Rashba and Dresselhaus Effects in Hybrid Organic-Inorganic Perovskites: From Basics to Devices. *ACS Nano* **9**, 1557–11567 (2015).
109. Du, M.-H. Density Functional Calculations of Native Defects in $\text{CH}_3\text{NH}_3\text{PbI}_3$: Effects of Spin–Orbit Coupling and Self-Interaction Error. *J. Phys. Chem. Lett.* **6**, 1461–1466 (2015).
110. Zacharias, M. & Giustino, F. One-shot calculation of temperature-dependent optical spectra and phonon-induced band-gap renormalization. *Phys. Rev. B* **94**, 075125 (7 2016).
111. Li, Y. *et al.* Direct Observation of Long Electron-Hole Diffusion Distance in $\text{CH}_3\text{NH}_3\text{PbI}_3$ Perovskite Thin Film. *Sci. Rep.* **5**, 14485 (2015).
112. Karakus, M. *et al.* Phonon-electron-scattering limits free charge mobility in methylammonium lead iodide perovskites. *J. Phys. Chem. Lett.* **6**, 4991–4996 (2015).
113. Yi, H. T., Wu, X., Zhu, X. & Podzorov, V. Intrinsic Charge Transport across Phase Transitions in Hybrid Organo-Inorganic Perovskites. *Adv. Mater.* **28**, 6509–6514 (2016).
114. Leguy, A. M. A. *et al.* Dynamic disorder, phonon lifetimes, and the assignment of modes to the vibrational spectra of methylammonium lead halide perovskites. *Phys. Chem. Chem. Phys.* **18**, 27051–27066 (2016).
115. Wright, A. D. *et al.* Electron–phonon coupling in hybrid lead halide perovskites. *Nat. Commun.* **7**, 11755 (2016).
116. Filippetti, A., Mattoni, A., Caddeo, C., Saba, M. I. & Delugas, P. Low electron-polar optical phonon scattering as a fundamental aspect of carrier mobility in methylammonium lead halide $\text{CH}_3\text{NH}_3\text{PbI}_3$ perovskites. *Phys. Chem. Chem. Phys.* **18**, 15352–15362 (2016).
117. Ball, J. M. & Petrozza, A. Defects in perovskite-halides and their effects in solar cells. *Nat. Energy* **1**, 16149 (2016).
118. Ma, J. & Wang, L.-W. Nanoscale charge localization induced by random orientations of organic molecules in hybrid perovskite $\text{CH}_3\text{NH}_3\text{PbI}_3$. *Nano Lett.* **15**, 248–253 (2014).
119. Brivio, F., Caetano, C. & Walsh, A. Thermodynamic Origin of Photoinstability in the $\text{CH}_3\text{NH}_3\text{Pb}(\text{I}_{1-x}\text{Br}_x)_3$ Hybrid Halide Perovskite Alloy. *J. Phys. Chem. Lett.* **7**, 1083–1087 (2016).
120. Slotcavage, D. J., Karunadasa, H. I. & McGehee, M. D. Light-Induced Phase Segregation in Halide-Perovskite Absorbers. *ACS Energy Lett.* **1**, 1199–1205 (2016).

121. Eames, C. *et al.* Ionic transport in hybrid lead iodide perovskite solar cells. en. *Nat. Commun.* **6**, 7497 (2015).
122. Richardson, G. *et al.* Can slow-moving ions explain hysteresis in the current-voltage curves of perovskite solar cells? *Energy Environ. Sci.* **9**, 1476–1485 (4 2016).
123. Whalley, L. D., Crespo-Otero, R. & Walsh, A. H-Center and V-Center Defects in Hybrid Halide Perovskites. *ACS Energy Lett.* **2** (2017).
124. Walsh, A. Principles of Chemical Bonding and Band Gap Engineering in Hybrid Organic-Inorganic Halide Perovskites. *J. Phys. Chem. C* **119**, 5755–5760 (2015).
125. Meloni, S. *et al.* Ionic polarization-induced current-voltage hysteresis in $\text{CH}_3\text{NH}_3\text{PbX}_3$ perovskite solar cells. *Nat. Commun.* **7**, 10334 (2016).
126. Bryant, D. *et al.* Observable hysteresis at low temperature in ‘hysteresis free’ lead halide perovskite solar cells. *J. Phys. Chem. Lett.* **6**, 3190–3194 (2015).
127. Game, O. S., Buchsbaum, G. J., Zhou, Y., Padture, N. P. & Kingon, A. I. Ions Matter: Description of the Anomalous Electronic Behavior in Methylammonium Lead Halide Perovskite Devices. *Adv. Funct. Mater.* **27** (16 2017).
128. Shao, Y. *et al.* Grain boundary dominated ion migration in polycrystalline organic–inorganic halide perovskite films. *Energy Environ. Sci.* **9**, 1752–1759 (2016).
129. Critical Role of Grain Boundaries for Ion Migration in Formamidinium and Methylammonium Lead Halide Perovskite Solar Cells. *Adv. Energy Mater.* **6** (13 2016).
130. Chandra, S. & C. Agrawal, R. Surface Diffusion Coefficient of Iodine in Some Superionic Solid Films. *J. Phys. Soc. Japan* **48**, 2171–2172 (1980).
131. Van Reenen, S., Kemerink, M. & Snaith, H. J. Modeling Anomalous Hysteresis in Perovskite Solar Cells. *J. Phys. Chem. Lett.* **6**, 3808–3814 (2015).
132. Article, E. *et al.* Reversible photo-induced trap formation in mixed-halide hybrid perovskites for photovoltaics. en. *Chem. Sci.* **6**, 613–617 (2015).
133. Steirer, K. X. *et al.* Defect Tolerance in Methylammonium Lead Triiodide Perovskite. *ACS Energy Lett.* **1**, 360–366 (2016).
134. Azarhoosh, P., McKechnie, S., Frost, J. M., Walsh, A. & van Schilfgaarde, M. Relativistic origin of slow electron-hole recombination in hybrid halide perovskite solar cells. *APL Mater.* **4**, 091501 (2016).
135. Zheng, F., Tan, L. Z., Liu, S. & Rappe, A. M. Rashba spin-orbit coupling enhanced carrier lifetime in $\text{CH}_3\text{NH}_3\text{PbI}_3$. *Nano Lett.* **15**, 7794–7800 (2015).
136. Frost, J. M. *et al.* Atomistic origins of high-performance in hybrid halide perovskite solar cells. *Nano Lett.* **14**, 2584–2590 (2014).
137. Brandt, R. E., Stevanović, V., Ginley, D. S. & Buonassisi, T. Identifying defect-tolerant semiconductors with high minority carrier lifetimes: Beyond hybrid lead halide perovskites. *MRS Commun.* **2**, 265–275 (2015).
138. Shockley, W. & Read, W. T. Statistics of the Recombinations of Holes and Electrons. *Phys. Rev.* **87**, 835–842 (5 1952).
139. Yu, P. & Cardona, M. *Fundamentals of Semiconductors* (Springer, London, 1996).
140. Stoneham, A. M. *Theory of Defects in Solids* (OUP Oxford, Oxford, 1975).
141. Brivio, F., Butler, K. T., Walsh, A. & Van Schilfgaarde, M. Relativistic quasiparticle self-consistent electronic structure of hybrid halide perovskite photovoltaic absorbers. *Phys. Rev. B* **89**, 155204 (2014).

142. Hava, S. & Auslender, M. in *Springer Handbook of Electronic and Photonic Materials* 441–480 (Springer US, 2007).
143. Wang, K. A., Lian, C., Su, N., Jena, D. & Timler, J. Conduction band offset at the InN/GaN heterojunction. *Appl. Phys. Lett.* **91**, 232117–3 (2007).
144. Chen, J. *et al.* Origin of the high performance of perovskite solar cells with large grains. *App. Phys. Lett.* **108**, 053302 (2016).
145. Yin, W. J., Chen, H., Shi, T., Wei, S. H. & Yan, Y. Origin of High Electronic Quality in Structurally Disordered $\text{CH}_3\text{NH}_3\text{PbI}_3$ and the Passivation Effect of Cl and O at Grain Boundaries. *Adv. Electron. Mater.* **1**, 1500044 (2015).
146. De Quilettes, D. W. *et al.* Impact of microstructure on local carrier lifetime in perovskite solar cells. *Science* **348**, 683–686 (2015).
147. Bischak, C. G., Sanehira, E. M., Precht, J. T., Luther, J. M. & Ginsberg, N. S. Heterogeneous Charge Carrier Dynamics in Organic-Inorganic Hybrid Materials: Nanoscale Lateral and Depth-Dependent Variation of Recombination Rates in Methylammonium Lead Halide Perovskite Thin Films. *Nano Lett.* **15**, 4799 (2015).
148. Long, R., Liu, J. & Prezhdo, O. V. Unravelling the Effects of Grain Boundary and Chemical Doping on Electron–Hole Recombination in $\text{CH}_3\text{NH}_3\text{PbI}_3$ Perovskite by Time-Domain Atomistic Simulation. *J. Am. Chem. Soc.* **138**, 3884–3890 (2016).
149. Tai, Q. *et al.* Efficient and stable perovskite solar cells prepared in ambient air irrespective of the humidity. en. *Nat. Commun.* **7**, 11105 (2016).
150. Butler, K. T., Frost, J. M., Skelton, J. M., Svane, K. L. & Walsh, A. Computational materials design of crystalline solids. *Chem. Soc. Rev.* **45**, 6138–6146 (2016).
151. Murray, A. *et al.* Modular design of SPIRO-OMeTAD analogues as hole transport materials in solar cells. en. *Chem. Commun.* **51**, 8935–8938 (2015).
152. Tsai, H. *et al.* High-efficiency two-dimensional Ruddlesden–Popper perovskite solar cells. *Nature* **536**, 312–316 (2016).
153. $(\text{CH}_3\text{NH}_3)_2\text{Pb}(\text{SCN})_2\text{I}_2$: A New More Stable Structural Motif for Hybrid Halide Photovoltaics? *J. Phys. Chem. Lett.* **6**, 4594–4598 (2015).
154. McClure, E. T., Ball, M. R., Windl, W. & Woodward, P. M. $\text{Cs}_2\text{AgBiX}_6$ ($\text{X}=\text{Br}, \text{Cl}$) — New visible light absorbing, lead-free halide perovskite semiconductors. *Chem. Mater.* **6**, 2–4 (2016).
155. Wei, F. *et al.* The synthesis, structure and electronic properties of a lead-free hybrid inorganic–organic double perovskite $\text{MA}_2\text{KBiCl}_6$ (MA = methylammonium). *Mater. Horiz.* **3**, 328–332 (2016).
156. Hohenberg, P. & Kohn, W. Inhomogeneous Electron Gas. *Phys. Rev.* **136**, B864 (1964).
157. Kohn, W. & Sham, L. J. Self-Consistent Equations Including Exchange and Correlation Effects. *Phys. Rev.* **140**, A1133 (1965).
158. K. Burke and friends. *The ABC of DFT* <https://dft.uci.edu/doc/g1.pdf> (June 27, 2019).
159. Scuseria, G. E. & Staroverov, V. N. *Progress in the development of exchange-correlation functionals in In Theory and Application of Computational Chemistry: The First 40 Years* (2005), 669.
160. Perdew, J. P. & Ruzsinszky, A. Fourteen easy lessons in density functional theory. *Int. J. Quantum Chem.* **110**, 2801–2807 (2010).
161. Kohn, W. Nobel Lecture: Electronic structure of matter—wave functions and density functionals. *Rev. Mod. Phys.* **71**, 1253–1266 (5 1999).

162. Ceperley, D. M. & Alder, B. J. Ground State of the Electron Gas by a Stochastic Method. *Phys. Rev. Lett.* **45**, 566–569 (7 1980).
163. Hoffmann, R. *How Chemistry and Physics Meet in the Solid State* https://www.ch.ic.ac.uk/harrison/Group/Mallia.tmp/3year_lab_elec_str.AUTUMN2007/hoffmann.pdf (Apr. 1, 2019).
164. Lundstrom, M. *Fundamentals of Carrier Transport* (Cambridge University Press, 2000).
165. Kresse, G. & Furthmüller, J. Efficient iterative schemes for ab initio total-energy calculations using a plane-wave basis set. *Phys. Rev. B* **54**, 11169 (1996).
166. Lejaeghere, K. *et al.* Reproducibility in density functional theory calculations of solids. *Science* **351** (2016).
167. Alkauskas, A., McCluskey, M. D. & Van de Walle, C. G. Tutorial: Defects in semiconductors—Combining experiment and theory. *J. Appl. Phys.* **119**, 181101 (2016).
168. Menéndez-Proupin, E. & Orellana, W. Theoretical study of intrinsic defects in CdTe. *J. Phys. Conf. Ser.* **720**, 012031 (2016).
169. Durrant, T. R., Murphy, S. T., Watkins, M. B. & Shluger, A. L. Relation between image charge and potential alignment corrections for charged defects in periodic boundary conditions. *J. Chem. Phys.* **149**, 024103 (2018).
170. Vinichenko, D., Sensoy, M. G., Friend, C. M. & Kaxiras, E. Accurate formation energies of charged defects in solids: A systematic approach. *Phys. Rev. B* **95**, 235310 (23 2017).
171. Leslie, M & Gillan, N. J. The energy and elastic dipole tensor of defects in ionic crystals calculated by the supercell method. *J. Phys. C* **18**, 973–982 (1985).
172. Lany, S. & Zunger, A. Accurate prediction of defect properties in density functional supercell calculations. *Modell. Simul. Mater. Sci. Eng.* **17**, 084002 (2009).
173. Freysoldt, C., Neugebauer, J. & Van de Walle, C. G. Fully Ab Initio Finite-Size Corrections for Charged-Defect Supercell Calculations. *Phys. Rev. Lett.* **102**, 016402 (1 2009).
174. Kumagai, Y. & Oba, F. Electrostatics-based finite-size corrections for first-principles point defect calculations. *Phys. Rev. B* **89**, 195205 (19 2014).
175. Dove, M. T. *Introduction to Lattice Dynamics* (Cambridge University Press, 1993).
176. Silsbee, R. H. Thermal Broadening of the Mössbauer Line and of Narrow-Line Electronic Spectra in Solids. *Phys. Rev.* **128**, 1726–1733 (4 1962).
177. Hayes, W. & Stoneham, A. M. *Defects and Defect Processes in Nonmetallic Solids* (Dover, 1985).
178. Togo, A., Chaput, L. & Tanaka, I. Distribution of phonon lifetimes in Brillouin zones. *Phys. Rev. B* **91**, 094306 (2015).
179. Gibbs, Z. M. *et al.* Effective mass and Fermi surface complexity factor from ab initio band structure calculations. *npj Comput. Mater.* **3**, 8 (2017).
180. Mecholsky, N. A., Resca, L., Pegg, I. L. & Fornari, M. Theory of band warping and its effects on thermoelectronic transport properties. *Phys. Rev. B* **89**, 155131 (15 2014).
181. Ashcroft, N. W. & Mermin, N. D. *Solid State Physics* (Saunders College, 1976).
182. Ariel, V. & Natan, A. *Effective mass and the Energy-Mass relationship* <https://arxiv.org/abs/1205.3995> (Apr. 1, 2019).
183. Ruf, T. & Cardona, M. Nonparabolicity of the conduction band in GaAs. *Phys. Rev. B* **41**, 10747–10753 (15 1990).

184. E. O. Kane. Band structure of indium antimonide. *J. Phys. Chem. Solids* **1**, 249–261 (1957).
185. Segev, D. & Wei, S.-H. Structure-derived electronic and optical properties of transparent conducting oxides. *Phys. Rev. B* **71**, 125129 (2005).
186. Riffe, D. M. Temperature dependence of silicon carrier effective masses with application to femtosecond reflectivity measurements. *J. Opt. Soc. Am. B* **19**, 1092–1100 (2002).
187. Hautier, G., Miglio, A., Ceder, G., Rignanese, G.-M. & Gonze, X. Identification and design principles of low hole effective mass p-type transparent conducting oxides. *Nat. Commun.* **4**, 2292 (2013).
188. Huy, H. A., Aradi, B., Frauenheim, T. & Deák, P. Calculation of carrier-concentration-dependent effective mass in Nb-doped anatase crystals of TiO₂. *Phys. Rev. B* **83**, 155201 (15 2011).
189. Burstein, E. Anomalous Optical Absorption Limit in InSb. *Phys. Rev.* **93**, 632–633 (3 1954).
190. Moss, T. S. The Interpretation of the Properties of Indium Antimonide. *Proc. Phys. Soc. B* **67**, 775 (1954).
191. Manser, J. S. & Kamat, P. V. Band filling with free charge carriers in organometal halide perovskites. *Nat. Photon.* **8**, 737–743 (2014).
192. Yang, Y. *et al.* Observation of a hot-phonon bottleneck in lead-iodide perovskites. *Nat. Photon.* **10**, 53 (2015).
193. Price, M. B. *et al.* Hot-carrier cooling and photoinduced refractive index changes in organic–inorganic lead halide perovskites. *Nat. Commun.* **6**, 8420 (2015).
194. Law, C. *et al.* Performance and Stability of Lead Perovskite/TiO₂, Polymer/PCBM, and Dye Sensitized Solar Cells at Light Intensities up to 70 Suns. *Adv. Mater.* **26**, 6268–6273 (2014).
195. Van der Walt, S., Colbert, S. C. & Varoquaux, G. The NumPy array: a structure for efficient numerical computation. *Comput. Sci. Eng.* **13**, 22 (2011).
196. David Eberly, Geometric Tools. *Derivative Approximation by Finite Differences* <https://www.geometrictools.com/Documentation/FiniteDifferences.pdf> (Oct. 30, 2019).
197. Blöchl, P. Projector augmented-wave method. *Phys. Rev. B* **50**, 17953 (1994).
198. Rabadanov, M. K., Verin, I. A., Ivanov, Y. M. & Simonov, V. I. Refinement of the atomic structure of CdTe single crystals. *Crystallogr. Rep.* **46**, 636–641 (2001).
199. Lafond, A. *et al.* X-ray resonant single-crystal diffraction technique, a powerful tool to investigate the kesterite structure of the photovoltaic Cu₂ZnSnS₄ compound. *Acta. Crystallogr. B* **70**, 390–394 (2014).
200. Walsh Materials Design. *DFT optimised crystal structures of inorganic and hybrid halide perovskites* <https://github.com/WMD-group/hybrid-perovskites> (June 27, 2019).
201. Setyawan, W. & Curtarolo, S. High-throughput electronic band structure calculations: Challenges and tools. *Comput. Mater. Sci.* **49**, 299–312 (2010).
202. Perdew, J. P. *et al.* Restoring the Density-Gradient Expansion for Exchange in Solids and Surfaces. *Phys. Rev. Lett.* **100**, 136406 (2008).
203. Heyd, J., Scuseria, G. E. & Ernzerhof, M. Hybrid functionals based on a screened Coulomb potential. *J. Chem. Phys.* **118**, 8207–8215 (2003).
204. Nearing, J. *Mathematical Tools for Physics* (Dover, 2010).
205. Laflamme Janssen, J. *et al.* Precise effective masses from density functional perturbation theory. *Phys. Rev. B* **93**, 205147 (20 2016).

206. Deák, P., Aradi, B., Frauenheim, T., Janzén, E. & Gali, A. Accurate defect levels obtained from the HSE06 range-separated hybrid functional. *Phys. Rev. B* **81**, 153203 (15 2010).
207. Liu, Y. *et al.* Two-Inch-Sized Perovskite $\text{CH}_3\text{NH}_3\text{PbX}_3$ ($\text{X} = \text{Cl}, \text{Br}, \text{I}$) Crystals: Growth and Characterization. *Adv. Mater.* **27**, 5176–5183 (2015).
208. Kim, Y.-S., Marsman, M., Kresse, G., Tran, F. & Blaha, P. Towards efficient band structure and effective mass calculations for III-V direct band-gap semiconductors. *Phys. Rev. B* **82**, 205212 (20 2010).
209. Miyata, A. *et al.* Direct measurement of the exciton binding energy and effective masses for charge carriers in organic–inorganic tri-halide perovskites. *Nat. Phys.* **11**, 582–587 (2015).
210. Filip, M. R., Verdi, C. & Giustino, F. GW Band Structures and Carrier Effective Masses of $\text{CH}_3\text{NH}_3\text{PbI}_3$ and Hypothetical Perovskites of the Type APbI_3 : $\text{A} = \text{NH}_4$, PH_4 , AsH_4 , and SbH_4 . *J. Phys. Chem. C* **119**, 25209–25219 (2015).
211. Liu, H.-R. *et al.* First-principles study on the effective masses of zinc-blend-derived $\text{Cu}_2\text{Zn(IV)(VI)}_4$ (IV=Sn, Ge, Si and VI=S, Se). *J. Appl. Phys.* **112**, 093717 (2012).
212. Deguchi, D., Sato, K., Kino, H. & Kotani, T. Accurate energy bands calculated by the hybrid quasiparticle self-consistent GW method implemented in the ecalj package. *J. Appl. Phys.* **55**, 051201 (2016).
213. Richard, S., Aniel, F. & Fishman, G. Energy-band structure of Ge, Si, and GaAs: A thirty-band $\mathbf{k} \cdot \mathbf{p}$ method. *Phys. Rev. B* **70**, 235204 (23 2004).
214. Szmyd, D. M., Porro, P., Majerfeld, A. & Lagomarsino, S. Heavily doped GaAs:Se. I. Photoluminescence determination of the electron effective mass. *J. Appl. Phys.* **68**, 2367–2375 (1990).
215. Ito, K. *Copper Zinc Tin Sulfide Based Thin Film Solar Cells* (John Wiley and Sons, 2015).
216. Mosconi, E., Etienne, T. & De Angelis, F. Rashba Band Splitting in Organohalide Lead Perovskites: Bulk and Surface Effects. *J. Phys. Chem. Lett.* **8**, 2247–2252 (2017).
217. Tanaka, K. *et al.* Comparative study on the excitons in lead-halide-based perovskite-type crystals $\text{CH}_3\text{NH}_3\text{PbBr}_3$ and $\text{CH}_3\text{NH}_3\text{PbI}_3$. *Solid State Commun.* **127**, 619–623 (2003).
218. Hirasawa, M., Ishihara, T., Goto, T., Uchida, K. & Miura, N. Magnetoabsorption of the lowest exciton in perovskite-type compound $\text{CH}_3\text{NH}_3\text{PbI}_3$. *Phys. B* **201**, 427–430 (1994).
219. Walsh, A., Da Silva, J. L. F. & Wei, S.-H. Origins of band-gap renormalization in degenerately doped semiconductors. *Phys. Rev. B* **78**, 075211 (7 2008).
220. Umari, P., Mosconi, E. & De Angelis. Relativistic GW calculations on $\text{CH}_3\text{NH}_3\text{PbI}_3$ and $\text{CH}_3\text{NH}_3\text{SnI}_3$ Perovskites for Solar Cell Applications. *Sci. Rep.* **4**, 6050–6051 (2014).
221. Mott, N. F. The Basis of the Electron Theory of Metals, with Special Reference to the Transition Metals. *Proc. Phys. Soc. Sect. A* **62**, 416 (1949).
222. Frost, J. M., Whalley, L. D. & Walsh, A. Slow Cooling of Hot Polarons in Halide Perovskite Solar Cells. *ACS Energy Lett.* **2**, 2647–2652 (2017).
223. Richter, J. M. *et al.* Enhancing photoluminescence yields in lead halide perovskites by photon recycling and light out-coupling. *Nat. Commun.* **7**, 13941 (2016).
224. Gao, Y. *et al.* Room temperature three-photon pumped $\text{CH}_3\text{NH}_3\text{PbBr}_3$ perovskite microlasers. *Sci. Rep.* **7**, 45391 (2017).
225. Raymond, A., Robert, J. L. & Bernard, C. The electron effective mass in heavily doped GaAs. *J. Phys. C* **12**, 2289 (1979).

226. Frost, J. M. Calculating polaron mobility in halide perovskites. *Phys. Rev. B* **96**, 195202 (19 2017).
227. Poncé, S., Margine, E. R. & Giustino, F. Towards predictive many-body calculations of phonon-limited carrier mobilities in semiconductors. *Phys. Rev. B* **97**, 121201 (12 2018).
228. Whalley, L. D. *effmass: An effective mass calculator* <https://doi.org/10.5281/zenodo.1285137> (2018).
229. Whalley, L. D. effmass: An effective mass package. *J. Open Source Softw.* **3** (2019).
230. Frost, J. M. PolaronMobility.jl: Implementation of the Feynman variational polaron model. *J. Open Source Softw.* **3** (2018).
231. Yu, P. & Cardona, M. *Fundamentals of Semiconductors* (Springer-Verlag, 2010).
232. Giustino, F. Electron-phonon interactions from first principles. *Rev. Mod. Phys.* **89**, 015003 (1 2017).
233. Wallace, R. F. *Lattice Dynamics: Proceedings of the International Conference* (Pergamon Press, 1963).
234. Bardeen, J. & Shockley, W. Deformation Potentials and Mobilities in Non-Polar Crystals. *Phys. Rev.* **80**, 72–80 (1 1950).
235. Brenner, T. M. *et al.* Are Mobilities in Hybrid Organic-Inorganic Halide Perovskites Actually “High”? *J. Phys. Chem. Lett.* **6** (2015).
236. Yang, Y. *et al.* Observation of a hot-phonon bottleneck in lead-iodide perovskites. *Nat. Photon.* **10**, 53 (2015).
237. Yang, J. *et al.* Acoustic-optical phonon up-conversion and hot-phonon bottleneck in lead-halide perovskites. *Nat. Commun.* **8**, 14120 (2017).
238. Skelton, J. M. *et al.* Lattice dynamics of the tin sulphides SnS₂, SnS and Sn₂S₃: vibrational spectra and thermal transport. *Phys. Chem. Chem. Phys.* **19**, 12452–12465 (19 2017).
239. Kresse, G. & Furthmüller, J. Efficient iterative schemes for ab initio total-energy calculations using a plane-wave basis set. *Phys. Rev. B* **54**, 11169 (1996).
240. Perdew, J. P. *et al.* Restoring the Density-Gradient Expansion for Exchange in Solids and Surfaces. *Phys. Rev. Lett.* **100**, 136406 (2008).
241. Skelton, J. *A set of tools for mapping and analysing the potential-energy surfaces along phonon modes* <https://github.com/JMSkelton/ModeMap> (July 10, 2019).
242. Heyd, J. & Scuseria, G. Efficient Hybrid Density Functional Calculations in Solids: Assessment of the Heyd Scuseria Ernzerhof Screened Coulomb Hybrid Functional. *J. Chem. Phys.* **121**, 1187 (2004).
243. Heyd, J., Peralta, J., Scuseria, G. & Martin, R. Energy band gaps and lattice parameters evaluated with the Heyd-Scuseria-Ernzerhof screened hybrid functional. *J. Chem. Phys.* **123**, 174101 (2005).
244. Ganose, A. M., Jackson, A. J. & Scanlon, D. O. sumo: Command-line tools for plotting and analysis of periodic ab initio calculations. *J. Open Source Softw.* **3** (2018).
245. Francisco-López, A. *et al.* Equal Footing of Thermal Expansion and Electron–Phonon Interaction in the Temperature Dependence of Lead Halide Perovskite Band Gaps. *J. Phys. Chem. Lett.* **10**, 2971–2977 (2019).
246. McKechnie, S. *et al.* Dynamic symmetry breaking and spin splitting in metal halide perovskites. *Phys. Rev. B* **98**, 085108 (8 2018).

247. Wang, Y., Zhang, Y., Zhang, P. & Zhang, W. High intrinsic carrier mobility and photon absorption in perovskite $\text{CH}_3\text{NH}_3\text{PbI}_3$. *Phys. Chem. Chem. Phys.* (2015).
248. Skelton, J. M. *et al.* Anharmonicity in the high-temperature Cmcm phase of SnSe: soft modes and three-phonon interactions. *Phys. Rev. Lett.* **117**, 075502 (2016).
249. Kaganov M. L., L. I. M. & Tanatarov, L. V. Relaxation between electrons and the crystalline lattice. *J. Exp. Theor. Phys.* **4** (2 1956).
250. Sadasivam, S., Chan, M. K. Y. & Darancet, P. Theory of Thermal Relaxation of Electrons in Semiconductors. *Phys. Rev. Lett.* **119**, 136602 (13 2017).
251. Klein, J. R., Flender, O., Scholz, M., Oum, K. & Lenzer, T. Charge carrier dynamics of methylammonium lead iodide: from PbI_2 -rich to low-dimensional broadly emitting perovskites. *Phys. Chem. Chem. Phys.* **18**, 10800–10808 (16 2016).
252. Zhong, Y *et al.* Hot carrier relaxation in CdTe via phonon-plasmon modes. *J. Phys. Condens. Matter* **29**, 095701 (2017).
253. Rosenwaks, Y. *et al.* Hot-carrier cooling in GaAs: Quantum wells versus bulk. *Phys. Rev. B* **48**, 14675–14678 (19 1993).
254. Jackson, A. *Blender extensions for illustrations of phonons* <https://github.com/ajackson/ascii-phonons> (July 27, 2019).
255. Shockley, W. *Transistor technology evokes new physics* <https://www.nobelprize.org/uploads/2018/06/shockley-lecture.pdf> (Aug. 2, 2019).
256. Alkauskas, A., Yan, Q. & Van De Walle, C. G. First-principles theory of nonradiative carrier capture via multiphonon emission. *Phys. Rev. B* **90**, 1–17 (2014).
257. *Exponential growth of supercomputing power as recorded by the TOP500 list* <https://www.top500.org/statistics/perfdevel/> (Aug. 2, 2019).
258. Kim, S., Park, J.-S. & Walsh, A. Identification of Killer Defects in Kesterite Thin-Film Solar Cells. *ACS Energy Lett.* **3**, 496–500 (2018).
259. Walsh, A., Scanlon, D. O., Chen, S., Gong, X. G. & Wei, S.-H. Self-regulation mechanism for charged point defects in hybrid halide perovskites. *Angew. Chemie Int. Ed.* **54**, 1791 (2015).
260. Meggiolaro, D. *et al.* Iodine chemistry determines the defect tolerance of lead-halide perovskites. *Energy Environ. Sci.* **11**, 702–713 (3 2018).
261. Senocrate, A. *et al.* The Nature of Ion Conduction in Methylammonium Lead Iodide: A Multimethod Approach. *Angew. Chemie Int. Ed.* **56**, 7755–7759 (2017).
262. deQuilettes, D. W. *et al.* Photo-induced halide redistribution in organic–inorganic perovskite films. *Nat. Commun.* **7**, 11683 (May 2016).
263. Rosenberg, J. W., Legodi, M. J., Rakita, Y., Cahen, D. & Diale, M. Laplace current deep level transient spectroscopy measurements of defect states in methylammonium lead bromide single crystals. *J. Appl. Phys.* **122**, 145701 (2017).
264. Almora, O., García-Batlle, M. & Garcia-Belmonte, G. Utilization of Temperature-Sweeping Capacitive Techniques to Evaluate Band Gap Defect Densities in Photovoltaic Perovskites. *J. Phys. Chem. Lett.* **10**, 3661–3669 (2019).
265. Castner, T. G. & Känzig, W. The electronic structure of V-centers. *J. Phys. Chem. Sol.* **3** (1957).
266. Sphinx project. *Welcome to the SPHInX repository* <https://sxrepo.mpie.de/> (Aug. 2, 2019).

267. Walsh Materials Design. *Package to compute trap-assisted electron and hole capture rates in semiconducting compounds* <https://github.com/WMD-group/carriercapture.jl> (July 27, 2019).
268. Kim, S., Hood, S. N. & Walsh, A. Anharmonic lattice relaxation during nonradiative carrier capture. *Phys. Rev. B* **100**, 041202 (4 2019).
269. Barbary, K. *Julia library for 1-d and 2-d splines* <https://github.com/kbarbary/Dierckx.jl> (Aug. 2, 2019).
270. *Solve the N-D time-independent Schrödinger equation for a single particle* <https://github.com/RedPointyJackson/Brooglie> (Aug. 2, 2019).
271. Bystrom, K. *Parallel C/Python package for numerical analysis of PAW DFT wavefunctions* <https://github.com/kylebystrom/pawpyseed> (Aug. 2, 2019).
272. Leguy, A. M. A. *et al.* Experimental and theoretical optical properties of methylammonium lead halide perovskites. *Nanoscale* **8**, 6317–6327 (12 2016).
273. Aidas, K. *et al.* The Dalton quantum chemistry program system. *Wiley Interdiscip. Rev. Comput. Mol. Sci.* **4**, 269–284 (2014).
274. Douglas, M. & Kroll, N. M. Quantum electrodynamical corrections to the fine structure of helium. *Ann. Phys.* **82**, 89–155 (1974).
275. Chen, E. C. M. & Wentworth, W. E. Negative ion states of the halogens. *J. Phys. Chem.* **89**, 4099–4105 (1985).
276. Finney, A. J. T. *The structure and stability of simple tri-iodides* PhD thesis (University of Tasmania, 1973).
277. Shluger, A. L., Puchin, V. E., Suzuki, T., Tanimura, K. & Itoh, N. Optical transitions of the H centers in alkali halides. *Phys. Rev. B* **52**, 4017–4028 (6 1995).
278. Hughes, A. Zero-phonon transitions and vibrational structure. *J. Phys. Colloq.* **28** (1967).
279. Li, C., Guerrero, A., Huettner, S. & Bisquert, J. Unravelling the role of vacancies in lead halide perovskite through electrical switching of photoluminescence. *Nat. Commun.* **9**, 5113–5113 (2018).
280. Chen, B., Rudd, P. N., Yang, S., Yuan, Y. & Huang, J. Imperfections and their passivation in halide perovskite solar cells. *Chem. Soc. Rev.* **48**, 3842–3867 (14 2019).
281. Whalley, L. *Crystal structures and lattice dynamics data for the iodine interstitial in MAPI* https://github.com/lucydot/MAPI_iodine_vibrations (Aug. 2, 2019).
282. Frost, J. M. *Julia codes to play with phonons* <https://github.com/jarvist/Julia-Phonons> (Aug. 2, 2019).
283. Ledinský, M. *et al.* Raman Spectroscopy of Organic-Inorganic Halide Perovskites. *J. Phys. Chem. Lett.* **6** (2015).
284. B. Morgan. *vasppy: A Python suite for manipulating VASP input and output* <https://doi.org/10.5281/zenodo.1263753> (2018).
285. Ganose, A. M., Jackson, A. J. & Scanlon, D. O. sumo: Command-line tools for plotting and analysis of periodic ab initio calculations. *J. Open Source Softw.* **3** (2018).
286. Fornari, A. & Sutton, C. *Effective Mass Calculator* <https://github.com/afonari/emc> (2012).
287. Ong, S. P. *et al.* Python Materials Genomics (pymatgen): A robust, open-source python library for materials analysis. *Computational Mater. Sci.* **68**, 314–319 (2013).
288. Ingersoll, L. R., Zobel, O. & Ingersoll, A. *Heat conduction with engineering, geological and other applications* (Thames and Hudson, 1948).